



**HAL**  
open science

# Characterization of spinal cord lesions in the marmoset EAE model using MRI and histopathology techniques

Jennifer Lefeuvre

► **To cite this version:**

Jennifer Lefeuvre. Characterization of spinal cord lesions in the marmoset EAE model using MRI and histopathology techniques. Bioengineering. Sorbonne Université; National Institute of Health (États-Unis; 1930-1948), 2019. English. NNT : 2019SORUS208 . tel-03028836

**HAL Id: tel-03028836**

**<https://theses.hal.science/tel-03028836v1>**

Submitted on 27 Nov 2020

**HAL** is a multi-disciplinary open access archive for the deposit and dissemination of scientific research documents, whether they are published or not. The documents may come from teaching and research institutions in France or abroad, or from public or private research centers.

L'archive ouverte pluridisciplinaire **HAL**, est destinée au dépôt et à la diffusion de documents scientifiques de niveau recherche, publiés ou non, émanant des établissements d'enseignement et de recherche français ou étrangers, des laboratoires publics ou privés.



**UNIVERSITE PIERRE ET MARIE CURIE**

**Ecole doctorale N° 158: Cerveau Cognition Comportement  
(ED3C)**

**Characterization of spinal cord lesions in  
the marmoset EAE model using MRI and  
histopathology techniques**

par

**Jennifer Lefeuvre**

Sous la direction de **Daniel S. Reich** et **Stéphane Lehéricy**

Présentée et soutenue publiquement le **2 Juillet 2019**

Devant le jury composé de:

**Rapporteurs:**

Itamar Ronen	Associate Professor, Leiden University - C.J Gorter Center, Netherlands
Jean-Philippe Ranjeva	Professor, Aix-Marseille University - CRMBM, France

**Examineurs:**

Bruno Stankoff	Professor, Sorbonne University - ICM, France
Anne Baron-Van Evercooren	Research director, Inserm - ICM, France
Traian Popa	Senior researcher, Ecole Polytechnique de Lausanne - CNP, Switzerland

**Thesis directors:**

Daniel S. Reich	Principal Investigator - NIH, USA
Stéphane Lehéricy	Professor, Sorbonne University - ICM, France

# *Abstract*

Multiple sclerosis (MS) is a complex multifactorial auto-immune disease which represents the most common cause of non-traumatic disability among young adults (20-40 years old). The lesions, defined by demyelination and inflammatory processes, are the hallmark of MS and frequently found in the spinal cord (up to 90% of the patients affected). Furthermore, the clinical presentation seems to be associated with these spinal cord lesions, including motor-sensory deficits and bladder/bowel dysfunction. Despite successful technical advances in magnetic resonance imaging (MRI) allowing nowadays to visualize precisely the brain lesions, the identification and characterization of spinal cord lesions by MRI remain a difficult challenge due to the small dimensions and the anatomical location of the spinal cord. Consequently, the evolution of spinal cord lesions in MS and their contribution to disease progression remain poorly understood.

To better understand the disease pathophysiology of MS, the experimental autoimmune encephalomyelitis (EAE) model has been developed in several animal species. In contrast to rodent models, the brain of the common marmoset with EAE, a non human primate from South America, displays closer radiological and immunological features with MS. In that context, we investigated the spinal cord of the marmoset EAE model in order to provide new insights into the pathogenesis of the spinal cord lesions.

The main objective of this thesis was to develop and apply new MRI protocols at 7 Tesla in association with histopathological analysis to better identify and characterize the spinal cord lesions, and to understand their spatiotemporal evolution as well as their relation with clinical symptoms. A first postmortem study was conducted and defined two types of lesions along the entire spinal cord length: (1) focal lesions, and (2) subpial lesions, which presented various degrees of demyelination and inflammation. Secondly, in order to adapt to the morphology of the animals, we implemented a robust in vivo experimental setup and created a 12-element phase-array coil. This new setup enabled us to image for the first time the entire spinal cord of a nonhuman primate with EAE. Finally, we conducted a longitudinal MRI study with weekly follow-up scans to measure the progression of the focal and subpial EAE spinal cord lesions during the disease.

Our results demonstrated a strong resemblance to MS focal lesions in terms of shape and distribution. Whereas our knowledge of this subpial lesions in MS spinal cord is very limited, we identified a heterogeneous subpial pathology between animals and along the spinal cord segments. We also found a strong association between the lesion load and the disability scores, similarly to MS. Overall, this thesis brings new findings that highlight the relevance of the spinal cord lesions in the marmoset EAE model for studying the disease mechanisms of spinal cord lesions in MS, and confirms the strength of the marmoset EAE as a pre-clinical model to bridge the gap between rodent EAE and human MS.

# *Résumé*

La sclérose en plaque (SEP) est une maladie auto-immune complexe et multifactorielle qui représente la première cause de handicap non-traumatique chez le jeune adulte (20-40 ans). Les lésions, définies par leur caractère démyelinisant et inflammatoire, sont le trait distinctif de la SEP et sont retrouvées très fréquemment au niveau de la moelle épinière de patients SEP (jusqu'à 90% des patients atteints). De plus, les symptômes cliniques semblent être fortement corrélés avec cette atteinte spinale, incluant des troubles sensori-moteurs, ainsi que des dysfonctionnements de la vessie et des intestins. En dépit des nombreux progrès techniques en imagerie par résonance magnétique (IRM) permettant aujourd'hui de visualiser très précisément les lésions cérébrales, l'identification and caractérisation des lésions de la moelle épinière demeure un challenge difficile de part ses petites dimensions et son emplacement anatomique. Par conséquent, le développement des lésions dans la moelle épinière et le lien avec la progression clinique du patient restent à ce jour fortement méconnus.

Afin de mieux comprendre les mécanismes physiopathologiques de la SEP, le modèle EAE (ou Encéphalomyélite Auto-immune Expérimentale) a été développé chez de nombreuses espèces animales. En regard des modèles murins, le cerveau du marmoset EAE, primate non-humain sud-américain, présente des caractéristiques lésionnelles bien plus proches avec les patients SEP. C'est dans ce contexte que nous nous sommes intéressés à la moelle épinière chez le marmoset EAE afin de mieux comprendre les mécanismes de développement des lésions médullaires.

L'objectif principal de cette thèse a donc été de développer et d'appliquer de nouveaux protocoles IRM à 7 Tesla en association avec des analyses histopathologiques afin de suivre l'évolution spatio-temporelles des lésions médullaires. Notre première étude postmortem nous a permis de distinguer deux types de lésions le long de la moelle épinière: (1) des lésions focales et (2) des lésions subpiales, présentant différents degrés de démyélinisation et d'inflammation. Dans un second temps, afin de nous adapter à la morphologie de l'animal, nous avons mis en place une routine expérimentale robuste ainsi que la création d'une antenne 12-canaux en réseau phasé. Cette nouvelle installation nous a permis, pour la toute première fois, d'imager in vivo la totalité de la moelle épinière de nos primates. Enfin, nous avons mené une étude longitudinale avec un suivi IRM hebdomadaire afin de mesurer la progression des lésions médullaires focales et subpiales au cours de la maladie.

Nos résultats démontrent une forte ressemblance de distribution et de forme des lésions focales en regard de celles retrouvées chez nos patients SEP. Alors que notre connaissance des lésions subpiales médullaires est très limitée chez les patients SEP, nous avons trouvé que ces lésions subpiales chez le marmoset EAE présentent quand à elles une grande hétérogénéité entre les animaux mais également à travers les différents segments de la moelle épinière. Nous avons également mis en évidence une forte corrélation entre la charge lésionnelle médullaire et les scores cliniques, aussi décrit dans la littérature SEP. Nos résultats apportent de nouveaux éléments qui soulignent la pertinence des lésions

---

médullaires chez le marmoset EAE pour étudier les mécanismes de développement des lésions chez les patients SEP. Cette étude permet aussi de confirmer la force de ce modèle pré-clinique pour de combler l'écart entre les modèles murins EAE et la SEP humaine.

# *Acknowledgements*

I would like to express my sincere gratitude to my supervisors to have made this american adventure possible. Pascal and Danny, you have provided me a very exciting and challenging project. Thank you for your support and trust during all those years. I would have never imagined five years ago everything I would have accomplished by now. Thank you to have guided me, and allowed me to have the freedom in exploring and leading this project. My sincere thanks also go to Stéphane Lehericy with whom everything started from my master's internship in 2012 to the co-direction of my thesis, and Mathieu Santin to have let me discovered the experimental aspect of neuroscience and its endless possibilities.

Besides my supervisors, I would like to thank every person that made this project possible. A very special thanks to Afonso Silva for providing the access of the imaging pre-clinical system and the marmosets. His relevant advice helped me along the many steps of my project. Having worked closely with many members of your team was for sure a big part of my project success, especially Wen-Yang Chiang for our long summer afternoons and evenings to create this amazing coil (and very robust, as you promised!!), and Cecil Yen for helping on the technical imaging side. Thanks to Emily Leibovitch for teaching me everything about the animal's preparation and experimentation. Your calm and meticulousness were so appreciable and make things so easy.

I would like to thank Seung-Kwon Ha, our veterinarian histopathologist for teaching me your valuable skills in histopathology. Your patience, tenacity and love for your job are contagious!

I am also very happy to have had the chance to participate to various side projects with Govind Bhagavatheeshwaran. Imaging MS patients added a clinical perspective and motivations that were worthwhile.

Thanks to our postbacs in our laboratory that provide an important support. Special thanks to Nick for helping me developing the technical tools of my studies with all your creativity and hard-working. We spent such a big amount of time at the MRI dreaming of our monkey island.

Thanks to our technician Roger for helping me during all the steps of the implementation of our in vivo experimental setup, the many troubleshoots to figured it out, and for your care with our marmosets.

Thanks to all my labmates, especially Sonya, Varun, Matthew, you were like a second-family to me when I arrived in USA.

Thanks to everyone that contributed to review my thesis and provided guidance from different aspects: Gail to have helped me getting started with your precious edits, Hadar for your inputs on neurology, my good friends: Nicky and Isaac for your last pertinent

---

edits. Isaac, I would never been so grateful when you helped me with my English (which was a lot of work from where I was started...) from when we met at the ICM to getting through my NIH interview process, and finally with reading my thesis report.

I am extremely grateful for every professor that gives me the chance to study and explore the field of medical physics: when I transitioned to midwifery school to a physics major, when I was accepted to Orsay, Paris XI for my Master: a challenging step and an important opportunity; Finally, many thanks to the Pr. Felblinger (IADI, Nancy) for letting me discovering the field of MRI during my bachelor and making sure I am on track along my university years.

In addition to the scientific and professional development, this thesis journey also has been an important personal growth by living abroad far from everyone. It was the most wonderful and difficult experience.

Christian, I could not thank you enough for your optimism and the stability you gave me on the last steps of this thesis. Meeting you on the most difficult year of my thesis with all my craziness could have been a challenge but we went through and I am so excited to see what brings us next (I guarantee you will keep learning neuroscience “by procurement”).

Of course, last but not the least, I would like to thank my mom whom supported me during every single step of this adventure. It may seem obvious to say, but yes, what does not kill you makes you stronger!!! We would have prefer not going through all of that while being far from each other but I am so grateful we avoided the worse. It really makes me realize every simple moment in life is precious.

<b>Abstract</b>	<b>i</b>
<b>Resume</b>	<b>ii</b>
<b>Acknowledgements</b>	<b>iv</b>
<b>List of Figures</b>	<b>x</b>
<b>List of Tables</b>	<b>xiv</b>
<b>Abbreviations</b>	<b>xv</b>
<b>Introduction</b>	<b>xviii</b>
<b>1 Multiple Sclerosis - Background</b>	<b>1</b>
1.1 Multiple Sclerosis - Generalities . . . . .	2
1.1.1 Multiple sclerosis subtypes and clinical courses . . . . .	3
1.1.2 Diagnosis . . . . .	3
1.1.3 Treatments . . . . .	5
1.1.4 Symptoms and disease severity assessment . . . . .	5
1.1.5 Pathogenesis of multiple sclerosis lesions . . . . .	6
1.1.6 Application of ultra-high-field MRI in MS . . . . .	9
1.1.6.1 Basic principles of MRI . . . . .	9
1.1.6.2 Ultra-high-field (7T) MRI in MS . . . . .	12
1.2 Role of the spinal cord . . . . .	16
1.2.1 Spinal cord anatomy . . . . .	16
1.2.2 Spinal cord tract pathways . . . . .	19



1.3	The spinal cord in multiple sclerosis . . . . .	21
1.3.1	Morphology of spinal cord lesions . . . . .	21
1.3.2	Pathogenesis of MS spinal cord lesions . . . . .	23
1.3.3	MRI detection of spinal cord lesions in MS . . . . .	25
1.3.3.1	Challenges for imaging the spinal cord . . . . .	25
1.3.3.2	Spinal cord imaging for clinical practice . . . . .	26
1.3.3.3	Spinal cord imaging at 7T . . . . .	29
1.3.3.4	Spinal cord imaging findings from clinical MS studies . . . . .	32
1.4	Summary . . . . .	34
<b>2</b>	<b>Experimental Autoimmune Encephalomyelitis (EAE) models</b>	<b>35</b>
2.1	EAE models . . . . .	36
2.1.1	Introduction . . . . .	36
2.1.2	EAE immunization protocols . . . . .	37
2.1.3	Rodent EAE models . . . . .	38
2.2	Marmoset EAE models . . . . .	41
2.2.1	Generalities . . . . .	41
2.2.2	Clinical and pathological findings . . . . .	42
2.2.3	Imaging findings . . . . .	45
2.3	The marmoset spinal cord . . . . .	49
2.3.1	Spinal cord anatomy – functional structures . . . . .	49
2.3.2	Pathological features in the marmoset EAE spinal cord . . . . .	51
2.4	Summary . . . . .	53
<b>3</b>	<b>Combined postmortem MRI and histopathology study of spinal cord lesions in the marmoset EAE model</b>	<b>54</b>
3.1	Introduction . . . . .	55
3.2	Materials and Methods . . . . .	55
3.2.1	EAE induction . . . . .	55
3.2.2	Sample preparation . . . . .	56
3.2.3	MRI acquisition . . . . .	57
3.2.4	Image analysis . . . . .	58
3.2.5	Histopathology . . . . .	59
3.2.6	MRI-histopathological comparison . . . . .	60
3.2.7	Statistical analysis . . . . .	61
3.3	Results . . . . .	63
3.3.1	Advantages of spinal cord extraction for improved image quality . . . . .	63

3.3.2	Evolution of spinal cord-related EAE neurological symptoms . . . . .	65
3.3.3	Characterization of spinal cord lesions by MRI and histopathology confirmation . . . . .	66
3.3.4	MRI signal-histopathology features correlation . . . . .	69
3.4	Discussion . . . . .	73
3.5	Conclusions . . . . .	75
<b>4</b>	<b>Technical development for imaging in vivo the spinal cord of marmoset</b>	<b>76</b>
4.1	Introduction . . . . .	77
4.2	Materials and Methods . . . . .	79
4.2.1	General . . . . .	79
4.2.1.1	Animals . . . . .	79
4.2.1.2	MRI equipment setup . . . . .	80
4.2.1.3	Animal preparation . . . . .	80
4.2.2	Customized MRI hardware . . . . .	81
4.2.2.1	Construction of a marmoset-shaped (brain spinal cord) MRI phantom . . . . .	81
4.2.2.2	Construction of the spine coil array and its customized marmoset-shaped cradle . . . . .	83
4.2.2.3	Imaging evaluation of the coil performances . . . . .	84
4.3	Results . . . . .	87
4.3.1	Advantages of the animal imaging setup . . . . .	87
4.3.2	Sensitivity of the 12-element phased-array . . . . .	87
4.4	Discussion . . . . .	92
4.5	Conclusion . . . . .	93
<b>5</b>	<b>Spatiotemporal evolution of the spinal cord lesions in the marmoset EAE model</b>	<b>94</b>
5.1	Introduction . . . . .	95
5.2	Materials and Methods . . . . .	96
5.2.1	Study Design . . . . .	96
5.2.2	Image processing and analysis . . . . .	99
5.2.2.1	Image processing . . . . .	99
5.2.2.2	Image analysis . . . . .	100
5.2.3	Correlation between clinical scores and spinal cord abnormalities . . . . .	103
5.2.4	Histopathological analysis . . . . .	104
5.3	Results . . . . .	106

5.3.1	Evolution of spinal cord-related EAE neurological symptoms . . . . .	106
5.3.2	In vivo lesion analysis . . . . .	108
5.3.2.1	Spatiotemporal evolution of focal lesions . . . . .	108
5.3.2.2	Spatiotemporal evolution of subpial lesions . . . . .	113
5.3.3	Analysis of MRI findings and disability . . . . .	121
5.3.3.1	Correlations between MRI findings and disability scores for the whole marmoset cohort . . . . .	121
5.3.3.2	Associations between lesion location and clinical symptoms at the individual level . . . . .	122
5.3.4	Postmortem lesion analysis . . . . .	124
5.3.4.1	Histopathology description by animal and lesion age group . . . . .	124
5.3.4.2	Quantitative analysis for myelin and inflammatory cells contents . . . . .	132
5.4	Discussions . . . . .	135
5.5	Conclusion . . . . .	139
<b>6</b>	<b>Discussion and future perspectives</b>	<b>140</b>
6.1	Summary . . . . .	141
6.2	Current challenges and proposed solutions . . . . .	142
6.2.1	Difficult detection of early subpial lesion . . . . .	142
6.2.2	Poor reliability for lesion volume/CSA measurements . . . . .	142
6.2.3	Lack of specific MRI information . . . . .	144
6.2.4	Long acquisition times of in vivo MRI sequences . . . . .	146
6.2.5	Incomplete coverage of the CNS . . . . .	147
6.2.6	Tedious manual segmentation . . . . .	147
6.2.7	Variable, and sometime very short, disease course . . . . .	148
6.3	Perspectives . . . . .	150
	<b>Publications and communications</b>	<b>152</b>
<b>A</b>	<b>Additional Figures</b>	<b>153</b>
A.1	Chapter 3: additional figures . . . . .	153
<b>B</b>	<b>Additional Tables</b>	<b>155</b>
B.1	Tables for Chapter 3 . . . . .	155
<b>C</b>	<b>Additional Methods</b>	<b>156</b>
C.1	Chapter 3: methods for histopathology . . . . .	156

<b>D Published Manuscript</b>	<b>158</b>
D.1 Article . . . . .	158
<b>Bibliography</b>	<b>169</b>

## LIST OF FIGURES

1.1	Topography of MS lesions across the entire CNS . . . . .	2
1.2	MS disease courses: the 2013 revisions . . . . .	4
1.3	Clinical evolution of MS related to inflammation and neurodegeneration . . . . .	7
1.4	Examples of histopathological MS brain lesions . . . . .	8
1.5	Neuropathological classification criteria . . . . .	8
1.6	Excitation and relaxations processes . . . . .	10
1.7	Fast spin-echo pulse sequence . . . . .	11
1.8	T2* GRE imaging features for MS lesions at 7T . . . . .	13
1.9	MP2RAGE sequence image quality improvement at 7T and visualization of lesion subtypes . . . . .	15
1.10	Cross-sectional anatomy of the spinal cord and its surrounding tissues . . . . .	16
1.11	Spinal cord levels respective to the exit of their corresponding spinal nerves . . . . .	17
1.12	Spinal cord cross sections at different cord levels . . . . .	18
1.13	Spinal cord vasculature . . . . .	19
1.14	Spinal cord tracts . . . . .	20
1.15	Morphology of spinal cord lesions . . . . .	22
1.16	MS spinal cord lesion activity through histopathology . . . . .	24
1.17	Demyelination patterns in the MS spinal cord . . . . .	24
1.18	Types of motion artifacts . . . . .	26
1.19	Recommendations for routine spinal cord imaging . . . . .	27
1.20	Comparison of 3T imaging sequences of the MS cervical cord . . . . .	28
1.21	Improvement of lesion visualization with MP2RAGE at 3T . . . . .	29
1.22	Image quality of the cervical spinal cord at 3T and 7T . . . . .	31
1.23	MS cervical cord lesions at 7T . . . . .	31
1.24	MS thoracic cord lesions at 7T . . . . .	32
2.1	Summary of clinical and pathological findings across EAE animal species . . . . .	37
2.2	Processes for obtaining the CNS elements for EAE immunization . . . . .	38
2.3	EAE score for rodent EAE . . . . .	38
2.4	Spinal cord histopathology in the DA rat EAE model . . . . .	39
2.5	CNS lesion distribution in MS and rodent EAE models . . . . .	41
2.6	Histopathological features for an acute lesion in the marmoset EAE model . . . . .	43
2.7	Cortical lesions in the marmoset EAE model . . . . .	44

2.8	Multi-contrast imaging sequences of the marmoset brain . . . . .	45
2.9	Matching between in vivo MRI, ex vivo MRI and histology of the marmoset brain . . . . .	46
2.10	Radiological features of the marmoset EAE brain . . . . .	47
2.11	In vivo serial MRIs of representative subacute and late subacute lesions in the marmoset EAE model . . . . .	48
2.12	The clinico-radiological paradox of the marmoset EAE brain . . . . .	49
2.13	Subdivision of the mammalian spinal cord . . . . .	50
2.14	Corticospinal tracts location between species . . . . .	51
2.15	Spinal cord pathological features in a marmoset EAE model . . . . .	52
3.1	Preparation of spinal cord tissue for postmortem MRI. . . . .	57
3.2	Segmentation methodology of subpial lesions . . . . .	59
3.3	Analysis pipeline between ex vivo MRI and histopathology findings . . . . .	60
3.4	ROIs analysis between the coregistered MRI and the LFB . . . . .	61
3.5	Nested design from the MRI-histopathology data analysis . . . . .	62
3.6	MRI image quality before and after spinal cord extraction. . . . .	64
3.7	Evolution of EAE score and body weight during the disease course . . . . .	66
3.8	High-resolution spinal cord postmortem MRI from EAE animals . . . . .	67
3.9	Comparisons between MRI-histopathology . . . . .	69
3.10	Representative examples displaying heterogeneity of MRI contrast and histopathology contents . . . . .	70
3.11	Correlation between MRI contrast values and histopathology scores . . . . .	70
3.12	The effect of correcting for random effect on the relationship between MRI and LFB signal . . . . .	72
3.13	The effect of manual MRI standardization correction on the relationship between MRI and LFB signal . . . . .	72
4.1	The first human phased-array prototype for spinal cord imaging from Roemer et al. (1990) . . . . .	78
4.2	19-element receive phased-array for human cervical spinal cord imaging . . . . .	78
4.3	Workflow for building the marmoset-shaped MRI phantom and cradle . . . . .	82
4.4	The 12-element phased-array marmoset spine coil . . . . .	84
4.5	Illustration of the data acquisition regarding the respiratory cycle respective to the sequence parameters . . . . .	87
4.6	In vivo MRI coverage of the entire marmoset spinal cord . . . . .	88
4.7	Mid-sagittal sensitivity profiles of the 12-element phased-array spine coil used with a MRI phantom . . . . .	89
4.8	Mid-sagittal sensitivity profiles of the 12-element phased-array coil with in vivo marmoset . . . . .	89
4.9	Mid-sagittal high-resolution PD-w 2D RARE images . . . . .	90
4.10	Axial high-resolution PD-w 2D RARE images with enlarged views . . . . .	91
5.1	Workflow of the co-registration pipeline for spinal cord realignment . . . . .	100
5.2	Examples of focal and subpial lesions . . . . .	101
5.3	Semi-quantitative methods for subpial lesion assessment . . . . .	102
5.4	Semi-automated segmentation for assessment of subpial lesions . . . . .	103

5.5	Temporal changes of the EAE/mEDSS scores and body weight during the course of the disease . . . . .	107
5.6	Evolution of the number of focal abnormalities . . . . .	108
5.7	Temporal evolution of the lesion area for selected focal lesions . . . . .	109
5.8	Serial in vivo axial PD-w of lesions visible on a single slice . . . . .	110
5.9	Serial in vivo axial PD-w of lesions visible on two consecutive slices . . . . .	111
5.10	Spatiotemporal evolution of a lesion visible on four consecutive slices . . . . .	112
5.11	Percentage of slices affected by subpial lesions across animals . . . . .	113
5.12	Boxplot of the cord cross-sectional area along the three spinal levels . . . . .	116
5.13	Evolution of the cross-sectional area at the cervical level along the time points for M#2 . . . . .	117
5.14	Evolution of the cross-sectional area at the thoracic level along the time points for M#2 . . . . .	118
5.15	Evolution of the cross-sectional area at the lumbar level along the time points for M#2 . . . . .	119
5.16	Evolution of the CSA changes on the terminal MRI across the spinal levels	120
5.17	Association between the EAE and mEDSS scores with teh total number of focal lesions . . . . .	121
5.18	Representative histopathological images of two early acute lesions . . . . .	126
5.19	Representative histopathological images of two acute lesions . . . . .	128
5.20	Representative histopathological images of two subacute lesions . . . . .	129
5.21	Representative histopathological images of a lesion from animal M#3 . . . . .	130
5.22	Evolution of the white matter myelin content based on the lesion age . . . . .	131
5.23	Quantification of LFB and PLP myelin density for selected lesions . . . . .	133
5.24	Quantification of Iba-1 and MRP14 inflammatory cells density for selected lesions . . . . .	134
6.1	Increased visualization of the MS lesions at the cord edge with MP2RAGE	143
6.2	in vivo artifacts affecting the CSA measurement . . . . .	143
6.3	Improved image quality with MP2RAGE for a more reliable CSA measurement	144
6.4	Signal losses with T2*-w GRE sequence in healthy marmoset . . . . .	145
6.5	Preliminary segmentation results using a supervised neural network model .	148
6.6	Comparisons of disease duration between marmoset EAE studies . . . . .	149
A.1	Validation of blood deposits by iron-Turnbull staining . . . . .	153
A.2	Regression fit from the mixed-effect model $M_2$ for myelin . . . . .	154
A.3	Relationship between the MRI signal and the histopathology cellular density	154

## LIST OF TABLES

3.1	Demographic and clinical information of the five marmosets included in the postmortem EAE study. . . . .	56
3.2	Sequence parameters of the 3D T2*-w GRE sequences for the two ex vivo MRI protocols. . . . .	58
3.4	Postmortem characterization of the subpial lesions for selected spinal levels	67
3.3	Characterization of the focal lesions by spinal cord level, size, and white matter location in the four marmosets with EAE. . . . .	68
3.5	Summary of the different regression models . . . . .	71
3.6	Results of the linear mixed-effect model M2 for the LFB . . . . .	71
4.1	MRI sequence parameters for building the custom MRI hardware and the different in vivo imaging protocols . . . . .	86
5.1	Demographic and clinical information of the five EAE animals included in the longitudinal study . . . . .	97
5.2	EAE score for clinical assessment of marmosets from Kap et al. (2008) . . .	98
5.3	mEDSS score for clinical assessment of EAE marmosets adapted from Villoslada et al. (2000) . . . . .	98
5.4	Classification of the selected MRI lesions by lesion age groups and by location for each animal . . . . .	105
5.5	Correlation between MRI findings by spinal cord level and disability scores	122
5.6	Correlation between MRI abnormalities by WM columns and disability scores	122
B.1	Contrast lesion-to-GM values with the corresponding myelin and inflammatory score for individual lesions . . . . .	155



## Symbols

$\vec{M}_0$	net magnetization at equilibrium
$\vec{M}_{xy}$	transverse magnetization
$\vec{M}_z$	longitudinal magnetization
<b>T</b>	Tesla
<b>T1</b>	spin-lattice relaxation time
<b>T2</b>	spin-spin relaxation time

## Abbreviations

<b>AMF</b>	Anterior Median Fissure
<b>BBB</b>	Blood-Brain Barrier
<b>CNS</b>	Central Nervous System
<b>CSF</b>	CerebroSpinal Fluid
<b>CIS</b>	Clinically Isolated Syndrome
<b>CD</b>	Cluster of Differentiation
<b>CFA</b>	Complete Freund Adjuvant
<b>CNR</b>	Contrast-to-Noise Ratio
<b>CSA</b>	Cross-Sectional Area
<b>EDSS</b>	Expanded Disability Status Scale
<b>EAE</b>	Experimental Autoimmune Encephalomyelitis

<b>FSE</b>	Fast Spin-Echo
<b>FSS</b>	Functional System Score
<b>GRE</b>	Gradient Echo
<b>GM</b>	Gray Matter
<b>IFA</b>	Incomplete Freund Adjuvant
<b>LFB-PAS</b>	Luxol Fast Blue-Periodic Acid Schiff
<b>MRI</b>	Magnetic Resonance Imaging
<b>MPRAGE</b>	Magnetization Prepared Rapid Acquisition Gradient Echo
<b>mEDSS</b>	marmoset Expanded Disability Status Scale
<b>MEDIC</b>	Multi-Echo Data Image combination
<b>MS</b>	Multiple Sclerosis
<b>MBP</b>	Myelin Basic Protein
<b>MOG</b>	Myelin Oligodendrocyte Glycoprotein
<b>PLP</b>	Proteolipid Protein
<b>NAWM</b>	Normal Appearing White Matter
<b>PI</b>	Post-immunization
<b>PPMS</b>	Primary Progressive multiple sclerosis
<b>PD</b>	Proton Density
<b>RF</b>	Radiofrequency
<b>RARE</b>	Rapid Acquisition with Relaxation Enhancement
<b>rhMOG</b>	recombinant human Myelin Oligodendrocyte Glycoprotein
<b>RRMS</b>	Relapsing-Remitting multiple sclerosis
<b>TE</b>	Echo Time
<b>TR</b>	Repetition Time
<b>SPMS</b>	Secondary Progressive multiple sclerosis
<b>STIR</b>	Short-TI Inversion Recovery
<b>SNR</b>	Signal-to-Noise Ratio
<b>SAR</b>	Specific Absorption Ratio
<b>SE</b>	Spin-Echo
<b>SC</b>	Spinal Cord
<b>T1-w</b>	T1-weighted
<b>WM</b>	White Matter

Multiple sclerosis (MS) is a chronic auto-immune disease that affects the entire central nervous system. The disease is characterized by a complex underlying pathology, composed of inflammatory, demyelinating and neurodegenerative processes. Most of the patients develop clinical symptoms associated with spinal cord damage, such as poor discoordination, sensory disturbances, spasticity, bladder and bowel dysfunctions. Technical advances, including multimodal imaging of the brain at ultra-high field (7 Tesla), have provided new insights into the pathophysiology of lesion development in the brain. However, the spinal cord is a more complex organ to image compared to the brain, and therefore the spatiotemporal development of spinal cord lesions *in vivo* in MS remains poorly understood.

The experimental autoimmune encephalomyelitis (EAE) model is the most commonly used experimental animal model for studying MS and related auto-immune inflammatory diseases. Rodent EAE models have largely contributed to our understanding of inflammation and immune-mediated injury. However, these models have limited capacity to recapitulate MS pathology and are largely unsuccessful when used as a screening tool for MS therapies. The non human primate, the marmoset EAE model shows a closer similarity with MS in terms of radiological, pathological and immunological features. Although the brain of marmoset immunized with EAE has been well investigated using both MRI and histopathology, spinal cord involvement in these animals has never been characterized using MRI. Studying the progression of the spinal cord lesions *in vivo* using this model gives us the opportunity to look into the early stages of lesions evolution, which is rarely possible in MS.

My research project has been conducted at the Translational Neuroradiology Section at the NIH under the supervision of Dr. Daniel S. Reich. The laboratory main research focus is to understand the development of MS by studying focal inflammatory demyelinating lesions of the CNS, which is possible by integrating ultra-high field clinical and animal

MRI, histopathological approaches, and, more recently, molecular studies.

In this project, we used histopathological and MRI techniques to characterize the underlying pathological events of spinal cord lesions in the common marmoset EAE model. To that end, we developed several new methods to image postmortem tissues and to perform serial MRIs that follow the evolution of those lesions during the disease course. This thesis is structured into several parts:

- The first part (chapters 1-2) presents a review of the literature on MS with an emphasis on the role of the spinal cord damage, and on EAE models with a comparison between rodents and marmosets.
- The second part (chapters 3-4-5) describes the different studies conducted in this thesis. Chapter 3 focuses entirely on characterizing the types of spinal cord lesions in the marmoset EAE model using a postmortem MRI-histopathological analysis approach and providing a thorough distribution of the lesion load for a total of four EAE postmortem tissues. Chapter 4 is dedicated to the development and performances of a new in vivo MRI setup, which includes the creation of a phased-array coil integrated into a conformed cradle, and the optimization of MRI sequences. Chapter 5 investigates the spatiotemporal evolution of the different types of spinal cord lesions in three EAE animals using the new in vivo MRI setup, and describes the pathological characteristics of lesions classified by age based on serial in vivo MRIs.
- Finally, the third part (chapter 6) recapitulates the main findings and limitations of this thesis, suggests ways to address these limitations; and offers perspectives for future imaging studies.

# CHAPTER 1

## MULTIPLE SCLEROSIS - BACKGROUND

### This Chapter contains:

1.1	Multiple Sclerosis - Generalities . . . . .	2
1.1.1	Multiple sclerosis subtypes and clinical courses . . . . .	3
1.1.2	Diagnosis . . . . .	3
1.1.3	Treatments . . . . .	5
1.1.4	Symptoms and disease severity assessment . . . . .	5
1.1.5	Pathogenesis of multiple sclerosis lesions . . . . .	6
1.1.6	Application of ultra-high-field MRI in MS . . . . .	9
1.1.6.1	Basic principles of MRI . . . . .	9
1.1.6.2	Ultra-high-field (7T) MRI in MS . . . . .	12
1.2	Role of the spinal cord . . . . .	16
1.2.1	Spinal cord anatomy . . . . .	16
1.2.2	Spinal cord tract pathways . . . . .	19
1.3	The spinal cord in multiple sclerosis . . . . .	21
1.3.1	Morphology of spinal cord lesions . . . . .	21
1.3.2	Pathogenesis of MS spinal cord lesions . . . . .	23
1.3.3	MRI detection of spinal cord lesions in MS . . . . .	25
1.3.3.1	Challenges for imaging the spinal cord . . . . .	25
1.3.3.2	Spinal cord imaging for clinical practice . . . . .	26
1.3.3.3	Spinal cord imaging at 7T . . . . .	29
1.3.3.4	Spinal cord imaging findings from clinical MS studies . . . . .	32
1.4	Summary . . . . .	34

## 1.1 Multiple Sclerosis - Generalities

Multiple sclerosis is an autoimmune disease defined primarily as an inflammatory demyelinating process affecting the entire central nervous system (CNS) and characterized by multifocal lesions in the brain, spinal cord (SC) and optic nerves, as illustrated in Figure 1.1. It is the most common disabling neurological disease among young and middle-aged people with an estimated 2.3 million patients worldwide (Browne et al., 2014). The underlying cause of MS remains elusive, but it is thought that a combination of genetic, environmental and lifestyle factors contribute to the disease development (Reich et al., 2018).

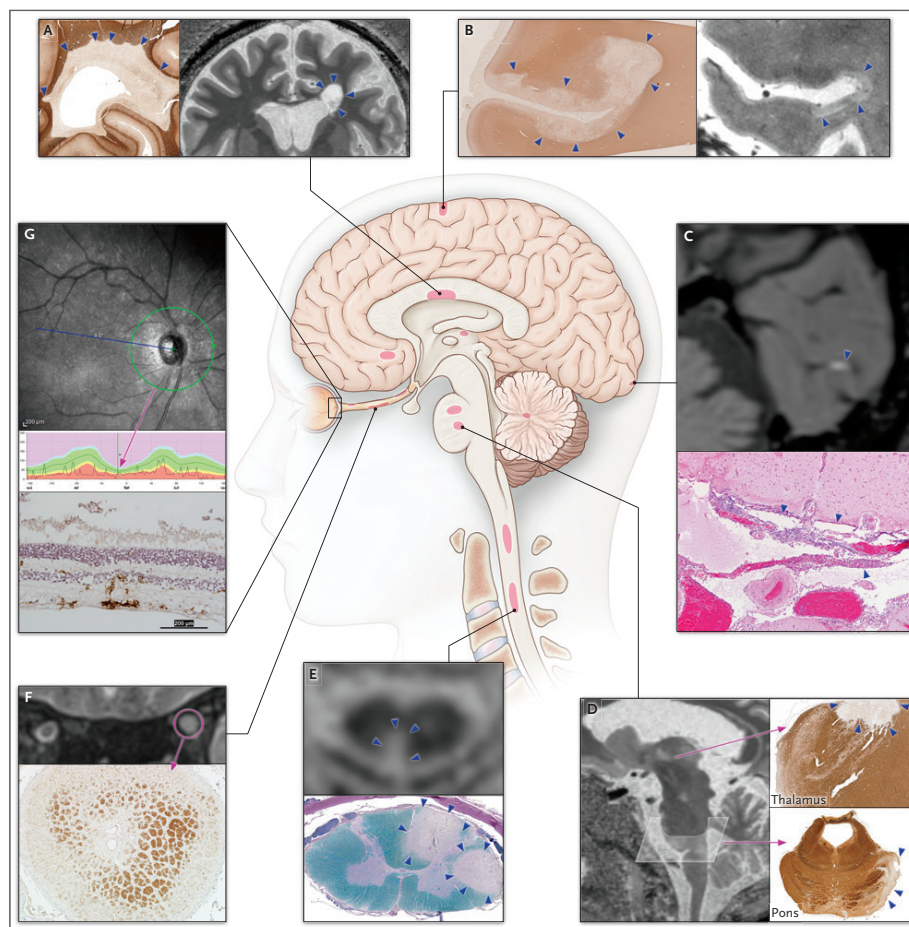


**Figure 1.1:** Topography of MS lesions across the entire CNS: (A) periventricular white matter, (B) subpial cortex, (C) leptomeninges, (D) thalamus and pons, (E) spinal cord, (F) optic nerve, (G) retina. Each lesion location is associated with representative imaging and pathology. Figure from (Reich et al., 2018)

### **1.1.1 Multiple sclerosis subtypes and clinical courses**

There are three primary MS subtypes classified according to the clinical course of the disease (Figure 1.2) (Lublin et al., 1996, 2014). The most common subtype, which affects 85% of patients, is the relapsing-remitting (RRMS) course, defined by periods of exacerbation with the appearance of new or worsening neurologic symptoms (relapses), alternated with periods of partial or complete recovery (remissions). Over 50% of people who are diagnosed with RRMS will eventually transition to a secondary progressive course (SPMS). SPMS is retrospectively diagnosed, defined by at least a year of gradual clinical deterioration and accumulation of neurological deficits irrespective of relapses. 10-20% of patients experience a gradual neurological deterioration from symptom onset, without relapses or remissions, and are diagnosed with primary progressive MS (PPMS).

### **1.1.2 Diagnosis**

The diagnosis of MS is based on neurological symptoms and signs, with the characteristic of dissemination in time (evidence of damage at different time points) and dissemination in space (evidence of damage at different locations of the CNS). In 2001, an international panel of MS specialists established a consensus guideline (McDonald et al., 2001), well-known as the McDonald criteria, and integrated MRI for the first time. Over the years, many revisions were done (Polman et al., 2011; Thompson et al., 2018) with recommendations that now combine clinical and imaging findings, as well biological and immunological markers. The incorporation of these paraclinical investigations has been proved extremely useful for an early and accurate diagnosis (Brownlee et al., 2015).

**2013 DISEASE-COURSE REVISIONS\***

**Relapsing-Remitting (RRMS)** — episodes of acute worsening of neurologic functioning (new symptoms or the worsening of existing symptoms) with total or partial recovery and no apparent progression of disease. RRMS can be further characterized as:

**Active** — showing evidence of new relapses, new gadolinium-enhancing lesions and/or new or enlarging T2 lesions on MRI over a specified time period

**OR**

**Not active** — showing no evidence of disease activity

**AND**

**Worsening** — defined as increased disability confirmed over a specified time period following a relapse

**OR**

**Stable** — defined no evidence of increasing disability over a specified time period following a relapse

**Primary Progressive (PPMS)** — steadily worsening neurologic function from the onset of symptoms without initial relapses or remissions. PPMS can be further characterized as:

**Active** — showing evidence of new relapses, new gadolinium-enhancing lesions and/or new or enlarging T2 lesions on MRI over a specified time period

**OR**

**Not active** — showing no evidence of disease activity

**AND**

**With progression** — evidence of disease worsening on an objective measure of change\*\*, confirmed over a specified period of time, with or without relapses

**OR**

**Without progression** — no evidence of disease worsening on an objective measure of change\*\* over a specified period of time

**Secondary Progressive (SPMS)** — following an initial relapsing-remitting course, the disease becomes more steadily progressive, with or without relapses. SPMS can be further characterized as:

**Active** — showing evidence of new relapses, new gadolinium-enhancing lesions and/or new or enlarging T2 lesions on MRI over a specified time period

**OR**

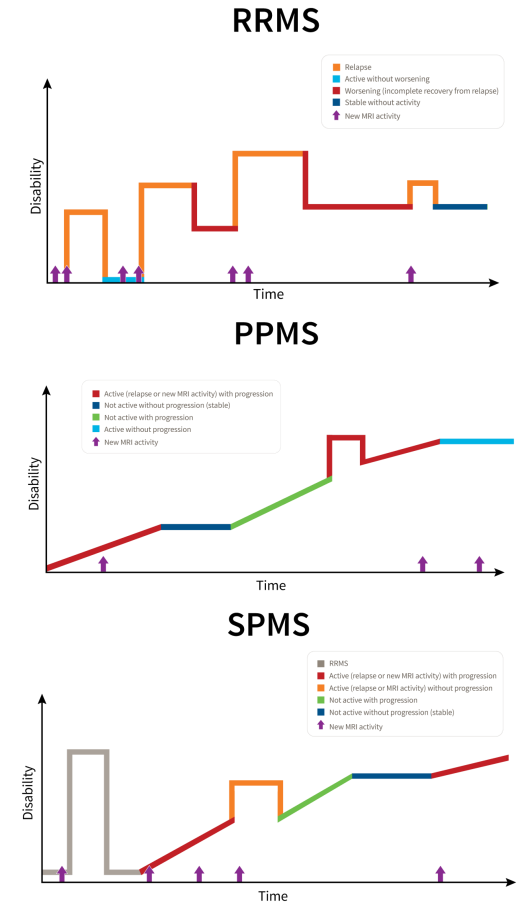
**Not active** — showing no evidence of disease activity

**AND**

**With progression** — evidence of disease worsening on an objective measure of change\*\*, confirmed over a specified period of time, with or without relapses

**OR**

**Without progression** — no evidence of disease worsening on an objective measure of change\*\* over a specified period of time



\* Lublin et al. Defining the clinical course of multiple sclerosis; the 2013 revisions. Neurology 2014;83:278---286.

**Figure 1.2:** Definitions of disease activity and disease progression for the three main disease courses seen in MS. Their respective graphics on the right describe the evolution over time of the disability. Figure adapted from <https://www.nationalmssociety.org/> and Costello et al. (2018)



### 1.1.3 Treatments

Since the 1990s, MS therapies, collectively known as disease-modifying therapies (DMTs) (Costello et al., 2018), are primarily targeted at reducing relapses, and consequently delaying the disability progression. These drugs vary in their efficacy and safety profile and, apart from two drugs, are only approved for the relapsing form. The two drugs currently approved for progressive MS are the anti-neoplastic agent mitoxantrone for SPMS (Boneschi et al., 2013) and anti-CD20 ocrelizumab for PPMS (Montalban et al., 2017). However, the choice of putting a patient on these drugs is not without consequences (Reen et al., 2017). DMTs can be very aggressive with adverse side effects, such as cardiotoxicity and therapy-related acute leukemia for mitoxantrone or an increased risk of developing progressive multifocal leukoencephalopathy (PML) due to the suppression of the immune system during treatment. It is now recognized that misdiagnosis is a recurrent problem that needs to be solved in order to avoid unnecessary side-effects from DMTs treatments and putting patients lives at risk. This ultimately puts more pressure on clinicians to accurately diagnose MS patients since it also has been demonstrated that treating MS patients earlier improves their prognosis.

### 1.1.4 Symptoms and disease severity assessment

The most common signs and symptoms of MS may be general (such as pain, fatigue, cognitive problems) but also more specific based on the location of the lesions within the CNS (tingling and numbness, imbalance, loss of sensation, weakness, paralysis, bladder dysfunction). Indeed, MS lesions may affect many parts of the body simultaneously. To assess the disease severity and quantify the disease progression of MS patients, a neurological examination is performed by a neurologist who will use different clinical scores. The most commonly used score is the Expanded Disability Status Scale (EDSS). The EDSS scale (Kurtzke, 1983) ranges between 0 to 10 where a higher disability corresponds to a higher number. The EDSS is based on measures of impairment in the eight “functional systems”: pyramidal for weakness; cerebellar for ataxia; brainstem for speech, swallowing and nystagmus; sensory for numbness or loss of sensation; bowel and bladder functions; visual function; mental functions.

### 1.1.5 Pathogenesis of multiple sclerosis lesions

The main pathological processes that play a role in the pathogenesis of MS are: inflammation, demyelination, neurodegeneration. Multifocal lesions, which are the pathological hallmark of MS, may have varying contributions from these different pathological processes which may also change over time. The classical view of MS pathology is seen as two disease components: predominant inflammation in the relapsing remitting form; whereas in the progressive form, the permanent damage and deficits are thought to be due to neurodegeneration (Figure 1.3). The pathological mechanisms related to neurodegeneration are not fully understood yet, which explains the lack of treatments for the progressive forms of MS. The pathological mechanisms are a source of controversy due to many inconsistencies in findings and selection bias of the available pathological specimens (mostly longstanding MS, oftentimes PPMS). Thus, it is not clear whether neurodegeneration follows an initial breakdown of the blood-brain barrier (BBB) with inflammation and then destruction of axons afterwards, which is called the “outside-in” (the traditional view); or if a primary cyto-neurodegeneration within the CNS triggers a secondary inflammatory response, called “the inside-out.”

MS lesions can be classified based on their pathological features in three main groups: “active,” “chronic active” and “chronic inactive.” Different criteria exist to assess the ongoing activity occurring within a lesion. Activity is usually associated with inflammatory and/or demyelination. Figure 1.4 shows histopathological sections from different lesions classified according to the criteria by [Kuhlmann et al. \(2017\)](#). Whereas Figure 1.5 recapitulates the criteria used for the classification by [Reynolds et al. \(2011\)](#) which is based on the different stages of demyelination. In this classification, an active demyelination is associated with the presence of myelin degradation products within macrophages. Histopathological assessment of tissues from patients obtained through either biopsies and autopsies is the best method to extensively characterize MS lesions. However, in vivo MRI can also be an useful method to further characterize MS lesions since it provides the temporal information about the lesions that is typically missing in pathological studies. Both methods are therefore complimentary, and when combined together could be an extremely powerful approach to unravel the mechanisms of tissue injury in the different patient subtypes.

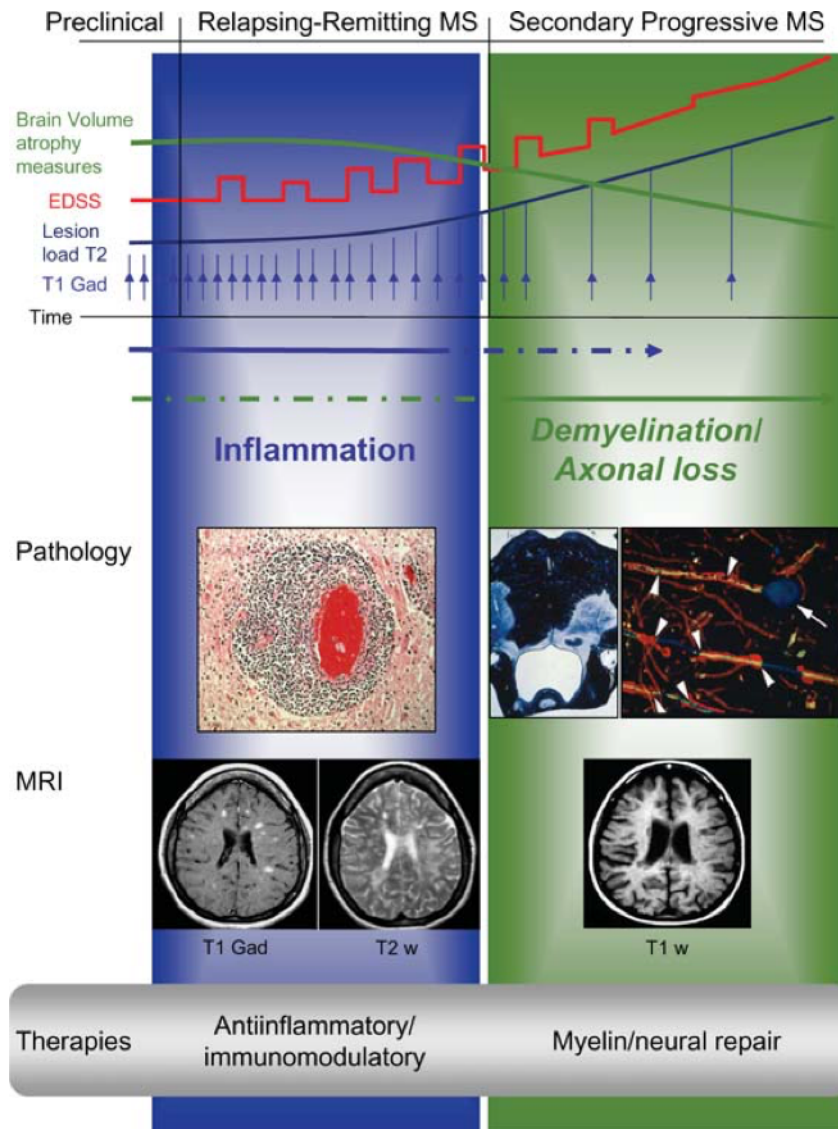


**Figure 1.3:** Summary of the two main types of clinical evolution (relapsing form in blue on the left and progressive form in green on the right) of MS related to their respective main imaging and pathological characteristics. For the relapsing-remitting form, inflammation is the main finding depicted here by perivascular inflammation with an open blood brain barrier on the pathology and associated with gadolinium enhancement on T1-weighted (T1-w) contrast on the imaging. For the progressive form, neurodegeneration is the main finding depicted by demyelination and axonal loss visualized by axonal transections on these pathological sections. Imaging is often associated with atrophy with enlargement of the lateral ventricles seen on this T1-w contrast. Figure adapted from *Sospedra and Martin (2005)*

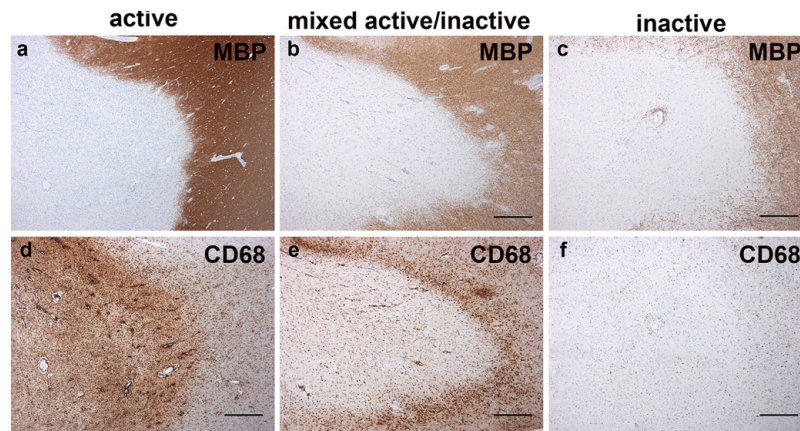


**Figure 1.4:** Example of MS lesions classified according to their different patterns on MBP (for myelin) and CD68 (for inflammation) immunohistochemistry. The active lesion (a, d) is hypercellular with loss of myelin and diffuse dense inflammatory CD68+ cells (activated microglia/macrophages) throughout the entire lesion; the mixed active/inactive lesion (b, e) is demyelinated with a hypocellular center and is defined by a rim of CD68+ cells at the lesion border; the inactive lesion (c, f) is demyelinated and hypocellular with a strongly reduced number of microglia that are absent from the lesion border. Figure adapted from [Kuhlmann et al. \(2017\)](#).

Type of plaque	Key pathological features
Preactive	Aggregates of microglia in absence of or minimal myelin breakdown
Early active	Hypercellularity with microglial activation Alteration in myelin staining Myelin phagocytosis and degradation Luxol-fast blue positive fragments of myelin or positivity for MOG in macrophages Relative axonal preservation Perivascular inflammation
Late active	Variable cellularity Demyelination with myelin and variable oligodendrocyte loss Fat-filled macrophages Astrocytosis Perivascular inflammation (slight) Relative axonal preservation Microglial activation at plaque edge
Chronic active	Hypocellular in lesion centre with hypercellular edge Active myelin breakdown at lesion edge HLA-DR+ macrophages containing early stage myelin breakdown products at lesion edge (LFB or MOG+)
Chronic inactive	Hypocellularity Myelin and oligodendrocyte loss No phagocytosis Paucity of microglia Relative axonal preservation
Shadow	An extensive area of partial reduction in myelin density, often at the edge of a demyelinated lesion Palely staining myelin, caused by reduction in the number and thickness of individual myelin sheaths

(Courtesy of Prof. Dame I Allen, <http://www.ICDNS.org>)

**Figure 1.5:** Classification of pathological changes within MS plaques established by [Reynolds et al. \(2011\)](#) and based on different stages of demyelination.

### 1.1.6 Application of ultra-high-field MRI in MS

Unlike CT or X-ray imaging, MRI is noninvasive (no ionizing radiation) and can provide high resolution images of soft tissues. Therefore, MRI is the modality of choice to image the various anatomical structures and biological changes within the CNS. Since the invention of MRI, which is an application derived from nuclear magnetic resonance (NMR), there have been significant technical advances which have led to improved image quality and increased image resolution, ultimately allowing for a better visualization of the pathology. The increase in strength of the magnetic field has been one of the major technical improvements over time. For clinical use, MRI magnets at 1.5 Tesla (T) and 3T are currently the most common. Ultra-high-field MRI magnets ( $\geq 7$  T) are mostly found at academic research centers, primarily for research applications. However, with the recent FDA-approval of the first 7T MRI, some academic centers recently started to incorporate 7T imaging into their routine clinical use.

#### 1.1.6.1 Basic principles of MRI

Using the fundamental concepts of nuclear resonance, MRI images are obtained by placing the hydrogen nuclei (found in water or lipid molecules, which represent  $\sim 75$ – $80\%$  of the human body) under a strong magnetic field and exciting them with radiofrequency (RF) pulses. By using additional gradient coils, the received signal can be spatially encoded to produce an image of the body. Figure 1.6 recapitulates the principles of MR excitation and relaxation. The signal to be measured is an average magnetic moment of a group of protons and is commonly represented by the vector  $\vec{M}_0$  (Figure 1.6a). An excitation RF  $90^\circ$  pulse will tip  $\vec{M}_0$  within the transverse plane  $xy$  (Figure 1.6b). Once the RF is turned off, the signal will precess to return to its initial equilibrium state, called the relaxation. Simultaneously, the transverse magnetization ( $\vec{M}_{xy}$ ) decays (called the spin-spin relaxation which is a dephasing process caused by the dipolar interactions between spins), the longitudinal magnetization ( $\vec{M}_z$ ) recovers (called the spin-lattice relaxation which allows for the realignment along  $z$  due to the loss of energy initially absorbed by the protons) (Figure 1.6c).

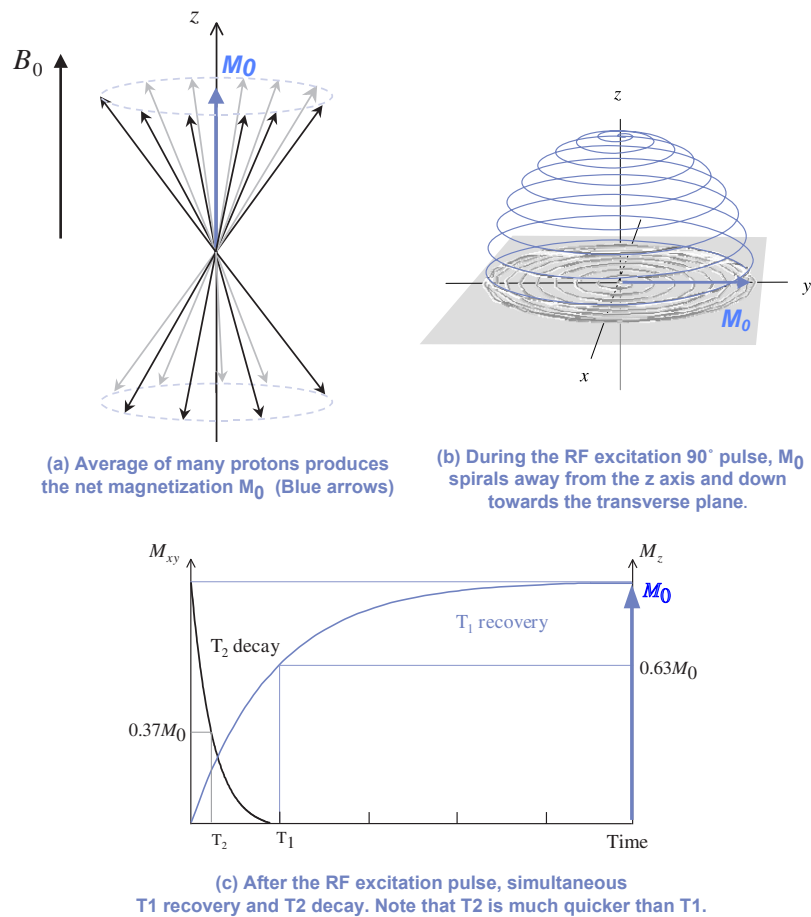


**Figure 1.6:** Schematic of the excitation and relaxations processes. Figure adapted from McRobbie et al. (2006)

Anatomical images can be obtained with different contrasts between tissues, which are based on the tissue biophysical properties (such as proton density (PD), spin-lattice relaxation time ( $T_1$ ), spin-spin relaxation time ( $T_2$ )). For example, an image with a  $T_1$ -weighted ( $T_1$ -w) contrast will enhance the  $T_1$  differences between tissues. The desired contrast is generated by modifying the timings of the different elements of the pulse sequence, such as the time between successive RF excitation pulses (TR: repetition time), and the time between the RF excitation pulse and the MR signal sampling (TE: echo time). The sequence type, obtained by modifying the setting of the RF pulses and gradients, will determine the main characteristics of an image such as its quality in terms of artefacts or the suppression of signal from specific tissues.

MRI sequences can be classified in two main categories: spin-echo based or gradient-echo based. The spin-echo (SE) sequence is the most robust due to its  $180^\circ$  refocusing pulses that allow to reverse the effects of the static field inhomogeneity for a short time. Spin-echo images usually display high image quality although they require a long acquisition time.

One way to acquire faster images is to use a fast spin-echo sequence (FSE), also known as RARE (Rapid Acquisition with Relaxation Enhancement), which uses multiple refocusing pulses to acquire multiple lines at different TE within the same TR. Because multiple echoes are acquired within the k-space, the contrast is dominated by echoes acquired in the center of k-space and called the effective echo time. Figure 1.7 displays the respective pulse sequence for RARE sequence. However, the increased speed comes with some limitations like the restriction in the slice number. Furthermore, a high number of RF refocusing pulses will increase the amount of energy deposited in the tissues (called the specific absorption ratio, SAR) and will generate stimulated echoes which add a component to the signal. Consequently, on the image the fat appears very bright due to the increased T2 signal. Magnetization transfer interactions may occur by off-resonance RF from adjacent slices, which will induce variation in the image contrast. Using fat-suppression techniques and interleaved slice acquisition is commonly used for FSE sequence. The gradient-echo (GRE) sequence uses magnetic gradients instead of refocusing RF pulses, thus reducing significantly the SAR level. Additionally, it allows for the use of small flip angles with a short TR, which can also reduce significantly the acquisition time. However, GRE sequences are highly sensitive to the effect of magnetic field inhomogeneities and do not compensate for the local susceptibility changes (unlike SE sequences). Nonetheless, GRE-based sequences may take advantages of the local tissue susceptibility effects to enhance visualization of blood vessels or iron deposition.

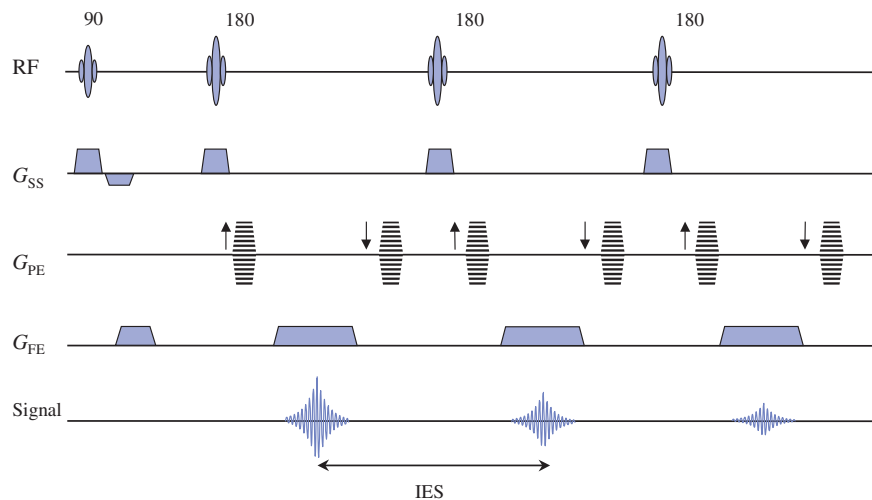


**Figure 1.7:** *Fast spin-echo pulse sequence. In this example, three  $180^\circ$  refocusing pulses are applied (also named turbo factor or echo train length).  $G_{SS}$ : gradient for slice selection (to select the position of the slice);  $G_{PE}$  : gradient for the phase encoding which are different between successive echoes in order to select a different line in the k-space;  $G_{FE}$  : gradient for frequency encoding to collect the signal (also called the readout). IES (inter echo spacing): time between successive echoes. Figure adapted from [McRobbie et al. \(2006\)](#)*

MRI contrasts can be further manipulated by using an inversion-recovery pulse before the application of the RF excitation pulse of any sequence. Applying first a  $180^\circ$  inversion pulse (instead of the initial  $90^\circ$ ) doubles the longitudinal magnetization recovery time, and the time between the  $180^\circ$ - $90^\circ$ , called the inversion time (TI), determines which tissues will be suppressed on the image. Indeed, it is possible to cancel the signal of a specific type of tissue when the longitudinal magnetization of the tissue of interest is null ( $\vec{M}_z=0$ ) at the time the RF excitation pulse. This method allows to cancel the cerebrospinal fluid (CSF) signal as done in the T2-weighted (T2-w) FLAIR (FLuid-Attenuated Inversion Recovery) sequence using relatively long inversion time ( $\sim 2500$  ms). The counterpart of this approach for T1-w imaging is the MPRAGE (Magnetization Prepared Rapid Acquisition Gradient Echo) sequence. An optimized version of MPRAGE has been proposed more recently and combined two gradient-echo images acquired at two different inversion times, called MP2RAGE (Marques et al. 2010). The images obtained with MP2RAGE are independent of  $B_1$  inhomogeneity with a reduction of the proton density and T2\* contributions. Finally, fat tissues can also be suppressed using a STIR T2-w sequence (Short-TI inversion recovery) with relatively short inversion time ( $\sim 150$  ms).

#### **1.1.6.2 Ultra-high-field (7T) MRI in MS**

The MS imaging community has produced several guidelines that recommend standardized MR imaging protocols [MAGNIMS network (Rovira et al., 2015; Wattjes et al., 2015), Consortium of MS Centers (Traboulsee et al., 2016)] for diagnosing and monitoring MS patients with MRI at clinical field strengths (1.5T, 3T). Indeed, MRI is an extremely sensitive paraclinical tool that allows to detect objectively the presence of pathology in the CNS. However, clinical MRI lacks specificity toward the different pathological processes involved in MS lesions. Interestingly, ultra-high-field (7T) MRI can provide new insights into the pathophysiology of the lesion development (Absinta et al. 2016). The increased signal-to-noise ratio (SNR) and the improved contrast between the different CNS tissues allow to visualize anatomical and biological features with higher details, such as blood vessels, microbleeds and small lesions (Duyn, 2012). This is illustrated in Figure 1.8 showing a 7T T2\*-weighted (T2\*-w) GRE image acquired on a MS patient. Additionally, recent 7T studies have triggered a lot of interest in the development of novel imaging biomarkers that would increase the accuracy of the diagnosis. This is particularly important since misdiagnosis of MS has been recognized to be a frequent and recurrent problem in clinical



practice (Solomon and Weinschenker, 2013; Solomon et al., 2019). The following paragraph will present some of these recent 7T MRI findings that are relevant to MS.

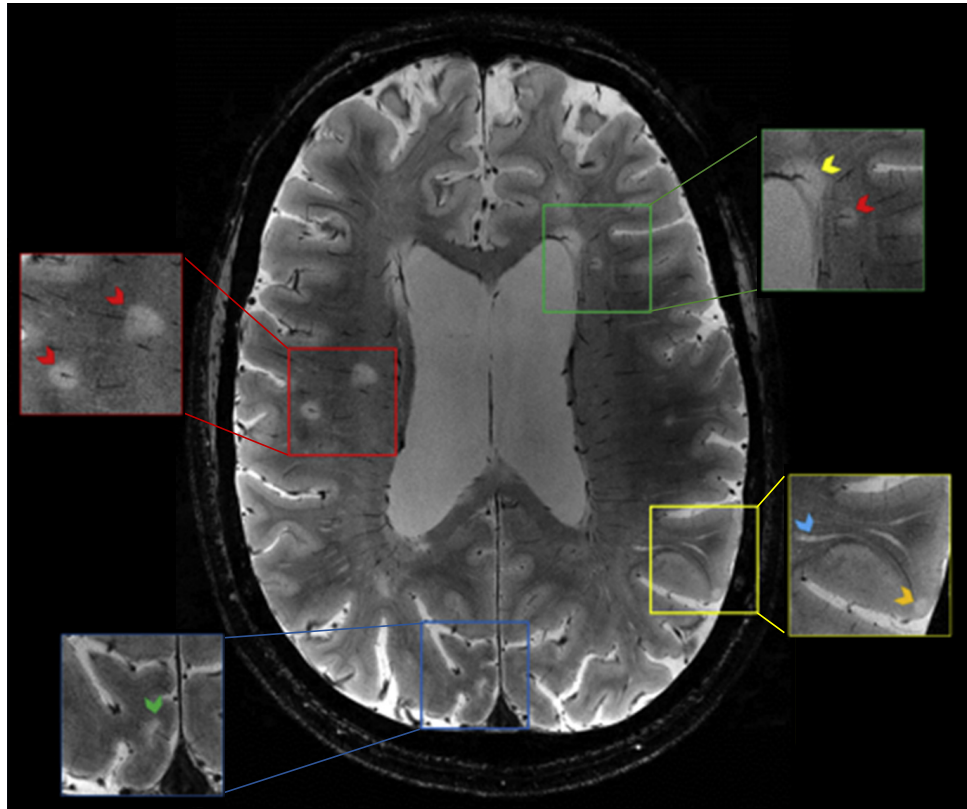


**Figure 1.8:** *T2\*-weighted gradient-echo (GRE) image acquired at 7T on a relapsing-remitting MS patient. Axial brain section depicting representative examples of lesion locations related with the vasculature with magnified view. Green and red boxes: deep WM lesions with the typical central vein (red arrows), and a periventricular lesion with a vein (yellow arrow). Blue box: subcortical lesion with a cortical vein (green arrow). Yellow box: intracortical lesion. Figure adapted from Schindler et al. (2017).*

Cortical demyelinated lesions have been shown to be specific to MS ((Fischer et al., 2013)) and are strongly associated with higher disability and the progressive form of the disease (Kutzelnigg et al., 2005; Calabrese et al., 2013). However, the sensitivity of 3T MRI is limited due to many reasons: the lower myelin density in the cortex (compared to WM) which decreases the contrast between normal cortex and demyelinated lesions, the relatively small size of cortical lesions as well as their low inflammation content compared to WM lesions. It was recently demonstrated that the higher tissue contrast obtained at 7T allows a higher detection and a better characterization of the different subtypes of cortical lesions (intracortical, leukocortical, juxtacortical) using ex vivo imaging (Kilsdonk et al., 2016) and in vivo imaging (Beck et al., 2018). Since subpial lesions constitute up to 60% of the total cortical lesions and may involve all the cortical layers, it would be interesting to study by MRI. However, subpial lesions are the most challenging to image due to their

proximity to the CSF which increases the risk for partial volume effect. Interestingly, sequences with T1-weighting provide the best contrast for the cortical structures ([Haast et al., 2016](#)). Notably, the optimized MP2RAGE sequence, which allows to overcome the field inhomogeneity issues characteristic of ultra-high field MRI, was recently shown to detect and differentiate the different types of cortical lesions ([Beck et al., 2018](#)), as seen on [Figure 1.9](#).

The BBB opening is another pathological event present in MS and is associated with a leakage of inflammatory cells into the parenchyma at the very early stage of lesion development. This event can be visualized by MRI using a T1-w sequence acquired after the injection of gadolinium-based contrast which penetrates the CNS through a compromised BBB and modifies the T1 relaxation time of the surrounding tissue (enhancing lesion). Using dynamic contrast-enhanced MRI, information about the spatiotemporal dynamics of the BBB opening of active lesions can also be obtained. Studies from [Gaitán et al. \(2011, 2013\)](#) described two main patterns of gadolinium enhancement within the WM lesions, centrifugal if leaking from the lesion center, centripetal if leaking at the lesion edge (seen as a ring), with a rapid change from centrifugal to centripetal associated with the growth of the lesion. It was hypothesized in these studies that the active lesions, with a centrifugal pattern, develop around a central inflamed vein.

This central vein can actually be better imaged at higher field strength by using susceptibility-based T2\*-w sequences. The shortening of T2\* relaxation times of venous blood (due to the paramagnetic deoxyhemoglobin) allows to visualize the venous cerebral vasculature with exquisite details at 7T due to the increased susceptibility effects and increase image resolution. Using 7T MRI, MS white matter lesions have been described to have a perivenular configuration, consistent with previous histopathological reports ([Lucchinetti et al., 2000](#)). Several 7T studies have demonstrated that a high percentage of MS lesions shows perivenular topography, whereas non-MS lesions rarely displayed a central vein. As a consequence, recent guidelines from the MAGNIMS and NAIMS consortia ([Sati et al., 2016](#)) have proposed to include the central vein sign as part of the diagnostic criteria for MS.

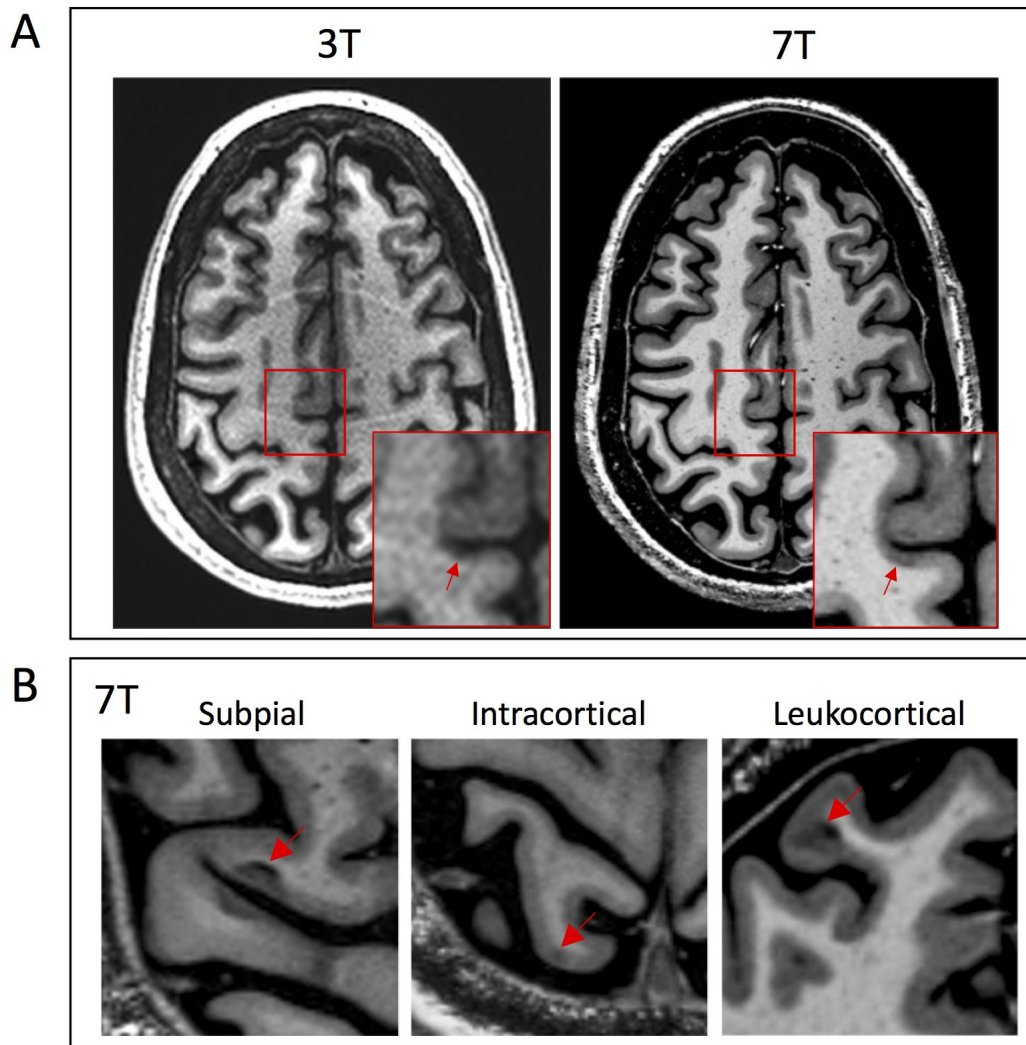


**Figure 1.9:** MP2RAGE sequence image quality improvement at 7T and visualization of lesion subtypes. A. Comparison of the image quality between 3T and 7T of an axial MP2RAGE acquired on a MS patient brain. 3T images ( $1\text{ mm}^3$  isotropic) and 7T image ( $0.5\text{ mm}^3$  isotropic, number of repetitions=4). We can appreciate a more homogeneous signal intensity through the brain, higher contrast and delineation of WM/GM tissues. B. Increased visualization of lesion subtypes at 7T. Pure GM lesions includes the subpial (here seen extending through the entire cortical thickness and intracortical lesions (here seen as small focal lesion), whereas leukocortical lesions involve both the WM and the cortex. Images provided by Erin Beck (MD-PhD) NIH, TNS.

## 1.2 Role of the spinal cord

The spinal cord is a central relay station for sensation, movement, balance and coordination, connecting the different parts of the brain with essentially all other parts of our body. Any injury to the spinal cord could result in a loss of function below the site of injury. As expected, the spinal cord is thought to play an important role in the development of the disease and its severity, despite representing only 2% of the entire CNS.

### 1.2.1 Spinal cord anatomy

Located within the spinal column, which is made of the vertebrae and disks of cartilages (Figure 1.10A), the spinal cord is a long, continuous, thin cylinder made up of different segments. The SC is surrounded by the meninges, which consist of three membranous layers: the most inner layer is the pia mater, which consists of a thin layer of connective tissue and is attached to the surface of the cord; the intermediate layer is the arachnoid mater and contains the CSF; finally, the outer layer is the dura mater, made of a tough, dense membrane, which is separated from the vertebral column by the epidural space. The pia and the arachnoid space are often referred to the leptomeninges. The spinal cord is divided into 4 different segments: cervical (C1-C8), thoracic (T1-T12), lumbar (L1-L5) and sacral, based on the location of the emergence of the 31 pairs of spinal nerves (Figure 1.11). Each spinal nerve is made of a dorsal root conveying the ascending sensory input to the CNS and a ventral root carrying the descending motor output to the muscles and organs.

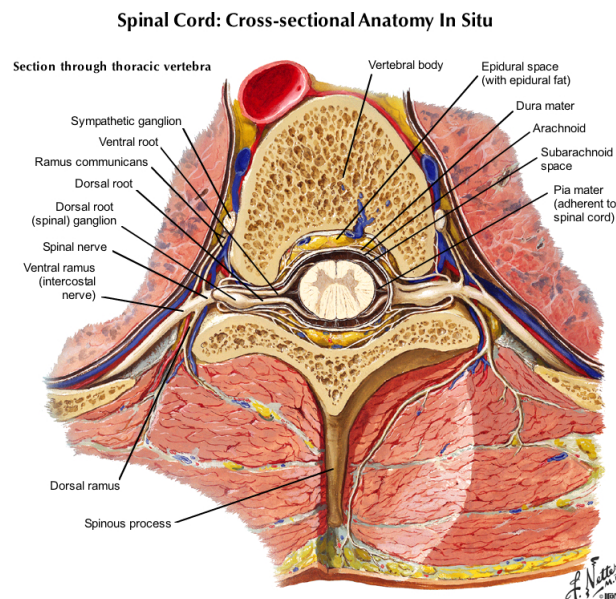


**Figure 1.10:** *Cross-sectional anatomy of the spinal cord and its surrounding tissues (Netter).*

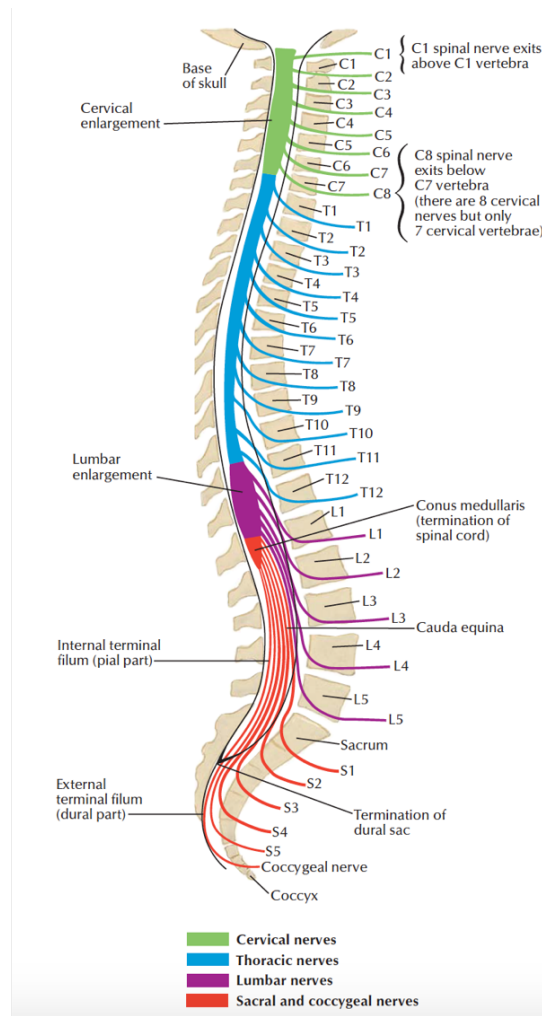


**Figure 1.11:** *The different spinal cord levels respective to the exit of their corresponding spinal nerves (Netter).*

Figure 1.12 shows the anatomical arrangement of the spinal cord in transverse sections across different spinal levels. The spinal cord is composed of the gray matter (GM) in the center with its specific butterfly (or “H”) shape containing the central canal (which includes the CSF), and of the white matter (WM) on the periphery. The spinal cord WM consists mostly of longitudinally-oriented myelinated axons and glial cells subdivided into three main columns. Each column contains organized bundle of nerve fibers, called nerve tracts (Figure 1.14A), which each individual tract being associated to specific functions. The anterior column carries mostly descending motor tracts for voluntary motor control, postural adjustments and an ascending sensory tract for pressure and crude touch. The lateral columns carry some motor tracts located medially and sensory tracts located on the edges. Finally, the posterior column includes mainly pathways to carry proprioceptive information. The posterior and anterior columns are virtually separated from the lateral columns by the posterolateral and anterolateral sulcus, corresponding respectively to the

entrance and exit of the nerve roots. On the ventral side, the anterior median fissure (AMF) separates medially the anterior column and contains a prolongation of the pia matter. On the dorsal side, the posterior median sulcus also separates medially the posterior column and is composed of pial tissues. The spinal cord GM primarily consists of neuronal cell bodies, dendrites, axons and glial cells, organized into successive layers of cells from dorsal to ventral called lamina. The GM also maintains a topographical arrangement with the sensory neurons located in the dorsal horns, and the motor neurons located in the ventral horns.

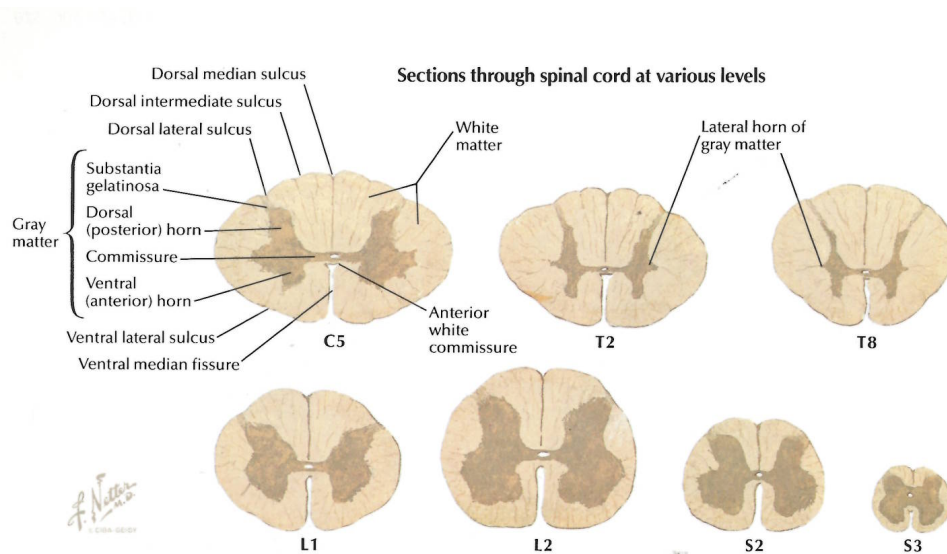


**Figure 1.12:** *Spinal cord structures visualized in cross-sectional orientation at different spinal cord levels (Netter)*

Compared to the brain, the vascular network of the spinal cord is less complicated and well structured. It is composed of an arterial system that supply the spinal cord and a venous system that drain the spinal cord. Both include an extrinsic and intrinsic network vasculatures. As seen in figure 1.13, the extrinsic network, located at the periphery of the cord, consist of large longitudinal arteries (or veins) running along the entire spinal cord length which form an extensive superficial anastomotic network of much smaller caliber expanding around the spinal cord edge. On the anterior side, we can find next to each other the anterior spinal artery and the anterior spinal vein. Whereas, on the posterior side, only a posterior median spinal vein can be found centrally, and more laterally on each side the postero-lateral spinal arteries and veins. The intrinsic network by contrast supply/drain the spinal cord parenchyma. It consists of central arteries/veins originating from the anterior spinal artery/vein and running into the AMF.

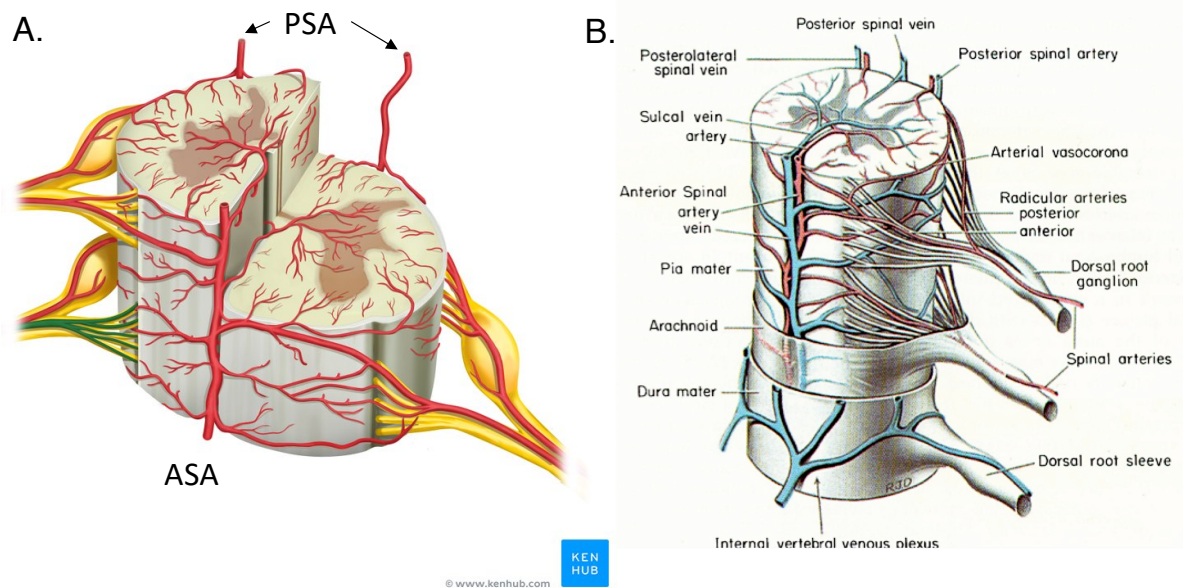


**Figure 1.13:** Vasculature for the spinal cord. A. Arterial network. ASA: anterior spinal artery, PSA: posterior spinal artery. B. Juxtapsed arterial supply (red) and venous drainage (blue).

### 1.2.2 Spinal cord tract pathways

The spinal tracts, also called pathways, consist of a series of neurons that transmit information from one location to a target. Depending on the function of the tract, it will involve various CNS structures (spinal cord, cerebellum, medulla, thalamus, cerebral cortex), illustrated in an example of a pathway in Figure 1.14B.

For the sensory pathways, the signal is carried from the sensing organs or “peripheral” receptors through the spinal cord to the brain structures, which can be either the cerebral cortex with an intermediate relay through the thalamus, or the cerebellum. The main sensory pathways associated with their functions are the following:

- Dorsal column-medial lemniscus system for detection of mechanical stimuli, such as fine touch, vibration, pressure and conscious proprioception;
- Dorsal spinocerebellar pathway for unconscious proprioception;
- Anterolateral system, which includes the lateral spinothalamic and spinothalamic tracts for pain and temperature perception, and the anterior spinothalamic tract for crude touch sensation.

For the motor pathways, the signal is sent from the cortex where the upper motor neurons (UMN) descend at the appropriate spinal level to activate the lower motor neurons located within the dorsal horns. The main motor pathways associated with their functions are the following:

- Corticospinal pathways for voluntary control muscles. This pathway is divided into two separate tracts: the lateral corticospinal tract for movement of limbs and the anterior corticospinal tract for movements of muscles of the trunk. The latter one is not found below the mid-thoracic level;
- Corticobulbar pathway for control of the muscles of the face and head;
- Two other important descending pathways, vestibulospinal and reticulospinal tracts, originate from the brainstem and are involved for the adjustments of posture.

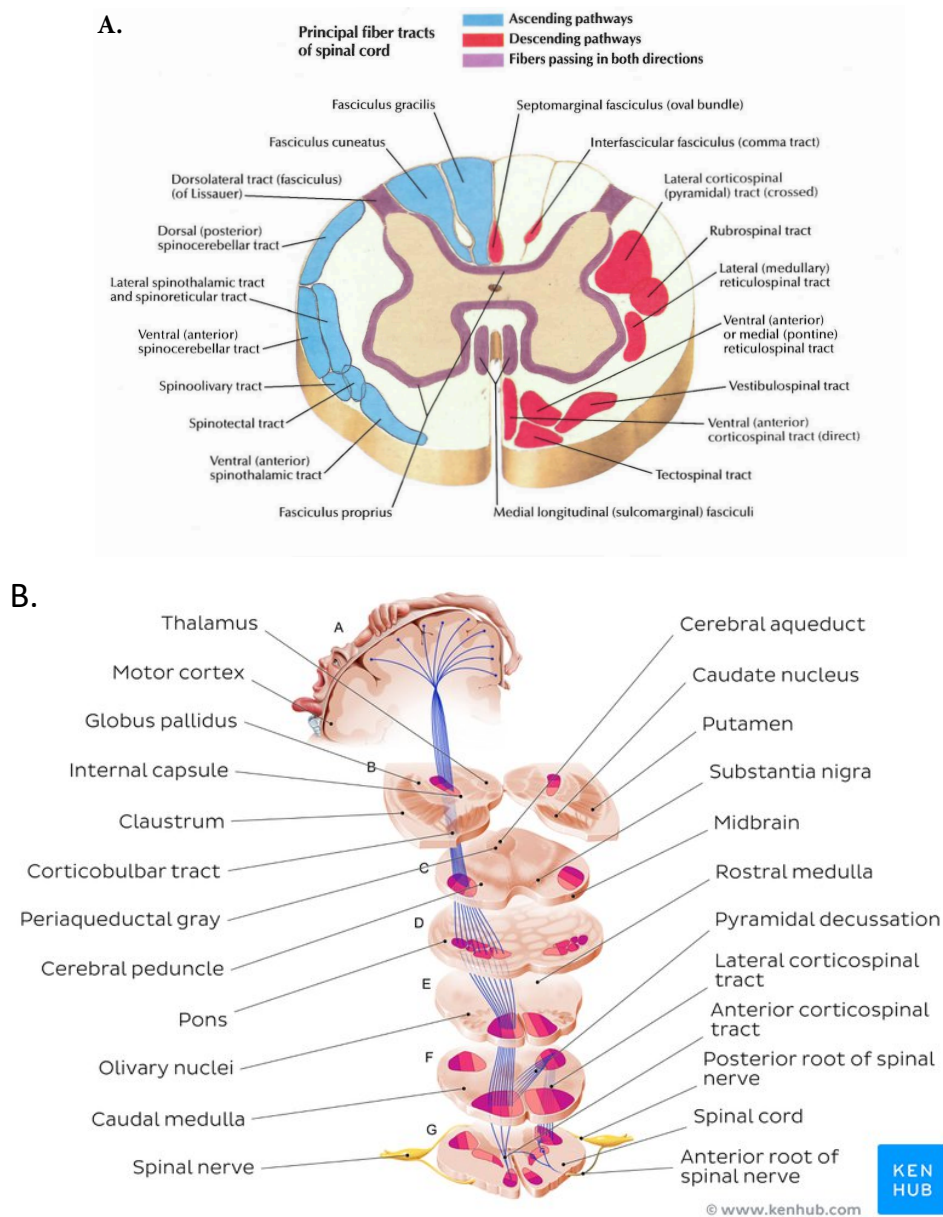


**Figure 1.14:** A. *Principal ascending and descending fiber tracts of the white matter spinal cord (Netter)* B. *Example of the corticospinal tract pathway (www.kenhub.com).*



## 1.3 The spinal cord in multiple sclerosis

### 1.3.1 Morphology of spinal cord lesions

First pathological reports on spinal cord lesions are dated from the mid-20<sup>th</sup> century (Winkelman and Eckel, 1932; Falkiewicz, 1926). Fog (1950) and Oppenheimer (1978) reported in great details the morphology of cord lesions using dissection and histopathology techniques. Fog (1950) analyzed 8 MS cases by staining sections at regular intervals through the entire cord length. He precisely described the shape of the lesions, their longitudinal progression (in the cranio-caudal direction), and their relation to vasculature. An association between the shape of the plaques and the venous distribution pattern was first found by Herren and Alexander (1939), which described that the maximal diameter of the lesion in cross section corresponded to the greater area of a radial vein. In terms of lesion morphology, the spinal cord lesions in MS present a wide range of heterogeneity in shape. Figure 1.15 summarizes the main morphological characteristics of MS WM lesions in the spinal cord.

Within the posterior column, lesions with a large radiating vein were commonly found in the central portion. The wedge-shaped lesion, oval and elongated were the most common types of lesions in the posterior column (Figure 1.15A) (Fog 1950, Oppenheimer 1978). Within the lateral column, the fan-shaped lesion (Figure 1.15B) was the most prominent lesion type, which seemed to progress through the cord length along the veins and occupied more commonly the center and posterior areas. Through the entire cord, small isolated perivascular sleeves may be detected in large numbers, and highly resembled the postinfectious acute encephalomyelitis. Interestingly, narrow bands of demyelination were found between the GM dorsal horn and the lateral surface of the cord. Plaques within the anterior column were found to be symmetric along the AMF (Figure 1.15B). In terms of distribution, MS spinal cord lesions were more commonly found within the lateral, posterior columns, and the central commissure. Rarely, MS lesions would extend to involve the entire spinal cord cross section (Gilmore et al., 2006).

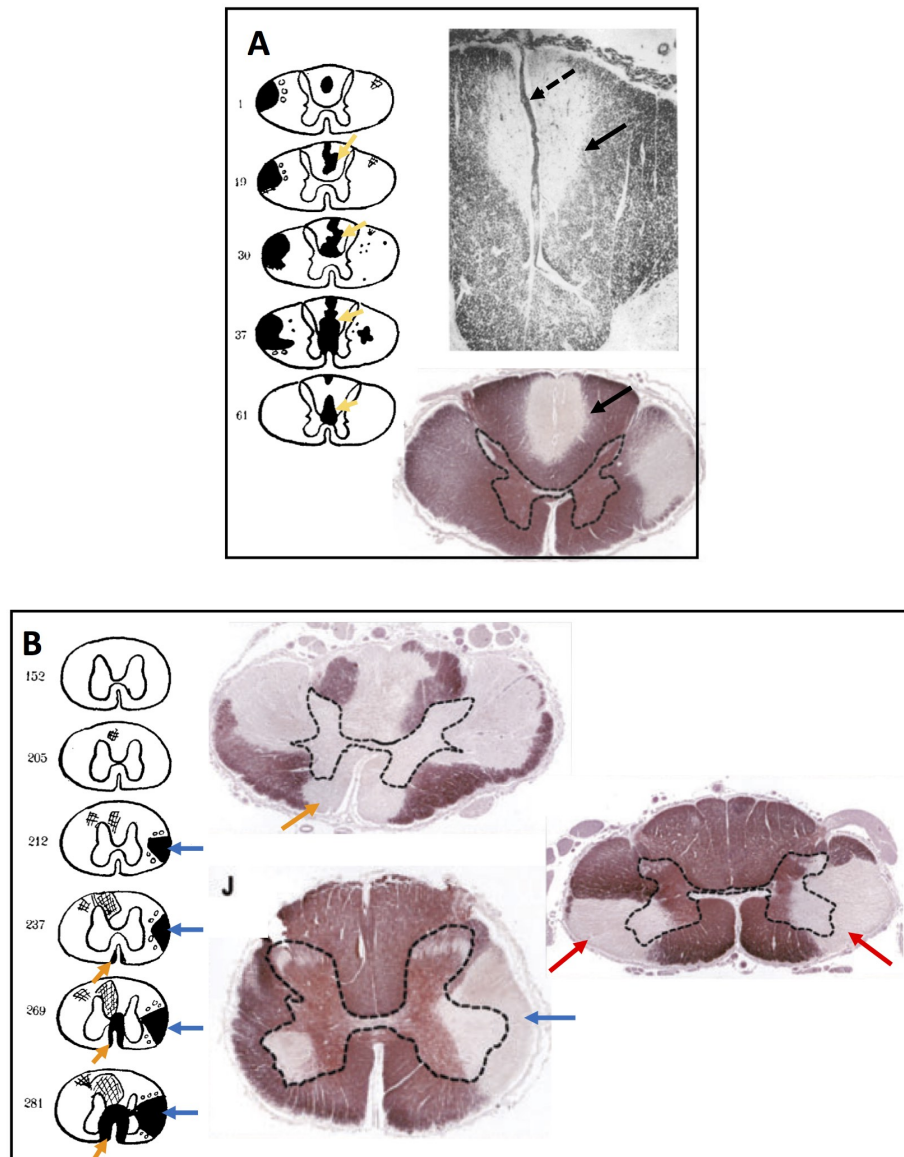


**Figure 1.15:** Spinal cord lesion shapes. Transverse, paraffin embedded cord sections for myelin staining (PLP) at various levels and hand-drawing based on myelin staining of adjacent sections for two MS cords. A. Examples of lesions within the posterior column. The yellow arrows show the spatial evolution (along the long axis of the cord) of an elongated shaped lesion around the posterior median sulcus. The black arrows show a typical lesion within the posterior column related to the radial vein (dotted black arrow). B. Examples of lesion within the anterior column with a typical symmetrical paramedian lesion along the anterior median fissure (orange arrows) and within the lateral column with a fan-shaped lesion (blue arrows) and a wedge-shaped lesion (red arrows). Figure adapted using various figures from [Fog \(1950\)](#), [Oppenheimer \(1978\)](#) and [Gilmore et al. \(2006\)](#).

### 1.3.2 Pathogenesis of MS spinal cord lesions

The main pathological processes that contribute to the development of brain lesions have also been identified in the spinal cord lesions, such as: demyelination, inflammation and axonal loss. However, remyelination has not been well investigated yet in the spinal cord. Studies that attempted to classify the pathological features of spinal cord lesions are based on criteria for brain lesions. There is currently no specific histopathological classification for spinal cord lesions.

[Androdias et al. \(2010\)](#) and [Gilmore et al. \(2009\)](#) classified the spinal cord lesions into three categories: “active”, “chronic active” and “chronic inactive”. The definition of activity was assessed by the degree and pattern of inflammation (defined by MHC class II-positive cells with antibodies against HLA DR, and corresponds to activated macroglia and macrophages) in the demyelinated lesions (Figure 1.16). Active lesions were defined by a dense inflammation through the entire lesion; the chronic active by a dense inflammation at the lesion edge only; and the chronic inactive have a very low or absent inflammation through the entire lesion. [Nijeholt et al. \(2001\)](#) and colleagues found various degrees of demyelination within the WM spinal cord lesions., demonstrated in Figure 1.17. A complete demyelination was associated with a well-demarcated area displaying the typical shape of focal lesions. A partial demyelination was associated with a less well-defined area extending more diffusely. A more diffuse and widespread abnormality was usually found in the primary progressive form of MS. In addition to WM lesions, the spinal cord GM can also display GM damage. In the study from [Gilmore et al. \(2009\)](#), the mixed GM-WM lesions constituted the majority of SC lesions, but pure GM lesions (respect WM-GM border) were also found. [DeLuca et al. \(2013\)](#) found a similar proportion of active lesions throughout the cord length, although the inflammation which extended at the lesion edge (defined by CD3+ T cells density), was more prominent at the cervical cord compared to lumbar cord. In a study from [Androdias et al. \(2010\)](#), which analyzed only C1-C3 cervical cord levels, the density of meningeal inflammatory cells in the spinal cord exceeded the density within the parenchyma by a factor of 15. Within the meninges, T cells were the main finding (both CD4+ and CD8+ T cells, with CD8 predominant), compared to the parenchyma where a diffuse inflammation was marked by CD68+ macrophages/microglia. On the other hand, infiltration by B cells was sparse. These findings were consistent with the study from [DeLuca et al. \(2013\)](#) described above, in which the cord was sampled at all three segments, demonstrated significant meningeal inflammation along the cord length.

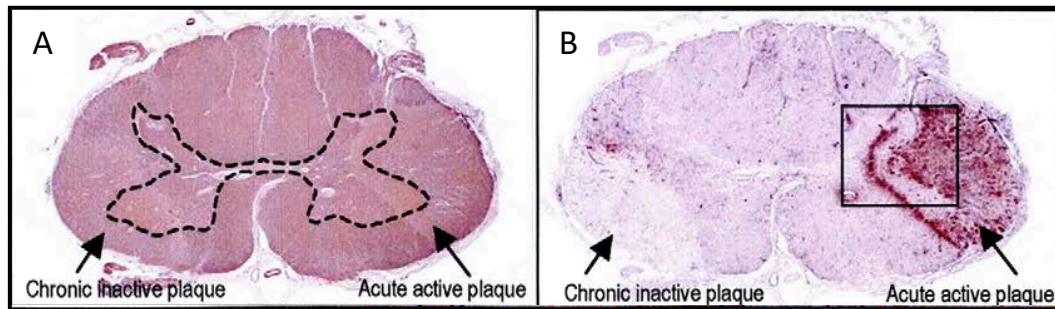


**Figure 1.16:** Histopathology sections displaying different lesion activity types from a MS spinal cord. Myelin is stained using anti-Myelin Basic protein (MBP) (A), and activated microglia/macrophages with anti-HLA DR staining (B). Both lesions on this cord section are a mixed WM/GM lesions. The acute active plaque presents prominent HLA-DR positive stain for the entire WM portion but only at the plaque border for the GM portion. The chronic plaque is defined by the absence of activated microglia/macrophages. Figure adapted from Gilmore et al. (2009).

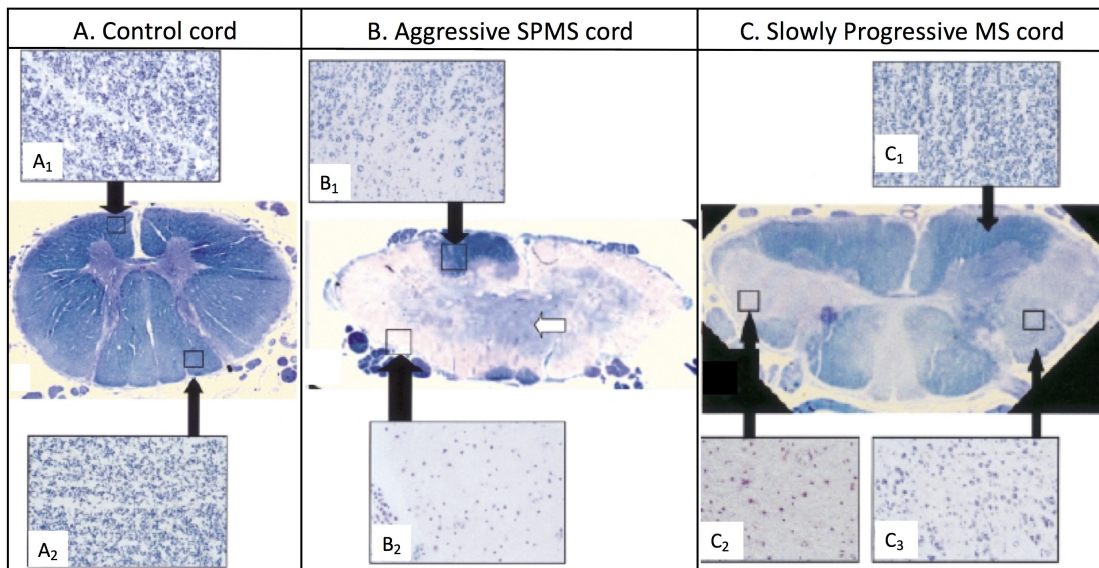


**Figure 1.17:** Demyelination patterns in the spinal cord of MS patients with different disease severity. Sections were stained with Luxol Fast Blue (LFB) with cresyl violet for myelin assessment. A. Control tissue with higher magnification of the anterior column and posterior columns for comparisons with MS cord tissues. B. Extensive complete demyelination ( $B_2$ ) makes difficult to distinguish the GM. Partial demyelination ( $B_1$ ) is seen at the border of the anterior column, where only a small area seems unaffected. C. Focal lesions with different degree of demyelination are found within the same cord section: a wedge-shaped lesion with complete demyelination ( $C_2$ ), and a partial demyelinated area ( $C_3$ ) compared to a control normal appearing WM ( $C_1$ ). Figure adapted from Nijeholt et al. (2001).

However, it is almost impossible to characterize the entire spinal cord through histopathology techniques alone due to the anatomy of the cord (long thin cylindrical structure). Consequently, random sections of the cord are usually analyzed. Obtaining good quality postmortem spinal cord is also an additional challenge due to the complication to extract the cord (compared to the brain). MRI imaging could alleviate some of these challenges. Postmortem MRI may be used to guide the selection of lesions for the histopathology, an approach that had already shown its efficacy to depict a broader range of MS lesion activity in the brain (De Groot et al., 2001).

### 1.3.3 MRI detection of spinal cord lesions in MS

#### 1.3.3.1 Challenges for imaging the spinal cord

Looking at the spinal cord dimensions, its transverse diameter is extremely small with an average 7 mm at the lower lumbar to reach 13 mm for the cervical enlargement (Frostell et al., 2016) for a healthy cord whereas its average length is about 45 cm. These small cross-sectional dimensions require small voxel size ( $\leq 1$  mm of in-plane resolution) with a slice thickness of  $\sim 3$ -5 mm to allow sufficient SNR when imaging the cord in transverse plane. Imaging transverse sections is needed to obtain higher anatomical details of the cord configuration and its potential pathology, but the acquisition time due to the large number of slices may be very long. The composition of the immediate surrounding tissues can also be a source of technical issues since it can hide the spinal cord pathology, depending on which image contrast is applied. The spinal extradural space, located between the dura mater and the vertebral column, contains various substances like connective tissues, ligaments, fat, among others. Cartilaginous/fibrous tissues, like ligaments, have a relatively short T2 ( $\sim 1$ -10 ms) which makes them undetectable on conventional T2-w sequence. However, their relaxation times and susceptibilities will vary based on their orientation with  $B_0$  which, consequently, will induce ultra bright signal at a specific angle, called the magic angle phenomenon. On T2\*-w GRE, the differences in magnetic susceptibility between these tissues and the normal cord may induce signal loss. The CSF with its long T2 value usually displays intense signal on T2-w sequence. Because the CSF is a flowing pulsating liquid in the cranial-caudal direction, artefacts can occur as patchy areas of signal loss. This is a common artifact when using a STIR sequence in sagittal plane. Truncation, or also called Gibbs artifact, occurs when there is an abrupt change in intensity, usually with the CSF. Truncation is seen on the images as successive rings of dark or bright lines.

Being located within the thorax and abdomen, the spinal cord is affected by its more distant environment such as the heart and lungs. The periodic respiratory movements from the lungs will induce a local variation of magnetic field (due to the differences in susceptibility between air/bones/soft tissues) that will propagate to the spinal cord. This can be seen on T2\*-w sequence by areas of signal dropout. In general, periodic motion, like the periodic abdomen motion from breathing or the heart pulsation, will produce ghosting on the images in the phase encoding direction (Figure 1.18A-B). However, random motion, like swallowing, tremor, gross movement of the patient, will produce blurry images (Figure 1.18A-B). This can be anticipated by increasing the number of averages, using a respiratory gating, or more complex techniques as respiratory reordering or navigator echoes.

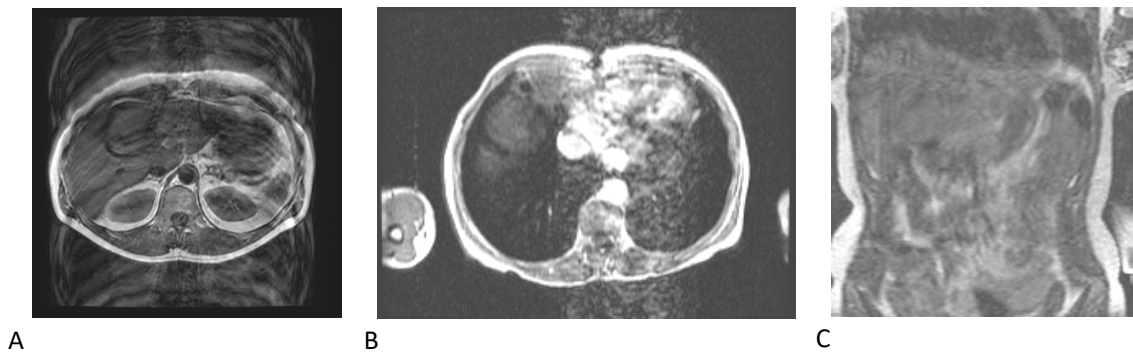


**Figure 1.18:** *Examples motion artifacts: (A) Abdomen respiratory motion, (B) Cardiac pulsation, (C) Gastrointestinal Peristalsis. Figure adapted from “MRI: From Picture to Proton” Second edition 2006.*

### 1.3.3.2 Spinal cord imaging for clinical practice

As previously mentioned in the section 1.1.2, the MS imaging community has been actively involved in providing standardised MRI protocols. Recently, the spinal cord has been added to the current recommendations (Consortium of MS Centers, [Traboulsee et al. \(2016\)](#)) and some guidance was provided in terms of imaging sequences, spatial coverage, and image resolution (Figure 1.19). While brain imaging is mandatory for any suspicion of MS, spinal cord imaging is not used yet for routine monitoring but rather limited to specific situations where a clinical presentation suggests the presence of spinal cord lesion. Spinal cord imaging is also recommended if patients present a primary progressive course, or to increase the diagnostic confidence when brain imaging did not provide enough information ([Traboulsee et al., 2016](#)).

## Spinal cord MRI protocol

Parameter	Description
Field strength	Scans should be of good quality, with adequate SNR and resolution (in-section pixel resolution of $\leq 1 \times 1$ mm) Closed magnets (large bore for patients with claustrophobia) preferred
Coverage	Cervical cord coverage <sup>a</sup>
Core sequences	Sagittal T2 Sagittal proton attenuation, STIR, or PST1-IR Axial T2 through lesions
Section thickness and gap	Sagittal: $\leq 3$ mm, no gap Axial: 5 mm, no gap
Optional sequences	Axial T2 through complete cervical cord Gadolinium <sup>b</sup> and postgadolinium sagittal T1 Sagittal T1

**Figure 1.19:** Revised Recommendations of the Consortium of MS Centers Task Force for a Standardized MRI Protocol and Clinical Guidelines (Traboulsee et al., 2016)

Despite the MRI protocol guidelines for spinal cord imaging, there is still a need for establishing the sequences that provide the best detection of spine lesions. The sagittal T2-w, which is a core sequence in the 2016 recommendations, has been outperformed by other sequences in many studies (Dietemann et al., 2000; Philpott and Brotchie, 2011; Chong et al., 2016). The sagittal T2-w STIR has been widely used for MS spinal cord imaging due to the higher lesion contrast. However, STIR was shown to be prone to CSF flow and motion artifacts, which may limit the interpretation of pathology and was associated with a poor inter-observer agreement (Bot et al., 2000). Recently, inversion recovery sequences with a T1-w contrast have displayed higher lesion detection and better lesion conspicuity, such as MPRAGE (Nair et al., 2013), PSIR (phase sensitive inversion recovery) (Poonawalla et al., 2008), and MP2RAGE (Lefevre et al., 2017). PSIR has an inversion time set to null the signal from the normal white matter. Images are then reconstructed as a phase sensitive image, which means the sign of the signal is preserved (also called the polarity of  $M_z$ ) and therefore a broader range of signal intensity is obtained. While a sagittal PSIR sequence showed a good performance for lesion detection at the cervical level compared to STIR and T2-w (Poonawalla et al., 2008), it did not performed well at the thoracic level in the study from Alcaide-Leon et al. (2016), especially in overweight patients with an increased fat thickness in their back. It has been hypothesized that the dielectric effect may change the angle of the 180 inversion pulse, but it may also be related to the phase unwrapping methods.

In a study from Nair et al. (2013), the sagittal 3D MPRAGE sequence proved its potential for improving the lesion visualization and lesion volume for both cervical and thoracic cords compared to the conventional T2-w, STIR and T2\* GRE sequences (Figure 1.20). To

correct for  $B_0$  inhomogeneities and cancel the residual T2\*/PD contrast, MP2RAGE with uniform-denoise (UNI-DEN) (O'Brien et al., 2014), which consists of applying a denoise-filter to correct for the amplifying noise background, improved the delineation of anatomical structures. Because of its robustness for brain imaging, MP2RAGE was implemented in vivo for spinal cord imaging in a pilot study I conducted during my PhD (Lefevre et al., 2017). In the spinal cord, MP2RAGE has demonstrated its robustness against motion (Figure 1.21B) compared to sagittal STIR (Figure 1.21A) and axial T2\*GRE (Figure 1.21C-E). The denoise-filter in MP2RAGE increased the contrast-to-noise ratio (CNR) by a factor of 4-5 in comparison with MPRAGE, thereby providing an excellent visualization and delineation of both the normal appearing cord and the MS lesions (Figure 1.21F-H).

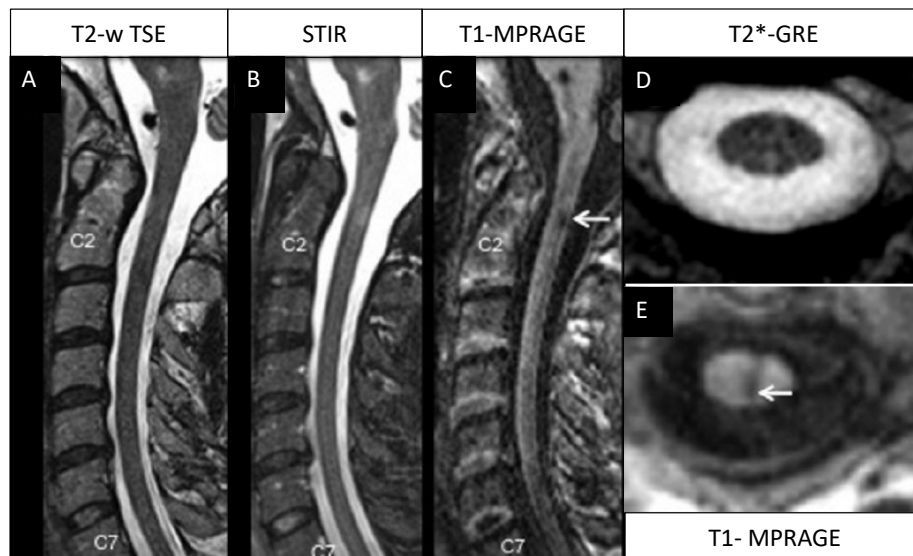


**Figure 1.20:** Comparison of imaging sequences at 3T of the cervical cord in a patient with relapsing-remitting MS. In sagittal, T1-MPRAGE (C) performed better than the conventional sequences T2-w TSE (A), STIR (B). The focal lesion (white arrow) was clearly seen on sagittal T1-MPRAGE with a higher contrast-to-noise ratio than the STIR sequence. The T2-w TSE did not depict the lesion here. Reformating the T1-MPRAGE in axial plane (E) was possible due to the 3D acquisition with 1 mm isotropic resolution and confirmed the focal lesion. The same lesion was also visible on MEDIC T2\* GRE (D). Figure adapted from Nair et al. (2013)



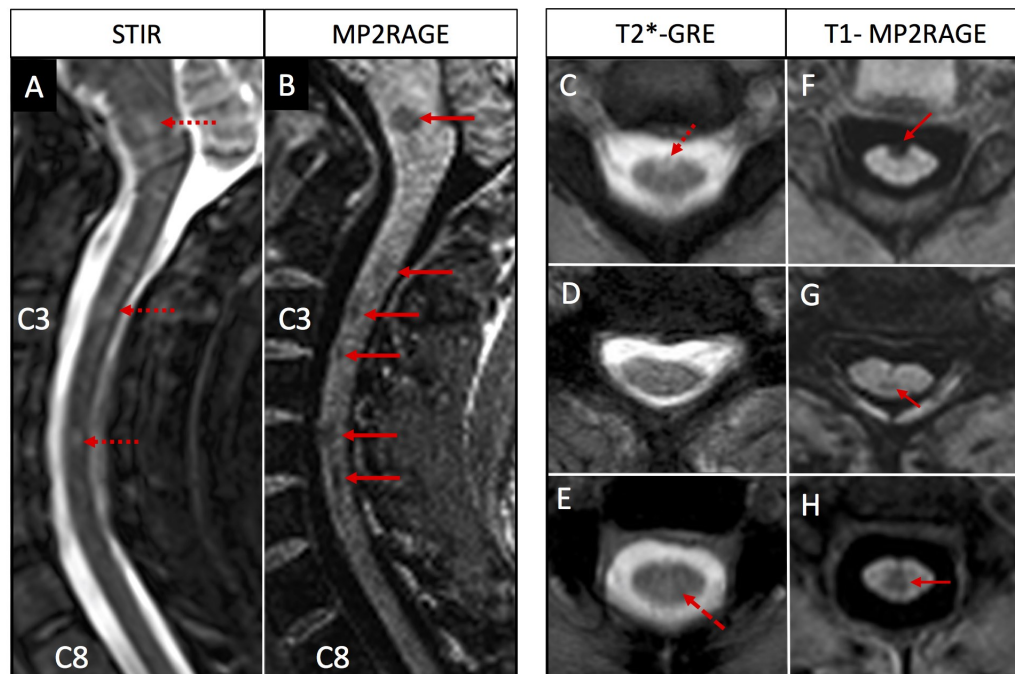


**Figure 1.21:** Comparison of images acquired at the cervical cord between standard sequence STIR (A), T2\* MEDIC (C-E) and the optimized MP2RAGE UNI-DEN (B, F-H) in two different MS patients (sagittal images: 29 y.o woman with RRMS; axial images: 36y.o man with RRMS). While lesions are clearly seen on MP2RAGE (red arrows), STIR and T2\*-MEDIC sequences are more susceptible to motion artifacts. Consequently, the lesions are difficult to visualize due to the lower contrast lesion-to-cord and the lack of sharpness (red dotted arrows), even some lesions are missed on STIR and axial T2\* MEDIC (D). Images acquired from NIH, TNS.

MEDIC (Multi-Echo Data Image Combination), a spoiled T2\*-w sequence, has shown advantages for spinal cord imaging when acquired in the axial plane. This sequence consists in generating several gradient echoes at different TEs (Held et al., 2003). Once combined using a ‘sum-of-squares’ technique, MEDIC images display an increased contrast between the WM and GM tissues, as well a good visualization of MS lesions for the cervical cord (Ozturk et al., 2013; Martin et al., 2012).

Finally, imaging in the sagittal plane is usually privileged for faster time acquisition due to the larger field of view covered in the cranio-caudal direction. However, it is more prone to magnetic field inhomogeneities which will decrease the efficiency of a chemical shift-based suppression.

### 1.3.3.3 Spinal cord imaging at 7T

Imaging the spinal cord at ultra high field MRI brings additional technical challenges to overcome. These are mainly related to: the increased inhomogeneity of the main static  $B_0$  magnetic field and the radiofrequency  $B_1$  field, the increased RF power deposition in

the patient (measured by the SAR), and the absence of robust  $B_0$  shimming along the cord. Unlike brain imaging, the feasibility of spinal cord imaging at 7T was demonstrated only in the last few years. There is no consensus yet for the design of RF spinal cord at 7T. Most of the coils are built in-house while a few commercial coil exists, and most of these coils are only focused on the cervical cord (Barry et al., 2018). The coil configuration is extremely important for optimizing the radiofrequency  $B_1$  patterns, and therefore the coil efficiency. By increasing the number of coil elements, it is possible to obtain larger field of view through the spinal cord length and an increased penetration of the signal to reach the spinal cord. In addition, one can observe dielectric resonance effects or “RF interferences” as the  $B_0$  field increases. The shorter electromagnetic RF wavelength at 7T becomes comparable to the dimensions of the object to image, which can result in signal drop-out or significant changes in contrast. There are also important issues related to the  $B_0$  field inhomogeneities coming from the differences in magnetic susceptibility between the various tissues and surrounding environment. These are even more prominent at 7T with important geometric distortion artifacts, incomplete fat suppression, and substantial signal loss on GRE images. The interface between bone and water-based soft tissues at the intervertebral junctions causes highly localized field distortions that are difficult to correct by using standard  $B_0$  shimming techniques. More advanced shimming techniques developed for 7T brain imaging may be useful for spinal cord. The respiratory-related field variations also scale with the field strength with a field shift that reach 140 Hz at 7T at the lower cervical cord (Vannesjo et al., 2016). For comparison, the field shifts in the brain is only a few Hz ( $\sim 7$ Hz) at 7T.

Despite the challenges related to higher field strength, imaging the cord at 7T have an important impact in terms of lesion visualization. The increase SNR and contrast is extremely useful while imaging such small structures as the cord and allow higher spatial resolution. Zhao et al. (2014) applied an axial T2\* multi-echo FLASH (Fast low angle shot) and showed a 4.2 times increased of the SNR compared to the 3T images with matched resolutions. Comparison of 3T and 7T of the lower cervical cord images are shown in Figure 1.22. The increased SNR was due to the contributions of the higher field strength and the improved arrangement of the 19-channel receive-only array coil 7T. Figure 1.23 shows representative examples of MS lesions imaged at 7T using an axial T2\*-w 3D GRE. Lesions displayed an excellent location discrimination using a similar clinical setting than at 3T which covered C2-C5 in a relatively short acquisition time ( $\sim 5$  min) (Dula et al., 2016).

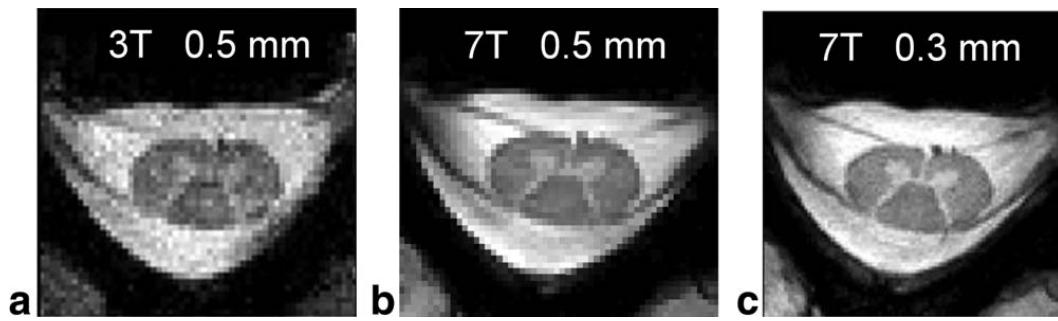


**Figure 1.22:** Improved image quality and cervical cord delineation at 7T compared to 3T. Same resolution (0.5 x 0.5 x 3 mm) were acquired between 3T (a) and 7T (b). A higher resolution (0.3 x 0.3 x 3 mm) improved the visualization of cord structures with better sharpness. (Zhao et al., 2014)

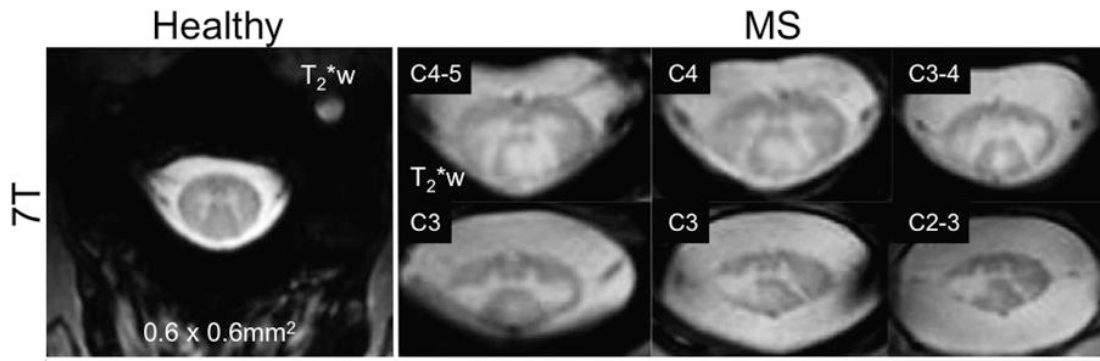


**Figure 1.23:** Cervical spinal cord imaging at 7T in a healthy volunteer and MS patient acquired using a axial T2\*-w GRE (20 slices, 0.6 x 0.6 x 4 mm<sup>3</sup>) with a number of 8 averages. Figure adapted from Dula et al. (2016)

Duan et al. (2015) improved the efficiency of a transmit dipole elements, and combined with eight receive loops (Figure 1.24A), showed excellent image quality of the thoracolumbar spinal cord (Figure 1.24B), as well the improved visualization of a MS thoracic lesion (Figure 1.24E-F). The use of a navigator-based correction improved greatly the image quality (Figure 1.24C and Figure 1.24F) by correcting for the phase fluctuations caused by breathing. However, single-slice were acquired using the MRI protocol from Duan et al. (2015). The long acquisition time was the major limitation in this study, but it is worth knowing that the thoracic imaging at ultra-high field is promising.

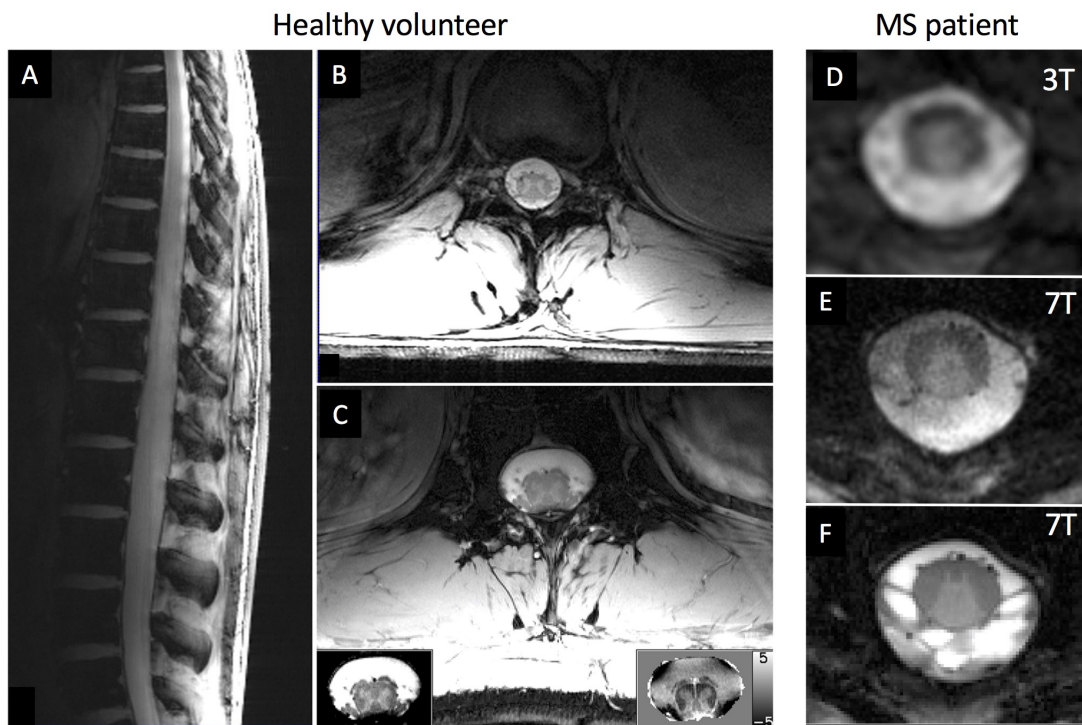


**Figure 1.24:** Thoraco-lumbar spinal cord imaged at 7T on a healthy volunteer (A-C) and a MS patient (D-F). (A) 2D sagittal GRE image display an excellent sensitivity of the lower spinal cord ( $0.78 \times 0.78 \times 3 \text{ mm}^3$ ). (B) Example of an axial T2\*-w GRE acquired with a resolution of  $0.52 \times 0.52 \times 3 \text{ mm}^3$ . (C) Same axial T2\*-w GRE acquired with a higher resolution in-plane ( $0.31 \times 0.31 \times 3 \text{ mm}^3$ ) and a navigator-based correction. On the left bottom, the magnitude image is rescaled for a better contrast; On the right bottom, the phase image rescaled shows a higher contrast between WM and GM. Comparison 3T – 7T cord images acquired on a relapsing-remitting MS patient. (D) The MS thoracic lesion (T7-T8) can be detected on at 3T using an axial T2\*-w GRE ( $0.58 \times 0.58 \times ? \text{ mm}$ ). Using the same coil as [Duan et al. \(2015\)](#), the increased SNR at 7T combined with a radial T2\*-w GRE (E) improved greatly the lesion delineation compared to 3T. (F) A similar axial T2\*-w GRE with a prospective navigator-based correction improved the clarity of the cord tissues compared to the radial T2\*-w GRE with a higher SNR and contrast white-grey matter. (A-C) Figure adapted from [Duan et al. \(2015\)](#). (D-F) Images aquired at the NIH.

### 1.3.3.4 Spinal cord imaging findings from clinical MS studies

Spinal cord imaging can provide an important information for both diagnosis and prognosis. While silent cord lesions are rare in other neurological disorders and in normal aging, they are frequent in MS ([Bot et al., 2002](#)). Spinal cord lesions may develop early in the disease course. In patients with a clinically isolated syndrome (CIS) (defined by a first episode of neurological symptoms for at least 24 hours, and do not fulfill the dissemination in space and time criteria yet), a good proportion already present spinal cord lesions, 43% in the study from [Kearney et al. \(2016\)](#) and 68% in the study from [Sombekke et al. \(2013\)](#). Asymptomatic spinal cord lesions in CIS patients also confer an increased risk of conversion

to clinically definite MS (Sombekke et al., 2013). This same study found that CIS patients with SC lesions will face a second relapse much faster.

Correlations between the spinal cord abnormalities and the disease progression are not strong, as demonstrated by the weak association between the number of cord lesions at presentation and the number of relapses in the MS cohort from Cordonnier et al. (2003). A trend was observed between the mean number of focal lesions and the clinical subtypes, with the lower rate seen in CIS patients (0.8), followed by the RRMS form (2.8), PPMS form (3.5) and, finally, SPMS form (4.7) in the study from Kearney et al. (2016), although these results were restrained to the upper cervical cord. Interestingly, same trend and similar results were obtained for the entire cord (Weier et al., 2012). Many studies have reported similar results for the type of lesions by disease subtypes. A higher proportion of diffuse abnormalities seems associated with the progressive MS forms (Nijeholt et al., 2001; Kearney et al., 2016).

Regarding the distribution of spinal cord lesions along the cord length, the cervical cord seems to be a predilection sites. The histopathology study from Oppenheimer (1978) showed that the cervical cord was affected the most by lesions (with 90% of the sections affected) compared to thoracic (46% affected) and lumbar (41% affected) cords. In line with the previous study, an in vivo imaging study from Alcaide-Leon (2016) found a similar ratio between the cervical and the thoraco-lumbar cord (84% for the cervical examinations were affected by lesions and 85% for the thoraco-lumbar). Multiple studies have looked at which spinal level had the highest number of lesions. The C7 cord level was the most affected from Oppenheimer (1978) histopathology study. Some in vivo studies instead have reported a greater number of lesions detected at C1-C2 levels for whole cord in vivo imaging study (Nair et al., 2013; Weier et al., 2012), and C2 from a cervical cord in vivo imaging study (Chong et al., 2016). Finally, most of the lesions were found in the posterior column center and the lateral columns; the anterior columns being a very rare location (Oppenheimer, 1978; Nijeholt et al., 2001; Gilmore et al., 2006; Kearney et al., 2013, 2016).

The disruption of the blood spinal cord barrier has not been well investigated compared to brain lesions. It has been reported that acute lesions display gadolinium contrast enhancement with an open-ring or nodular pattern, and rarely persist after 3 months (Kranz and Amrhein, 2019). They are also less frequent than brain lesion enhancement.

## 1.4 Summary

Although brain imaging has been the predominant source of studies for analyzing the MS lesions, it is not enough to explain the neurological disability. The typical clinical presentation of MS patients is suggestive of spinal cord damage complemented by muscle weakness, sensory problems, discoordination, bladder and bowel dysfunctions. While lesions in the spinal cord has been demonstrated for a long time through pathology, this technique has several limitations for spinal cord analysis, primarily due to the long length of this organ and the lack of heterogeneity of MS disease courses among the available postmortem tissues. The incorporation of MRI for the spinal cord would be extremely important paraclinical tool for earlier and more accurate diagnosis.

However, spinal cord is a more challenging organ to image compared to the brain. Only recently, the MS community has been actively involved by providing spinal cord imaging protocol recommendations for clinical practice. While 3T whole cord imaging can be useful to give the distribution of lesions along the cord length, only ultra-high field MRI at 7T can provide an excellent resolution and contrast to improve the visualization and location of the lesions within the cord cross-section, as well as the detection of smaller lesions. Brain imaging at ultra-high field has improved finding specific MRI biomarkers that correlate with the underlying biological event.

Applying this promising field of research to the spinal cord would help to better understand the pathogenesis of MS lesions. A lot of progress has been done these past few years for imaging the cord at 7T, but imaging the entire spinal cord is not available yet in a reasonable acquisition time. Furthermore, there has been no longitudinal in vivo studies of the evolution of spinal cord lesions with respect to volume and shapes. Having a better characterization of the spinal cord lesion evolution during the disease course could help: to distinguish better the MS subtypes, to correlate better with the clinical presentation, and to assess the efficacy of disease-modifying treatment but also improve outcome of clinical trials in MS.

## CHAPTER 2

---

# EXPERIMENTAL AUTOIMMUNE ENCEPHALOMYELITIS (EAE) MODELS

### **This Chapter contains:**

2.1	EAE models . . . . .	36
2.1.1	Introduction . . . . .	36
2.1.2	EAE immunization protocols . . . . .	37
2.1.3	Rodent EAE models . . . . .	38
2.2	Marmoset EAE models . . . . .	41
2.2.1	Generalities . . . . .	41
2.2.2	Clinical and pathological findings . . . . .	42
2.2.3	Imaging findings . . . . .	45
2.3	The marmoset spinal cord . . . . .	49
2.3.1	Spinal cord anatomy – functional structures . . . . .	49
2.3.2	Pathological features in the marmoset EAE spinal cord . . . . .	51
2.4	Summary . . . . .	53

## 2.1 EAE models

### 2.1.1 Introduction

Experimental Autoimmune Encephalomyelitis is the most commonly used experimental model to study autoimmune inflammatory diseases of the CNS. The origin of EAE dates back to the early 1930s when Thomas Rivers and colleagues performed the first injections of uninfected rabbit brain extracts into rhesus macaques and observed an ascending paralysis, which was associated with perivascular infiltrates and demyelination in the brain (Rivers et al., 1933). In 1947, Kabat et al. reported the resemblance of EAE to human demyelinating diseases, especially MS and post-infectious encephalomyelitis. Since then, EAE models have been widely performed in a variety of animal species, including nonhuman primates, rodents, rabbits and guinea pigs, among others. Many different models exist based on the species and the immunization protocol employed, which lead to a large spectrum of disease features (figure 2.1).

Current animal models do not recapitulate all the features of MS (neurological, pathological and immunological), but taken together, these models can provide insight into specific pathological events relevant to MS. In particular, rodent EAE models allow monitoring early-stage of the disease, identifying some aspects of inflammation and immune-mediated tissue injury, and even helping in the development of some MS treatments, including glatiramer acetate, mitoxantrone, and natalizumab (Denic et al., 2011). However, there is an extremely high rate of failure when testing drugs in clinical trials on MS patients, even if they were effective in EAE. Reasons for these shortcomings may include the lack of genetic variability in these inbred rodents, and the anatomical and immunological differences with human.

The marmoset EAE model was developed to address some of these issues. Nearly 25 years after marmoset EAE was first described, it has become clear that the model can successfully recapitulate many of the radiological and immunological features of MS (Absinta et al., 2016) has come to be seen as a bridge between the rodent EAE and MS (Hart et al., 2015).

In this chapter, I report different immunization protocols, clinical courses, and histopathological patterns associated with some commonly used rodent EAE models and discuss their major limitations. Then, I describe the particular advantages of using the marmoset EAE model, including the questions that can specifically be addressed with this model (but not with rodent models). Finally, I review the main pathological and imaging findings observed



in the marmoset EAE that are relevant for translational research with MS.

Species	Clinical signs	Pathological findings	Ref
Macaque	Acute primary progressive and relapsing-remitting disease; trunk ataxia, limb weakness and facial weakness, including ptosis of eye lids, muscular twitches and visual impairment	Perivascular inflammation with neutrophils, histiocytes and giant cell formation; haemorrhage, necrosis, axon damage and demyelination; mostly localized to brain stem and cerebellum; optic nerves affected	Rivers et al. 1947
Guinea pig	Flaccid (usually) paralysis of hind limbs; urinary incontinence	Meningitis; vessel-associated foci of haemorrhage and infiltrates of monocytes and granulocytes; astrocytosis; cerebral hemispheres most affected	Freund et al. 1947
Rabbit	Progressive weakness, especially of the limbs; lack of coordination; some loss of tendon reflexes	Meningitis; disseminated perivascular lymphocytic infiltrates of grey and white matter; microglial hyperplasia and demyelination	Morrison et al. 1947
Mouse	Pattern of disease varies; ascending weakness and paralysis	Multiple perivascular foci of mononuclear inflammation; may involve demyelination in chronic models	Levine et al. 1973
Rat	Flaccid paralysis of hind limbs; occasional urinary incontinence and faecal impaction	Perivascular infiltrates of lymphocytes, monocytes and occasionally granulocytes	Lipton et al. 1952
Hamster	Very variable course, including tremor, ataxia and circling; weakness and paralysis of limbs; occasionally urinary incontinence and faecal impaction	Perivascular 'granulomas' of lymphocytes, histiocytes, plasma cells and sometimes granulocytes; demyelination associated with infiltrates or isolated plaques	Tal et al. 1958
Dog	Sudden onset of ataxia rapidly followed by paralysis; some blindness	Perivascular focal demyelination associated with infiltrates of neutrophils and lymphocytes; spinal cord most affected; some haemorrhage; necrosis	Thomas et al. 1950
Sheep	Coarse tremors, stumbling, ataxia and spastic paralysis	Extensive lesions throughout the central nervous system, including the meninges; perivascular inflammation, mostly lymphocyte infiltrate; granulomas; no microglial response; little demyelination	Innes et al. 1951
Marmoset	Relapsing-remitting or primary progressive disease; ataxia; paraparesis; sensory loss; gaze palsies; dysarthria; visual loss	Primary demyelination and gliosis surrounding mononuclear cell perivascular infiltrates; frequently in deep periventricular white matter	Genain et al. 1995

**Figure 2.1:** Summary of clinical signs and pathological findings for different species with EAE (Adapted from *Baxter (2007)*)

### 2.1.2 EAE immunization protocols

Figure 2.2 recapitulates the different CNS elements used for EAE immunization. EAE can be actively induced by using whole brain ([Freund et al., 1947](#); [Olitsky and Yager, 1949](#)), CNS white matter ([Waksman et al., 1954](#); [Massacesi et al., 1995](#)) or spinal cord homogenate ([Einstein et al., 1962](#)). It can also be induced by isolating some myelin antigens like myelin basic protein (MBP), myelin proteolipid protein (PLP), or myelin oligodendrocyte glycoprotein (MOG). In order to increase the pathogenicity and be more efficient, the complete freund adjuvant (CFA) was introduced ([Kabat et al., 1947](#)). CFA consists of a mixture of a mineral oil the incomplete Freund's adjuvant (IFA) and the dessicated mycobacterium tuberculosis (MT), which emulsified with the antigen, will prolonge the immune response. Bordetella pertussis, seen as an additional adjuvant, can also be used as a separate injection in addition to the CFA in order to increase the incidence of the disease ([Norton and Cammer, 1984](#)). EAE can also be passively induced by an adoptive transfer of cells from a donor which was actively induced with EAE. This passive induction will not be discussed here since we will study an active model. Very early on, the main goal of EAE experiments was to identify which CNS proteins were encephalitogenic, and it was observed that not all CNS elements could induce EAE ([Baxter, 2007](#)). The clinical signs and pathological

features varied depending on the species and/or strains, and the immunization protocol used.

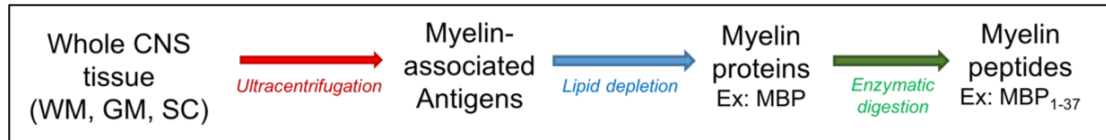


**Figure 2.2:** Flowchart that represents the processes of obtaining the various CNS elements used for EAE immunization.

### 2.1.3 Rodent EAE models

Mice models are the most frequently used EAE models since the emergence of transgenic and gene knockout models in the 1990s. Thanks to the absence of genetic variability of the inbred strains, most of the rodent models have a reproducible disease course. Therefore, it is easier to study experimentally the early-stage of the disease. The clinical symptoms of EAE usually develop at 7–15 days post-immunization followed by remission. The EAE Lewis rat model is an example of an acute monophasic disease with a total recovery of symptoms (Polman et al., 1988). Episodes of relapses can be observed with changes in the immunization protocol and the animal species (Hofstetter et al. (2002) with SLJ/J mice EAE; Tanuma et al. (2000) with DA rat EAE). The usual symptoms include weight loss, an ascending paralysis beginning with tail weakness (called tail atonia) followed by weakness of hind limb and sometimes forelimb. To monitor the disease, clinical examinations are regularly performed during the entire disease course. Table 2.1 shows a typical EAE score for rodent EAE (see Figure 2.3).

EAE score	Clinical disease
0	No clinical disease
1	Tail weakness
2	Hemi- or paraparesis (incomplete paralysis of one or two hindlimbs)
3	Hemi- or paraplegia (complete paralysis of one or two hindlimbs)
4	Paraplegia with forelimb weakness or paralysis
5	Moribund or dead animals

**Figure 2.3:** EAE score with the associated clinical signs for a mice EAE model. Adapted from Lavi and Constantinescu (2008, chapter A2)

Heterogeneity in terms of pathological features are also found depending on the immunization protocol. The acute monophasic disease course tends to have limited or no demyelination. The EAE Lewis rat model is a perfect example with primarily acute inflammatory lesions, and demyelination that may eventually be restricted to the entrance of the dorsal roots and the exit of the ventral roots (Pender et al., 1989). Demyelination can be found for the multiphasic disease course in the EAE Lewis rat with combination of MBP-CFA and injection of anti-MOG monoclonal antibodies (Schluesener et al., 1988), although extensive remyelination occurs once the animals undergo remission. Perivascular and subpial inflammation is the major pathological event for the acute and chronic disease courses in DA rat EAE (Tanuma et al., 2000) (Figure 2.4). Interestingly, in this model, a marked demyelination only appeared during the second attack (mostly located within the dorsal column) while infiltrating inflammatory T cells and macrophages were already present during the acute phase. However, for the chronic phase, a large number of macrophages with a few T cells were seen. In both cases, B cells were rarely found.

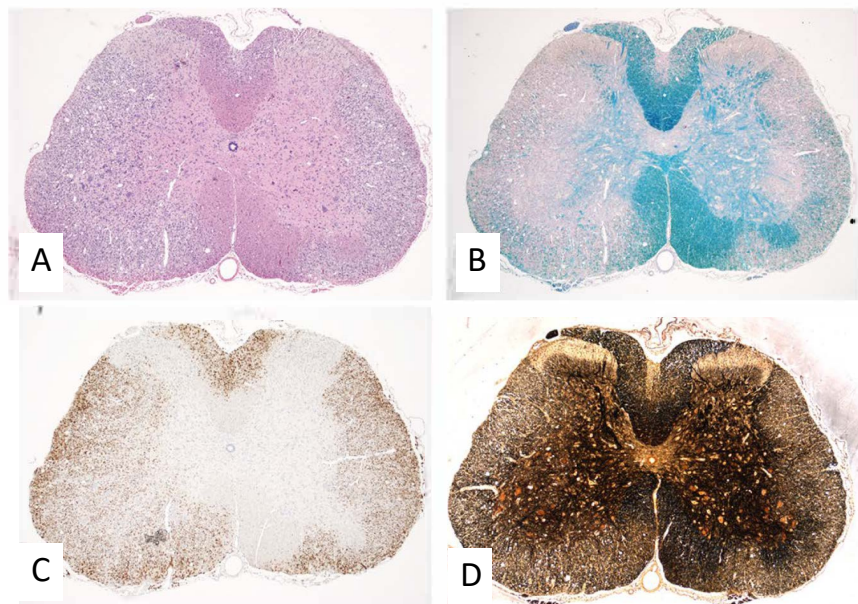


**Figure 2.4:** Extensive inflammatory demyelinating lesions in the DA rat EAE model. Pathology was performed in the chronic stage at 60 days after an active immunization with the recombinant myelin oligodendrocyte glycoprotein (MOG). The lesions present a profound inflammation (A, Hematoxylin and Eosin (HE) staining) and a widespread confluent demyelination (B, Luxol fast blue staining). There is an infiltration of macrophages (C, ED1 anti-CD68 staining) but axons were preserved (D, Bielschowski staining). Note that ED1 is a widely used monoclonal antibody directed against the CD68 protein to identify macrophages. Figure adapted from *Lassmann and Bradl (2017)*.

So far what we have learned from this brief description of rodent EAE models is that the majority of EAE models are mainly based on inflammation of the spinal cord with an acute monophasic course followed by a spontaneous recovery. While it is possible to obtain different types of disease course (chronic with multiple relapses) with demyelination of the CNS, this requires the use of immunization protocols that are more complicated.

The figure 2.5 illustrates the differences between rodents and MS in terms of distribution of lesions for the entire CNS. Here is a summary of the main limitations of rodent EAE models that need to be considered for translational research:

- The anatomical structures of the rodent brain are very different from the human brain;
- Rodent brain has a relatively small volume of white matter tissue;
- Limited neurobehavioral in rodents compared to primates;
- The distribution of EAE lesions differs from MS (mostly subpial pathology for the lumbar spinal cord in EAE rodents);
- Different EAE models are necessary to study all the different aspect of MS pathogenesis. The choice of the model will depend on the scientific question;
- Many drugs developed using rodent EAE models failed in clinical trials;
- The immune response of rodent models was intensively studied, whereas longitudinal studies using MRI are extremely rare.

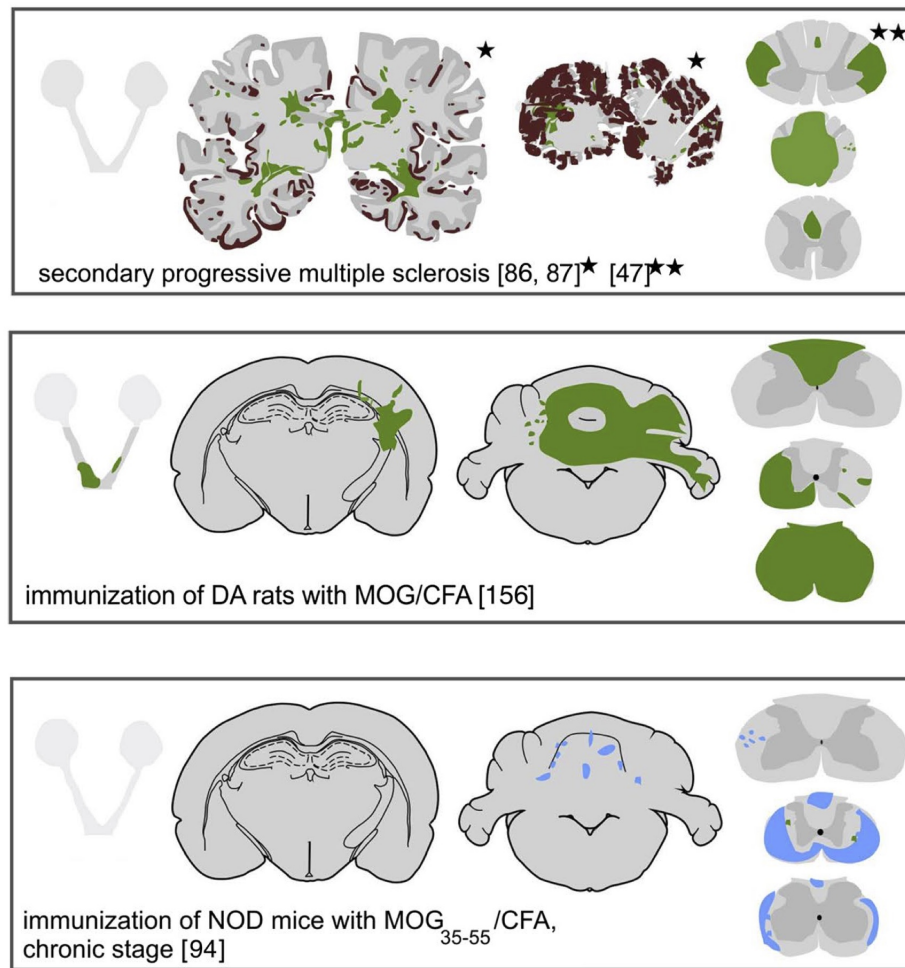


**Figure 2.5:** Schematic representation of the lesion distribution in MS and different EAE models. From left to right: Optic nerve, brain, cerebellum, and spinal cord sections. In green: areas of primary demyelination; in blue: areas of dominant axonal loss, and secondarily demyelination; in brown: cortical demyelination. In MS, the widespread of lesions throughout the entire brain and the prominent cortical lesions. The spinal cord also presents large focal demyelinating lesions. For the two EAE models represented, pathology in the brain was limited or absent. We can appreciate the pronounced anatomical differences in the brain and cerebellum between human and rodents. In the model with a primary demyelination (DA rats), pathology in the spinal cord was severe. In the model with a primary axonal loss (NOD mice), confluent subpial lesions were prominent for the thoracic and lumbar spinal cord. Figure adapted from [Lassmann and Bradl \(2017\)](#)

## 2.2 Marmoset EAE models

### 2.2.1 Generalities

The common marmoset *Callithrix jacchus*, a nonhuman primate “New World” monkey, has been widely used in the fields of neuroscience, reproductive biology, infectious disease, and behavioral research. The common marmoset is a relatively recent model for studying

MS (compared to the rodent models). Marmosets present many advantages for conducting experimental studies: small size with an adult weight of 300-400 g, maturity reached around 18-24 months, often born as a set of twins or triplets that are bone-marrow chimera which make them immunologically similar and useful for drug testing (one sibling with placebo and the other with drug). Due to their evolutionary proximity to humans, this “higher species” shares closer features with human than rodents in terms of neuroanatomy (higher white matter to gray matter ratio), immunology and genetics. Additionally, their outbreeding and the presence of pathogens in the laboratory environment make them a more realistic animal model of MS.

### 2.2.2 Clinical and pathological findings

The two main EAE immunization protocols that have been mostly investigated in the marmoset are the inductions with human brain white matter homogenate (WMH) or with recombinant human MOG (rhMOG). Both inductions have similar pathological features (Brok et al., 2000). However, it has been reported that the WMH immunization displays a broader range of inflammatory demyelinating lesions compared to the rhMOG immunization where lesions are primarily in the early active stage (A’t Hart et al., 2004b). Note that disease progression is an important factor for the lesion heterogeneity. Massacesi and colleagues described for the first time an active induction of EAE in the marmoset using a protocol with human brain WMH in CFA and a boost of Bordetella pertussis (Massacesi et al., 1995). The rate of immunized animals affected by the disease was excellent (100% of the immunized animals developed the disease) and usually followed a relapsing remitting/secondary progressive course. A few years later, the group of Bert A. ‘t Hart reproduced this immunization protocol without the injection of Bordetella pertussis to obtain a more chronic disease course with moderate severity (A’t Hart et al., 1998). Compared to rodents, the disease course in the marmoset can not be predicted and is quite heterogeneous in terms of duration (several weeks or months). Clinical signs such as loss of pain sensation, tremor, and motor deficits, were reported. The disease usually progresses until paraplegia or quadriplegia. The common pathological features of this EAE model induced with the WMH protocol from Massacesi et al. (1995) were a primary demyelination with dense macrophages infiltration and perivenous inflammatory lesions throughout the brain and the spinal cord. The acute lesions could be distinguished from the chronic lesions. Acute lesions were defined by their large size and sharply delineated areas of primary demyelination, with early reactive gliosis. The chronic lesions were defined by the additional

presence of a dense reactive gliosis extending diffusively through the WM parenchyma. No hemorrhages or necrosis were found within the lesions, which is a hallmark of EAE pathology in rabbits and macaques. Since the results of these first experimental studies in the marmoset showed pathological similarities with MS lesions, further investigations were undertaken in the following years to assess in greater details the pathological features of EAE lesions. It was for example reported that different lesion maturation stages (early active to late active, as well remyelination) can be found within the same animals, thus further confirming the pathological heterogeneity of this model and its closeness to MS pathology. Maggi et al. (2014) grouped the pathological features based on the lesion age characterized by serial in vivo MRIs. The acute lesions (less than one week old on the MRI) coincided with the peak with BBB permeability and were defined by a complete loss of myelin on Luxol Fast Blue (LFB) staining, axonal disruption on Bielschowski, and dense inflammation with ionized calcium-binding adapter molecule 1 (Iba-1) as well with myeloid-related protein 14 (MRP14) cells through the entire lesional area. Figure 2.6 displays a representative example for an acute lesion. The BBB permeability decreased to finally return to baseline for lesions between 2-4 weeks old. These subacute lesions (1-5 weeks old) were defined by an active demyelination and MRP14+ cells both located at the lesion edge. The late acute (5-9 weeks old) were defined by a decreased of Iba1+ cells and absence of MRP14+ cells throughout the parenchymal lesion.

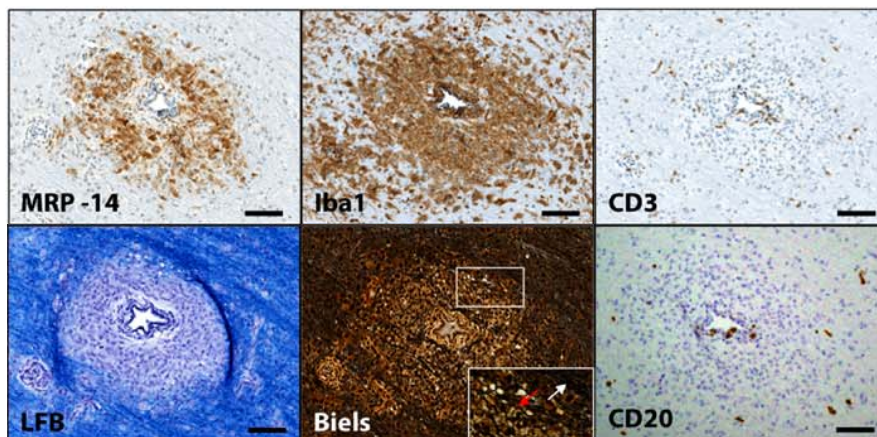


**Figure 2.6:** Representative histopathological features for an acute lesion. Magnified views of the acute lesions using a panel of histopathological techniques to characterize inflammatory cells (MRP14, Iba1, CD3, CD20), myelin (LFB), and axons (Bielschowski). This lesion displays the typical inflamed central vein. Both MRP14+ and Iba-1+ cells are present through the entire lesion, although MRP14 is rarely seen within the perivascular space. CD3+ T cells are found predominantly within the perivascular space whereas CD20+ B cells are also spread within the parenchyma. LFB confirms the complete demyelination. Axons are disrupted on Bielschowski. Figure adapted from Maggi et al. (2014)

Cortical demyelinated lesions, an important pathological hallmark of MS, have been described in the marmoset EAE, and share many morphological and pathological features with MS. Divided into three categories (leukocortical, intracortical and subpial lesions) (Figure 2.7, left panel), the density of inflammation in cortical lesions was lower compared to WM lesions. The subpial lesions were the most commonly found, with the lowest density of parenchymal inflammatory cells of the three types (Pomeroy et al., 2005). Interestingly, Kramann et al. (2015) reported a significant increased of inflammatory cells in the meninges adjacent to the subpial cortical lesion (Figure 2.7, right panel).

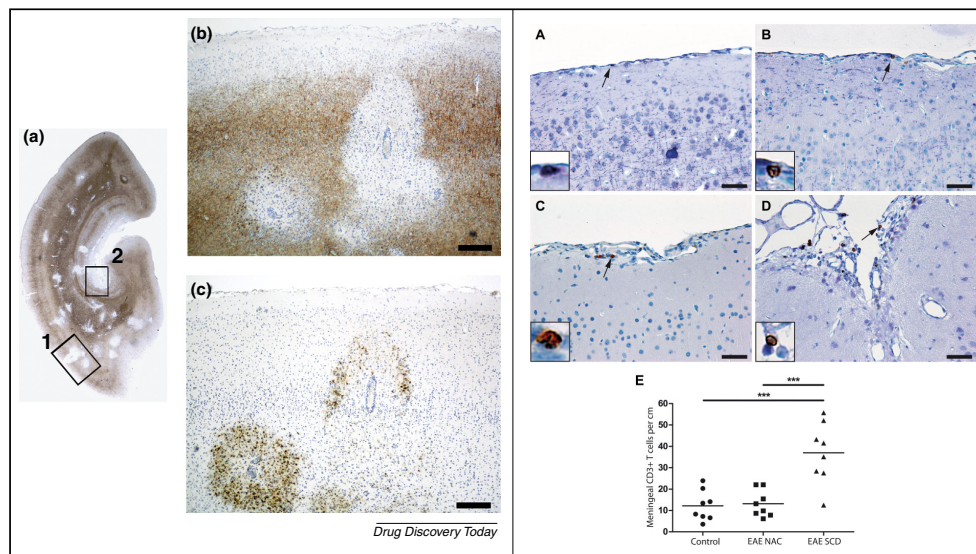


**Figure 2.7:** Cortical lesions in the marmoset EAE model immunized with the recombinant MOG 1-125 (rMOG). Left: (a) Distribution of the brain lesions visualized on the proteolipid protein (PLP) histochemistry staining with a half brain hemisphere section. Box 1 is displayed with a higher magnification of two intracortical lesions on PLP (b). MRP14 histochemistry staining can differentiate lesions with different levels of activity: active lesion with MRP14+ macrophages throughout the entire lesional area and a late active lesion with only MRP14+ macrophages found at the lesion edge. Box 2 corresponds to a subpial lesion, no magnified view. (Figure adapted from Kap et al. (2011)). Right: Meningeal inflammation characterized by an increased T cell infiltration. Double staining for myelin basic protein (MBP) and CD3+ T cells (seen as brown). Only one meningeal T cell was found in the healthy control tissue (A) and in the normal appearing cortex (NAC) of a EAE animal (B). Increased meningeal T cells adjacent to a subpial lesions in a EAE animal (C-D). The sulcus adjacent to the cingulate gyrus displayed a higher number (D). (E) Quantitative analysis of meningeal T cells between control, NAC and subpial EAE lesions. (Figure adapted from Kramann et al. (2015)). Pathology on the left and right were obtained using different immunization protocols.



### 2.2.3 Imaging findings

The small size of this nonhuman primate is an important benefit for pre-clinical imaging at ultra-high-field. Thanks to the longer imaging scan times allowed by the anesthesia, it is possible to perform multi-contrast imaging at high-resolution during one MRI session (Figure 2.8). Moreover, the experimental setup for imaging marmosets usually enables to restrain their head and body during imaging, thus significantly minimizing motion artefacts. Recently, it was shown that in vivo serial MRI combined with customized postmortem 3D-holders and slicers increased the reliability for tissue histopathology analysis (Guy et al., 2016). In figure 2.9, the excellent match obtained between a EAE lesion detected in vivo by MRI and its corresponding ex vivo MRI and histology is illustrated.

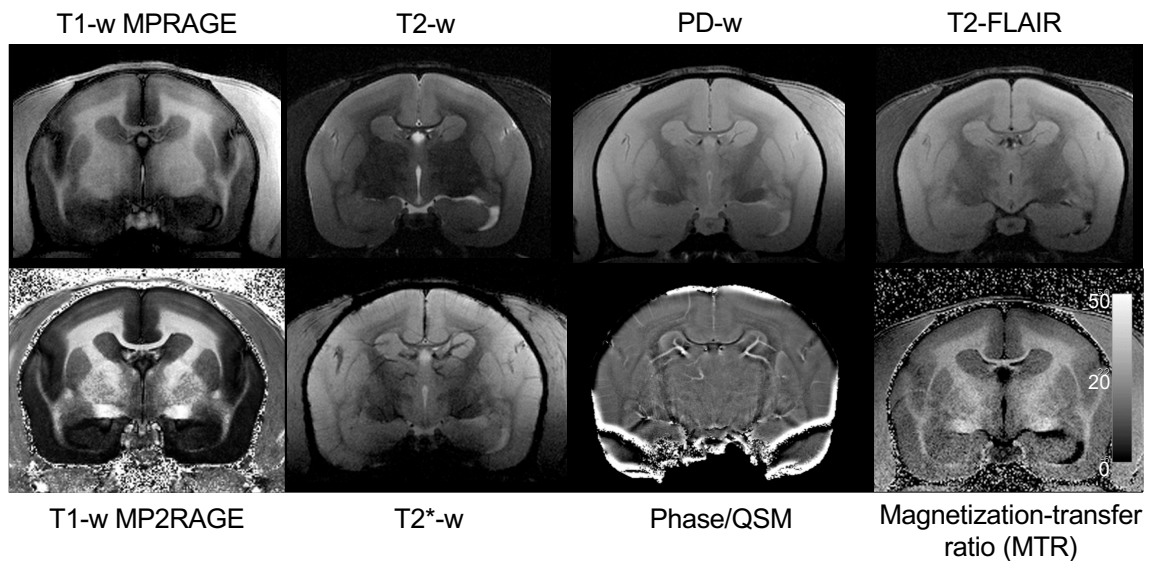


**Figure 2.8:** Multi-contrast imaging sequences of the marmoset EAE brain. Sequences were acquired in coronal orientation. T1 contrast sequences: T1-w MPRAGE and T1-w MP2RAGE show a strong contrast between WM and GM, even more pronounced on the MP2RAGE. T2 contrast sequences: T2-w and T2 FLAIR. T2 FLAIR which suppresses CSF fluid signal has been useful to improve visualization of periventricular lesions. Proton-density (PD-w). T2\*-w sequence enhances regional susceptibility magnetic effects, which allows visualization of vasculature, iron deposition. Phase/QSM is an advanced post-processing technique of a T2\* multi-echo GRE sequence, and provides a quantitative map of local tissue magnetic susceptibility. Magnetization-transfer ratio is an advanced sequence which provides a new contrast for water content by applying off-resonance RF pulses to the restricted macromolecules proton pool, which lead to an exchange energy from the restricted proton pool to the free mobile water. Differences in MTR may reflect demyelination, but has been also associated with inflammation and edema. Images provided by Pascal Sati (PhD) NIH, TNS.

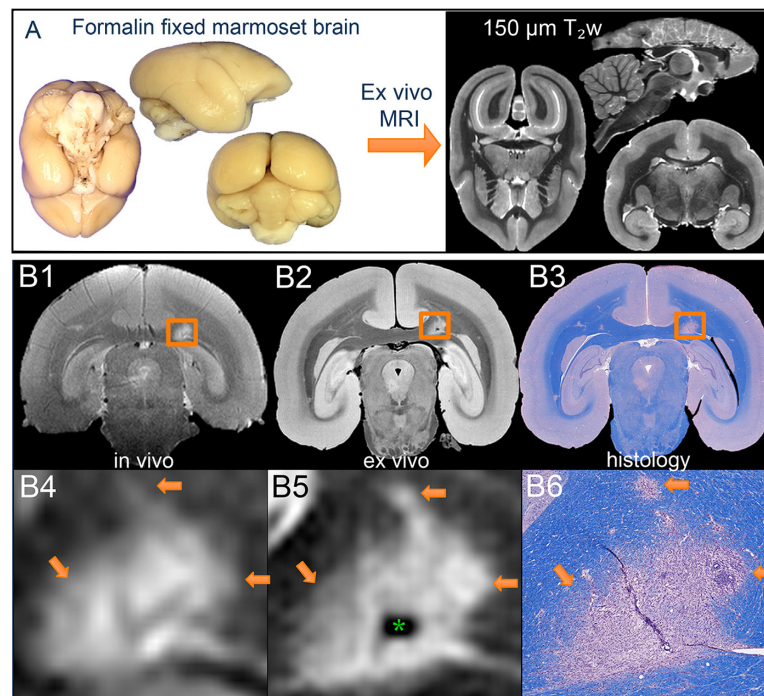


**Figure 2.9:** Accurate matching between in vivo MRI, ex vivo MRI and histology from Guy et al. using a 3D printed brain holder and brain slicer. (A) Photograph of a marmoset brain after paraformaldehyde fixation and the corresponding ex vivo T2-weighted 150 m isotropic resolution in the three anatomical plans (axial, sagittal, coronal). (B) A marmoset EAE lesion is detected in vivo using a 2D PD-weighted sequence on a 7T Bruker platform with 150 m in plane resolution and 600 m slice thickness (B1: whole brain, B4: magnified view). Note the excellent match with the ex vivo T2\* (B2: whole brain and B5: magnified view) and the histology LFB-cresyl violet (LFB-CV) for myelin (B3: whole brain, B6: magnified view). The hyperintense signal on the in vivo and ex vivo MRIs corresponds perfectly in terms of location and shape with the area of demyelination on histology. A punctuate signal loss on the ex vivo MRI may be related to iron deposition due to a local hemorrhage (intravascular blood is removed during the necropsy process). Figure adapted from Guy et al. (2016)

Marmoset EAE brain has been thoroughly investigated by serial in vivo MRI and was shown to share many radiological features with MS (Absinta et al., 2016; Maggi et al., 2017). White matter lesions were found to be distributed throughout the entire brain (A't Hart et al., 2004a) and were commonly located in the subcortical WM areas around superficial medullary veins (Gaitán et al., 2014). Intravenous injection of Gadolinium contrast agent can be performed in the marmoset EAE. Active EAE lesions can be visualized by a nodular enhancement (also named centrifugal pattern which we described in MS) on T1-weighted images (Figure 2.10B). However, a ring (also named centripetal) enhancement lesions has not been described yet in this marmoset EAE model. Dynamic contrast-enhancement MRI over several minutes have not been reported neither. Because of their perivenular configuration (Figure 2.10A), a study by Maggi et al. (2014) investigated in vivo at 7T the BBB permeability of EAE lesions on a weekly basis by comparing their T1 relaxation times

before and after gadolinium contrast injection. They found early changes in the vascular permeability of the BBB up to four weeks before the lesion appearance on anatomical in vivo MRI. On histopathology, these areas of subtle BBB permeability corresponded to nodules with perivascular inflammation and microglial activation without any demyelination. They showed that the BBB permeability gradually decreased to return to its baseline level in 2-4 weeks after lesion appearance.

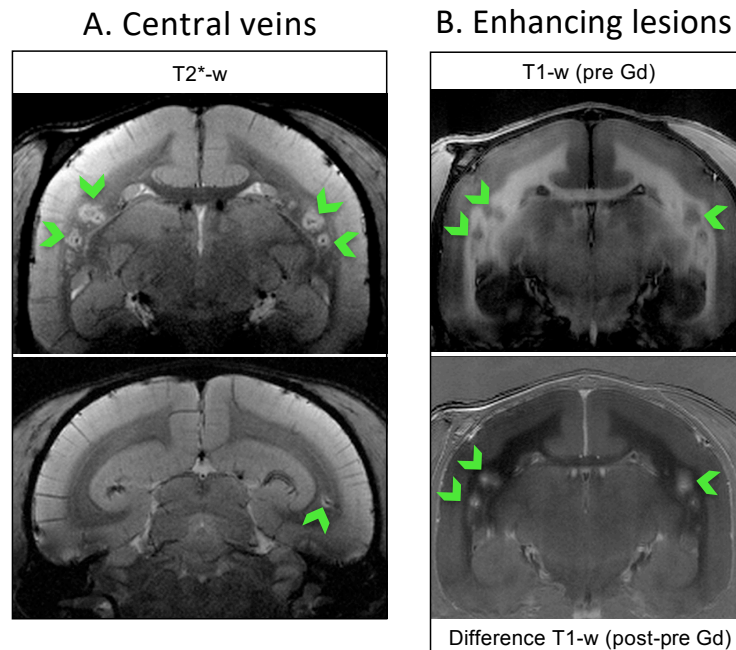


**Figure 2.10:** Radiological features in the marmoset EAE brain imaged at 7T. **A.** Central vein can be visualized on several lesions through the entire WM using T2\*-w GRE image. **B.** Enhancing lesions on T1-w MPRAGE sequence. Before gadolinium (pre-Gd image): large focal lesions display hypointense signal. After gadolinium injection (post-Gd image): the difference image reveals better the location of enhancement (very bright signal) relative to the lesion (hyperintense signal). Figure adapted from Maggi et al. (2017)

The same study from Maggi et al. (2014) provided information about the evolution of the lesion volume according to their in vivo age category in a subset of 31 analyzed lesions. The subacute lesions, between 1 to 5 weeks old, kept increasing in size despite the closed BBB (Figure 2.11A). The late subacute lesions, between 5 to 9 weeks old, already showed a decrease in size over time (Figure 2.11B), coincided with an overall decreased of Iba-1 inflammatory cells and absence of early-activated MRP14+. In MS, similar chronic lesions with a decreased inflammatory processes decreases in size over 3-5 months (Rovira et al., 2013).

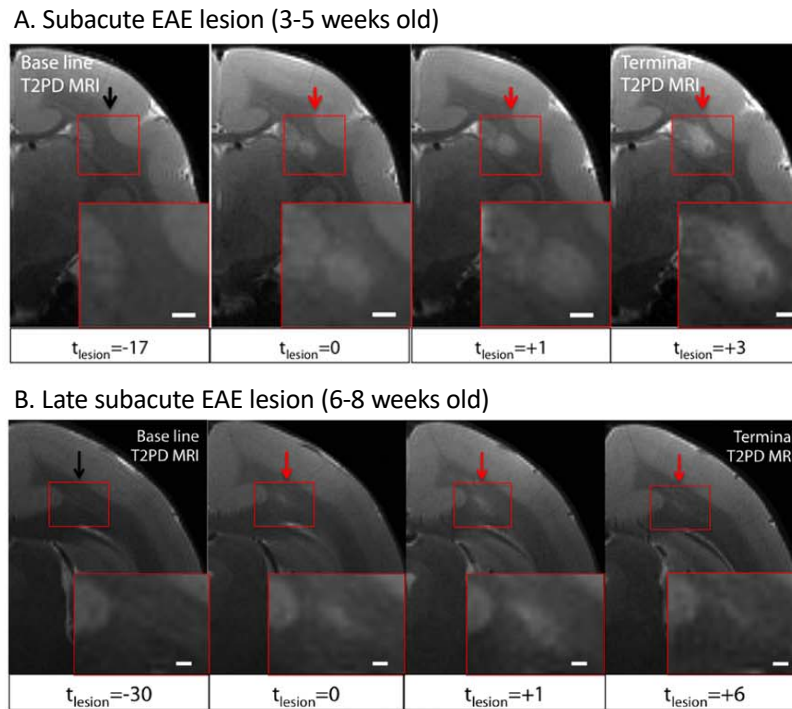


**Figure 2.11:** Representative subacute (A) and late subacute (B) lesions detected *in vivo* using serial MRIs. Serial T2PD (an average between T2-w and PD-w sequences) *in vivo* MRIs. The lesions appeared hyperintense from their appearance ( $t=0$ ) until the terminal MRI (which coincided on the day of the animal necropsy). The subacute lesion kept increasing in size, whereas the late subacute lesion, which was clearly visualized at 1 week ( $t=+1$ ) after its appearance, was barely visible on the terminal MRI ( $t=+6$ ). Figure adapted from Maggi *et al.* (2014)

We mentioned in the previous section that cortical lesions are a common pathological finding in the marmoset EAE model. However, these lesions have not been characterized through *in vivo* MRI. ‘t Hart group using the rhMOG-CFA model found that subcortical lesion tend to expand into the cortex toward the end of the disease ((‘t Hart *et al.*, 2015)). The clinico-radiological paradox seen in MS (when the MRI findings do not correlate with the clinical presentation of patients) is still an unresolved question in the marmoset EAE. Usually the clinical onset coincides with the first MRI lesions but the lesion volume does not correlate with the severity of the disease, as illustrated in Figure 2.12.

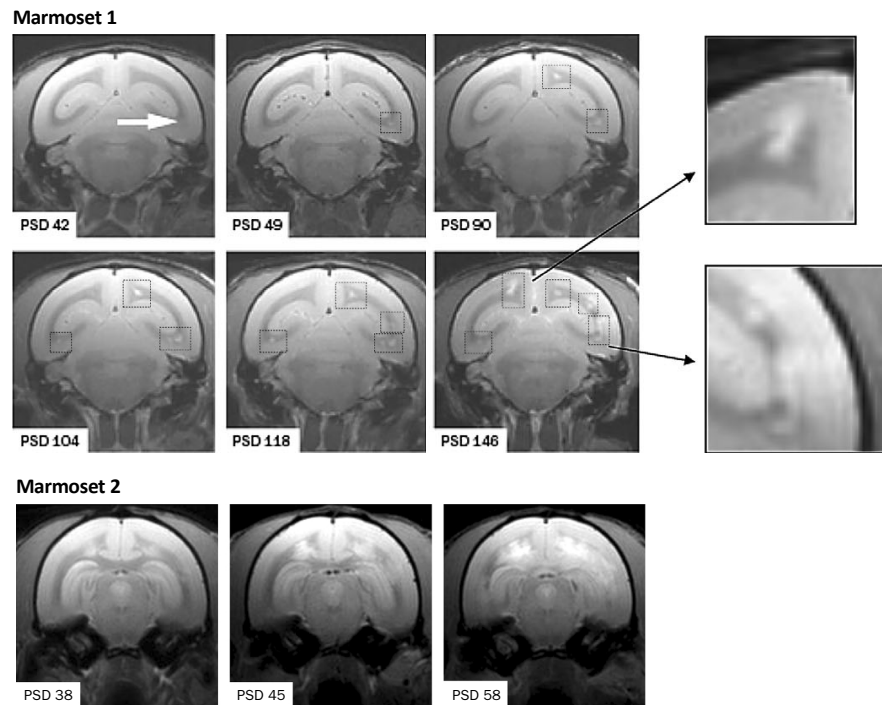


**Figure 2.12:** Spatiotemporal evolution of brain lesions and the clinico-radiological paradox in the marmoset immunized with rhMOG CFA using T2-weighted sequence. Marmoset 1 presented neurological deficits (ataxia) when the lesion first appeared at the MRI at 42 days post-immunization. However, marmoset 2 which presented larger lesion loads at 38 days post-immunization did not have any neurological deficits at this time. Figure adapted from A't Hart *et al.* (2004a)

## 2.3 The marmoset spinal cord

### 2.3.1 Spinal cord anatomy – functional structures

The spinal cord of mammals is thought to have a consistent macroscopic anatomy across species. However, it does exist some specific variations between species. A collaborative study between Watson and Tokuno provided maps of the spinal cord sections for marmosets, rhesus monkeys, rats, mice, and humans (Sengul *et al.*, 2013). It was reported that the numbers of vertebrae differ from humans. In marmosets, Casteleyn *et al.* (2012) analyzed the skeletons from 10 healthy marmoset animals and found the vertebral column being composed of: seven cervical vertebrae, 12 or 13 thoracic vertebrae, six or seven lumbar vertebrae and two or three sacral vertebrae. Despite differences in the numbers between animals, the thoraco-lumbar was always made of 19 vertebrae. The functional organization of the marmoset spinal cord was found to be very close to humans (Watson *et al.*, 2015).

Figure 2.13 represents the schematic divisions with the levels of cervical and lumbar enlargements, which matched the presence of motor neurons that supply the upper and lower limbs, respectively.

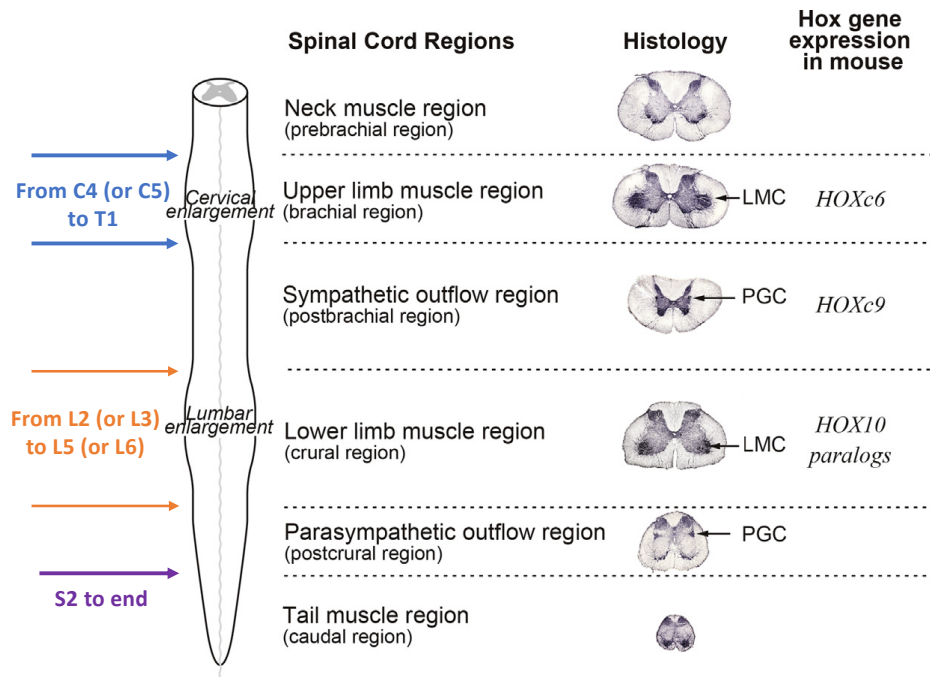


**Figure 2.13:** Subdivision of the mammalian spinal cord from [Watson et al. \(2015\)](#). The spinal nerves that supply the upper limb (blue), lower limb (orange), and the tail (purple) regions are annotated specifically for the marmoset in this diagram.

[Sengul et al. \(2013\)](#) provided transverse sections of the marmoset spinal cord stained for neurons and glia cells. They described in great detail the structural organization within the GM of the marmoset but could not identify the individual WM tracts, except for the posterior column and the corticospinal tracts. They hypothesized that the location of the WM tracts pathways were similar to the mouse, except for the corticospinal tracts, which were found within the lateral column, like in human.

Interestingly, some differences have been reported in the neuroanatomy between rodents and primates, especially for the motor cortex and its associated descending corticospinal tract. The evolution from rodents to primates led to the appearance of a fast conducting component of the CST and changed from the dorsal to the lateral column (see figure 2.14). The higher level of manual dexterity found in the nonhuman primates was correlated with the number of direct connections between cortex and motor neuron ([Courtine et al., 2007](#)). Possibility of testing motor performances (such as grasp) in nonhuman primates is also a clear advantage for clinical assessment of the disease progression. These

observations provide another advantage in favor of using marmosets over rodents to study spinal cord injury.

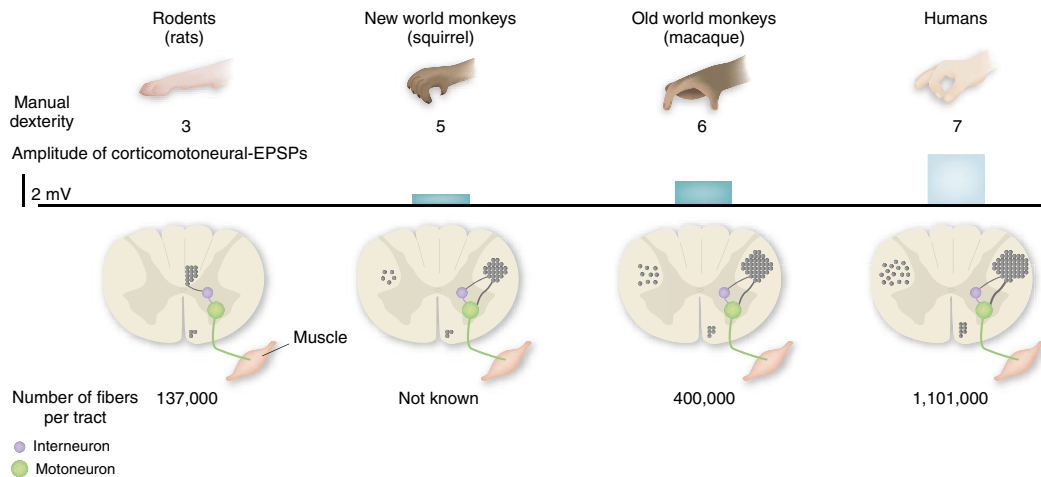


**Figure 2.14:** Comparison of the corticospinal tracts location and their relation with fine motor abilities between species (rodents, nonhuman primates, and humans). Figure adapted from (Courtine et al., 2007).

Finally, it is worth emphasizing on the distinct locomotion between species. The marmoset, a nonhuman primate, is quadrupedal with a similar arboreal locomotion that squirrels, which makes them moving through trees with vertical climbing. They also can sit on their hindlimbs with an upright position. The rodents are quadrupedal as well, but mainly on their four limbs with less sitting upright position. The human primate evolved by using bipedal locomotion and uses mainly standing upright position. Interestingly, it has been demonstrated that the body position influences the CSF pressure gradient. The CSF is a dynamic fluid which consists on a “secretion-circulation-absorption” cycle. A good balance between secretion and absorption is necessary to avoid accumulation of fluid and increase in intracranial pressure. A correct pressure gradient is necessary as well for circulation of the CSF within the cranial and spinal CSF space. It has been shown that changes from horizontal to upright position (could be sitting or standing) results in changes in the pressure gradient which promote a cranio-caudal CSF redistribution ((Klarica et al., 2014). This observation may be important due to the involvement of leptomeninges in neuroinflammatory diseases.

### 2.3.2 Pathological features in the marmoset EAE spinal cord

Several studies on the marmoset EAE reported the damage in the spinal cord as part of the whole CNS assessment. Massacesi et al. (1995) using the WMH protocol with Bordetella

pertussis (BP) bacterium, reported a prominent involvement of the spinal cord, which corresponded to an aggressive disease course with an average survival of 30 days. Three animals (among a total of 9 animals) developed a much longer disease course (from 114 days to 550 days) and was typical of a relapsing-remitting disease course. The spinal cord in this three animals presented a little meningeal and /or subpial inflammation. The 't Hart group (A't Hart et al., 1998) which replicated the protocol from Massacesi also described an extensive SC involvement for animal with an aggressive disease course (13 days average, [range 11-21days] life span). By removing the BP bacterium, they obtained a less aggressive disease with spinal cord tissues showing limited to moderate involvement. Kap et al. (2011), which uses the marmoset EAE model induced with the rhMOG(1-125) in CFA, performed a quantitative analysis on 8 selected spinal cord sections per animal (8 marmoset in total). They found a wide range of subpial severity with an average of 32% of the total WM affected by demyelination. Besides describing subpial demyelination, they did not provide a thorough description of the pathology seen in the spinal cord, such as the lesion shape or the spinal level affected. Figure 2.15 shows the pathological features in a EAE marmoset which includes subpial and extensive focal demyelinated lesions.

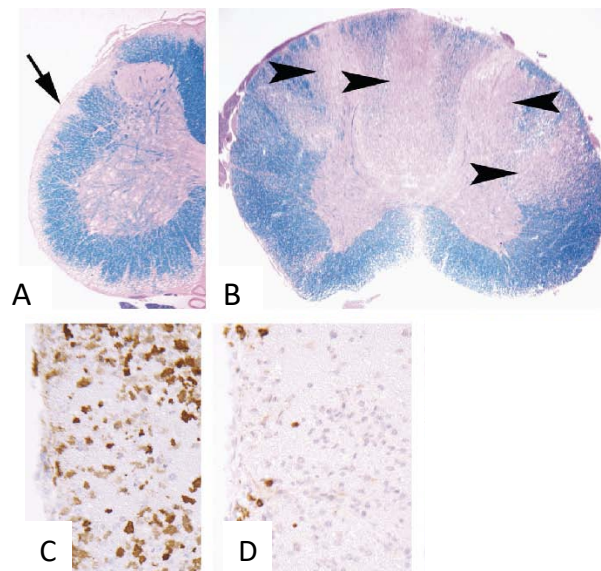


**Figure 2.15:** Spinal cord pathological features in a marmoset immunized with MOG 34-56 peptide IFA. Subpial lesions (A) and large focal lesions (B) show complete demyelination on the Luxol fast Blue-periodic acid Schiff. (C-D) Magnified view of the subpial lesions. MRP14+ macrophages cells are present (C) and some meningeal CD3+ T cells are also found. Figure adapted from Jagessar et al. (2010)



## 2.4 Summary

The EAE model have been extremely useful to understand some of the mechanisms of MS and develop novel therapies. However, depending on the animal species and the immunization protocol chosen, different features of the MS disease can be obtained, thus making it very difficult the translation from rodent EAE to human clinical trials.

The marmoset EAE model is thought to be a promising model since it recapitulates many of the radiological and immunological features of MS, in addition to sharing similar neuroanatomy and genetics with human. Marmoset EAE brain has been well investigated using *in vivo* serial MRIs, and proved to be an excellent system for studying the mechanisms of lesion formation in the brain. When combined with postmortem imaging and 3D printed techniques, accuracy of the histopathology is greatly improved. Heterogeneity of lesions is the specificity of this model and are found through the entire brain WM with a perivenular configuration. Demyelinated inflammatory WM lesions evolve during the span of several weeks from early acute to more chronic. Cortical subpial demyelination is also an important pathological feature. Other major advantages of a nonhuman primate model is the higher skills/dexterity available for the clinical assessment compared to rodents, as well a closer similitude of SC tract locations.

Despite the presence of spinal cord damage described in the marmoset EAE using histopathology and symptoms related to SC injury, no quantitative analysis has been performed on the entire spinal cord for characterizing the distribution and the type of lesions. The extent of spinal cord pathology have been reported to be heterogeneous, and may be associated with the aggressivity of the disease course, but remains still underinvestigated. Because the brain of marmoset with EAE has already shown high pathological and radiological similarities with MS, we hypothesize that the spinal cord lesions in this model may also share pathological features with MS, and be a highly valuable tool to understand the underlying mechanisms that lead to lesion development. The work presented in the following chapters is aimed at investigating the distribution of spinal cord lesions in a non-human primate model of MS using MR imaging modality combined with histopathology techniques.

# CHAPTER 3

## COMBINED POSTMORTEM MRI AND HISTOPATHOLOGY STUDY OF SPINAL CORD LESIONS IN THE MARMOSSET EAE MODEL

### **This Chapter contains:**

3.1	Introduction . . . . .	55
3.2	Materials and Methods . . . . .	55
3.2.1	EAE induction . . . . .	55
3.2.2	Sample preparation . . . . .	56
3.2.3	MRI acquisition . . . . .	57
3.2.4	Image analysis . . . . .	58
3.2.5	Histopathology . . . . .	59
3.2.6	MRI-histopathological comparison . . . . .	60
3.2.7	Statistical analysis . . . . .	61
3.3	Results . . . . .	63
3.3.1	Advantages of spinal cord extraction for improved image quality . . . . .	63
3.3.2	Evolution of spinal cord-related EAE neurological symptoms . . . . .	65
3.3.3	Characterization of spinal cord lesions by MRI and histopathology confirmation . . . . .	66
3.3.4	MRI signal-histopathology features correlation . . . . .	69
3.4	Discussion . . . . .	73
3.5	Conclusions . . . . .	75

## 3.1 Introduction

As already described in section 2.2, the marmoset EAE model, a nonhuman primate model of MS, seems to be the closest model to MS in terms of pathological, immunological and radiological features (Absinta et al., 2016; 't Hart et al., 2015). With a heterogeneous disease course and duration, this model covers a large panel of brain lesions found throughout the entire brain, such as the cortical subpial area, subcortical area, periventricular area, among many others. Similarly to MS, motor-sensory and bladder dysfunctions are often present, which strongly suggest the presence of demyelinated lesions in the spinal cord. A few histopathological studies have reported the presence of pathology in spinal cord tissues from marmosets with EAE (Massacesi et al., 1995; A't Hart et al., 1998; 't Hart and Massacesi, 2009; Laman et al., 1998; Villoslada et al., 2000). However, these studies did not characterize in a comprehensive manner the extent of the spinal cord pathology.

In order to characterize the distribution of the spinal cord lesions in this marmoset EAE model, I investigate in this chapter postmortem spinal cords by taking advantage of ultra-high field MRI, where high SNR can be obtained to produce high-quality and high-resolution images. These ex vivo MRI images are used to guide precisely any subsequent tissue sampling for histology, and to evaluate pathologically specific areas of the spinal cord. In this study, I use an experimental approach that combines ex vivo MRI and histopathology, with the goal of characterizing the extent and nature of the pathology affecting the spinal cord in the marmoset model of MS.

## 3.2 Materials and Methods

### 3.2.1 EAE induction

All common marmosets (*Callithrix jacchus*) used in this study were housed at the NIH Intramural Research facilities, in accordance with the standards of the American Association for Accreditation of Laboratory Animal Care and the NINDS Animal Care and Use Committee. Five adult marmosets [average age 3.5 years (min-max: 1.5–4.9), 4 females] were included in this study. Four animals were immunized with 200 mg fresh-frozen human WMH (normal-appearing white matter obtained from a MS patient autopsy) emulsified in CFA containing the IFA oil with 1.8 mg/ml of killed *Mycobacterium tuberculosis* H37 Ra strain (BD Difco, Sparks, USA). Each animal received a total volume of 0.8 mL, divided into four intradermal injections, two on the dorsal axilla and two others in the dorsal inguinal area. The fifth animal was used as a healthy, non-EAE control. Animals were frequently weighed and scored according to an EAE scale based on clinical symptoms (Kap et al., 2008). Table 3.1 provides the demographics and clinical summary of these animals. Once the animals

showed paraplegia and/or 20% weight loss, the experiment was terminated by performing transcatheter perfusion fixation with cold 4% paraformaldehyde under anesthesia. The spine was removed (Figure 3.1A) and stored in 4% neutral buffered formalin.

**Table 3.1:** Demographic and clinical information of the five marmosets included in the postmortem EAE study.

Animal	Induction	Sex	Age (years)	Disease duration (days)	EAE score at sacrifice	Clinical signs at sacrifice
M#1	WMH	M	3.6	134	3	Weight loss, lethargy, ataxia, severe weakness, sensory loss, vision loss
M#2	WMH	F	4.6	159	3	Apathy, tetraparesis, ataxia, sensory loss, vision loss
M#3	WMH	F	2.9	123	N/A	N/A
M#4	WMH	F	1.5	89	N/A	N/A
M#5	None	F	4.9	-	-	-

Disease duration is measured as time from immunization to termination.

WMH: white matter homogenate, M: male, F: female, N/A: not available.

### 3.2.2 Sample preparation

The spinal cord tissues (from C3-C4 down to the cauda equina) were extracted from the formalin-fixed spines by performing a laminectomy (Figure 3.1B). After extraction, the entire cord of the animal was divided into four or five pieces. A 3D-printed SC holder (Figure 3.1C) was created using 3D-printing Netfabb Professional 5.0 software (Autodesk Inc., San Rafael, CA, USA). This holder enabled precise alignment of each piece of the cord while restricting motion using cotton thread (Figure 3.1D) and allowed scanning of all the pieces simultaneously. The holder was inserted into a 15 ml plastic tube and immersed in a proton-free, susceptibility-matched fluid (Fomblin, Solvay S.A, Brussels, Belgium).

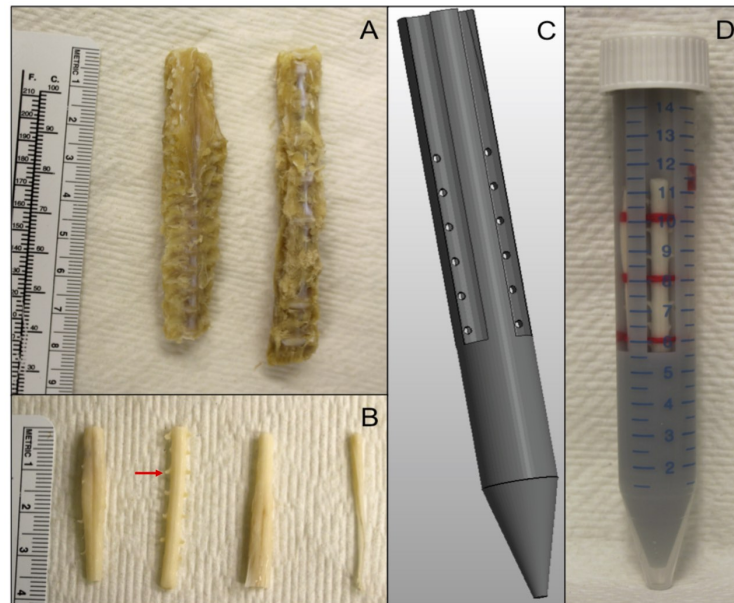


**Figure 3.1:** Preparation of spinal cord tissue for postmortem MRI. (A) The upper (left) and lower (right) spine are collected at necropsy, before cord extraction. (B) Four spinal cord pieces were obtained after extraction (from the upper cervical on the left to the lower lumbo-sacral on the right). Note: the thoracic nerve roots (red arrow) were most easily preserved. (C) The 3D-printed model of the SC holder was designed with four slots to insert and align all portions of the cord. (D) Final spinal cord postmortem MRI setup, showing the spinal cord tissues restrained with cotton thread within the 3D-printed holder, which was subsequently inserted into a 15 ml tube. The same SC holder was used for all marmosets.

### 3.2.3 MRI acquisition

MRI was performed on a 7T/30 cm MRI scanner (Bruker BioSpin Corp., Ettlingen, Germany) equipped with a 15 cm gradient set of 450 mT/m strength (Resonance Research Inc., Billerica, MA, USA). The non-extracted (Figure 3.1A) and the extracted spinal cord tissues (Figure 3.1B) were imaged using a similar MRI protocol. A proton-only transmit-receive volume coil (Bruker) was used for imaging the tissue samples (35 mm and 25 mm inner diameter for the non-extracted and extracted tissues, respectively), which were loaded in the plastic tubes. During each scanning session, a 3-dimensional (3D) T2\*-w gradient-echo sequence was acquired. For the non-extracted cord tissues, four separate MRI sessions were required to cover the entire cord length (two for the upper spine, two for the lower spine) with an isotropic resolution of  $100 \mu\text{m}^3$  and five consecutive repetitions for a total acquisition time of 30 hours (Table 3.2, left column). For the extracted cord tissues, one single MRI session was sufficient to obtain the entire cord length with an in plane resolution of  $70 \mu\text{m}^2$  and a slice thickness of  $200 \mu\text{m}$  and four consecutive repetitions for a total acquisition time of 12 hours (Table 3.2, right column).

**Table 3.2:** Sequence parameters of the 3D T2\*-w GRE sequences for the two ex vivo MRI protocols.

	Non-extracted protocol	Extracted protocol
Field-of-view (mm)	25.6 x 25.6 x 60	11 x 11 x 38
Matrix size	256 x 256 x 600	157 x 157 x 190
Spatial resolution (mm)	0.1 x 0.1 x 0.1	0.07 x 0.07 x 0.20
Repetition time (ms)	80	50
Echo time (ms)	15	10 ms
Excitation pulse angle	20°	12°
Number of averages	1	8
Scan time per acquisition	1h 27min	2h 40min
Number of repetitions	5	4
Total acquisition time (entire spine)	~ 30h	~ 12h

Note: Field of view and matrix size were adapted to the different tissue dimensions while maintaining the same spatial resolution.

### 3.2.4 Image analysis

Regarding the extracted protocol images, all four acquisitions were first averaged using the MIPAV image analysis software (National Institutes of Health, Bethesda, Maryland; <http://mipav.cit.nih.gov>). A N4-bias-field correction (Tustison et al., 2010) was applied to correct for intensity inhomogeneity. Then, the images were upsampled to an in-plane axial resolution of  $35 \mu\text{m}^2$  and a  $70 \mu\text{m}$  slice thickness and concatenated to generate a single image volume of the entire spinal cord using ImageJ software (National Institutes of Health, Bethesda, Maryland, <https://imagej.nih.gov/ij/>) and MIPAV. Finally, the different spinal level segments were annotated based on the location of the nerve roots (Sengul et al., 2013).

Focal lesions (areas of abnormal signal intensity within the white matter (WM)) were manually segmented (ITK-SNAP version 3.2.0) using triplanar viewing mode. Lesions were classified according to their volume using the following arbitrary categories: small ( $0.009 - 0.06 \text{ mm}^3$ ), medium ( $0.06 - 0.4 \text{ mm}^3$ ), and large ( $> 0.4 \text{ mm}^3$ ). The specific position of the focal lesions was also recorded as anterior, posterior, and lateral (left/right). Subpial lesions were also manually segmented on select images at three different levels of the cord (C7, T7, and L3). Regions-of-interest (ROIs) of the entire cross-sectional cord, normal appearing white matter (NAWM), and GM were drawn manually (Figure 5.4) using a semi-automated tool in JIM V.7.0 (Xinapse Systems, Leicester, UK). The relative thickness of subpial lesions (areas of abnormal signal intensity along the edge of the WM) was characterized as

a percentage of total WM using the following formula:

$$\frac{ROI_{\text{subpial area}}}{ROI_{\text{CSA cord}} - ROI_{\text{GM area}}} \times 100$$

where CSA cord is the cross-sectional area of the cord. The degree of severity for the subpial lesions was arbitrarily defined as: low if < 20%; intermediate if between 20–50%; and high if > 50%.

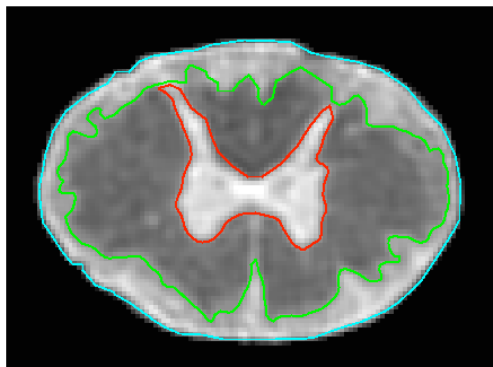


**Figure 3.2:** *Regions of interest drawn manually to compute the extent of subpial white matter lesions as a percentage of the total white matter. Light blue line: entire cross-section of the spinal cord; green line: edge of the NAWM; red line: GM.*

### 3.2.5 Histopathology

Focal and subpial lesions with various sizes, shapes, and locations identified by ex vivo MRI were targeted during the cutting process (transaxial cuts of 3 mm-thick slabs). Slabs from the control animal were selected at similar cord levels for comparison purposes. A total of 32 slabs were cut, and then embedded in paraffin wax. These paraffin-embedded slabs were sectioned in 5  $\mu$ m-thick slices to find the lesions detected by MRI. Luxol fast blue with periodic acid-Schiff (LFB-PAS) staining for myelin, and ionized calcium-binding adapter molecule 1 (Iba-1) immunohistochemistry for activated macrophages and microglia inflammatory cells were performed on a subset of slices containing lesions. The 3,3'-diaminobenzidine (DAB)-enhanced Turnbull staining was performed on slices with suspicious hypointense signal to confirm the presence or absence of extracellular blood deposition. Details of the staining protocols are provided in the C.1. Digital pictures of the stained slides were generated using a Zeiss Observer 1 microscope (ZEN blue software (Zeiss, Thornwood, NY) at 10x optical zoom with a pixel resolution 0.7  $\mu$ m, and exported as TIFF files.

### 3.2.6 MRI-histopathological comparison

Figure 3.3 summarizes the three main steps we followed to perform the analysis between the ex vivo MRI signal and the histopathology findings.

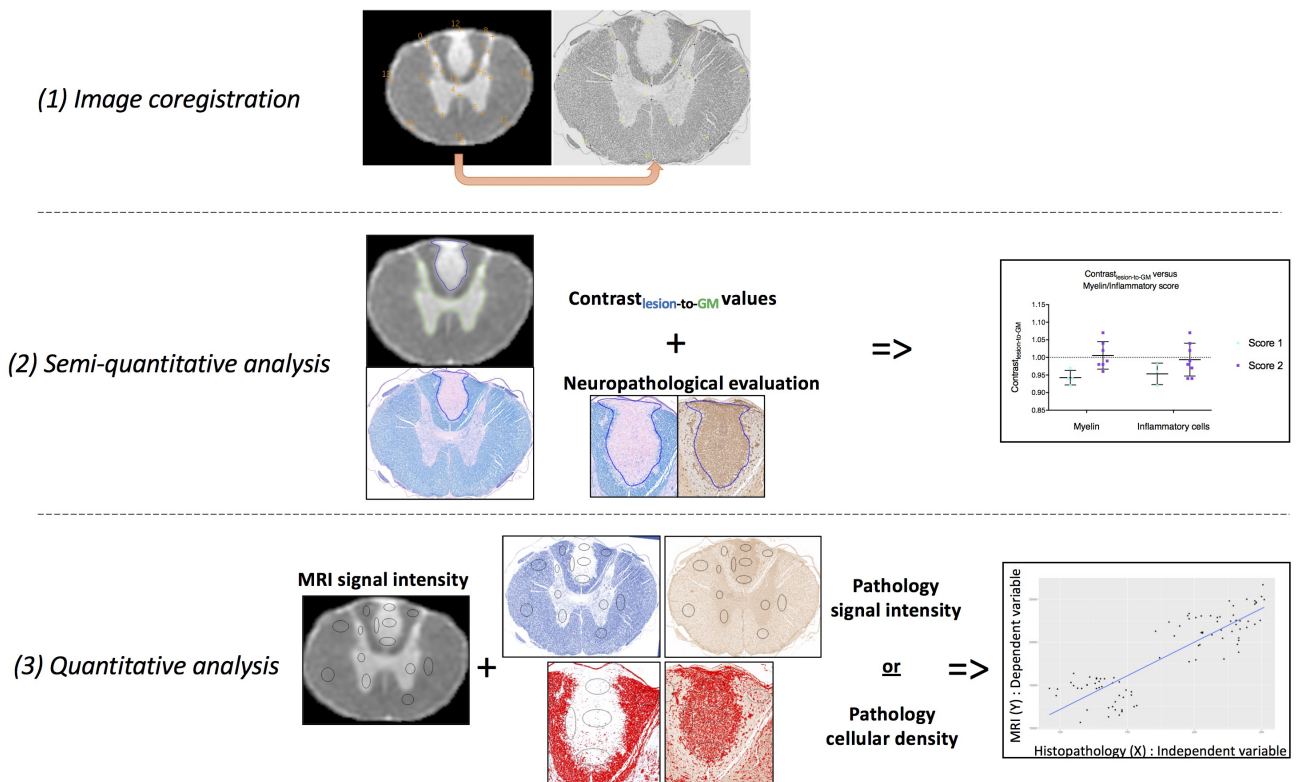


**Figure 3.3:** Analysis pipeline between ex vivo MRI and histopathology findings. (1) Image coregistration from ex vivo MRI (with 35 m in plane resolution) to histopathology section (with 0.7  $\mu\text{m}$  in plane the resolution). (2) Semi-quantitative analysis consists of the  $Contrast_{\text{lesion-to-GM}}$  and the neuropathological evaluation. Corresponding coregistered ex vivo MRI and LFB-PAS display the ROI used to perform the analysis. (3) Quantitative analysis consists of finding association between the MRI signal intensity (dependent variable) and the pathology signal intensity (or pathology cellular density) (independent variable).

MRI images were first coregistered to the corresponding LFB-PAS histology images using thin-plate splines with control points initialized manually (MIPAV). A semi-quantitative comparison was performed by selecting 11 different lesions (9 focal and 2 subpial) on MRI. Lesions were then segmented on the coregistered MRI images by using an intensity level threshold (MIPAV). The contrast between lesion and GM was computed as the following and reported for these selected lesions:

$$Contrast_{\text{lesion-to-GM}} = \frac{\text{Signal intensity}_{\text{lesion}}}{\text{Signal intensity}_{\text{GM}}}$$

The corresponding contour line was defined using the ROI tool and propagated to



the histological images in order to perform a neuropathological evaluation. The level of demyelination inside the contoured lesions was rated on LFB-PAS using the following grading system: 0 = normal myelin density; 1 = reduced myelin density; 2 = completely demyelinated. The level of inflammation was rated on Iba-1 using the following grading system: 0 = absent/few inflammatory cells; 1 = moderate density of inflammatory cells; 2 = high density of inflammatory cells.

A more quantitative comparison between MRI and histopathology was performed using regression models (see “Statistical analysis”, 3.2.7) on the coregistered ex vivo MRI, LFB-PAS, and Iba-1 images. To generate data for fitting the statistical models, a total of 92 ROIs were drawn manually on LFB-PAS images using ImageJ at different cross-sectional cord locations (WM, GM, and lesion) of several sections (8–14 ROIs per section) (Figure 3.4). ROIs were then propagated to the corresponding MRI images and Iba-1 staining. From each staining, the function “color deconvolution” (ImageJ, plug-in) was applied to extract the channel corresponding to the stain of interest. For the myelin component, the vector “FastRed-FastBlue-DAB” was chosen to obtain the LFB blue channel from the LFB-PAS staining. For the inflammatory cells, the vector “H-DAB” was chosen to obtain the DAB red channel from Iba-1 staining. Mean signal intensity for each ROI was computed on both MRI and grayscale-deconvoluted staining images. Instead of measuring the signal intensity on the deconvoluted staining images, we also measured the density of cells within the same ROIs. An automatic level threshold was applied on the deconvoluted images and then manually adjusted if needed.

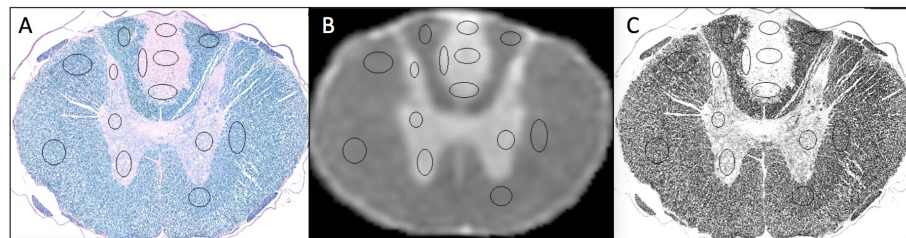


**Figure 3.4:** Example of regions of interests (black lines) manually drawn on the LFB-PAS (A) and propagated to the co-registered MRI (B) and LFB-deconvoluted gray level (C). ROIs were placed through the entire cord cross section to include NAWM, GM, and lesions.

### 3.2.7 Statistical analysis

The nonparametric two-tailed Mann Whitney test (Prism v7.0b) was performed to test any association between the  $\text{Contrast}_{\text{lesion-to-GM}}$  values and histopathology scores. To assess the association between MRI and histopathology signals and identify which variables influenced

the MRI signal, we performed regression models and evaluated different statistical models. A schematic representation of the nested design can be visualized in figure 3.5.

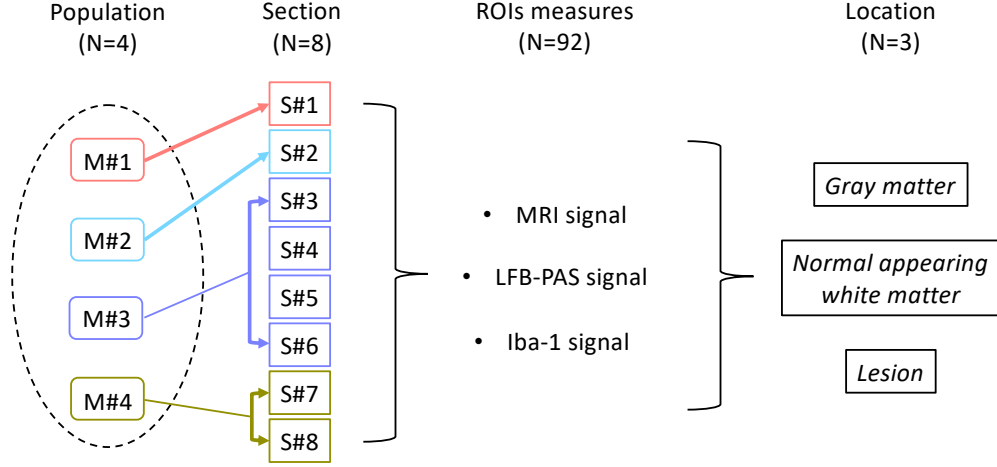


**Figure 3.5:** Nested design from our MRI-histopathology data analysis. Measurements were taken from 4 marmosets, and on each different sections were extracted. For each section, we obtained the ex vivo MRI, the pathology LFB-PAS and Iba-1. Repeated measures were performed with a total of 92 ROIs across the 8 sections, from which three locations were defined (gray matter, normal-appearing white matter and lesion).

In all models, the independent variable was the histopathology and the dependent variable was the MRI signal intensity. The following data were used for the different models: MRI raw values ( $MRI_{raw}$ ), histopathology (PATH) signal values after deconvolution, section, and tissue type (NAWM, GM, lesion). Another dataset for MRI values was also employed to correct for signal variation between MRI images. For that, histograms for each MRI section were adjusted by adding or subtracting the difference between the mean NAWM value with a reference NAWM to obtain the MRI standardized values ( $MRI_{shift}$ ). The statistical models analyzed were the following:

$$\begin{aligned}
 M_0 \quad MRI_{ij} &= \beta_0 + \beta_1.lesion_{ij} + \beta_2.NAWM_{ij} + \beta_3.PATH_{ij} + \epsilon_{ij} \\
 M_1 \quad MRI_{ij} &= \beta_0 + \beta_1.lesion_{ij} + \beta_2.NAWM_{ij} + \beta_3.PATH_{ij} + b_{0i} + \epsilon_{ij} \\
 M_2 \quad MRI_{ij} &= \beta_0 + \beta_1.lesion_{ij} + \beta_2.NAWM_{ij} + \beta_3.PATH_{ij} \\
 &\quad + \beta_4.PATH_{ij}.lesion_{ij} + \beta_5.PATH.NAWM_{ij} + b_{0i} + \epsilon_{ij}
 \end{aligned}$$

In these models, the predicted MRI value (either  $MRI_{raw}$  or  $MRI_{shift}$  for section  $i$  and ROI  $j$  is determined by the pathology (PATH), identified as the fixed effects, represented by the  $\beta$  coefficients ( $\beta_0, \beta_1, \beta_2$  being the intercepts components,  $\beta_3, \beta_4, \beta_5$  being the slope components) and the section-specific, identified as the random effect, specified by the  $b$  coefficient. Lesion and NAWM are binary indicator.  $\epsilon$  is the residual term, seen as the

portion that is not explained either by fixed effect or random effects. Finally, due to the interaction term for tissue type, three regression fits were obtained for each of the tissue type.

For simplification, the equation M2, the most complex, can be summarized as the following:

$$M_2 \quad MRI_{ij} = (\beta_{\text{intercept}} + \beta_{\text{slope}} \cdot PATH)_{ij} \cdot \text{tissuetype} + b_i + \epsilon_{ij}$$

The observed MRI signal contains several contributors that are estimated through the model: a fixed effect component, a random effect component and a residual factor.

Two linear mixed-effects models ( $M_1$  and  $M_2$ ) were used with random effect of section, to account for the correlated observations taken from the same section. A simple linear model M0 was run for completeness. M2, the most complex model, included an interaction term to test the hypothesis that the relationship between MRI and pathology depends on the tissue type (NAWM, GM, lesions). We evaluated these different regression models for both LFB (called the myelin model) and Iba-1 (called the inflammation model) by comparing their Akaike Information Criteria (AIC) values (AKAIKE, H. 1973); the best model was considered to have the lowest AIC value. Because AIC values are ordinal and give a rank of the model goodness-of-fit, the  $\Delta AIC$  values were reported as well:

$$\Delta AIC(n) = AIC(n) - AIC_{\min}$$

where  $n$  denotes the model of interest and  $AIC_{\min}$  the minimum AIC of all the models tested.

Regression results were considered significant for  $p \leq .05$ . The coefficient of determination,  $R^2$ , was reported to evaluate the goodness-of-fit using the method of Nakagawa and Schielzeth (2013) adapted for the linear mixed-effects models. Statistical analysis and graphical visualization were performed using R version 3.3.3 and Rstudio (1.0.143). The lme4 package version 1.1-16 was used to fit the mixed-effects model using restricted maximum likelihood estimation.

## 3.3 Results

### 3.3.1 Advantages of spinal cord extraction for improved image quality

The main benefit of extracting the spinal cord was to allow the use of the circularly polarized transceiver volume coil which provided homogeneous image quality. Because the cord tissues were positioned symmetrically to each other within the SC holder at the coil

center, each tissue received similar RF signal. By removing the tissues (muscles, bones) surrounding the spinal cord, the visualization of the SC white matter was also significantly improved. Indeed, the non-extracted cord images were mainly affected by susceptibility artifacts from the different susceptibility properties of the surrounding tissues. Signal dropout and distortions were seen at several junctions, such as the interspinous ligaments with the posterior edge of the cord (Figure 3.6, yellow arrows), but also by the intervertebral disk within the anterior edge of the cord (Figure 3.6, orange arrows), or the nerve roots located more laterally. After extraction of the spinal cord, the cord edge was completely visible, which allowed to accurately detect confluent subpial abnormal signal areas along the edges of the SC (Figure 3.6, green arrows) and the focal areas of abnormal signal.

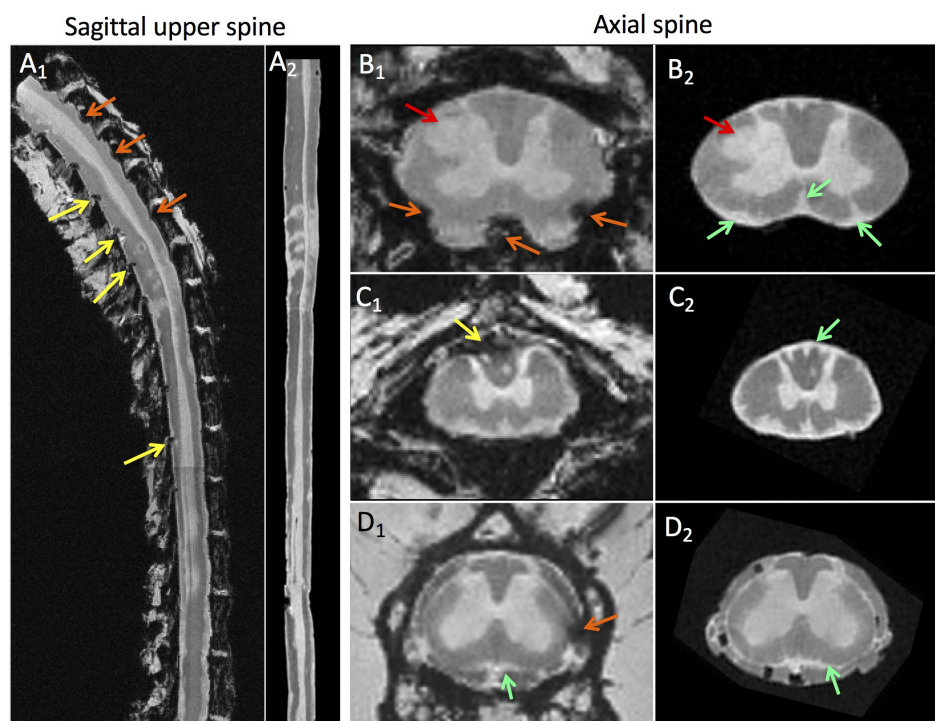


**Figure 3.6:** Comparison of MRI image quality before and after spinal cord extraction. T2\*-w 3D GRE images from the two MRI protocols described in table 3.2 performed on EAE animal spinal cords. Images of the extracted cord were interpolated during post-processing with an axial in-plane resolution of  $35 \times 35 \mu\text{m}^2$  and  $70 \mu\text{m}$  slice thickness. Before extraction of the spinal cord ( $A_1$ ,  $B_1$ ,  $C_1$ ,  $D_1$ ), susceptibility artifacts seen as areas of signal loss are prominent hiding the edges of the spinal cord. On the posterior side, periodic signal loss (yellow arrows) are found at the junction of the interspinous ligament with the cord. On the anterior side (orange arrows), distorted signal loss artifacts correspond to the periodic intervertebral disk in the midline and the junction of nerve roots located more laterally. After extraction of the spinal cord ( $A_2$ ,  $B_2$ ,  $C_2$ ,  $D_2$ ), the cord edge is completely apparent. The subpial lesions, which were obscured at the cervical level, are now visualized on the extracted cord image. Subpial at the thoracic and lumbar levels are confirmed. The focal lesion (red arrow) is also better delineated due to the higher in-plane resolution of the extracted imaging protocol.

### **3.3.2 Evolution of spinal cord-related EAE neurological symptoms**

All immunized animals developed clinical signs between 65 and 100 days post-immunization and reached EAE scores  $\geq 2.5$  at the time of sacrifice. Disease duration (from immunization to death) ranged from 71 to 159 days (mean: 113 days) (Table 3.1).

Detailed clinical signs were obtained only in two animals (M#1 and M#2), whereas we still had EAE scores for M#4 from our record (see figure 3.7). Apathy was the only first abnormal sign observed in animal M#1, which appeared at 8 weeks post-immunization and only lasted three weeks. At 14 weeks, symptoms were more severe with altered walking, loss of motor grip and tonicity, bladder dysfunction. The last two weeks before sacrifice, more limbs were affected with higher severity and the animal developed additional symptoms like a positive Babinski, tail atonia, lethargy. For animal M#2, mild symptoms appeared at the 7<sup>th</sup> week after immunization, as altered walking and apathy. Within three weeks, symptoms worsen and reached an EAE score of 2.5 as weakness, sensory loss and a positive Babinski. These symptoms did not disappear but fluctuated until one week before the end of the experiment. By the 23<sup>rd</sup> week, the animals presented, in addition of the previous symptoms, severe weakness of all limbs (with complete paralysis for the left arm), tail atonia and discoordination.

A constant weight loss was observed in two animals and coincided with the apparition of the clinical symptoms. It severe was for animal M#4 with 29% weight loss at sacrifice and moderate for animal M#1 with 9% weight loss. Contrarily, we observed a continuous weight gain that matched with the first clinical symptoms for animal M#2.

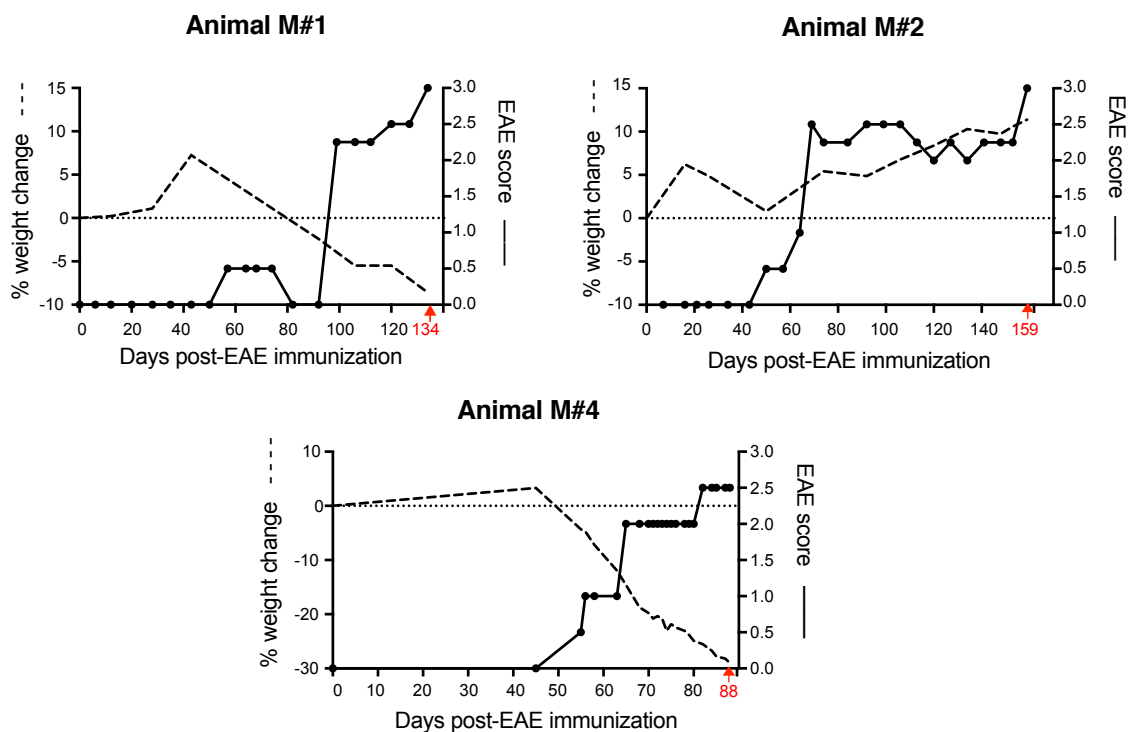


**Figure 3.7:** Temporal changes of the EAE score and body weight during the course of the disease. The percentage weight change is the left-y-axis (black dotted line, relative change compared to baseline on day 0). EAE clinical score is on the right-y-axis (black line, maximum score of 5). Each black round mark corresponds to a clinical assessment performed on the animal. The red arrows represent the terminal MRI with its corresponding disease duration (number of days in red).

### 3.3.3 Characterization of spinal cord lesions by MRI and histopathology confirmation

All four EAE animals displayed SC abnormalities on postmortem MRI images. Focal WM lesions with various sizes and shapes were observed at different cord levels (Figure 3.8, red arrows). A total of 85 focal WM lesions were segmented on the MRI images across the four EAE animals. Thirty-four lesions (40%) were found at the cervical level, 40 (47%) at the thoracic level, and 11 (13%) at the lumbar level (see Table 3.3). Fifty-seven lesions (67%) were classified as small (average volume:  $0.028 \text{ mm}^3$ , 24 lesions (28%) as medium-sized ( $0.11 \text{ mm}^3$ ), and 4 lesions (5%) as large ( $2.54 \text{ mm}^3$  (Table 3). Sixty-nine focal WM lesions (81%) were located in the lateral WM, fifteen lesions (18%) were located in the posterior WM, and only 1 lesion was found in the anterior WM (Table 3.3). Subpial WM lesions were also observed along the entire cord, with variable thickness (Figure 3.8, green arrows). Three animals (M#1, M#2, and M#3) displayed thin subpial WM lesions (relative thickness < 21%) throughout their entire cords, whereas one animal (M#4) showed thicker subpial WM lesions (relative thickness > 39%) in the lumbar portion of the cord (Table 3.4).

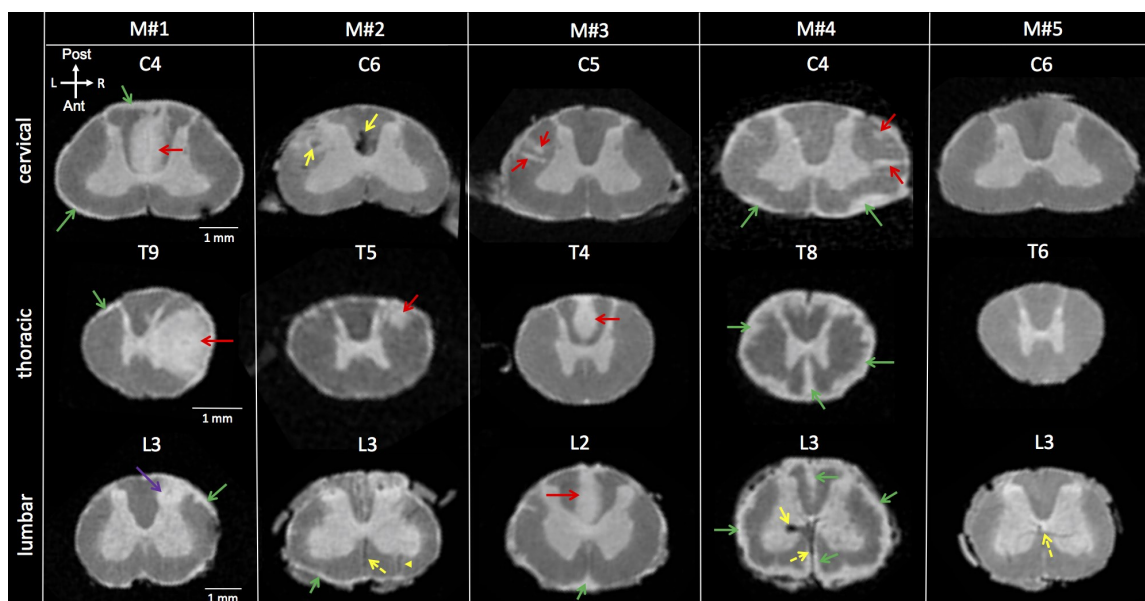


**Figure 3.8:** High-resolution postmortem MRI scans of four marmoset spinal cords with EAE (M#1, M#2, M#3, M#4) and one healthy control (M#5) showing cervical, thoracic, and lumbar spinal cord levels. Anatomical orientation axes are included (white arrows): anterior (ant), posterior (post), left (L) and right (R). The heterogeneity of the focal lesions (red arrows) and subpial lesions (green arrows) in terms of size, shape and location can be observed across the marmosets with EAE. Areas of hypointense signal (yellow arrows) were sometimes observed in these animals (M#2, C6 and M#4, L3), most likely originating from blood deposits. Parenchymal vessels with deoxygenated blood could also be visualized as dark thin lines (yellow dotted arrows, L3 for M#2, M#4 and M#5), sometimes running centrally through a focal lesion (plain yellow arrow, M#2, L3). Note the mass effect produced by a large tumefactive lesion (M#1, T9, red arrow) that involves most of the right lateral column and some of the GM. Another lesion affecting the GM (purple arrow) could also be found within the dorsal horn at the lumbar level (M#1, L3). Various degree of confluence for the subpial lesions can be appreciated. For three animals (M#1, M#2, M#3), subpial lesions were subtle and not confluent compared to animal M#4 that displayed partially confluent (C4) and completely confluent at the lower levels of the SC (T8 and L3).

**Table 3.4:** Characterization of the subpial lesions as a percentage of the total white matter for selected spinal levels in the four marmosets with EAE.

	Animal	M#1	M#2	M#3	M#4	Average across animals
Relative thickness (% of WM) of subpial lesions by cord level	Cervical C7	18	15	5	30	17
	Thoracic T7	16	20	11	54	25
	Lumbar L3	19	14	10	39	21

**Table 3.3:** Characterization of the focal lesions by spinal cord level, size, and white matter location in the four marmosets with EAE.

	<b>Animal</b>	<b>M#1</b>	<b>M#2</b>	<b>M#3</b>	<b>M#4</b>	<b>Average across animals</b>
Number of focal lesions by cord level	Cervical	11	5	10	8	8.5
	Thoracic	9	10	10	11	10
	Lumbar	1	2	5	3	2.8
Number of focal lesions by size and corresponding average volume [STD] in mm <sup>3</sup>	Small	10; 0.025 [0.013]	9; 0.033 [0.014]	21; 0.028 [0.009]	17; 0.026 [0.013]	14; 0.028 [0.01]
	Medium	9; 0.14 [0.1]	8; 0.13 [0.089]	2; 0.078 [0.003]	5; 0.086 [0.022]	6; 0.12 [0.08]
	Large	2; 4.18 [0.59]	0	2; 0.9 [0.68]	0	1; 2.54 [1.96]
Number of focal lesions by location	Posterior	9	1	3	2	3.8
	Lateral left	8	10	20	10	12
	Lateral right	3	6	2	10	5.3
	Anterior	1	0	0	0	0.25

STD: Standard deviation

Anatomical features observed on MRI were visually matched on histological sections in control and EAE animals (Figure 3.9). In the control animal, both MRI and histology depicted normal WM with dark gray (denoted here as “isointense”) MRI signal (Figure 3.9A<sub>1</sub>), normal LFB staining (Figure 3.9B<sub>1</sub>), and absence of “reactive” inflammatory cells on Iba-1 (Figure 3.9C<sub>1</sub>). In the EAE animals, focal and subpial WM cord lesions detected as areas of hyperintense MRI signal (Figure 3.9A<sub>2</sub>-A<sub>4</sub>) corresponded to areas of clear demyelination characterized by low LFB (Figure 3.9B<sub>2</sub>-B<sub>4</sub>) staining, as well as intense inflammation demonstrated by strong Iba-1 staining (Figure 3.9C<sub>2</sub>-C<sub>4</sub>). Areas of hypointense signal have been described in Figure (M#2, C6, yellow arrows). By performing iron Turnbull staining, we determined that these hypointense areas corresponded to the deposition of hemosiderin which is likely originating from extracellular blood deposits (see additional Figure A.1).



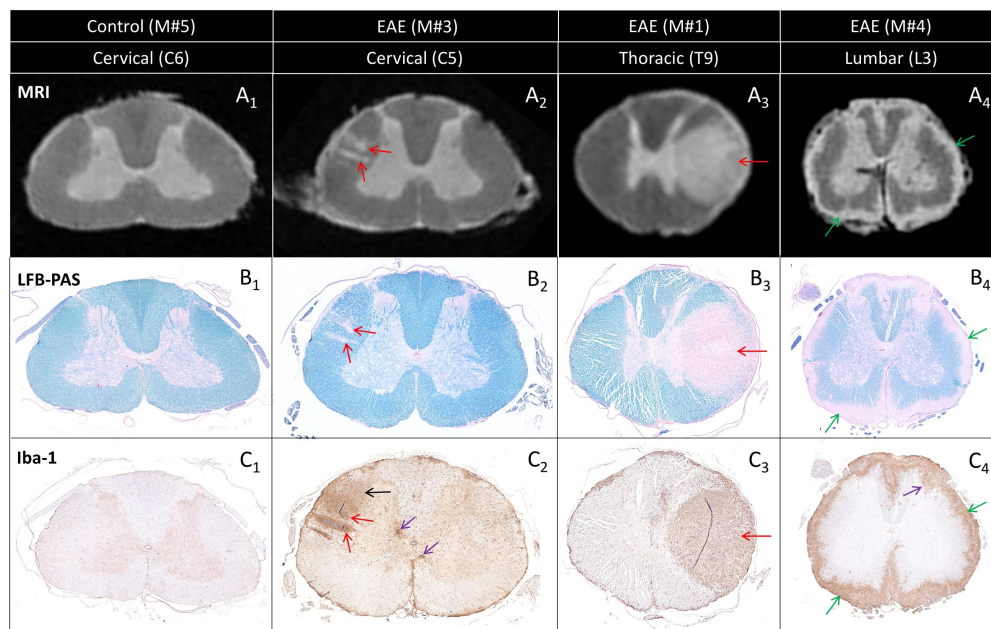


**Figure 3.9:** Comparison between MRI scans (A) and histopathology sections (B and C) from a control animal (M#5) and three EAE animals (M#3, M#1, and M#4). Two small focal lesions detected by MRI in the cervical section (A<sub>2</sub>, red arrows) correspond to two small demyelinated areas (B<sub>2</sub>, red arrows) with intense inflammatory cell infiltration (C<sub>2</sub>, red arrows). Note also the more diffuse inflammatory cell infiltration located above the two lesions, not captured by MRI (C<sub>2</sub>, black arrow). The large tumefactive focal lesion detected by MRI in the thoracic section (A<sub>3</sub>, red arrow) matches an area of demyelination (B<sub>3</sub>, red arrow) and inflammatory cell infiltration (C<sub>3</sub>, red arrow). A similar correspondence between MRI and histopathology is observed at the lumbar level (A<sub>4</sub>, B<sub>4</sub>, C<sub>4</sub>) for the subpial lesion (green arrows).

### 3.3.4 MRI signal-histopathology features correlation

The semi-quantitative analysis performed on a subset of 11 lesions revealed heterogeneity in myelin content and density of inflammation (see additional Table B.1). This heterogeneity is illustrated by representative examples of a completely demyelinated lesion (Figure 3.10A<sub>2-3</sub>) with intense inflammation (Figure 3.10A<sub>4</sub>) and a partially demyelinated lesion (Figure 3.10B<sub>2-3</sub>) with moderate inflammation (Figure B<sub>4</sub>). The semi-quantitative analysis indicated an association between MRI signal and the myelin content. Completely demyelinated lesions (score = 2) showed a significantly higher contrast<sub>lesion-to-GM</sub> value than lesions with partial demyelination (score = 1) (Figure 3.11). A similar trend was observed when comparing lesions with high density of Iba-1 cells (score = 2) against lesions with a moderate density of cells (score = 1), although the difference in contrast<sub>lesion-to-GM</sub> values was not significant in this case (Figure 3.11).

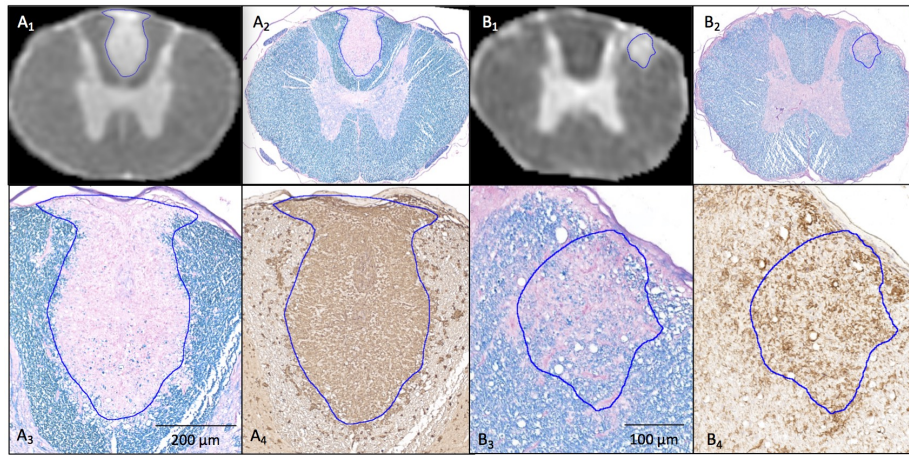


**Figure 3.10:** MRI scans ( $A_1$  and  $B_1$ ) coregistered to the corresponding LFB-PAS images ( $A_2$  and  $B_2$ ) for defining the lesion contour ROI (blue lines). Magnified views of the lesions for LFB-PAS ( $A_3$  and  $B_3$ ) and Iba-1 ( $A_4$  and  $B_4$ ).  $A_3$  and  $A_4$  show complete myelin loss and uniform intensity of inflammatory cells throughout the entire lesion.  $B_3$  and  $B_4$  show a partially demyelinated lesion with moderate inflammation.

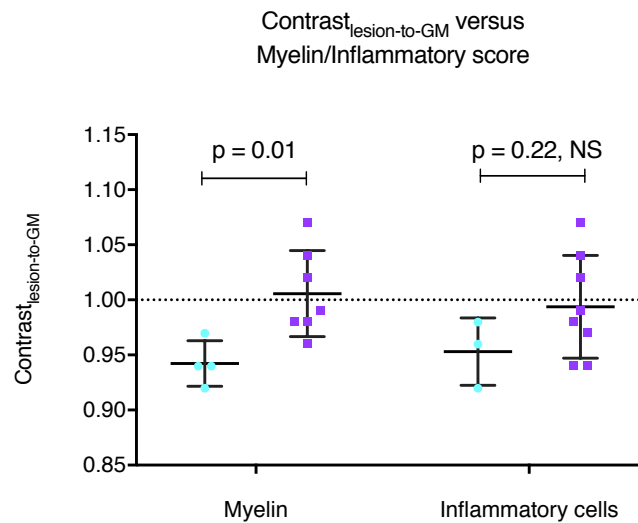


**Figure 3.11:**  $Contrast_{lesion-to-GM}$  values for each white matter lesion ( $n=11$ ) grouped according to histopathological scores for myelin and inflammatory cells (light blue: score = 1; purple: score = 2).

The quantitative analysis performed on the individual 92 ROIs revealed a lower AIC value when an interaction term for tissue type and random effect for sections were added in the myelin model ( $M_2$ ; see Table 3.5. Figure 3.12 illustrates the importance of the random effect when predicting MRI values. When applying the same model using the standardized MRI signal values, the relationship MRI-LFB signal was similar than when we previously corrected the  $MRI_{raw}$  with random effect for sections (Figure 3.13). In the  $M_2$  regression model,  $R^2$  of 0.96 indicated that 96% of the variability in the MRI data were explained by the predictors (fixed and random effects) in this model (additional Figure A.2). P-values

and mean slope coefficients from the linear mixed-effects model  $M_2$  are summarized in Table 3.6. Significant and strong positive associations were found between LFB and MRI values for both lesional and GM tissues. No significant association was seen between the LFB and MRI values in the NAWM, but the variation in MRI signal intensity within NAWM was comparatively small. A negligible difference in AIC values was observed when adding an interaction term in the inflammation models (Table 3.5). The lowest AIC value was obtained for  $M_1$ , which includes random effects but no interaction term. No significant association was found between the Iba-1 and the MRI signal (slope [standard error] = -10 [10.9],  $p=0.35$ ).

When the linear mixed-effects model was performed using the cellular density instead of the signal intensity, similar associations between the MRI signal and the LFB and Iba-1 inflammatory cells were obtained (See additional Figure A.3).

**Table 3.5:** Summary of the different regression models applied to the data with their respective Akaike information criteria results for the different myelin models (using the LFB-PAS histology) and inflammation models (using the Iba-1).

Models	Dependent variable	Fixed-Effects	Interaction Term	Random effect	Myelin model		Inflammation model	
					AIC	$\Delta$ AIC	AIC	$\Delta$ AIC
$M_0$	MRI	Histopathology, tissue type	No	No	1640.6	91.6	1618.4	20.1
$M_1$	MRI	Histopathology, tissue type	No	Section	1557.8	8.8	1598.3	0
$M_2$	MRI	Histopathology, tissue type	Yes	Section	1549	0	1599.3	1

**Table 3.6:** Results of the linear mixed-effect model M2 showing the mean slope coefficient, standard error (SE), and p-values for the LFB staining (\*\*\*:  $p \leq .001$ )

MRI <sub>raw</sub>	Slope (SE)	p-value
GM	56.3 (10.1)	2.2e-08***
Lesions	58.1 (8.2)	1.1e-12***
NAWM	17.3 (9.7)	0.07

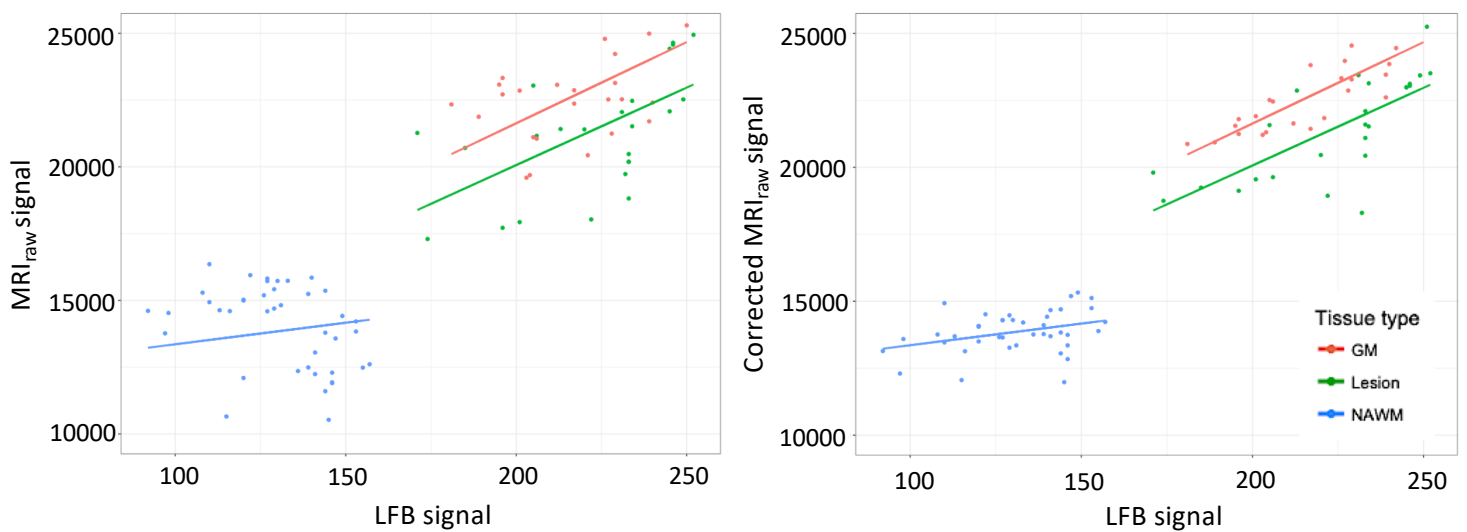


**Figure 3.12:** *Left:* Relationship between MRI signal intensity values and LFB signal intensity using myelin model  $M_2$ . Each dot represents the individual ROI values according to their tissue type. The fitted line represents the estimated MRI values for fixed effect only. *Right:* Representation of the random effect correction on the MRI value estimations. The residual variation, which is neither explained by fixed effect nor random effect, is shown by the distance between the individual dot and its corresponding value within the fitted line. Green: lesion; red: gray matter; blue: NAWM.

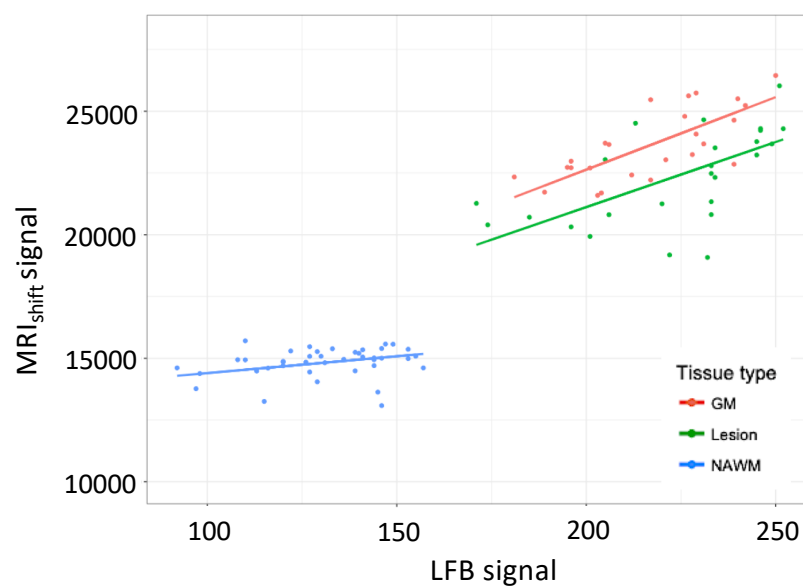


**Figure 3.13:** Relationship between  $MRI_{shift}$  signal intensity values and LFB signal intensity using myelin model  $M_2$ . Each dot represents the individual ROI values according to their tissue type. The fitted line represents the estimated MRI values for fixed effect only.

### 3.4 Discussion

In this study, we investigated the SC pathology in marmosets with EAE using a combined MRI-histopathological approach. By acquiring high-resolution ex vivo MRI, we first identified two types of lesions: (1) focal lesions located within the WM of the SC, and (2) subpial lesions along the WM abutting the subarachnoid space. By comparing our ex vivo MRI images with histology, we then demonstrated that these lesions corresponded to areas of demyelination and marked inflammation.

Similar to focal MS lesions (Oppenheimer, 1978; Weier et al., 2012), focal EAE lesions were found throughout the SC of the marmoset, with a prevalent localization in the lateral and posterior columns. We observed a heterogeneous distribution in terms of number and size of the focal lesions, which is also consistent with the lesion heterogeneity described in MS patients (Nijeholt et al., 2001). The shape of the medium and large lesions observed in our model showed high similarity with MS lesions as well.

In our model, subpial EAE lesions were distributed throughout the animal's SC and showed variable thicknesses across animals. This is a major difference compared to the rodent EAE models which usually present extensive inflammatory subpial lesions mostly located at the lumbar cord. A possible explanation (but not unique) could eventually be the differences of locomotion between species (chapter 2, section 2.2). The horizontal position of the spinal canal in rodents may decrease the CSF volume redistribution and amplify stasis of the CSF, which would explain why the lumbar cord is mainly affected by subpial lesions, whereas the more evenly distributed subpial lesions along the entire spinal cord length in the marmoset EAE model would be due to a more upright position contributing to the CSF circulation.

Compared to humans, only one histopathological study to our knowledge has reported the presence of diffuse subpial demyelination in the MS SC (Androdias et al., 2010). However, no study has done a thorough quantitative analysis of the distribution and extent of those subpial lesions. A recent in vivo imaging study of the cervical cord in MS found a decrease in magnetization transfer ratio (MTR) values for the outermost voxels of the SC (Kearney et al., 2014) suggesting that pathological changes may occur in this area of the cord, which could correspond to the subpial pathology observed in our study. However, the main limitation of this study was the lack of specificity in the interpretation of the biological meaning. Reduction in MTR values has been associated with demyelination (Schmierer et al., 2008) but inflammation also seems to be a contributing factor (Cook et al., 2004). Inflammation of the meninges and/or WM subpial parenchymal area associated or not with demyelination may be the reason for these changes in MTR signal. It would be very interesting to apply this imaging protocol to the entire spinal cord in order to compare with the thoraco-lumbar cord. This is supported by a study from DeLuca et al. (2013) which

found a significant meningeal inflammation along the entire spinal cord. The subpial lesions in our marmoset EAE model were difficult to visualize by postmortem MRI without first performing a laminectomy. Indeed, the tissues (bones, fat, and muscles) surrounding the SC generated magnetic susceptibility-related artifacts that hid these subtle lesions located at the edge of the cord. Thus, we hypothesize that the technical issues combined with comparatively low-resolution MRI might explain why subpial cord lesions have not yet been reported by MRI in MS patients.

Our histopathological evaluation revealed variable degrees of demyelination and inflammatory cell densities, which most likely reflects different stages of lesion development, as recently demonstrated for marmoset brain lesions (Maggi et al., 2014). The small focal inflammatory demyelinated lesions appeared to follow parenchymal blood vessels, whereas the larger subpial inflamed demyelinated lesions detected in our model are consistent with a leptomeningeal inflammatory origin, as is postulated to be the case for subpial cortical lesions (Reich et al., 2018; Choi et al., 2012).

By performing a quantitative comparison between MRI and histopathology using regression models, we established a strong association between the T2\*-w MRI signal intensity and the amount of myelin derived from the LFB-PAS stain intensity level within the GM and lesional areas. By contrast, the association between the MRI signal and the density of inflammatory cells was non-significant. The use of a linear mixed-effects model allowed us to improve the prediction of MRI values by correcting for the correlation within section. We validated the linear mixed-effects model for MRI signal correction by showing a similar relationship when the standardization method was applied on the MRI signal. These results highlight the fact that T2\*-weighted MRI signal can be highly sensitive to demyelination (although not specific) and corroborate previous postmortem studies investigating MRI and its pathological correlates in the MS (Schmierer et al., 2018; Bagnato et al., 2018).

Important limitations of this study were the use of a single, postmortem timepoint and a single MRI contrast, T2\*-weighted. The postmortem timepoint illuminates the SC lesion load when symptoms are severe (20% weight loss or paraplegia), but cannot provide spatiotemporal context of the pathology. In addition, because we were not able to scan these spinal cords in vivo, we had no information regarding the age and the blood–brain–barrier integrity of the lesions analyzed here. Both of these processes play a role in the development of vasogenic edema and expansion of the interstitial space, which can also impact signal intensity on postmortem MRI. Finally, our MRI sequence was optimized to provide the best delineation between lesions and NAWM. Therefore, lesions affecting the GM of the SC could not be easily identified by MRI in this study, although we detected GM pathology by histology in some of our sections (Figures 3.3.3 and 3.9, purple arrows).

The use of a single T2\*-w contrast limits the correlation analysis with the pathological substrates. Quantitative imaging techniques may provide more specificity with the

microstructural changes in the spinal cord, as quantitative mapping ( $T2^*/R2^*$  map was associated with myelin and iron contents (Bagnato et al., 2018), magnetization transfer techniques (MT) for myelin content, although axonal damage, and free water content from inflammation and edema may contribute to the signal (Vavasour et al., 2011).

Our postmortem spinal cord tissues presented a broad range of fixation time (1 year to 2.5 years). The fixative formaldehyde solutions have been shown to change the relaxation times of the fixed tissues with a decrease of T1, T2, MTR values (Schmierer et al., 2008). Therefore, the contrast between tissues will also appear different on the MRI based on the duration of the fixation. Formaldehyde solutions also may have had an impact on the histology and immunohistochemistry techniques, as demonstrated by the degradation of the staining ability of NeuN (for neuronal integrity) in a study from Lyck L. et al., (2008).

While we corrected for the MRI signal variation between sections, we did not correct for the possible heterogeneity coming from the staining techniques. Many steps are involved during the staining processes which may increase the risk for variations in the protocol, like applying different duration (longer LFB incubation, different LFB lithium carbonate differentiation time for WM/GM, different development times for DAB), the use of different product quality.

### **3.5 Conclusions**

In this study, we investigated SC tissues from marmosets with EAE showing symptoms suggestive of SC damage. Using a combined MRI-histopathological approach, we established the existence of two types of WM SC lesions: focal WM lesions with characteristics (location, distribution, and size) overlapping those found in human MS SC, and subpial WM lesions, which so far have not been reported in MS. We found that both focal and subpial EAE lesions detected by MRI corresponded to areas of demyelination and marked inflammation. Our findings underscore the relevance of this nonhuman primate model of MS for understanding mechanisms of lesion formation in the SC. The next step will be to investigate in vivo the spatiotemporal development of SC pathology in the marmoset with EAE (Chapter 5). For that, we need first to implement a new MRI setup in order to image in vivo the entire spinal cord of the marmoset, which would be the main focus in the following chapter 4.

## CHAPTER 4

# TECHNICAL DEVELOPMENT FOR IMAGING IN VIVO THE SPINAL CORD OF MARMOSET

### This Chapter contains:

4.1	Introduction . . . . .	77
4.2	Materials and Methods . . . . .	79
4.2.1	General . . . . .	79
4.2.1.1	Animals . . . . .	79
4.2.1.2	MRI equipment setup . . . . .	80
4.2.1.3	Animal preparation . . . . .	80
4.2.2	Customized MRI hardware . . . . .	81
4.2.2.1	Construction of a marmoset-shaped (brain spinal cord) MRI phantom . . . . .	81
4.2.2.2	Construction of the spine coil array and its customized marmoset-shaped cradle . . . . .	83
4.2.2.3	Imaging evaluation of the coil performances . . . . .	84
4.3	Results . . . . .	87
4.3.1	Advantages of the animal imaging setup . . . . .	87
4.3.2	Sensitivity of the 12-element phased-array . . . . .	87
4.4	Discussion . . . . .	92
4.5	Conclusion . . . . .	93



## 4.1 Introduction

As demonstrated in the previous chapter, the entire spinal cord length of marmosets with EAE can be affected by lesions. However, the dynamics of lesion formation and evolution in the spinal cord during the disease course remain completely unknown. Therefore, imaging in vivo the spinal cord is crucial to provide new insights into the spinal cord lesion development. To address this issue, I undertake the development of a new experimental setup that would allow to image in vivo the entire spinal cord of our marmosets. In this chapter, I first present a brief overview of the existing coil designs for human and rodent spinal cord imaging at ultra-high field. Then, I follow with a detailed description of our novel marmoset spinal cord coil developed in collaboration with Dr. Afonso Silva's laboratory (NINDS, NIH), our customized animal setup and optimized MRI protocol. Finally, I present a thorough evaluation of the performances of this new imaging setup in healthy animals.

Imaging the human spinal cord at 7T provides great benefits for lesion detection and delineation due to the increased SNR and tissue contrast. However, acquiring high-quality images of the entire spinal cord within a reasonable acquisition time ( $\sim 1-2$ h) is not feasible yet. The first phased-array coil, which was developed in 1989 by [Roemer et al. \(1990\)](#) (Figure 4.1), showed considerable improvement in terms of SNR and field-of-view (FOV) coverage by acquiring signal simultaneously and independently from several small surface coils, instead of the traditional single-element surface coil. The specific location and anatomy of the spinal cord, with a long, thin, approximately cylindrical shape, and variable depth along the length is well-suited for imaging with a phased-array coil in humans ([Barry et al. \(2018\)](#)) and rodents ([Gareis et al., 2007](#)). SNR can be further improved by incorporating additional coils to both sides of the linear phased-array ([Roemer and Edelstein, 1987](#)). With an orthogonal (or nearly orthogonal) coil design, one can take advantage of quadrature effects by obtaining a pure rotating B1 field, known as circularly polarized transmission. In receiver mode, the coil is able to capture the full phase information from the MR signal.

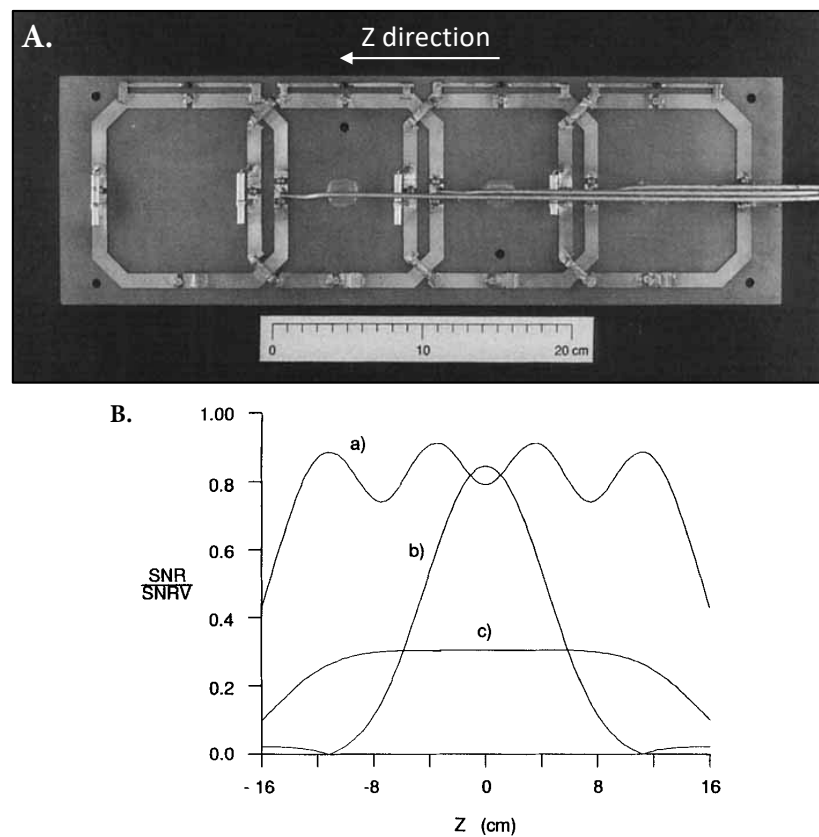


**Figure 4.1:** A. Coil design of the four-element spine array (diameter of 8 cm for each elements) from (Roemer et al., 1990). B. Comparisons of calculated SNR between three different coil configurations along z direction (superior-inferior or also  $B_0$  orientation). a) The four-element spine array; b) a single 8 cm square coil; c) a single large 30 cm rectangular coil. The phased-array design allows to cover a larger FOV with a higher SNR. Figure adapted from (Roemer et al., 1990)

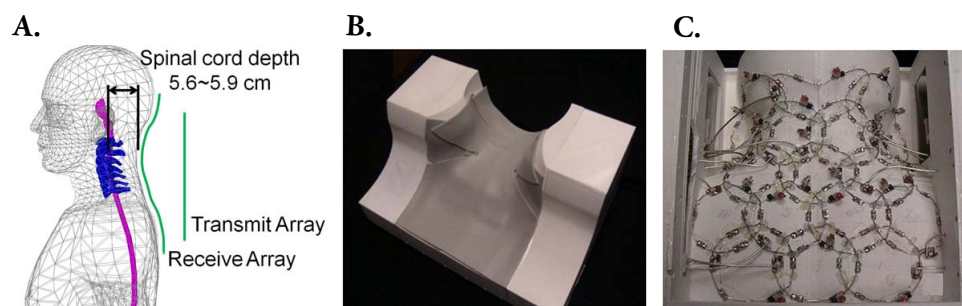


**Figure 4.2:** Nineteen-element receive array for cervical spinal cord imaging from Zhao et al. (2014). A. Representation of the area of interest with the corresponding position of the receive array and transmit array. B. The respective anatomical coil former (viewed from above) that includes both receive and transmit coils. C. Photograph of the receive array which consists on 19 overlapped loop elements.

Spinal cord imaging in animals is extremely practical, since the use of anesthesia allows longer acquisition times and a control of the respiratory motion. However, most spinal cord imaging studies in rodents with EAE are performed only at specific levels of the spinal cord: brainstem-cervical cord (Kim and Song, 2013) or lumbar cord (Schellenberg et al., 2007). Because the spinal cord length of mice is relatively small (approximately 4 cm), a smaller number of elements is required to image the entire cord, as demonstrated by Gareis et al. (2007), who used a four-element receive phased-array coil (dimensions: 48 mm length, 15 mm width) on healthy mice. In that study (Gareis et al., 2007), the mouse was lying in supine position on a cradle that included the entire setup (coil, preamplifiers and mouse holder). However, most rodent studies usually image the animals in prone position, since it does not require the immobilization of the animal's body, although this position is more likely to induce respiratory and spine motion. Kim and Song (2013) implemented a protocol that consisted of an anatomically shaped pair of coils with a device holder that enabled to restrain the brainstem and cervical spine and minimize respiratory motion from the thorax. Their detailed protocol is extremely useful for implementing spinal cord imaging in rodents and understanding the challenges in generating stable physiological conditions of the animals throughout the entire duration of the experiments.

In this study, in collaboration with Weng-Yang Chiang (a PhD student from Dr. Afonso Silva's laboratory), we take advantage of the phased-array coil design in order to cover the entire marmoset cord and inspire our design from a human spine coil that employs six pairs of loop-butterfly elements (Guclu et al., 2004). To fully exploit the coil performances and stabilize the animals during the scan, we propose an anatomical coil former that fits the body shape of the animals. Then, I develop different imaging protocols to achieve high-resolution imaging of the entire spine in a reasonable scan time.

## 4.2 Materials and Methods

### 4.2.1 General

#### 4.2.1.1 Animals

A total of 15 adult marmosets were used in this study, including five EAE animals (average age: 6.3 years old [min-max: 2.5 - 12.4], average weight: 432 g [min-max: 361-540], nine females). The study was conducted under an animal research protocol approved by the Institutional Animal Care and Use Committee of NINDS.

#### **4.2.1.2 MRI equipment setup**

All the experiments were performed on the same 7T pre-clinical MRI system mentioned in Chapter 3 (BioSpec 7T/30cm USR, Bruker Biospin) with a 15 cm gradient coil set (gradient strength of 450 mT/m, Resonance Research). A custom-built birdcage volume coil (inner diameter of 110 mm) was used either as a transmitter only or transceiver (RF excitation and reception). Image acquisition was performed under the software Paravision 5.1 (Bruker Biospin) running on a console AVANCE AIII console (Bruker Biospin).

#### **4.2.1.3 Animal preparation**

Once the animal was brought to the MRI room, anesthesia was induced by an intramuscular injection of ketamine (0.01 ml/100g) followed a few minutes later by 2% isoflurane delivered through a nose mask. The heart rate and SpO<sub>2</sub> were monitored during the entire experiment using a pulse oximeter optic sensor. Tracheal intubation was performed once the anesthesia was deep enough (usually indicated by the limbs being less responsive and the heart rate decreasing from  $\geq 350$  beats per minute (bpm) to approximately 300 bpm). The animal was then transported in the scanner room and installed in a supine position using the adequate setup with a surface array coil placed on a half-tube cradle (with a diameter smaller than the transmitter RF coil inner diameter).

The correct positioning of the animal was decisive for the quality of the images. First, the midline of the head and the body were aligned within the cradle. Second, the animal's head was tilted due to the limited available space within the magnet bore. We designed a 3D-printed anesthesia connector with an angle to facilitate the tube connections, which reduced the hyperflexion of the neck and therefore minimized a possible collapse of the anesthesia tube. To prevent heat loss, a heating pad was used during the entire experiment, and placed under the animal on the bench during the preparation for anesthesia, or on top of the animal during the MRI scan. Cotton pads were positioned all around the animal's body to isolate from the cradle and were also used to wrap around the tail.

During the entire experiment, the physiological signs were supervised using a vital sign monitoring system (SurgiVet) and a ventilator unit (SAR-1000 Ventilator, CWE Inc.) providing breaths per minute, CO<sub>2</sub> level, SpO<sub>2</sub> level, heart rate and temperature, which are essential measures to ensure the animal remains stable during the anesthesia. Obtaining a consistent breathing pattern was also crucial when imaging the spinal cord to obtain images free from respiratory-related artifacts. Four hours was the maximal length of time allowed for the animal under anesthesia. Otherwise, the experiment was stopped earlier if we reached the imaging protocol goals, or if major issues occurred during the procedure, such as deterioration of physiological signs or technical issues related to the MRI scanner.

## 4.2.2 Customized MRI hardware

### 4.2.2.1 Construction of a marmoset-shaped (brain spinal cord) MRI phantom

One marmoset (weight: 376g) was imaged in vivo with a 3D-FLASH sequence (see table 4.1 for imaging parameters details) using the birdcage volume coil as transceiver. After intubation, the anesthetized animal was placed in supine position on stacks of cotton pads in the half-tube cradle. The cotton pads helped preventing the body from moving and provided some thermal isolation. The upper back of the marmoset (neck area) was elevated and the head was tilted in order to fit the animal inside the inner magnet bore and prevent the anesthesia tube from collapsing. The lower part of the body (lower back and legs) was also elevated to allow for a stable and flat positioning of the back. To image the whole body of the marmoset, two segments of the marmoset body were successively scanned, and were stitched together offline manually using MIPAV software (Figure 4.3A<sub>1</sub>,A<sub>3</sub>).

Using ITK-SNAP, the brain/spinal cord and body of the marmoset were generated (Figure 4.3A<sub>2</sub>, A<sub>4</sub>) and saved as two separate binary masks. The masks were converted to 3D surfaces using a surface extraction algorithm (MIPAV) and then imported into Netfabb Professional (Autodesk, San Rafael, CA, USA) to apply surface repair and smoothing algorithms. The body mask was then cut down through the midline and mirrored to create a right-to-left symmetric body. Using MeshMixer (Autodesk, San Rafael, CA, USA), a grid of regular hollow spheres (10 mm diameter, 9.5 mm spacing) was added inside the body shell. Six openings (3.3 mm inner diameter, 5.8 mm outer diameter) were added at the extremities of the body phantom (one for the brain cavity, one for the lumbar spine, two for the head shell, two for the lower body). The marmoset-shaped MRI phantom was printed on a ProJet 3510 (3D Systems, Rockhill, SC, USA) using VisiJet Crystal material at a resolution of 0.16 mm, and post-processed in a heated mineral oil bath to remove wax support material. The physical dimensions of the phantom are: 172.5 mm (superior-inferior) x 60.8 mm (right-left) x 58.75 mm (anterior-posterior). The 6 openings were filled with a diluted solution of gadobutrol (4.5 g/L saline and 0.5 mM gadobutrol) and sealed by 4 plastic screws. The entire workflow is illustrated in Figure 4.3.

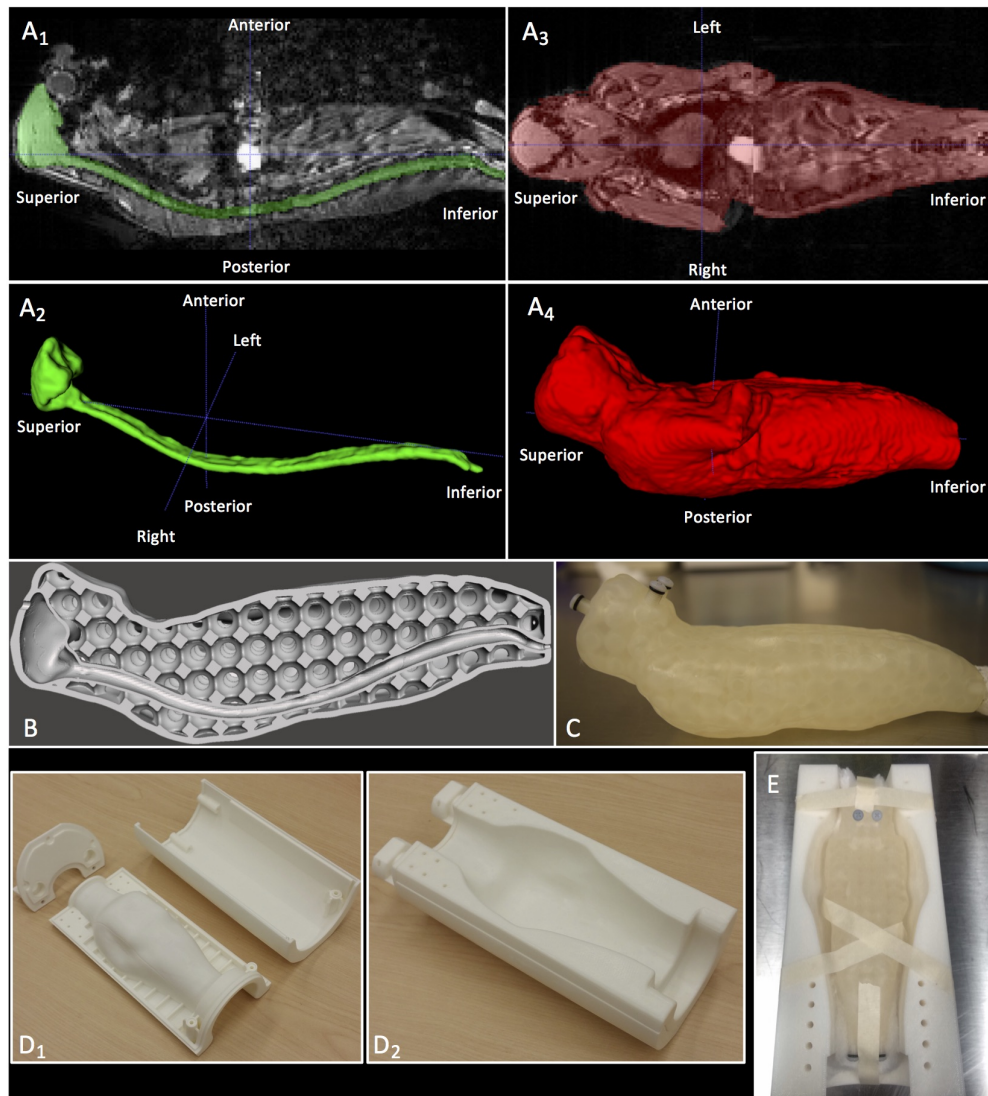


**Figure 4.3:** Workflow for building the marmoset-shaped (brain and spinal cord) MRI phantom and cradle. *A.* Segmentation of the brain and spinal cord (green), and body (red) of the marmoset using the 3D-FLASH whole-body images ( $A_1$ : sagittal view,  $A_3$ : coronal view) with their corresponding 3D volume visualized on ITK-SNAP ( $A_2$  and  $A_4$ ). Anatomical axes are annotated. *B.* Inside of the MeshMixer 3D model of the marmoset MRI phantom cut in mid-sagittal to visualize the sphere grid surrounding the grooves for brain and spine. *C.* Photograph of the 3D-printed spine phantom. *D<sub>1</sub>.* Different pieces of the coil cradle (bottom left: coil former; top right: coil cover). *D<sub>2</sub>.* Assembled 3D-printed coil cradle. *E.* Final setup with marmoset MRI phantom and coil cradle.

#### **4.2.2.2 Construction of the spine coil array and its customized marmoset-shaped cradle**

The cradle hosting the spine coil array was composed of two main pieces: a coil former and a coil cover (Figure 4.3D). The coil former was designed to follow the shape of a marmoset body using the 3D model of the marmoset body, and was expanded laterally to provide extra space for adding cotton sheet around the marmoset body. The coil former was 3D printed by Replicator 2 (MakerBot Industries, Brooklyn, NY) using polylactic acid material (PolyMax PLA, Polymaker, Shanghai, China). The coil cover was 3D printed by Fortus 360mc (Stratasys Inc., Eden Prairie, MN, USA) using polycarbonate building material and SR-100 soluble support material.

To provide spatial coverage of the entire length of the marmoset spinal cord, a 12-element coil array was built with shifted pairs of loops and butterfly coil elements that minimized inductive coupling between the elements (Figure 4.4). The coil elements were assembled on the 3D-printed cradle coil former. 3D-printed PLA coil clips were used to mount the coils by fusing the clips onto the coil former with tetrahydrofuran solvent to permanently secure the coils after an optimum geometric decoupling. Before including the coil inside the cradle, the dimensions of the 12-element coil array were: 179 mm (superior-inferior) x 30 mm (right-left). After the coil was deformed to adjust to the cradle shape, the coil length decreased to 154 mm (width unchanged). The first loop coil was placed under the cerebellum, and the last saddle coil was placed under the L7 vertebra segment of the spine. The length of the coil was chosen to fit the average size of an adult marmoset. In the study from [Casteleyn et al. \(2012\)](#) which analyzed the skeleton from 10 adults healthy marmosets, the length of the vertebral column was  $150 \text{ mm} \pm 10 \text{ mm}$  (SD) from the cervical vertebrae to the sacrum. From our experiments, the total length of our marmoset vertebral column from the upper cervical (C1-C2) to lower lumbar (L7) was varied from 128 mm to 146 mm. During the coil design development, an experiment was performed by inserting fiducial markers on the cradle former at regular intervals where the future coil elements will be placed. By imaging an animal in vivo using the birdcage volume coil, the distance between the future coil elements and the spinal cord was found to be consistent for the cervical level (average  $\pm$  SD =  $16.1 \pm 0.5 \text{ mm}$ ), and from the mid-thoracic to lower lumbar spinal cord (average  $\pm$  SD =  $15.4 \pm 1.9 \text{ mm}$ ). Only the upper thoracic spinal cord presented a higher distance (21.2 mm) with the future coil.

The performances of this spine phased-array coil were optimized by limiting cross-coupling at different steps of the construction (for example, through the use of an overlapping design and cable traps, or baluns, due to the proximity of the cables to the coil elements). Finally, the 12 elements were combined to an interface box containing two house-made preamplifiers with low-input impedance. The co-axial cables were grounded together to reduce interactions within the magnet with the RF cables.

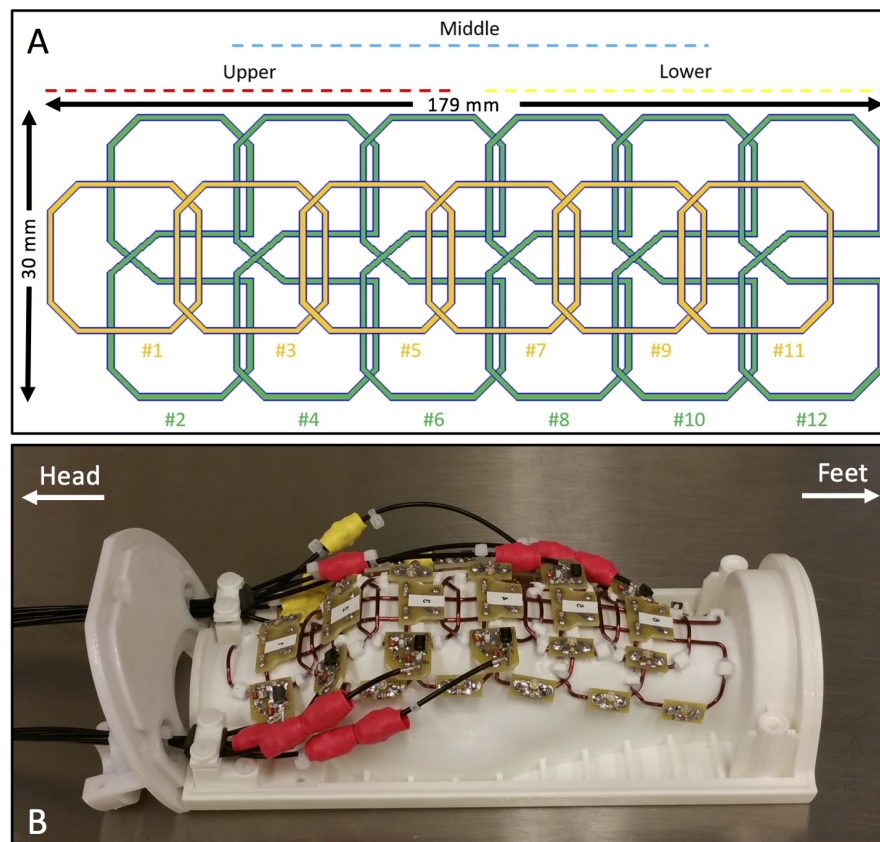


**Figure 4.4:** A. Schematic diagram of the spine phased-array coil design. The loop elements (yellow) have arbitrarily odd numbers (#1 to #11). The saddle elements (green) have even numbers (from #2 to #12). Dimensions of the coil are shown. B. Photograph of the spine phased-array coil mounted onto the coil former. The position of the cable traps can be appreciated (red and yellow caps).

#### 4.2.2.3 Imaging evaluation of the coil performances

After the entire spine coil was built, the receive sensitivity profiles of the 12 elements were measured with the marmoset-shaped MRI phantom and 12 live marmosets using two customized MRI protocols. Images from each element were generated in addition to the images reconstructed using the sum-of-square (SoS) method (selecting only the contributing elements). Due to the sensitivity profile of the birdcage transmit volume coil and length of the marmoset spine, the imaging session was divided into three segments.

The imaging of each segment was conducted according to the following procedure. The segment of interest was first placed at the isocenter of the transmit volume coil. To accurately determine the isocenter position, element 1 was activated for the upper segment (element 3 and element 5 for the middle segment and lower segment, respectively), and a spin-echo was applied to produce a 1-dimensional signal projection in the z direction. A  $B_0$  field map was acquired using a large field-of-view (FOV) covering the entire area of interest



by activating only the elements contributing to the signal. Then, a local shimming was acquired with a smaller FOV covering only the spine area on the sagittal localizer (longitudinal thin rectangular box). A single contrast, proton-density (PD), was acquired with a 2D RARE sequence for our high-quality anatomical images. Finally, imaging parameters were empirically optimized to improve tissue contrast, SNR, and acquisition time, while taking into account the SAR limitations and the reduction of motion artifacts.

Two different MRI protocols were established here: (1) ‘High-resolution’ protocol with restricted coverage of the spinal cord, (2) ‘Whole spine’ protocol with full coverage of the spinal cord. The core sequences included in these two protocols are mentioned in Table 4.1.

The ‘high-resolution’ protocol was implemented first in order to obtain high quality of the spinal cord anatomy. The spinal cord was imaged in sagittal and axial with the same high resolution in plane of  $0.125 \text{ mm}^2$  and  $0.6 \text{ mm}$  slice thickness, except for the axial slices for the upper spinal cord segment imaged with an in-plane resolution of  $0.135 \text{ mm}^2$ . Sagittal orientation with 10 slices covered the entire right-left diameter of the cord and three sagittal acquisitions were needed to obtain the entire spinal cord length. However, the axial orientation covered only  $\sim 2$ - $2.5$  vertebrae levels per acquisition with a total of 16 slices without gap between adjacent slices. For the sagittal acquisition, the phase encoding (PE) direction was chosen posterior-anterior (or row direction) to reduce the acquisition time. For the axial acquisition, the PE direction was chosen left-right (or row direction) to avoid the propagation of pulsation flow and motion artifacts through the spinal cord.

The ‘whole spine’ protocol was designed to cover the entire spinal cord in a single MRI session (not to exceed 4 hours of imaging). The spinal cord was imaged axially to better track the morphological changes of the spinal cord lesions. To provide sufficient SNR and image resolution for lesion detection, an in-plane resolution of  $0.15 \text{ mm}^2$  and  $0.8 \text{ mm}$  slice thickness were chosen. The total number of slices was mostly limited by the TR and the incidental magnetization transfer effect (iMT) that occurs for multislice turbo-spin-echo sequences (Chang et al., 2007). A total of 20 slices were acquired with a  $1.5 \text{ mm}$  gap thickness between adjacent slices. A fast sagittal scan was also performed to help position accurately the axial sequences. This step was crucial to provide consistent alignment of the axial slices between MRI sessions.

For both protocols, we applied a respiratory gating for the axial acquisition using the Bruker trigger module to synchronize the data acquisition with the breathing. For the upper and middle segments, the trigger was set with no delay corresponding to the beginning of the inspiration. For the lower segment, the trigger was set with a  $800 \text{ ms}$  delay corresponding to the beginning of the expiration in order to cancel the respiratory motion ghosting. The inspiration duration was set to be 45% of the expiration duration (Inspiration/expiration = 0.45). With a respiration rate between 35 and 38 breath per minute, we do have three complete respiratory cycles per TR, which includes the dead

**Table 4.1:** MRI sequence parameters for building the custom MRI hardware and the different in vivo imaging protocols

Imaging parameters	Generating phantom and coil former	Phantom imaging	High-resolution protocol		Whole spine protocol	
<b>Sequence type</b>	3D FLASH*	2D RARE**	2D RARE**	2D RARE**	2D RARE**	2D RARE**
Slice orientation	coronal	sagittal	sagittal	axial	sagittal	axial
Repetition time (ms)	50	700	3500	3500	3500	3500
Echo time (ms)	3	10	15	15	15	15
Number of averages	1	1	4	4	2	4
Matrix size (PE x RO)	128x128	256x256	256x400	288x192 (A) or 256x192 (B)	213x333	232x174
Field-of-view (mm <sup>2</sup> )	102.4x102.4	64x62	32x50	39x26 (A) or 32x24 (B)	32x50	34.8x26.1
Resolution in-plane (mm <sup>2</sup> )	0.8x.8	0.25x0.25	0.125x0.125	0.135x0.135 (A) or 0.125x0.125 (B)	0.15x0.15	0.15x0.15
Slice thickness (mm)	0.8	0.6	0.6	0.6	0.6	0.8
Slice gap	0	0	0	0	0	1.5
Number of slices	96	8	10	16	10	20
Scan time	10m 40s	1m 29s	29m 52s	33m 36s (A) or 29m 52s (B)	5m	25m***

\*: Flip angle = 30° for 3D FLASH sequence.

\*\* : RARE factor = 2 for 2D RARE sequence.

\*\*\*: acquisition can be longer due to the respiratory trigger.

(A) corresponds to the upper segment, (B) to the middle and lower segments. If not mentioned, parameters are the same for all three segments.

PE: Phase encoding; RO: readout (or frequency encoding); m: minutes; s: seconds; ms: milliseconds.

If a slice gap was introduced, it means an area between adjacent slices was left unsampled by MRI.

time. Figure 4.5 displays a schematic representation of the data acquisition relative to the respiratory cycle. Additionally, we activated the module motion suppression (Bruker, paravision 6) which consists on acquiring the second signal average after all the phase encoding of the first average have been encoded in order to keep a similar timing relationship between the PE step and the respiratory cycle.

Image quality was assessed at multiple different steps of the coil construction and during the coil testing process by visual assessment of the individual sensitivity profiles of the 12 elements. Signal-to-noise ratio was also computed on the magnitude images using the mean intensity of a ROI within the cord and divided by the standard deviation of the background noise.

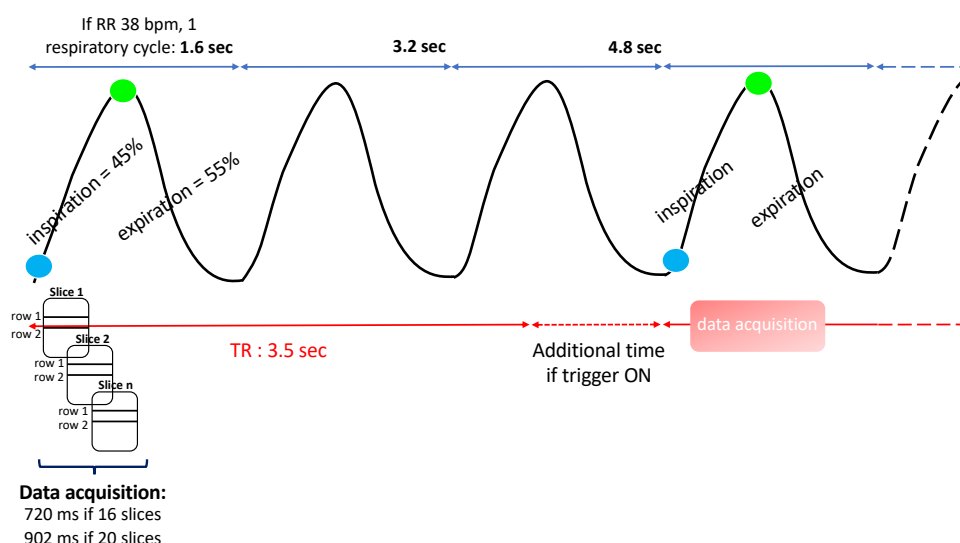


**Figure 4.5:** Illustration of the data acquisition regarding the respiratory cycle respective to the sequence parameters. Blue dot: MRI data acquisition synchronized with the beginning of the inspiration. Green dot: MRI data acquisition synchronized with the beginning of the expiration when a delay of 800 ms is applied. Several respiratory cycles (average respiratory rate (RR) = 38 breath per minute (bpm)) occurs during a TR of 3500 ms. An additional time can be necessary to match with the beginning of the next cycle. sec: seconds

## 4.3 Results

### 4.3.1 Advantages of the animal imaging setup

The custom-built 3D-printed cradle provided several advantages: (i) reduction of the preparation time of the animal (faster positioning of the animal within the scanner); (ii) consistent alignment of the spine between MRI sessions; (iii) easy localization of the mid-sagittal line on MRI (Figure 4.6). The use of supine position also significantly minimized the motion from the back of the animal. In addition to keeping the animal warm, the heating pad helped reduce the amplitude of the respiratory motion, which was mostly visible at the lumbar level (Figure 4.6B).

### 4.3.2 Sensitivity of the 12-element phased-array

MRI sessions performed on the marmoset-shaped MRI phantom demonstrated that the individual element of the 12-element phased-array coil presented excellent coil isolation (Figure 4.7). The combined sum-of-squares (SoS) images depicted strong and homogeneous signal along the entire segment length (Figure 4.7). The SNR measurements on these sagittal images obtained with the optimized 2D RARE sequence were uniform along the spine phantom length, with an average value ( $\pm$  SD) of  $104 \pm 15$ . MRI sessions performed

in vivo using the ‘high-resolution’ protocol demonstrated the consistency of the sensitivity profiles previously observed with the MRI phantom (Figure 4.8). The reconstructed SoS sagittal image (Figure 4.8) illustrates the uniform signal associated with an average SNR of  $33.1 \pm 7.2$  along the cervical and upper thoracic levels (values obtained from four different MRI sessions performed on three animals).

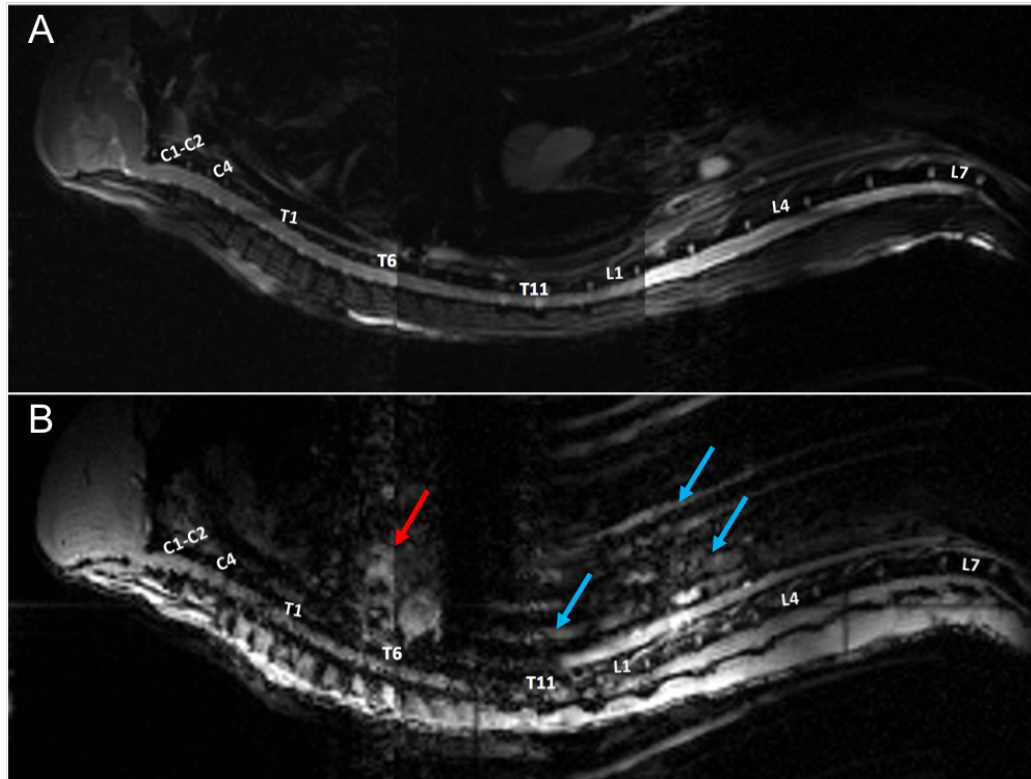


**Figure 4.6:** Mid-sagittal localizer (or scout) images illustrate the entire coverage of the spinal cord provided by the 12-element phased-array coil. All images are 0.6 mm in-plane resolution with 0.8 mm slice thickness and were concatenated offline. (A) The spinal cord is clearly discerned along the entire length due to the use of the custom-built cradle. Image obtained with a 2D RARE sequence ( $TR=3500\text{ms}$ ,  $TE=64\text{ ms}$ ,  $RARE\text{ factor}=16$ ). (B) Heart rate pulsation (red arrow) and respiratory motion (blue arrows) are visible. Image obtained with a 2D FLASH sequence ( $TR = 100\text{ ms}$ ,  $TE = 6\text{ ms}$  and  $FA = 30^\circ$ ).

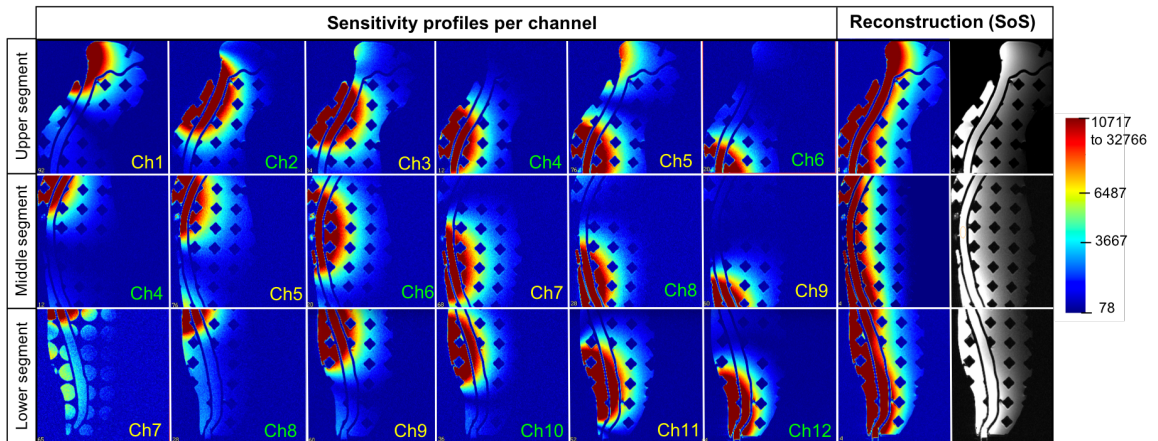


**Figure 4.7:** Mid-sagittal sensitivity profiles of the 12-element phased-array spine coil used with a MRI phantom. For each segment (top row: upper segment; middle row: middle segment; bottom row: lower segment), images show the sensitivity profile of each element contributing to the signal using a color-based intensity. The reconstructed sum-of-square (SoS) images are showed at the end of each row using the color-based scale and a gray scale.

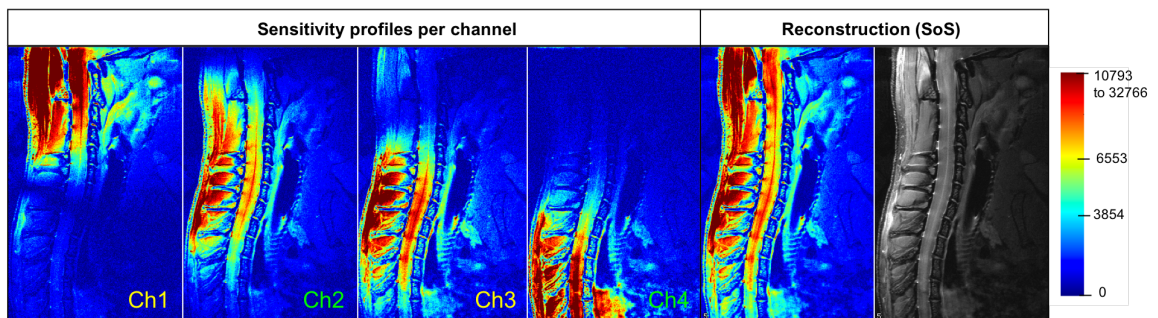


**Figure 4.8:** Mid-sagittal sensitivity profiles of the phased-array spine coil from an *in vivo* healthy marmoset (Weight=458g, Female 1). Images of the upper segment were acquired with the PD-w FSE high-resolution protocol.

Representative examples of high-resolution sagittal images of the cervical and thoracic (C1 to T12 vertebrae levels, two segments) and the lower lumbar (L4 vertebra level to the sacrum) are provided in Figure 4.9. The high-quality of the sagittal images allows a clear distinction between the WM and GM of the spinal cord on mid-sagittal section. Anatomy of the spine, such as the nerve roots, vertebral body, intervertebral disks, can also be readily visualized.

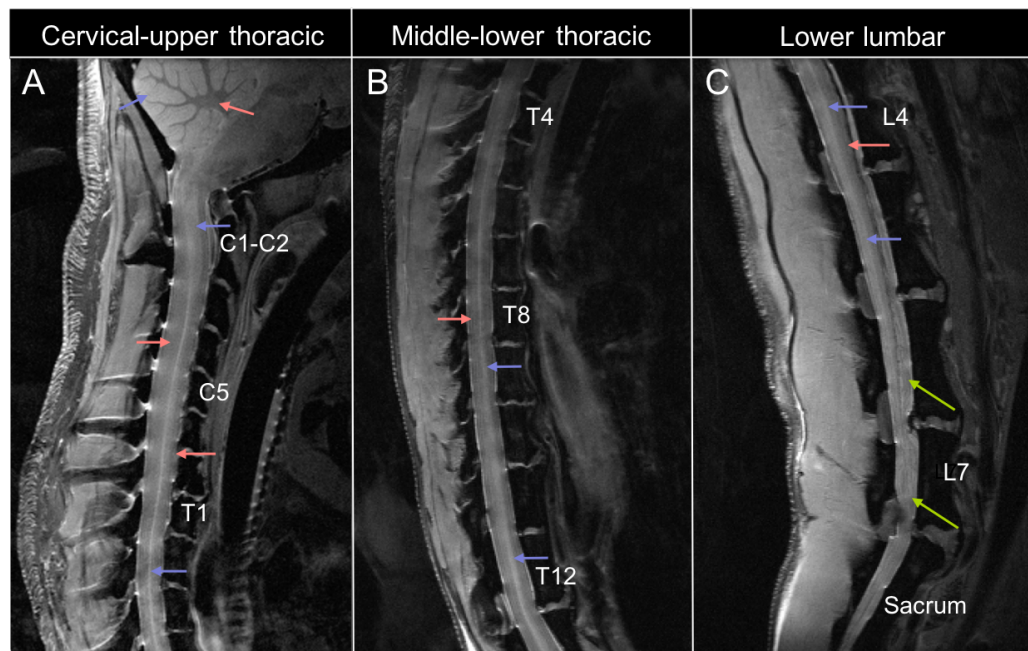


**Figure 4.9:** Mid-sagittal high-resolution PD-w 2D RARE images (FOV: 50 x 32 mm, voxel size = 0.125 x 0.125 x 0.6 mm) acquired on a healthy animal (animal weight = 490 g) during separate MRI sessions. Images show the cervical and upper thoracic spine (A), as well as middle and lower thoracic spine (B), and lower lumbar spine (C). The gray matter (GM) (hyperintense signal, blue arrows) was easily differentiated from the white matter (WM) (hypointense signal, rose arrows) inside the spinal cord. Note the perfect alignment of the spinal cord (represented by the thin GM line in the middle of the cord) and the high GM/WM contrast within the cerebellum. The cauda equina (bundles of spinal nerves, green arrows, in the lumbar spine) can also be visualized.

The image quality of the spine was also excellent on axial PD-w 2D RARE images (Figure 4.10). The average SNR of the cord was similar across various levels of the spinal cord and equal to  $44 \pm 5$  (values obtained from five different MRI sessions performed on two healthy animals, and one EAE animal). The different anatomical structures (GM, WM, nerve roots, and CSF) are clearly identified and delineated with average CNR between the GM and WM of  $12 \pm 2.5$ . We did not observe any differences in image quality between healthy and EAE animals.

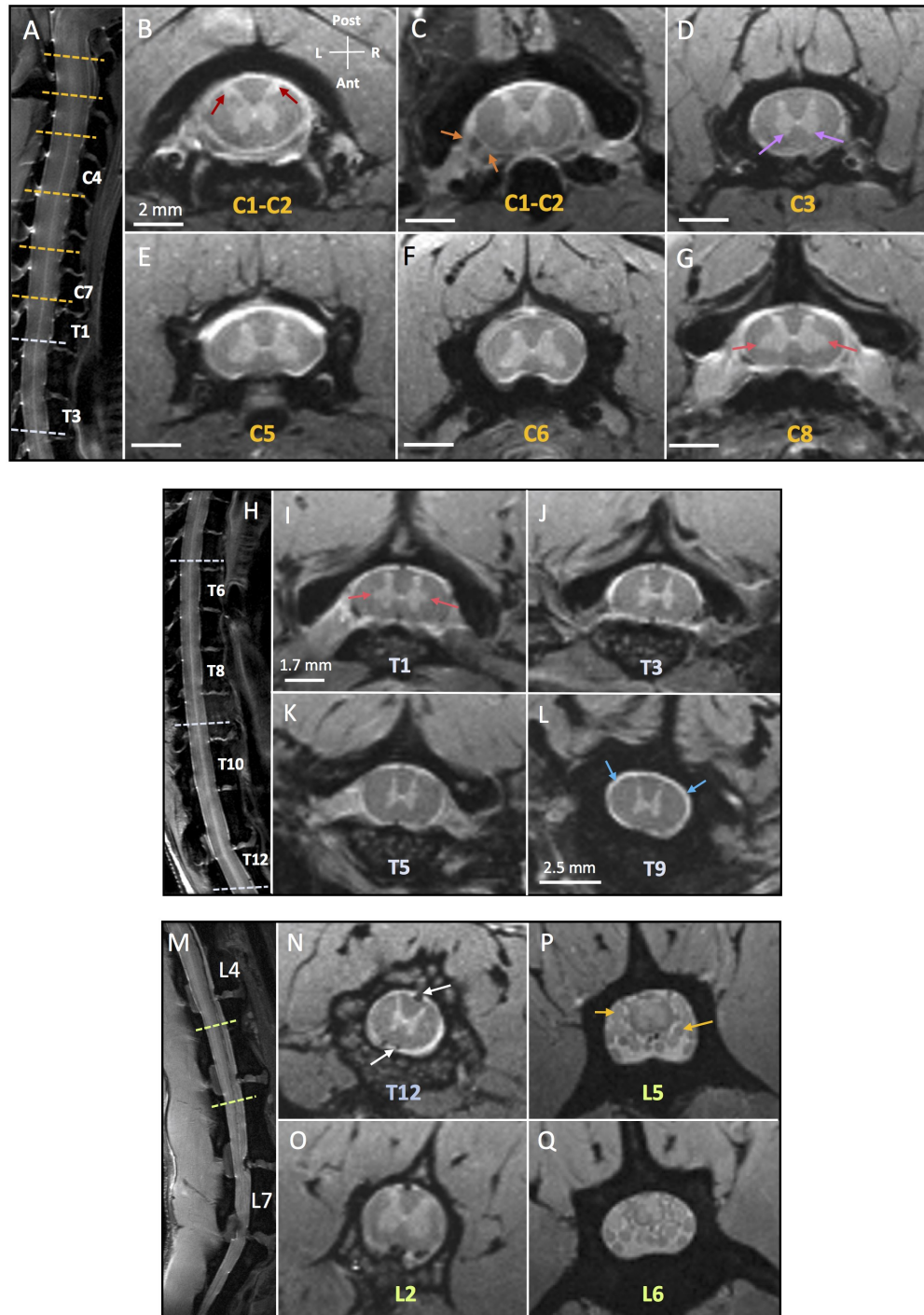


**Figure 4.10:** Enlarged views of the high-resolution axial PD-w 2D RARE images displaying the spinal cord at the cervical levels (B-G), thoracic levels (I-N) and lumbar levels (O-Q) in two healthy animals (B-G, L, P-Q) and one EAE animal without visible lesions (I-K, N-0). Anatomical features can be readily visualized, such as the dorsal horns (B, red arrows), lateral horns (G, I, pink arrows), ventral horns (D, purple arrows), anterior and posterior nerve roots (C, orange arrows), bundle of nerve roots (part of the cauda equina) (P, yellow arrows), CSF (L, blue arrows), and ventral and dorsal vasculature (N, white arrows). Sagittal PD-w 2D RARE images (A, H, M) show the slice positions of the axial slices (dotted lines) and the annotation of the vertebrae numbers.

## 4.4 Discussion

In this chapter, I presented a unique and robust MRI setup that allows to image in vivo, for the first time, the entire spinal cord length of a marmoset with high quality in a single MRI session. I demonstrated several advantages of a customized marmoset-shaped cradle combined with a 12-element phased array receive coil, such as: (1) the improvement of the animal physiological stability for better image quality, (2) an optimal sensitivity profile along the cord length, and (3) the implementation of an optimized PD-w sequence that allows excellent visualization of anatomical cord details in the axial plane.

One of the main challenges of this work was to stabilize the animals within the scanner in terms of physiological measures, but also to minimize motion in order to optimize the MRI image quality. Most of the troubleshooting was caused by a non-adequate position of the animal's head, which led to an inconsistent breathing pattern and lack of stability. We were able to minimize this problem by using a customized anesthesia connector and a 3D-printed cradle that supports the neck. With a total of 15 animals scanned in this study, I was able to confirm the stability and safety of our setup since no injury occurred to our animals during the experiments.

In this study, I also showed that using a cradle that fits the body shape of the animal, and followed closely the normal curvature of the cord, allowed an optimal and consistent SNR along the entire cord length. This marmoset-shaped cradle was designed based on the cervical human spinal cord surface coils (Barry et al., 2018). However, this kind of setup was never implemented before for small animal imaging. Mogatadakala et al. (2008) used a supine configuration in rat without a close-fitting coil former, and it led to variable distances between the different cord levels and the coil surface. The lack of imaging studies using supine position for small animal illustrates again the difficulty of stabilizing animal on their back while being under anesthesia. Only a few studies developed surface phased-array coil to image the entire spinal cord. However, like for most of the human spinal cord imaging at ultra-high-field, the main goal was to demonstrate the feasibility of their imaging protocol.

A turbo-spin-echo sequence with a proton-density contrast was used in this study for several reasons, among which its robustness against susceptibility artifacts and its ability to be combined with a RARE factor to decrease acquisition time (relative to standard spin-echo imaging). PD-w sequence has already been performed successfully in the brain of marmoset with EAE to follow longitudinally the evolution in vivo of EAE lesions (Lee et al., 2018; Leibovitch et al., 2018). Furthermore, PD-w TSE contrast showed a higher detection of lesions compared to a T2-w TSE in the spinal cord of MS patients (Chong et al., 2016).

The selection of the imaging plane was also crucial for the detection of spinal cord lesions. Ideally, combining both sagittal and axial planes should improve the confidence in



the detection of SC lesions (Weier et al., 2012). Because acquiring two planes (e.g. axial and sagittal) is very time-consuming without implementing parallel imaging techniques, we decided to restrain our protocol by imaging only in axial plane with high resolution. Indeed, two in vivo studies demonstrated an increased number of lesions detected on the axial plane (Breckwoldt et al., 2017; Galler et al., 2016). Breckwoldt et al. (2017), who acquired only the cervical cord, found a higher detection with up to 2.5 times more lesions compared to the sagittal plan, and all the lesions seen on sagittal were found in axial plan as well. It is possible that diffuse abnormalities seen on sagittal may be several focal lesions, which are easier to differentiate using the axial plan. The additional lesions seen on axial were smaller in size and located more laterally within the cord. Overall, the use of axial plan seems to improve the characterization of the lesions in vivo.

Finally, the image resolution of our axial PD-w TSE sequence was an important factor to optimize in order to obtain an optimal detection of the focal lesions. The main findings of our postmortem MRI study helped to design the resolution of the longitudinal in vivo MRI protocol. The focal lesions presented a wide-ranging size with an average volume of  $0.028 \text{ mm}^3$  for the smaller lesions up to  $2.5 \text{ mm}^3$  for the larger ones. Deciding on the in vivo voxel size required trading-off between a sufficient SNR and a reasonable acquisition time. We relied on the average volume size ( $0.12 \text{ mm}^3$ ) and length (0.81-0.88 mm) of the medium size category of focal lesions (category defined from our MRI postmortem study). With a resolution in-plane of  $0.15 \text{ mm}^2$  in-plane and 0.8 mm slice thickness, the in vivo voxel size obtained was  $0.018 \text{ mm}^3$ , which would be enough to detect the medium and large lesions, while it may be difficult for small lesions. The location of the axial slice would need to be centered exactly on the lesion in order to minimize partial volume effect.

## 4.5 Conclusion

In conclusion, this chapter introduced a novel marmoset spinal cord coil developed in collaboration with Dr. Afonso Silva's laboratory (NINDS, NIH), as well as an optimized MRI protocol and customized animal setup, which allow to obtain for the first time high-quality in vivo images of the entire spinal cord of the marmoset. This technical work opens the door to investigate the spatiotemporal evolution of spinal cord lesions by imaging serially marmosets with EAE, as shown in the next chapter of my thesis.

## CHAPTER 5

# SPATIOTEMPORAL EVOLUTION OF THE SPINAL CORD LESIONS IN THE MARMOSET EAE MODEL

### This Chapter contains:

5.1	Introduction . . . . .	95
5.2	Materials and Methods . . . . .	96
5.2.1	Study Design . . . . .	96
5.2.2	Image processing and analysis . . . . .	99
5.2.2.1	Image processing . . . . .	99
5.2.2.2	Image analysis . . . . .	100
5.2.3	Correlation between clinical scores and spinal cord abnormalities . . . . .	103
5.2.4	Histopathological analysis . . . . .	104
5.3	Results . . . . .	106
5.3.1	Evolution of spinal cord-related EAE neurological symptoms . . . . .	106
5.3.2	In vivo lesion analysis . . . . .	108
5.3.2.1	Spatiotemporal evolution of focal lesions . . . . .	108
5.3.2.2	Spatiotemporal evolution of subpial lesions . . . . .	113
5.3.3	Analysis of MRI findings and disability . . . . .	121
5.3.3.1	Correlations between MRI findings and disability scores for the whole marmoset cohort . . . . .	121
5.3.3.2	Associations between lesion location and clinical symptoms at the individual level . . . . .	122
5.3.4	Postmortem lesion analysis . . . . .	124
5.3.4.1	Histopathology description by animal and lesion age group . . . . .	124
5.3.4.2	Quantitative analysis for myelin and inflammatory cells contents . . . . .	132

5.4	Discussions	135
5.5	Conclusion	139

---

## 5.1 Introduction

As introduced in section 1.3.3.3, it is challenging to image robustly the entire spinal cord in vivo with high quality in a reasonable scanning time. Consequently, the scope of in vivo SC MRI studies in MS patients is often limited, with incomplete spatial coverage and infrequent temporal sampling. As such, little is known about where the lesions first appear in the spinal cord, and about how these lesions evolve in terms of size and shape over time. New insights into the spatiotemporal evolution of MS lesions would be extremely useful for better understanding the development of symptoms in MS patients.

Animal models confer many advantages when used in pre-clinical imaging studies, such as the higher degree of control over the experiments with more consistent temporal and spatial sampling (as explained in the chapter 4 introduction 4.1). However, the majority of the studies in rodent EAE typically describe ascending clinical symptoms with the lumbar spinal cord being mainly affected, which does not mirror findings in MS.

Using the whole spine MR imaging protocol developed in Chapter 4, the study described in this chapter was designed to investigate in vivo the spatiotemporal evolution of spinal cord lesions in our marmoset model of MS. Specifically, the main objective of this study was to characterize the development of focal and subpial lesions that were previously characterized ex vivo in Chapter 3. Here, I use the information provided by serial in vivo MRI for determining the age of lesions at the end of the experiment. Then, by grouping these lesions according to their age, I describe their pathological characteristics using a combined postmortem MRI-histopathology approach similar to the one previously introduced in Chapter 3.

## 5.2 Materials and Methods

### 5.2.1 Study Design

Five adult common marmosets were included in this study [*Callithrix jacchus*, average age 3.6 years (min-max: 0.8–4.4), 4 females]; (for more details about their demographics see Table 5.1). These marmosets were housed at the NIH Intramural Research facilities, in accordance with the standards of the American Association for Accreditation of Laboratory Animal Care and the National Institute of Neurological Disorders and Stroke’s Animal Care and Use Committee (ACUC).

First, the animals underwent an imaging session that included a limited brain MRI protocol (PD-w TSE, coronal slices) and a spinal cord MRI protocol (PD-w TSE sequence,  $0.15 \times 0.15 \times 0.8$  mm, axial and sagittal slices) (for more details about this protocol see Chapter 4, Table 4.1). The spatial coverage of the spinal cord MRI protocol was divided into three segments: 1) upper segment covering the cervical and upper thoracic levels [T1 → T5]; 2) middle segment covering the middle and lower thoracic levels [T5 → T12]; and 3) lower segment covering most lumbar levels.

After this baseline MRI session, all 5 animals were immunized using the WMH-CFA solution injected intradermally according to our laboratory protocol (previously described in Chapter 3, 3.2.1). Following the immunizations, the animals were imaged on a bi-weekly schedule with the same brain/spinal cord MRI protocols used for the baseline scan until the first spinal cord lesions were detected. Once these first lesions were detected, the animals were imaged using only the spinal cord MRI protocol and a weekly schedule, which provided more scan time to repeat any failed acquisitions during the imaging session, as well as a more frequent sampling of the temporal evolution of the spinal cord lesions.

In addition to the frequent in vivo imaging, the animals were clinically evaluated on a weekly basis and their symptoms were recorded. Based on the observed symptoms, clinical scores were also calculated using two different methods: 1) EAE scoring method from Kap et al. (2008) (see Table 5.2); 2) mEDSS (marmoset EDSS) scoring method adapted from Villoslada et al. (2000) (see Table 5.3). We decided to implement this score due to its high sensitivity to follow the evolution of motor and sensory deficits with only minor modifications. According to our ACUC guidelines, the animals were euthanized once they reached an EAE score  $\geq 3$  (paraplegia or hemiplegia). At the time of necropsy, spinal cords were extracted after performing a perfusion fixation (previously described in Chapter 3, section 3.2.2). Ex vivo MRIs were performed on the formalin-fixed spinal cord tissues using our optimized postmortem MRI protocol (see Chapter 3, 3.2.3).

Out of the 5 immunized animals, two animals (M#4 and M#5) had to be excluded from this in vivo study for the following reasons: animal M#4 did not develop any visible spinal cord lesions up to the 19<sup>th</sup> week post-immunization (PI); technical problems related to the MRI scanner hardware prevented the imaging of animal M#4 (after the 19<sup>th</sup> week PI) and animal M#5 (after the 2<sup>nd</sup> week PI). Animals M#4 and M#5 eventually met clinical endpoints and were euthanized.

**Table 5.1:** Demographic and clinical information of the five EAE animals included in the longitudinal study

Animal	Sex	Age (years)	Disease duration (days)	First motor sensory signs (days)	Description first motor sensory signs	Clinical signs at sacrifice
M#1	F	3.2	30	26	Tail, reduced tone, pain sensation loss	Paraplegia, tremor, sensory loss, bladder, tail
M#2	F	4.1	81	36	Reduced motor grip, pain sensation loss, mild tail	Paraplegia, Babinski, tail, bladder
M#3	F	4.4	22	16	Hand discoordination	Paraplegia, tail, bladder, tone loss, pain sensation loss lower limbs
M#4	F	0.8	216	14	Babinski, tone loss, motor grip loss	Paraplegia, weight loss
M#5	M	1.9	53	14	Tone loss, loss motor grip	Paraplegia, weight loss, bowel dysfunction

All animals were immunized with our white matter homogenate protocol  
M#1:marmoset 1; F: female; M: male

**Table 5.2:** EAE score for clinical assessment of marmosets from Kap et al. (2008)

Score	Symptoms associated
0	No clinical signs
0.5	Apathy, altered walking pattern without ataxia
1	Lethargy, anorexia, weight loss
2	Ataxia, sensory loss, optic disease
2.25	Monoparesis
2.5	Paraparesis
3	Paraplegia or hemiplegia
4	Quadriplegia
5	Spontaneous death due to EAE

Adapted from Kap et al. 2008

**Table 5.3:** marmoset Expanded Disability Status Scale (mEDSS) for EAE

	Function	Disability score	Maximal score
1	Alertness	0:normal; 1:reduced; 2:lethargic	2
2	Spontaneous mobility	0:normal; 1:mild slowing; 2:marked slowing; 3:absent	3
3	Tremor	0:none; 1:moderate; 2:severe	2
4	Tone*	0:normal; 1:mildly reduced; 2:markedly reduced**; 3:absent	12
5	Motor (grip)*	0:normal; 1:mildly reduced; 2:markedly reduced**; 3:absent	12
6	Sensory (pain)*	0:normal; 1:reduced; 2:absent**	8
7	Tail tone	0:normal; 1:reduced; 2:absent	2
8	Babinski	0:absent; 1:present	1
9	Eye movements	0:normal; 1:changed	1
10	Vision (including pupillary reflex)	0:absent; 1:abnormal; 2:absent	2
11	Vocalization	0:absent; 1:abnormal	1
12	Bladder function	0:normal; 1:abnormal	1

Adapted from Villoslada et al. 2000

The maximal score for the scale is 47.

\*: scored for each limb

\*\* : or abnormally increased. In some cases, we can observe an abnormal hypertonic muscles (the entire limbs or extremities, as the hand or foot) and hyperalgesia to any painful or touch stimuli.

## 5.2.2 Image processing and analysis

### 5.2.2.1 Image processing

Once the in vivo MRI acquisition was completed, DICOM images were exported from the scanner to our server and were processed using the following steps:

- A bias-field correction (Tustison et al., 2010) was first applied to correct the non-uniformity of the image intensity observed in the in vivo spinal cord axial PD-w images, which was primarily caused by the inhomogeneous reception profile of the custom-built phased-array receive coil.

- Intensity-corrected axial PD-w images were then manually matched between time points to ensure that each MRI slice was properly located and ordered inside every spinal cord segment (upper, middle or lower) at every time point.

- Image co-registration was performed to re-align the position of the spinal cord in each axial PD-w image. To perform this registration, a custom-built pipeline was developed and included the following two steps, also illustrated in Figure 5.1:

- (1) *spinal cord re-alignment within each segment*: each slice of a segment was registered to a reference slice belonging to the same segment. The reference slice was usually chosen in the middle of the segment, which corresponded to an inflection point for the cord curvature. This co-registration used a simple translation transformation ('imregtform' and 'imwarp' functions in Matlab) applied to the binary masks of the cord generated with ITK-SNAP (version 3.6) using an edge detection method by an "active contour" algorithm ("snake evolution" tool) and a manually-adjusted intensity threshold. The resulting geometric transformation matrices were then applied to the axial PD-w images using a cubic interpolation, which provided higher image quality than 'linear' or 'nearest' interpolations. This operation was repeated for every segment acquired at each time point;

- (2) *spinal cord re-alignment between time points*: the co-registered segments of each time point were registered to their corresponding segments at the first time point (baseline) using the same co-registration method described in the first step (affine transformation, binary masks). Once completed, the pipeline generated a 4D volume for each spinal cord segment where the cord was aligned between the various time points. These 4D volumes were subsequently used in the image analysis described below.

- (3) *spinal level reassignment*: Because the three segments (upper, middle, and lower) acquired in our in vivo protocol do not correspond to the anatomical spinal levels (cervical, thoracic, and lumbar), each MRI slice was assigned to a spinal level based on the location of the nerve root exit relative to the vertebral body level. At the lumbar level, it was difficult to locate the nerve root exit. Therefore, an approximate spinal level was assigned based on the published histology atlas of the marmoset spinal cord (Browne et al., 2014).

However, the 12<sup>th</sup> thoracic (T12) and the first lumbar (L1) were easily found in order to separate thoracic from lumbar.

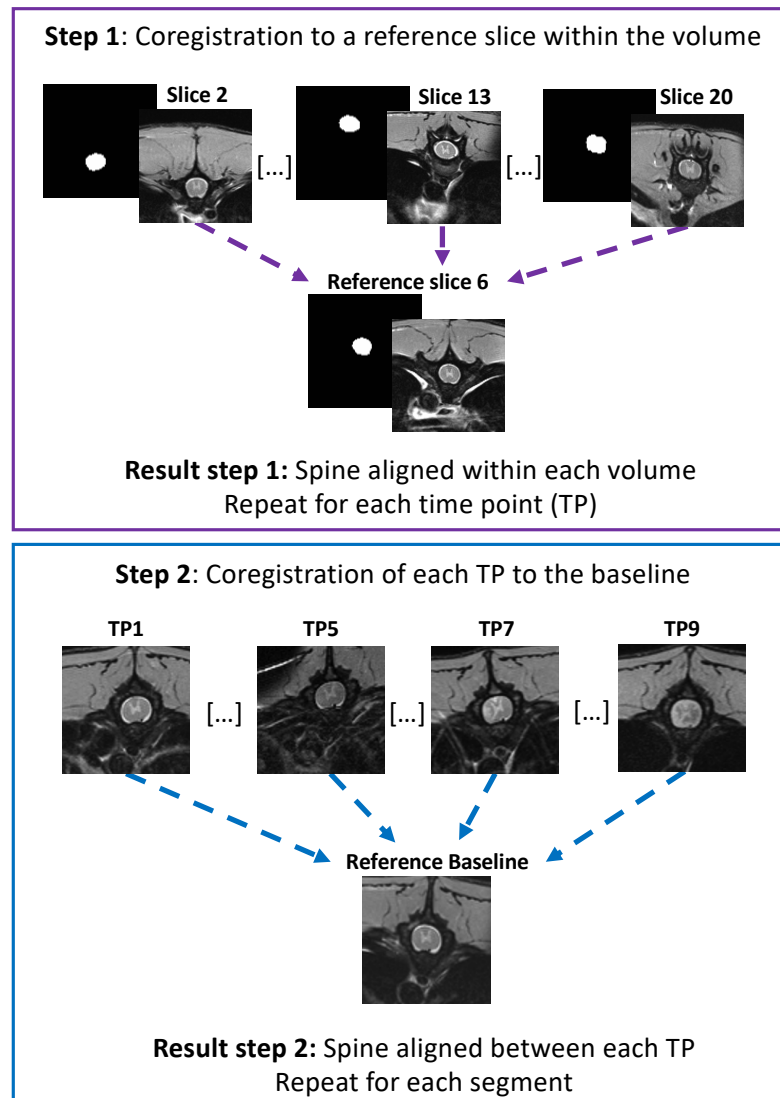


**Figure 5.1:** Workflow of the two-step co-registration pipeline used to re-align the spinal cord on axial PD-w images. For each volume of axial images [i.e. each segment (upper, middle, lower)] of each time point [baseline, TP1, TP2...TPn], a simple affine transformation (translation) was applied to correct for the displacement of the spinal cord between different MRI slices and scans.

### 5.2.2.2 Image analysis

Based on our observations made in the postmortem study (Chapter 3), we identified two types of spinal cord lesions, which we classified on the axial PD-w images using the following criteria:



- **Focal lesion:** discrete, round/oval/wedge-shaped, abnormal white matter area surrounding by normal white matter or partly in contact with the edge of the cord. Examples of focal lesions are provided in Figure 5.2A.

- **Subpial lesion:** abnormal white matter area located along the cord edge and abutting the subarachnoid space. Examples of subpial lesions are provided in Figure 5.2B.

Abnormal white matter area was defined here as an area of hyperintense signal that is different from the normal signal intensity level seen in the same area on the baseline images. In order to simplify the analysis, a lesion categorized as a focal or subpial lesion at first time point of appearance remained in that category, regardless of its evolution over time (e.g. focal lesion merging with subpial lesion).

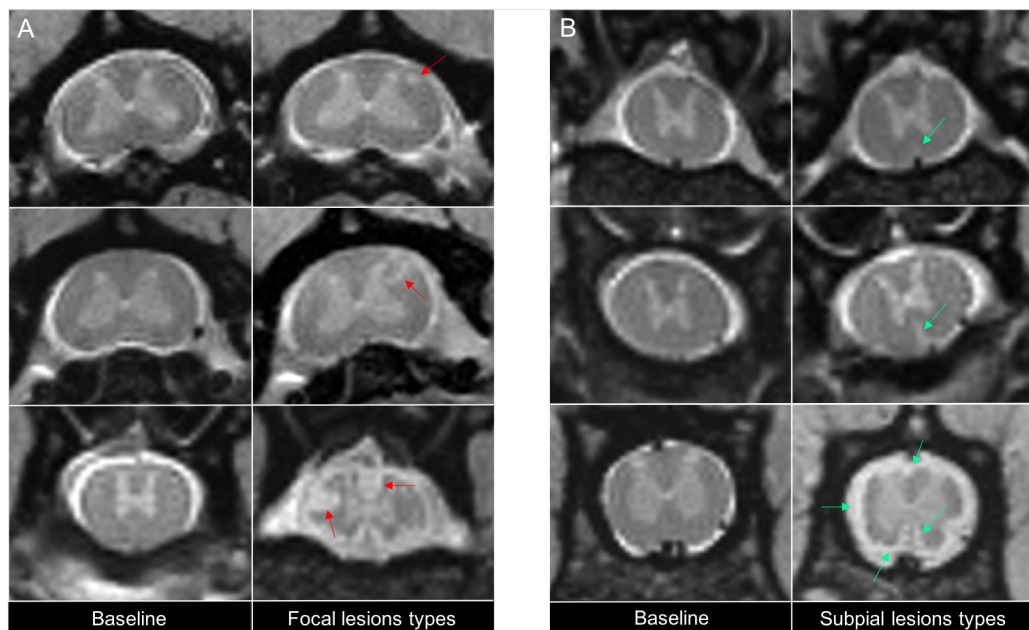


**Figure 5.2:** Example of focal (A, red arrows) and subpial (B, green arrows) lesions from all three animals (different time points and slices) with their corresponding baseline. A) Top: small round focal lesion; Middle: small line-shape focal lesion; Bottom: two large elongated focal lesions. B) Top: subpial lesion around the ventral vein; Middle: thin subpial along the AMF; Bottom: Thicker subpial located along the cord edge and the AMF.

**A semi-quantitative lesion analysis** was first performed with the goal to provide an estimate of the lesion load in each animal and characterize its evolution over time. For focal lesions, each lesion was manually marked and counted on each axial PD-w slice of the different cord segments for each time point and each animal. Due to the 1.5 mm slice gap in our axial PD-w acquisition, it is possible that an elongated lesion extending through n successive slices was counted n times. For subpial lesions, each axial PD-w slice affected by a subpial lesion was marked and counted in each segment. A percentage of affected slices per segment was then derived for each animal at each time point. An illustration of this measure for subpial pathology is provided in Figure 5.3.

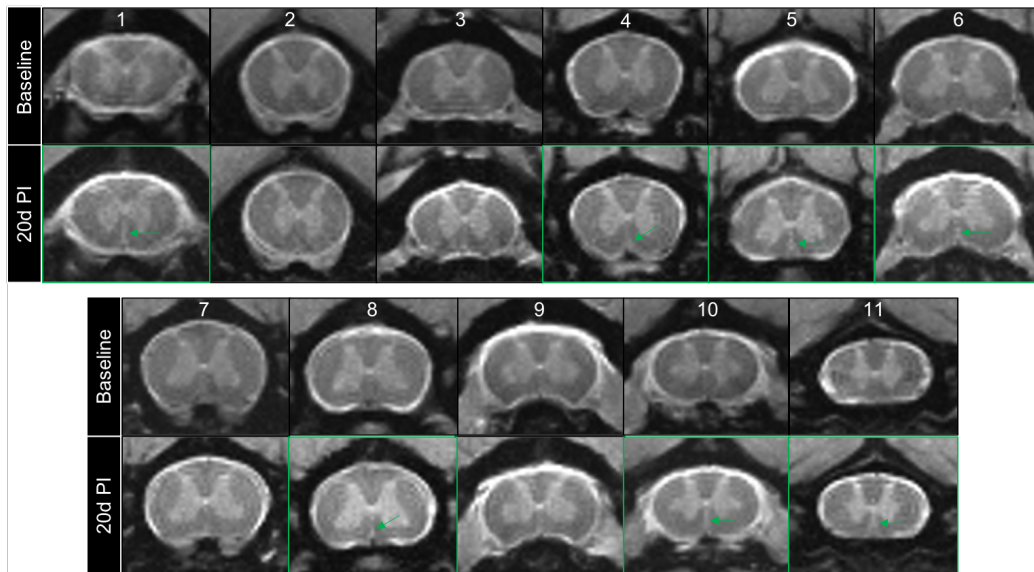


**Figure 5.3:** Example of the extent of subpial lesions within the cervical level for animal M#3 on TP1 MRI (20 days (d) post immunization (PI)). For comparison, the corresponding baseline images are included in the top rows indicating their slice number order within the segment (from the top to lower cervical). Green outline: slices where subpial lesions (indicated by the green arrows) were suspected. This example depicts 7 affected slices over a total of 11 slices, which reveal a proportion of 64% of the segment affected by subpial lesions.

**A quantitative lesion analysis** was then performed with the goal to quantify the evolution of the lesion volume over time. For focal lesions, a subset of eight discrete lesions clearly visible and well-delineated at all the time points were manually segmented (Jim, Xinapse Systems) across one animal (M#2). For subpial lesions, we could not obtain directly an accurate estimate of the subpial volume for the following reasons: similar range of signal intensity between the subpial lesions and the CSF and ligaments (See Figure 5.4), non consistency of the CSF signal between time points. Therefore, their extent was indirectly assessed by measuring the cross-sectional area (CSA) of the normal appearing white matter. This measure was generated by semi-automatically delineating the contour of the normal-appearing cord (Jim, Xinapse Systems) on each axial PD-w slice at each time point and for each animal. Cerebrospinal fluid and subpial lesions were excluded when visible. An example of this semi-automated delineation of the normal-appearing white matter cord is shown in Figure 5.4.

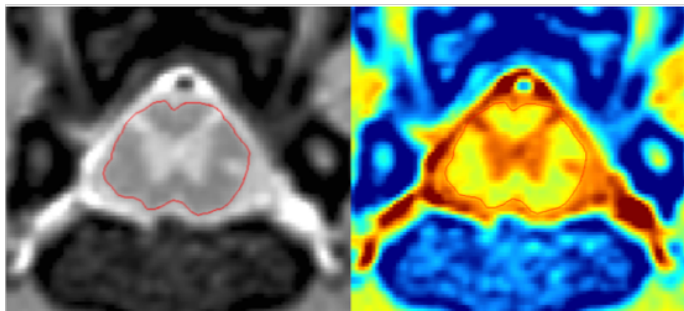


**Figure 5.4:** Example of the semi-automated contouring of the normal-appearing white matter cord (red line) used to compute the cross-sectional area at the lumbar level of the terminal MRI for animal M#2. Left image shows the axial PD-w slice using a gray scale; Right image shows the same slice using a colored scale. The colored scale was easier to appreciate subtle signal change and to delineate the subpial lesions with the NAWM.

### 5.2.3 Correlation between clinical scores and spinal cord abnormalities

Statistical analysis using the non-parametric Spearman correlation were performed between the MRI findings and the disability scores at the group level ( $n=3$ ). The Spearman's rank correlation coefficient  $\rho$  was obtained. The significance threshold was set at 0.05.

The MRI findings included the following variables: total number of focal lesions, CSA percentage change compared to baseline, and the combined number of abnormalities for each column (posterior column, lateral column, anterior column). For the combined number of abnormalities, we took into account the total number of focal lesions with the addition of the subpial lesions along the AMF. However, the other subpial lesions were not recorded by WM columns due to the difficulty in differentiating by columns accurately. The corresponding level (cervical, thoracic, lumbar) was recorded for each of these variables. Because of the length differences between the three levels (per our imaging protocol, thoracic is 2.6 times longer than cervical and 1.5 times longer than lumbar), lesions have a higher probability to develop through the thoracic level. To correct for that, the total number of focal lesions were renormalized to take account of the difference in length.

For assessing disability, three scores were used: the EAE score (table 5.2), the mEDSS (table 5.3), and the adapted functional system score (FSS) (see below). The adapted FSS score provides an additional clinical sub-scoring and was implemented by choosing four functions (out of the eight functional systems used in MS patient, see 1.1.4) due to the inability to evaluate the other systems in the marmoset. The four separate functions were recorded as the following:

- weakness or spasticity (hyperflexia) for the assessment of **pyramidal functions** (corticospinal tracts):

*Score 1:* mild weakness (decreased limbs and tail tone, spontaneous mobility)

*Score 2*: moderate weakness (paraparesis) – positive Babinski

*Score 3*: severe weakness (paraplegia) or severe limb hypertonicity with positive Babinski

- coordination for the assessment of **cerebellar functions** (spinocerebellar tracts):

*Score 1*: mild ataxia (tremor/clumsy movements)

*Score 2*: moderate ataxia (tremor/clumsy interfere with functions)

*Score 3*: severe ataxia (unable to coordinate movements)

- pain/temperature sensation for the assessment of **sensory function**:

*Score 1*: mild decrease in pain or temperature

*Score 2*: moderate decrease in pain or temperature

*Score 3*: severe decrease/complete loss in pain or temperature

- **bladder/bowel** function:

*Score 1*: abnormal bladder function (loss of control urine)

*Score 2*: abnormal bladder (severe loss of urine) and/or bowel functions (loss of control urine and bowel dysfunction, either diarrhea or constipation)

Additionally, an observational analysis was performed at the subject level (for marmoset M#2) to associate and understand the change in mEDSS with the appearance of new spinal cord lesions, particularly their spinal level and location within the WM columns. A change in mEDSS less than 5 points, was considered as a minimal change or no change.

## 5.2.4 Histopathological analysis

Lesion age was first determined for a group of 12 focal and 11 subpial lesions distributed across three animals. Lesion age was defined as the time interval between the time point when a lesion first appears, and the terminal time point when the animal was last imaged before euthanasia (which was performed on the same day). Due to the relatively small-time gap (two days) between the two in vivo MRIs performed after the immunization of animal M#3, the age of the lesions detected in this animal could only be estimated as ranging from two days to 20 days old, and, therefore, the lesions from this animal could not be classified according to the previously described age groups and were not included in the statistical analysis. The lesion age ranged from  $\leq 5$  days to 7.5-11.5 weeks (see table 5.4 for more details about their characteristics).

Using our postmortem MRI-guided tissue sampling technique (see chapter 3 for details on this methodology), the spinal cord tissue areas containing the lesions selected on the in vivo MRIs were cut in 2-4 mm thick slabs. After paraffin-embedding, these slabs were carefully cut in 5  $\mu\text{m}$  thick sections with a microtome until the targeted lesions were reached.

A total of 23 different lesions were identified from 15 different sections. Table 5.4 provides a summary of the selected lesions according to their age groups, lesion type and lesion location.

To analyze the changes in myelin content within these lesions, sections were stained with LFB-PAS staining and proteolipid protein (PLP; Bio-Rad, monoclonal) immunohistochemistry. To analyze the changes in inflammatory cells population, sections were stained using Iba-1 (Wako Pure Chemical Industries, polyclonal) and myeloid-related protein 14 (MRP14; Dako, monoclonal, clone MAC387) immunohistochemistry. The presence of lymphocytes was assessed by immunohistochemistry. CD3 was used to detect the presence of lymphocytes T cells and CD20 was used to detect the presence of lymphocytes B cells.

In order to accurately evaluate the cellular density on each staining on the selected area, the ex vivo MRI slice and histopathology sections were spatially matched (See chapter 3.2.6 for more details). Measurements of cellular density (Fiji) for each staining (except for CD3 and CD20) were performed in the lesion [using the lesion ROI segmented on the MRI (MIPAV)] and in the NAWM [using smaller ROIs positioned through the NAWM (Fiji)]. The percentage of cells within each ROI was reported. Statistical analysis was performed using Prism. For each staining, a one-way ANOVA was performed to assess whether there was an overall difference between the lesion age groups and a Tukey multiple comparisons test was applied to assess if they differ significantly from each other. The significance threshold was set at 0.05.

**Table 5.4:** Classification of the selected MRI lesions by lesion age groups and by location for each animal

Animal	Lesion age groups with lesion types			Lesion location			
	≤ 5d	5d-2.5w	5.5w-11.5w	Cervical	Thoracic	Lumbar	Total
M#1	5 (3 focal, 2 subpial)	-	-	1	2	2	5
M#2	2 (2 subpial)	7 (6 focal, 1 subpial)	4 (3 focal, 1 subpial)	2	8	3	13
M#3	-	5 (1 focal, 4 subpial)	-	1	2	2	5
<b>Total</b>	7	12	4	4	12	7	23

M#1: marmoset 1; d: days; w: weeks.

## 5.3 Results

### 5.3.1 Evolution of spinal cord-related EAE neurological symptoms

All three animals presented their first SC-related deficits between the third and the fifth weeks post immunization (see Fig 5.5). Symptoms were mild affecting both upper and lower body and included discoordination, sensory deficits, and loss of muscle tone. Animals M#1 and M#3 developed an aggressive progression of the disease and were euthanized within less than a week from the first time point where clinical symptoms were detected (4 days and 6 days for M#1 and M#3, respectively). Both the upper and lower limbs were affected in animal M#1. At the time of the terminal MRI, a hypertonicity of the limbs and hyperextension of the feet (usually signs of an upper motor neuron syndrome) were observed. Animal M#3 presented mild clinical signs at 16 days PI. The hand discoordination associated with lethargy progressed aggressively to the entire lower limbs, ultimately leading to the euthanasia of the animal.

By contrast, animal M#2 presented a slower progression of the disease with 45 days between the first symptoms and the end of the experiment. Once the first symptoms appeared, the EAE score remained stable, as shown by the plateau with an EAE score of 2 between the 35<sup>th</sup> day and the 73<sup>rd</sup> day. Based on the mEDSS scale, two attacks were detected (each lasting 11-14 days) separated by a partial remission of the symptoms that lasted 31 days. Symptoms of loss of muscle tone and abnormal pain sensation fluctuated during this remission phase. A positive Babinski sign accompanied by tremor preceded the second attack. During the last two weeks, the animal developed a hypersensitivity to pain stimuli at 73 days, which was followed by hypertonicity of the limbs and hyperflexion of the feet at 77 days. The aggravation of the tail atonia was concomitant with a worsening of the bladder incontinence during the five last days of the experiment, which was terminated at 81 days. The loss of control in the lower limbs was exacerbated over the course of a week, until there was complete paraplegia at termination.

The weight loss, minimal for M#1 but more pronounced for M#3, corresponded to the onset of the clinical sign. For M#2, the weight loss preceded clinical signs by one week and then continuously dropped. The initial gain weight was not attributed to the disease but was due to a supplemental diet preceding the immunization.

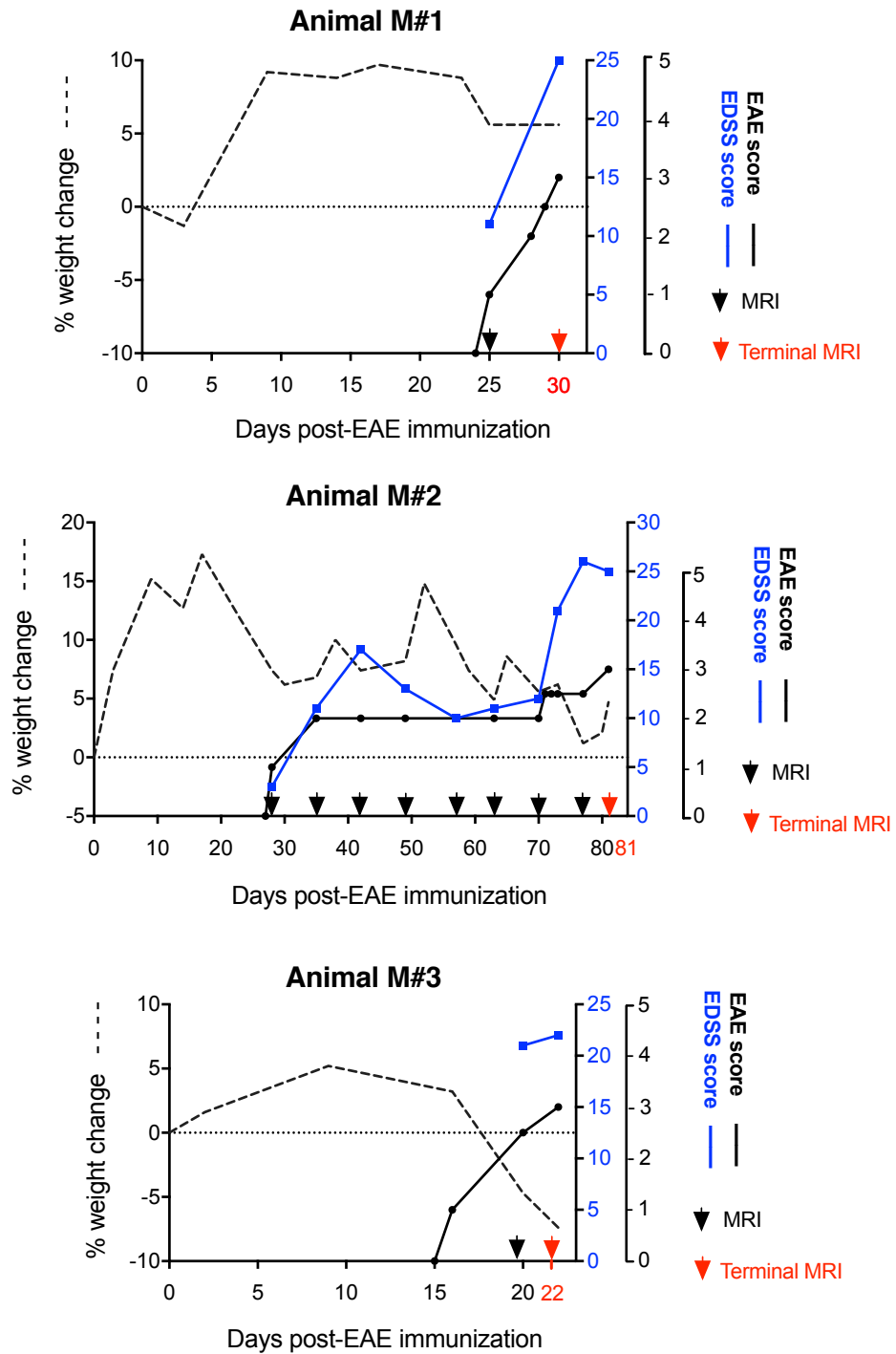


**Figure 5.5:** Temporal changes of the EAE/mEDSS scores and body weight during the course of the disease. The percentage weight change is the left-y-axis (black dotted line, relative change compared to baseline on day 0). Clinical scores are on the right-y-axis (solid lines) with the EAE score (blue line, maximum score of 5) and mEDSS score adapted to marmosets (black line, maximum score of 47). Each black circle blue square corresponds to a clinical assessment performed on the animal. Black arrows represent the MRI experiments. The red arrows represent the terminal MRI with its corresponding disease duration (number of days in red).

### 5.3.2 In vivo lesion analysis

#### 5.3.2.1 Spatiotemporal evolution of focal lesions

All three animals displayed focal lesions that formed throughout the disease course, and these were distributed along the entire spinal cord. The spatiotemporal evolution of the focal lesions for each animal is shown in Figure 5.6. Despite having different disease durations [22 days – 81 days], the animals presented some similarities: i) focal lesions appeared first in the thoracic and lumbar segments, ii) the rate of new focal lesions increased toward the end of the disease, iii) 70% of the focal lesions were located at the thoracic level by the time animals reached the study endpoint (paraplegia or hemiplegia).

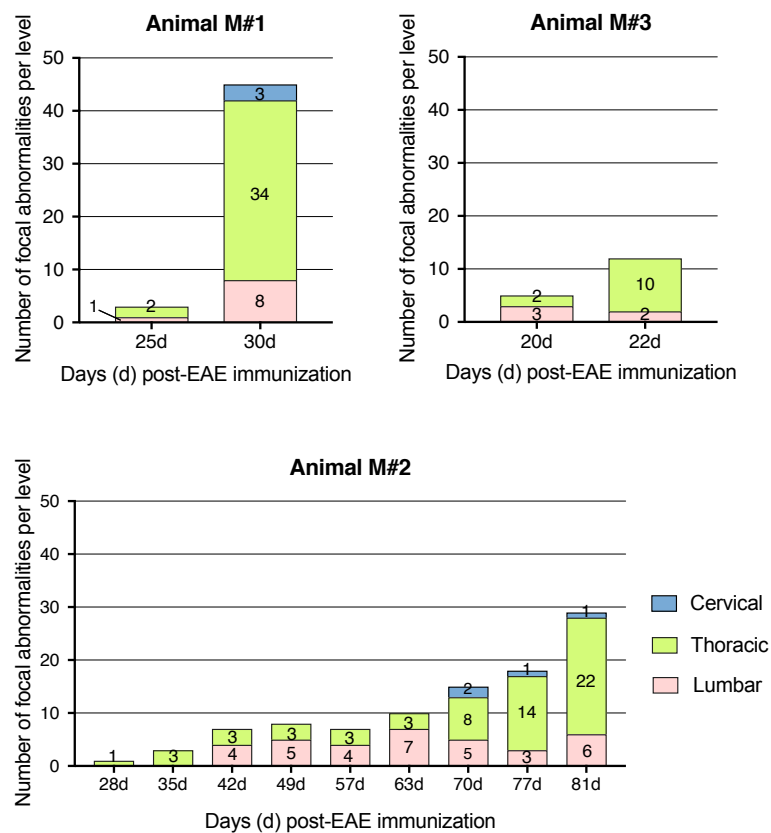


**Figure 5.6:** Number of focal lesions derived from the semi-quantitative lesion analysis for each animal during their respective disease course. The number of lesions by levels is reported for each spinal cord level (cervical, thoracic, and lumbar).

Since M#2 has the longest disease duration (81 days) and most time points (10 MRI scans in total), our quantitative lesion analysis focused on this animal. Lesion volumes for 8 different focal lesions were measured and their evolution over time is shown in Figure 5.7. These 8 lesions first appeared at different days post-immunization [28 days – 77



days] and showed differences in their lesion volume (small volume versus large volume) and corresponding temporal evolution (stable volume versus steep volume increase over time)

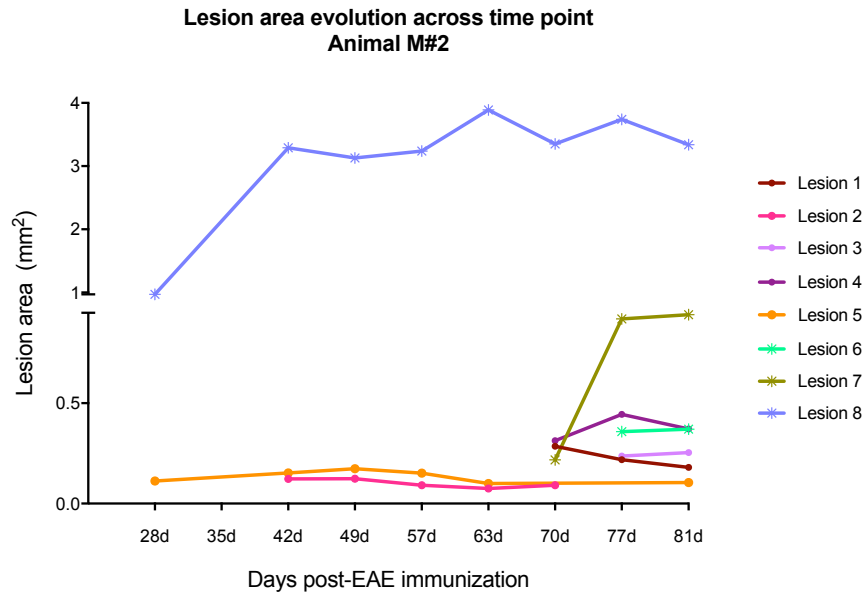


**Figure 5.7:** Temporal evolution of the lesion area for 8 focal lesions measured in animal M#2. Colored lines correspond to the different lesions. Each mark is related to an area measurement performed at a specific time point (absence of mark is due to the incapacity to measure at that time point). Round full circles correspond to lesions which affected only one MRI slice, stars-like marks correspond to lesions which affected more than one MRI slice.

Five out of the eight focal lesions (lesion 1 to lesion 5) were visible on a single MRI slice and had an average area of  $0.20 \text{ mm}^2 \pm 0.12$  at the terminal MRI. Two of these five lesions (lesion 1 and lesion 2) were located in the lateral column, and the three other lesions (lesion 3, lesion 4 and lesion 5) were oriented toward the ventral horn. The spatial location for these five small lesions is illustrated in Figure 5.8. Based on their lesion area (5.7) and visual appearance (5.8), these 5 lesions can be described as follows:

- Lesion 1 appeared at the time point 70 days post-immunization (PI) and its area decreased by a factor of 1.6 by the end of the experiment with a area size of  $0.18 \text{ mm}^2$  ( $\sim 8$  MRI pixels) on the terminal time point at 81 days PI;
- Lesion 2 appeared at the time point 42 days PI and had the smallest area which showed a slight decrease (range =  $0.12 \text{ mm}^2$  to  $0.08 \text{ mm}^2$ ;  $\sim 3$ -5 MRI pixels);
- Lesion 3 appeared at the time point 77 days PI and displayed a stable area ( $0.25 \text{ mm}^2$ ) on the following and last time point;
- Lesion 4 appeared at the time point 70 days PI and its area increased to  $0.44 \text{ mm}^2$  by 77 days PI. The presence of an extensive subpial lesion all around the cord edge on the last time point made difficult to measure accurately the focal lesion at that time point;

- Lesion 5 was already visible at the first time point 28 days PI. Its area remained relatively small throughout the disease course: 0.11 mm<sup>2</sup> at first appearance, maximum of 0.17 mm<sup>2</sup> at 49 days PI, and then slowly decreased, ultimately returning to its initial size.

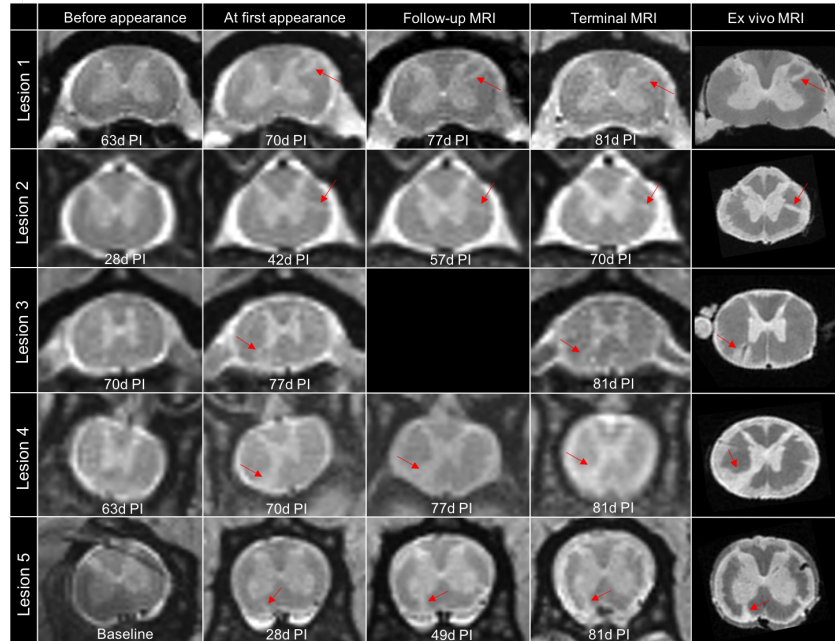


**Figure 5.8:** *In vivo* axial PD-w serial images showing lesion evolution over time for the five focal lesions visible on a single slice. Lesions are indicated by red arrows. The first column on left shows the spinal cord on the time point preceding the one when lesion first appeared. The other columns display from left to right the lesion when it first appeared, at a selected follow-up time point, and finally on the terminal time point at 11.5 weeks (or the last time point when the lesion was detected). The last column on the right shows the corresponding *ex vivo* images. The shape and size of the lesions depicted by the *in vivo* images highly resemble the ones observed on the *ex vivo* images. The days (d) post-immunization (PI) when each MRI image was taken are provided. Note for lesion 3 the absence of follow-up MRI because of the lesion first appeared one week before the terminal MRI.

The remaining three focal lesions (lesion 6 to lesion 8) were visible on multiple slices and had an average area of 1.55 mm<sup>2</sup> ± 1.58 at the terminal MRI. Two of them (lesion 6 and lesion 7) were located in the posterior column area and expanded over two consecutive axial slices by the terminal MRI. The spatial location for these two lesions is illustrated in Figure 5.9. The third and last lesion (lesion 8) was located within the lateral column and extended over four consecutive slices by the terminal MRI. The spatial location for this large lesion is illustrated in Figure .

Based on their lesion area (Figure 5.7) and visual appearance (Figures 5.9 and 5.10), these 3 lesions can be described as follows:

- Lesion 6 appeared on a single slice at the time point 77 days PI with an initial area of 0.36 mm<sup>2</sup>. Its area seemed to shrink over time on that slice but the lesion actually extended over to the next slice (Figure 5.9A);

- Lesion 7 was first visible at the time point 70 days PI and remained visible over the next two time points (terminal MRI included). Its size appears similar on the two consecutive slices it affected (Figure 5.9B). The total area of the lesion grew rapidly from 0.22 mm<sup>2</sup> to 0.94 mm<sup>2</sup>.

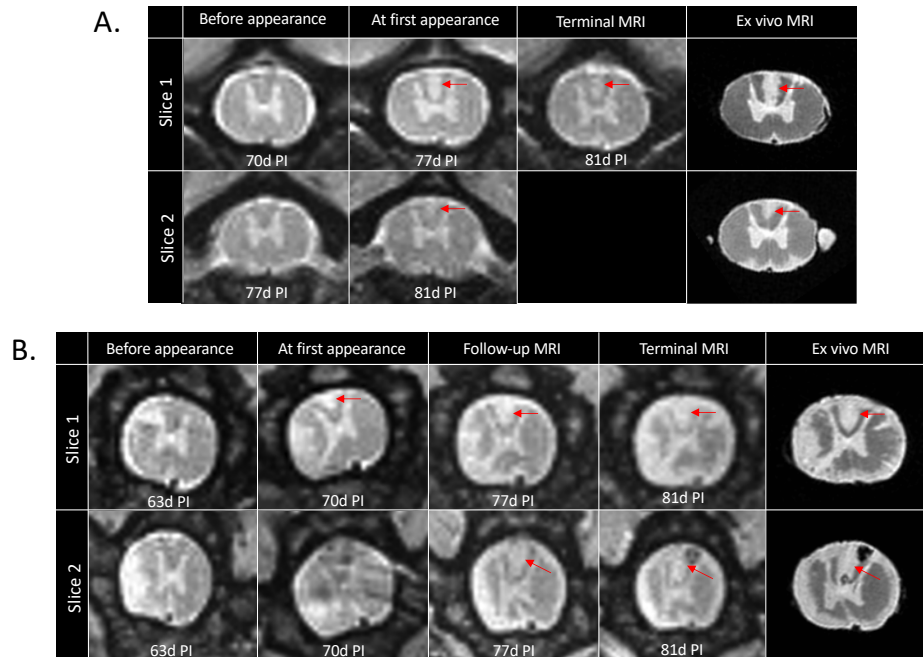


**Figure 5.9:** *In vivo* axial PD-w serial images showing lesion evolution over time for lesion 6 (A) and lesion 7 (B), both visible on two different consecutive slices (slice 1 and slice 2). Lesions are indicated by red arrows. The columns are the same as previously described in Figure 5.8. Note the motion artifact affecting the slice 2 when lesion 7 first appeared and possibly hide the lesion on that slice.

Lesion 8 was the largest lesion and was visible from the first time point (28 days PI) until the terminal time point. This lesion progressively affected four consecutive slices by the end of the experiment. This spatial distribution is illustrated in Figure 5.10. The total lesion area (sum of the areas measured of the different affected slices) tripled in its value within two weeks after the lesion first appeared (Figure 5.7), and remained stable until the last time point. When analyzing the lesion area slice-by-slice (Figure 5.10A), the lesion manifested first on slice 3 at 28 days PI and doubled its size within two weeks to reach 1.86 mm<sup>2</sup>, which was the maximum size observed across the slices. Rapidly after on 49 days PI, the lesion size reduced by factor of 1.4 to return to its initial size by the end-point. The lesion extended to the slices above and below at 42 days PI. Within two weeks, the lesion doubled its size on slice 4 to reach 0.92 mm<sup>2</sup> and stayed stable until the terminal MRI. On slice 2, the lesion size increased was less pronounced and progressed by 33% at 57 days PI to stabilize for two weeks (~ 1.35 mm<sup>2</sup>), then declined slowly to reach 0.71 mm<sup>2</sup> on the terminal MRI.

When considering the shape, the lesion was initially well-delineated and with a round shape (slice 3, Figure 5.10B). Then, the lesion started to expand to the next slices (above and below slice 3) and its border became more diffuse and less delineated. Its shape also evolved from a round focal lesion toward a subpial shape involving the entire lateral column at the cord edge.

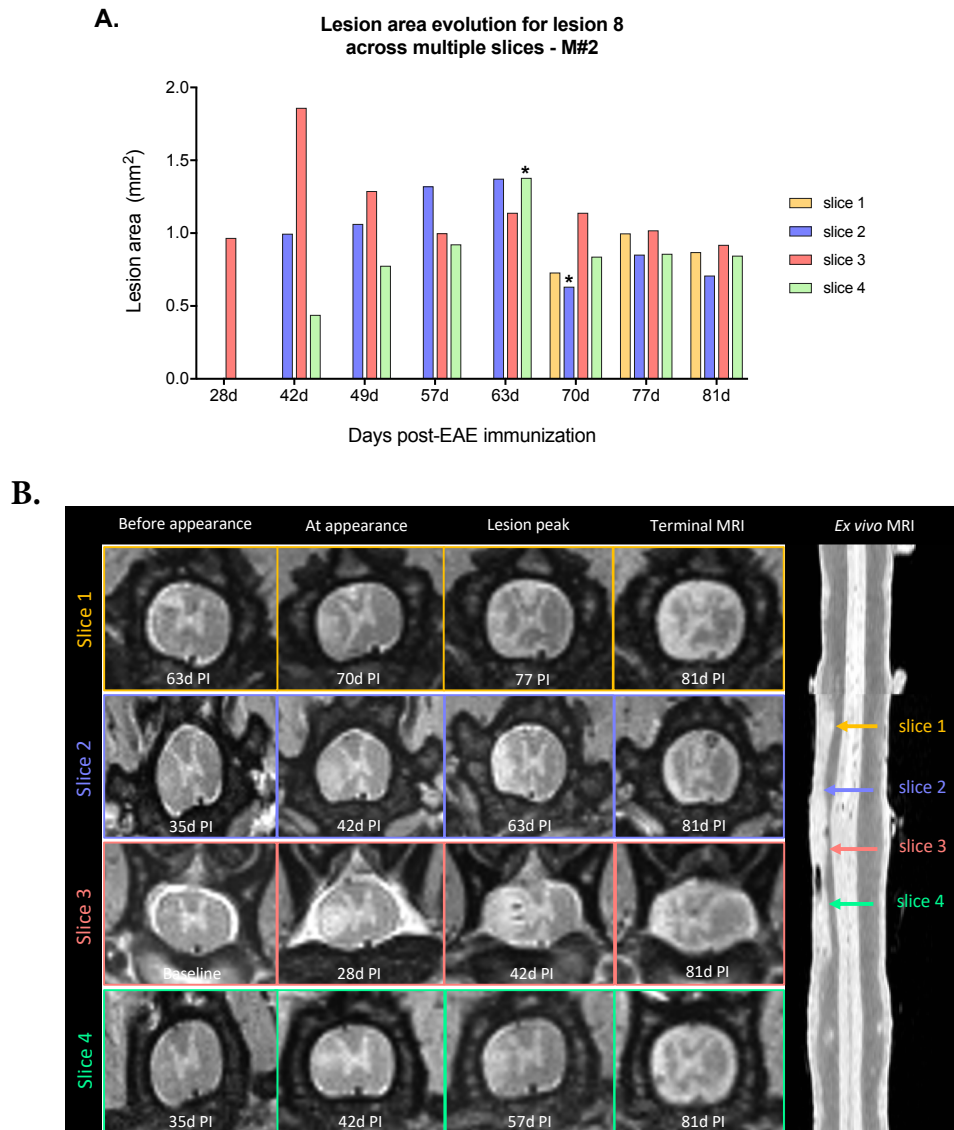


**Figure 5.10:** Spatiotemporal evolution of lesion 8. *A:* Temporal evolution of the lesion area measured for the four consecutive slices affected by the lesion. Colored columns correspond to different slices where the lesion appeared. Asterisks indicate where measurements are limited by artifacts on the images. *B:* In vivo axial PD-w serial images showing the evolution over time of lesion 8. The rows display the four consecutive slices affected by the lesion. Because the lesion developed on consecutive slices at different time points, the timeline of each slice is different. The columns are the same as those described in Figure 5.8, except for the follow-up MRI corresponding to the lesion's peak on each selected slice. The coronal orientation of the ex vivo image allows visualization of the spatial extent of the lesion. Note that both axial images at 35d PI presented shape distortions due to technical issues (failure of  $B_0$  shimming coils).

### 5.3.2.2 Spatiotemporal evolution of subpial lesions

All three animals displayed subpial lesions which appeared early in the disease course and were distributed along the entire spinal cord. The spatiotemporal evolution of the subpial lesions for each animal is shown in Figure 5.11.

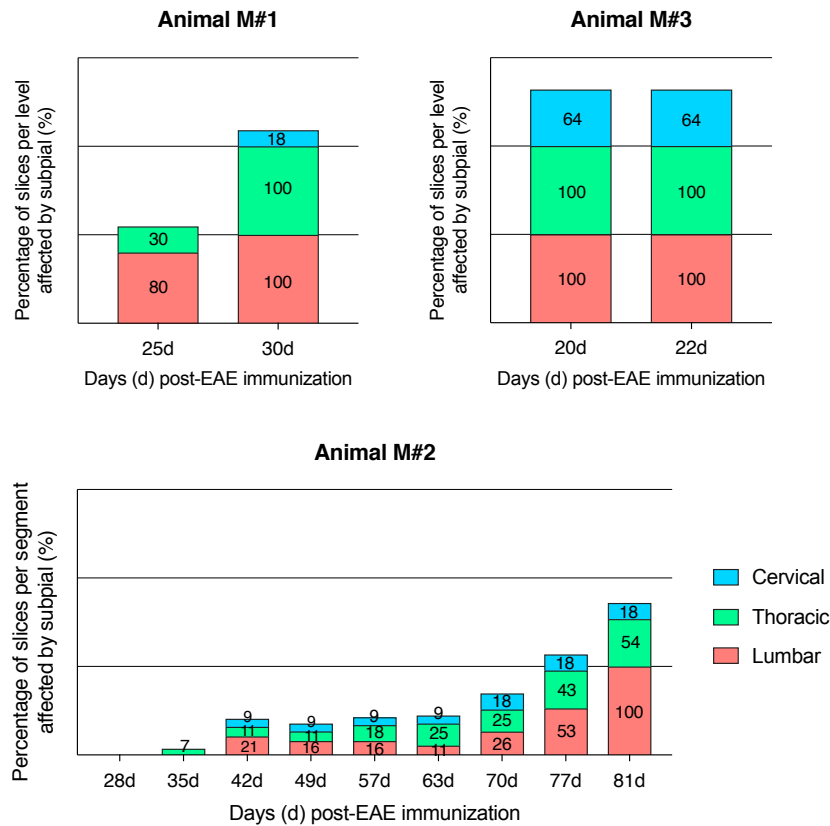


**Figure 5.11:** Percentage of slices affected by subpial lesions derived from the semi-quantitative lesion analysis performed for each animal during their respective disease course. This percentage is reported for each spinal cord level (cervical, thoracic and lumbar).

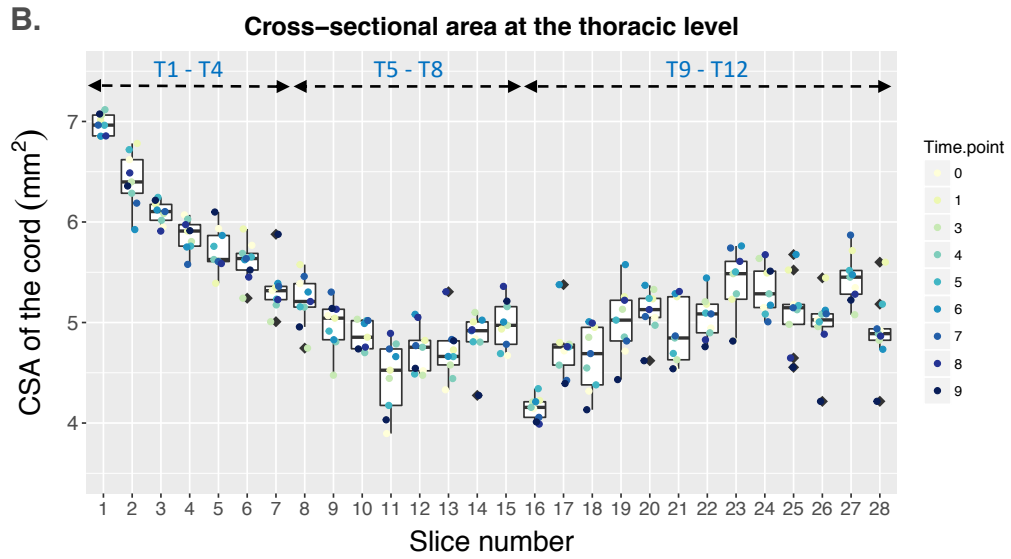
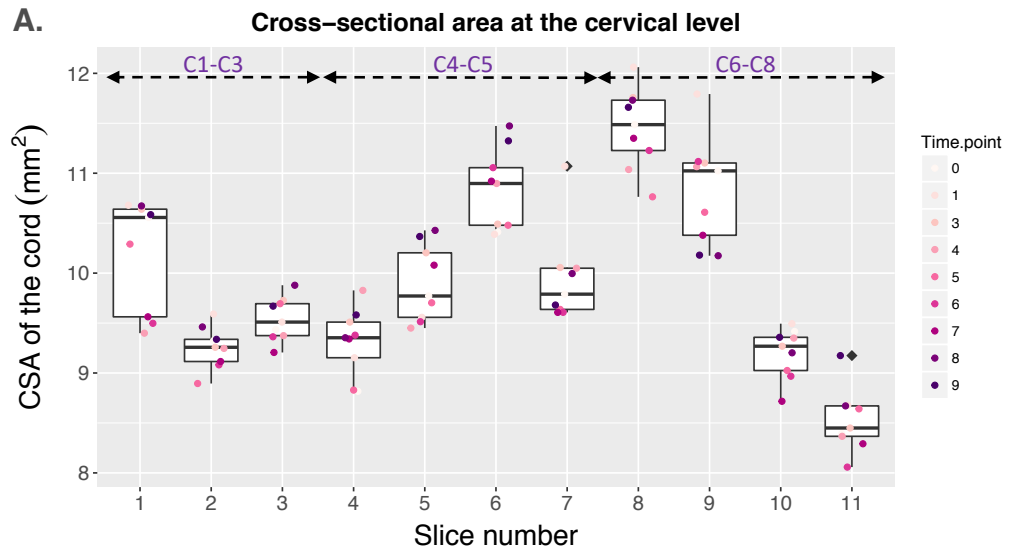
Interestingly, the three animals displayed different spatiotemporal evolution of their subpial pathology. In animal M#1, the subpial lesions first appeared at 25 days PI in the thoracic and lumbar levels, affecting 30% of the thoracic slices and 80% the lumbar slices. Over the span of just five days, these lesions spread over the cervical segment (affecting 18% of the cervical slices) and involved the entirety of the thoracic and lumbar slices. Compared to animal M#1, animal M#2 presented a slower progression of its subpial lesions with the first lesions appearing at 35 days PI in the thoracic level and affecting only 7% of the thoracic slices. All three segments became affected by subpial lesions seven days later (42 days PI) and the extent of these lesions (~ 9% cervical, ~ 11-25% thoracic and ~16-26% lumbar) remained quite stable until 63 days PI. By 70 days PI, an exacerbation of the subpial lesions started to occur primarily at the thoracic and lumbar levels which lasted

until the end of the experiment (81 days PI). At the last time point, the entirety of the lumbar segment and more than half of the thoracic segment were affected by the subpial pathology. Finally, animal M#3 showed a clear subpial pathology at the first time point 20 days PI affecting almost the totality of the spinal cord (64%: cervical, 100%: thoracic, 100%: lumbar). The extent of the subpial lesions slightly increased in the cervical segment over the next two days, at which point the experiment was ended (22 days PI).

Since animal M#2 had the longest disease duration (81 days) and most time points (10 MRI scans in total), our quantitative analysis of the subpial lesions primarily focuses on this animal. First, we assessed the variability of the CSA measurements done at the different time points for each slice of the spinal cord. To do that, the boxplot visualization helped to identify the slices with the most variability by comparing the position of the boxplots along the Y axis defined by the median, their size with the interquartile range (IQR) and the presence of outliers. The median was a better measure to evaluate the central tendency for data with a skewed distribution, due to the presence of outliers and the small sample size (n=10 measures for each slice).

By inspecting the evolution of the box positions across the slices, and noting the different scales of the vertical axis in the three panels, the changes in the anatomical size of the spinal cord can be appreciated: larger cord size at the cervical levels (average median = 9.9 mm<sup>2</sup>, min-max [8.4-11.5]) and middle lumbar levels (8.4 mm<sup>2</sup> [8.1-9]), smaller cord size along the thoracic slices (5.2 mm<sup>2</sup> [4.2-7]) and upper lumbar (5.9 mm<sup>2</sup> [4.5-7.1]), and smallest cord size values at the lower lumbar (3.6 mm<sup>2</sup> [2.1-5.9]). However, some slices presented extreme fluctuations when compared to their adjacent slices: slice 7 at the cervical level (figure 5.12A); slices 16, 26, 28 at the middle and lower thoracic levels (figure 5.12B); slice 5 the middle lumbar level (figure 5.12C).

When comparing the size of the boxes or IQR, most slices have a relatively small IQR which demonstrate a high consistency in the CSA measures across time points. Interestingly, some slices displayed high IQR: slices 1 and 9 at the cervical levels (figure 5.12A); slices 2, 11, 18, 21 at the thoracic level (figure 5.12B); slice 6 at the lumbar level (figure 5.12C). These slices with the most variability in the CSA measures are the ones most likely affected by biological changes (i.e. subpial lesions) or by technical issues.



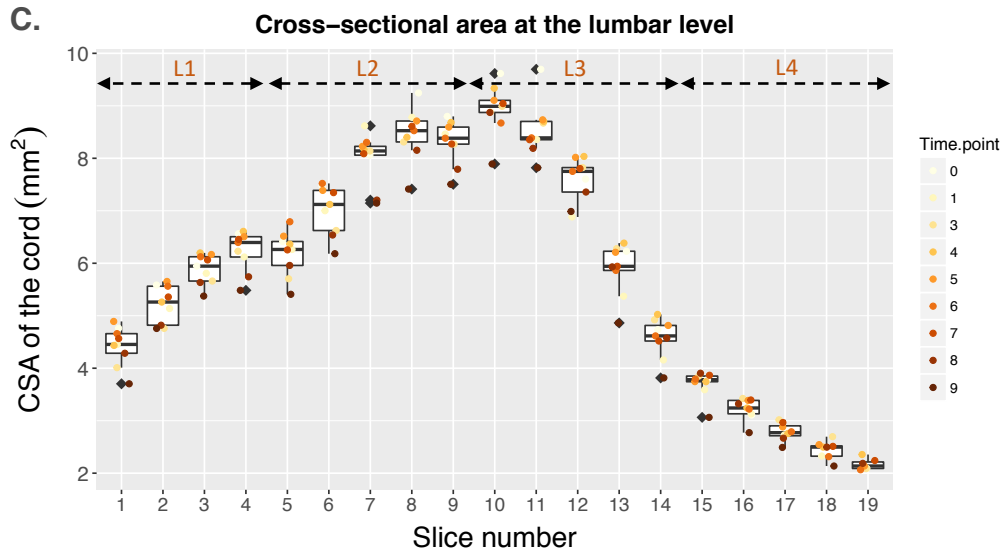


**Figure 5.12:** Boxplot for the cross-sectional area of the normal appearing cord edge along the three levels with each colored dot representing a time point. [A] Cervical level. (B) Thoracic level: upper thoracic (slices 1  $\rightarrow$  9), part of the first segment imaged; middle thoracic (slices 10  $\rightarrow$  17) and lower thoracic (slices 18  $\rightarrow$  28) part of the second segment imaged. (C) Lumbar level. The box width corresponds to the interquartile range (IQR), providing the first quartile Q1 (bottom), the median (black line) and the third quartile Q3 (top). The whiskers extend to the minimum and maximum values (within 1.5 x IQR from Q1 and Q3 respectively). Outliers (black diamond symbol) are extreme values located outside the whiskers.

To investigate the origin of the higher variation of the CSA measures observed for some slices of animal M#2, we analyzed the temporal evolution of these measures in each slice of the three cord levels, as shown in Figures 5.13, 5.14 and 5.15. In these figures, instead of days post-EAE immunization, we give the imaging time points (TP), with TP0 the baseline, TP1 the first MRI follow-up corresponding to the 28 days post-EAE, [...], TP9 the ninth MRI follow-up but also corresponding to the terminal MRI on the 81 days post-EAE.

At the cervical level (Figure 5.13), subpial lesions were not detected in slice 1 after visual inspection of the different time points. Therefore, the variations observed in the CSA measures were due to technical reasons. Indeed, slice 1 was positioned between the C1 and C2 vertebral bodies, where the shape and size of the cord can vary substantially. As a consequence, small displacements of the slice position between the different time points are most likely the cause of the CSA variability (see MRI in Figure 5.13). Visible subpial lesions were detected on the last three time points in slice 9 (see MRI in Fig 5.13 green arrows). Therefore, the fluctuations were primarily due to the pathological changes caused by the subpial lesions. We observed a clear decrease over time in the CSA measures (- 8% on the terminal MRI).



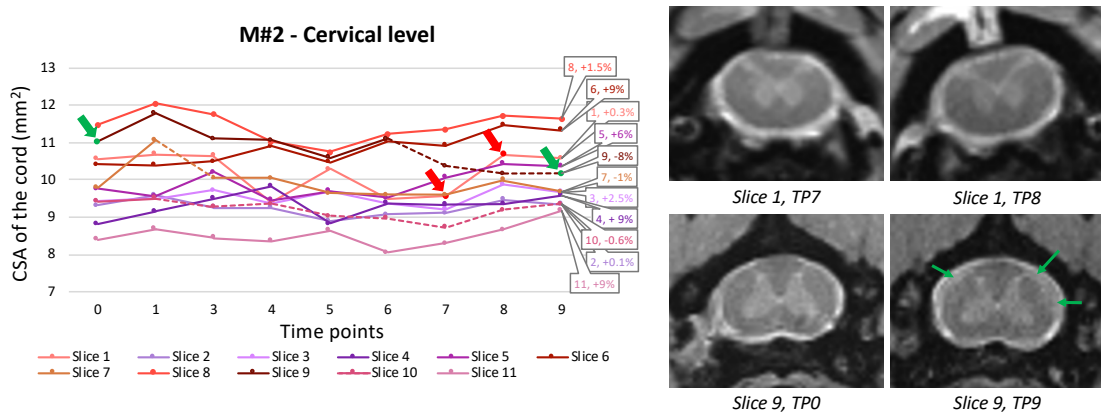


**Figure 5.13:** Cross-sectional area (CSA) of the normal appearing cord edge across the different MRI time points at the cervical level for animal M#2. Colored lines correspond to different slices. Information about the semi-quantitative subpial assessment is reported by different lines: solid lines if no subpial lesion was found, and dashed lines if any subpial lesion was detected. The labels on the terminal MRI (time point 9) indicate the slice number with its percentage decrease (or increase) of the CSA compared to the respective baseline (time point 0). Red dots identified by red arrows refer to the corresponding spinal cord MRI images on the right (slice 1) to highlight CSA measurement fluctuations due to technical reasons. Green dots identified by green arrows refer to the corresponding spinal cord MRI images on the right (slice 9) to highlight CSA measurement fluctuations due to pathology.

At the thoracic level (Figure 5.14), no subpial lesions were detected for slice 2. In this slice, the fluctuations in CSA were due to a bright artifact located at the junction of a ligament with the posterior cord edge and was hiding the edge of the cord in an inconsistent manner at the time points (see MRI images in Figure 5.14A, red arrows). For slices 11, 18, and 21, the cord had a distorted shape on some time points. The presence of nerve roots was inconsistent in these slices and was associated with changes in the shape of the cord (see MRI in Figure 5.14B, white arrows). Visible subpial lesions were detected on two points in slice 26 (see MRI in Figure 5.14C, green arrows). The fluctuations in the CSA measurements were primarily due to the pathological changes caused by the subpial lesions.

We observed a clear decrease over time in the CSA measures (-16% on the terminal MRI).

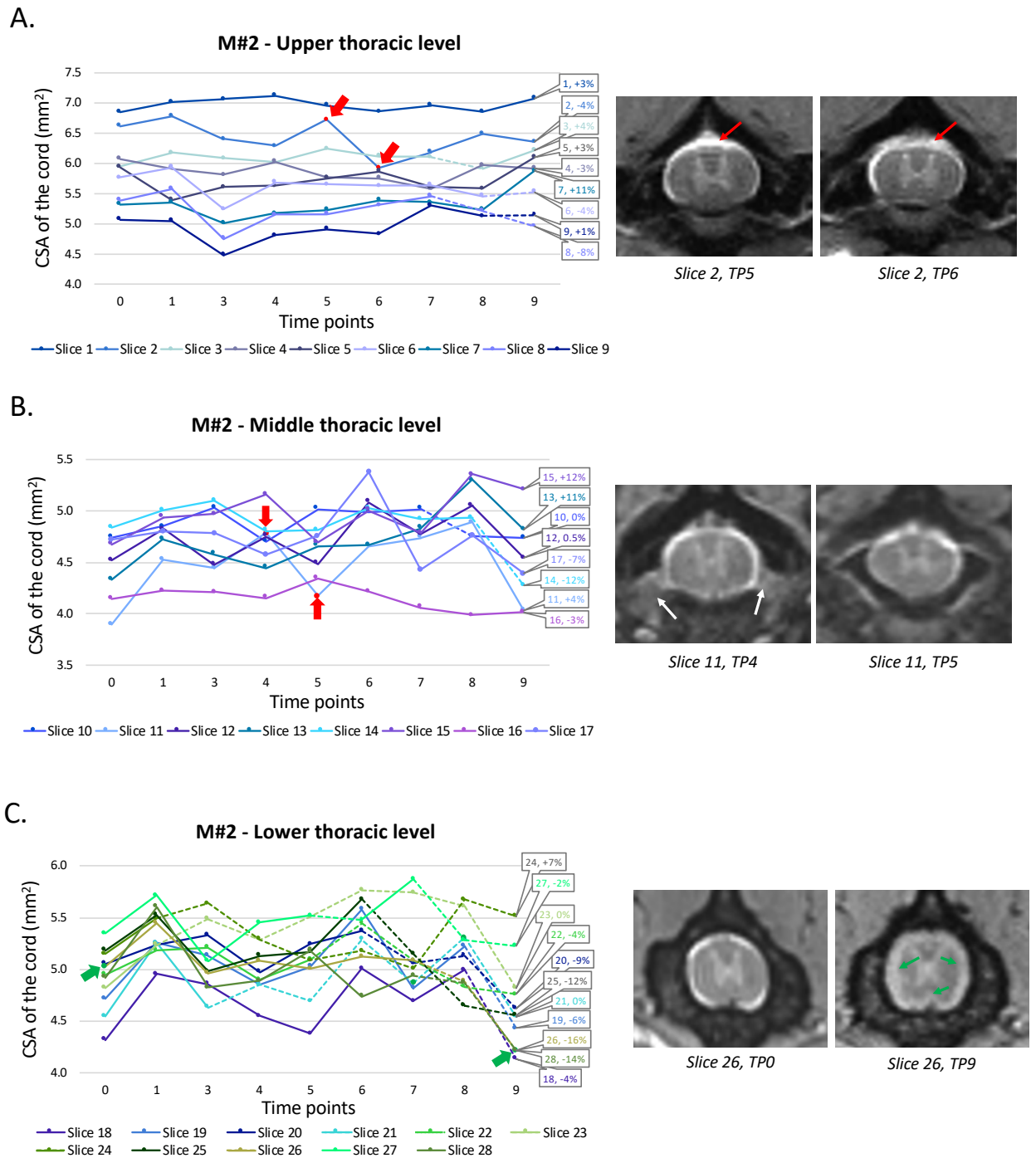


**Figure 5.14:** Cross-sectional area (CSA) of the normal appearing cord edge across the different MRI time points at the thoracic level for animal M#2. (A) Upper thoracic from T1 to T5 spinal levels. (B) Middle thoracic level from T5 to T8 spinal levels. (C) Lower thoracic from T9 to T12 spinal levels. Same descriptions regarding the colored lines, dashed lines and labels than Figure 5.13

At the lumbar level, slice 6 did not show any major differences compared to the other slices. Indeed, all the slices followed the same temporal evolution of their CSA measurements (Figure 5.15). For the upper lumbar level, there is an overall decrease at TP3 followed by an increase at TP5. The same phenomenon was observed for the caudal lumbar level. There is an inflection point at TP1 with an overall increase on TP3. A possible technical reason for these synchronized fluctuations across the lumbar slices could be related to the respiratory motion that primarily affects the lumbar cord in anesthetized marmosets. Any variations in the air cavities from the lung and diaphragm areas will create some perturbations of the static  $B_0$  magnetic field leading to geometrical distortions of the MRI images (see MR in Figure 5.15A, slice 2). Visible subpial lesions were detected over six time points and two time points in slice 8 and 13, respectively (see MRI 5.15A and MRI 5.15B, green arrows). The fluctuations in the CSA measurements were primarily due to the pathological changes caused by the subpial lesions. We observed a clear decrease over time in the CSA measures (- 20% for slice 8 and - 22% for slice 13, on the terminal MRI).

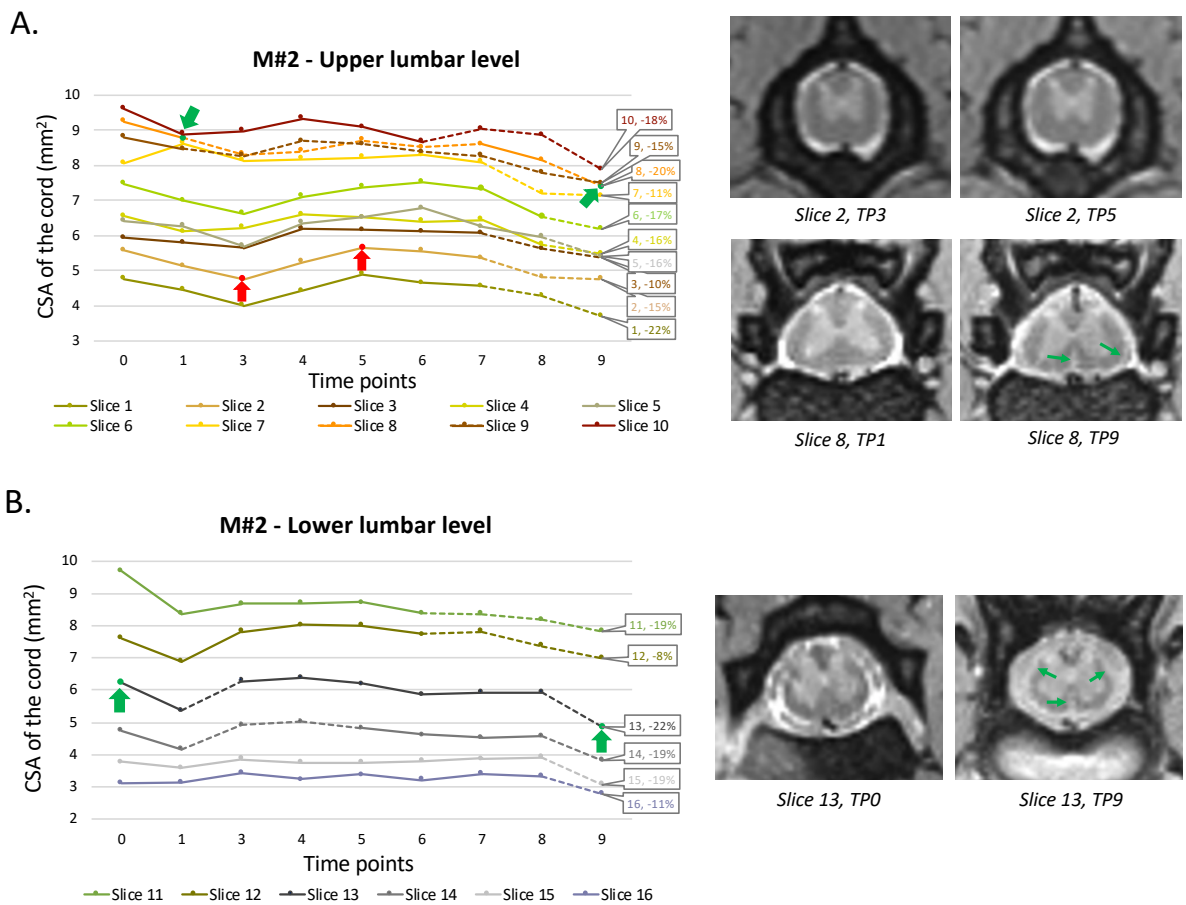


**Figure 5.15:** Cross-sectional area (CSA) of the normal appearing cord edge across the different MRI time points at the lumbar level for animal M#2. (A) Upper lumbar levels (B) Lower lumbar levels. Same descriptions regarding the colored lines, dashed lines and labels than Figure 5.13.

After a thorough analysis of the CSA measures at the animal level on a slice-by-slice basis, we compared the CSA measures to their respective baseline across our three animals. Figure 5.16 displays the averaged percentage CSA changes (%) on the terminal MRI by spinal levels. These CSA changes reflect the severity of the subpial lesions, where a higher percentage change corresponds to a higher subpial thickness. Some similarities were found across the three animals. The upper lumbar level presented the highest decrease which reached -41% for M#1, -16% for M#2 and -28% for M#3. Comparatively, the cervical level did not show any substantial changes over time. Some trends were also found when looking across levels for each animal. A gradual decrease of the CSA was found for animal M#1 along the upper, middle and lower thoracic level respectively with -7%, -23%, and -32% changes. Animal M#2 presented a slight decrease at the lower thoracic with -5.5% to reach an average maximum of -16% along the lumbar. For animal M#3, decreased changes appeared more uniform across the middle thoracic to upper lumbar ( $\sim -30\%$ ). Animals M#1 and M#3 presented both smaller changes at the lower lumbar levels ( $\sim -9\%$ ) despite displaying prominent subpial edge lesions.

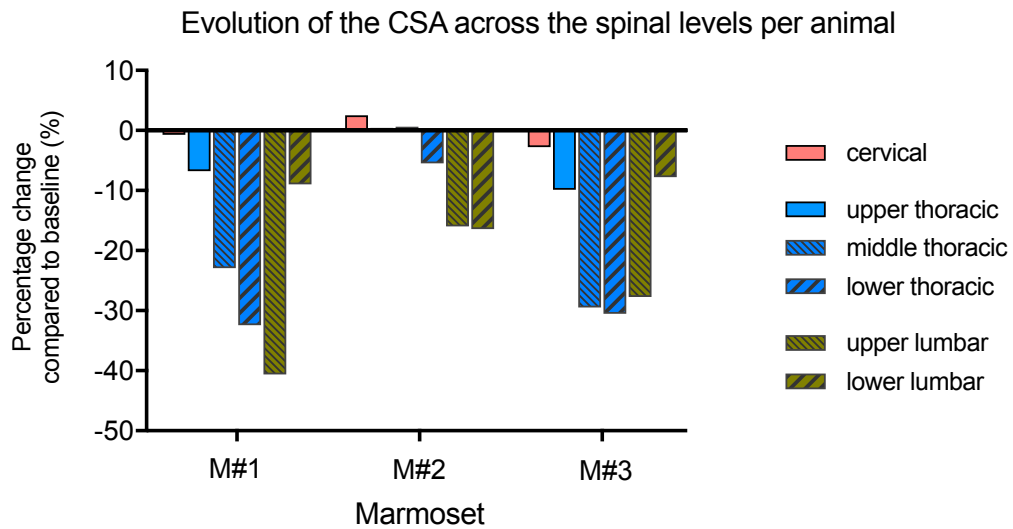


**Figure 5.16:** Evolution of the CSA changes on the terminal MRI across the spinal levels. Different colors correspond to different animals. The percentage change is annotated for each horizontal column.

### 5.3.3 Analysis of MRI findings and disability

#### 5.3.3.1 Correlations between MRI findings and disability scores for the whole marmoset cohort

When accounting for the MRI findings detected in the whole cord, statistical analysis showed a strong correlation between the total number of focal lesions and the EAE disability score ( $\rho = 0.78$ ,  $p = 0.004$ ). EAE and mEDSS scores showed similar results. The corresponding plots are visualized in figure 5.17.

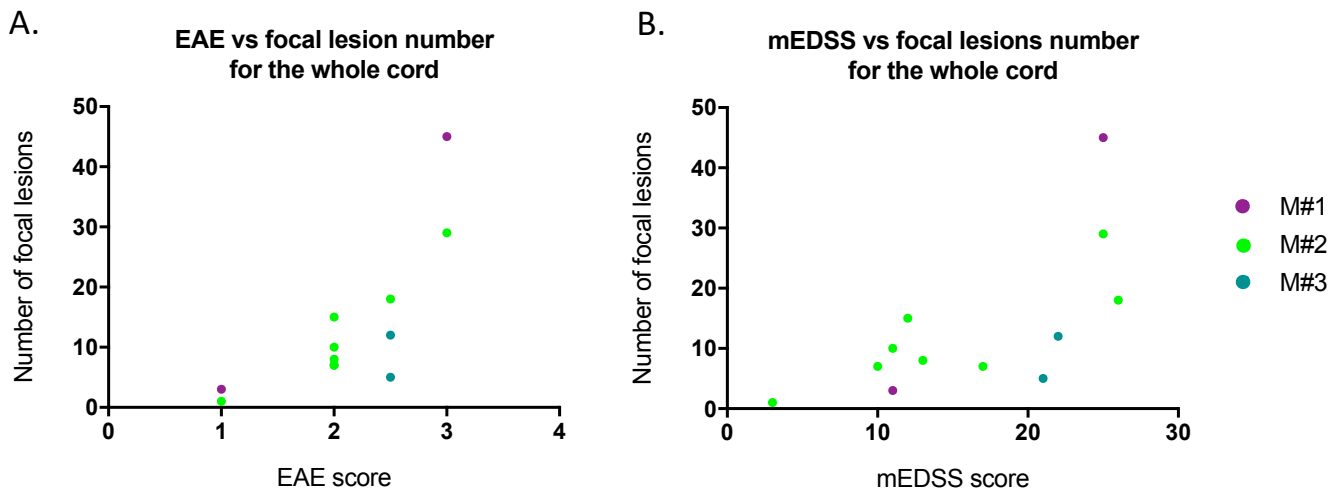


**Figure 5.17:** Association between the disability scores (A. EAE score, B. mEDSS for marmoset score) and the number of focal lesions for the whole spinal cord imaged. Colored dots correspond to different animals.

Statistical analyses with these scores at each level of the spinal cord showed that the number of focal lesions strongly correlated with both scores at the thoracic level only ( $\rho = 0.8$ ,  $p < 0.01$ ). After renormalization for the spinal cord length by level, similar results were obtained (not shown here). We previously found from our postmortem study that the severity of subpial lesions may gradually worsen along the cord for some animals. The CSA changes were then analyzed by spinal level as well. The lumbar level showed a significant negative correlation between the CSA changes and both EAE scores ( $\rho = -0.7$ ,  $p < 0.05$ ). The results are summarized in Table 5.5.

A more exhaustive statistical analysis was performed using the FSS scores of the four functional systems to estimate any potential correlations with the presence of lesions along the WM tracts. The strongest correlations were found for posterior column lesions with weakness and bladder dysfunctions ( $\rho = 0.92$ ,  $p < 0.01$ , and  $\rho = 0.83$ ,  $p < 0.01$  respectively). The sensory deficits did not correlate with any specific WM columns. The results are summarized in Table 5.6.

**Table 5.5:** Correlation between MRI findings by spinal cord level and disability scores

	Cervical level		Thoracic level		Lumbar level	
Scores	Focal lesion (n=12)	CSA (n=12)	Focal lesion (n=12)	CSA (n=12)	Focal lesion (n=12)	CSA (n=12)
EAE	$\rho = 0.49$ p=0.12 NS	$\rho = -0.14$ p=0.7, NS	<b><math>\rho = 0.8</math></b> <b>p=0.0027**</b>	$\rho = -0.51$ p=0.1, NS	$\rho = 0.4$ p=0.2, NS	<b><math>\rho = -0.70</math></b> <b>p=0.013*</b>
EDSS	$\rho = 0.57$ p=0.06, NS	$\rho = 0.03$ p=0.9, NS	<b><math>\rho = 0.77</math></b> <b>p=0.0048**</b>	$\rho = -0.48$ p=0.12, NS	$\rho = 0.28$ p=0.38, NS	<b><math>\rho = -0.72</math></b> <b>p=0.01*</b>

Significant results are represented in bold brown color.

Spearman rank correlation coefficients ( $\rho$ ) with its corresponding p-value (p) are shown in the table.

NS (non significant) if  $p \geq 0.05$ ; \* if  $p < 0.05$ ; \*\* if  $p < 0.01$ ; \*\*\* if  $p < 0.001$ ; \*\*\*\* if  $p < 0.0001$ .

**Table 5.6:** Correlation between MRI abnormalities by WM columns and disability scores

Scores	Lateral columns (n=12)	Posterior column (n=12)	Anterior column (n=12)
FSS Weakness	<b><math>\rho = 0.59</math>, p=0.045*</b>	<b><math>\rho = 0.92</math>, p=0.0002***</b>	<b><math>\rho = 0.65</math>, p=0.026*</b>
FSS Ataxia	<b><math>\rho = 0.67</math>, p=0.02*</b>	<b><math>\rho = 0.62</math>, p=0.037*</b>	$\rho = 0.42$ , p=0.18, NS
FSS Sensory	$\rho = 0.15$ , p=0.7, NS	$\rho = 0.45$ , p=0.14, NS	$\rho = 0.55$ , p= 0.07, NS
FSS Bladder	$\rho = 0.45$ , p=0.14, NS	<b><math>\rho = 0.83</math>, p=0.0036**</b>	<b><math>\rho = 0.6</math>, p= 0.042*</b>

Significant results are represented in bold brown color.

### 5.3.3.2 Associations between lesion location and clinical symptoms at the individual level

Since M#2 has the longest disease duration (81 days) and most time points (10 MRI scans in total), the observational analysis was focused on this animal. As already described in section 5.3.1 and figure 5.5, the first clinical attack occurred between the 28<sup>th</sup> and the 42<sup>nd</sup> days PI, followed by a 31-day period of partial remission, and finally the experiment ended with a final attack between the 73<sup>rd</sup> and 81<sup>st</sup> days PI.

The first nonzero mEDSS score was minimal, with a single focal lesion detected by MRI. The symptom was a sensory loss of the lower extremity and did not correlate with

the large focal lesion located at T11 within the lateral column. No subpial lesions that might have involved the spinothalamic tracts were visible at the lumbar level.

Despite a first significant increase in mEDSS score at 35 days PI, a clinical-radiological correlative analysis could not be performed at that time point due to the absence of imaging at the lumbar level. The next significant increase in mEDSS score at 42 days PI corresponded to an increased number of focal lesions and subpial involvement. Symptoms that involved the sacrococcygeal spinal levels (such as tail atonia) could not be assessed by imaging. The loss of pain sensation was observed in all four limbs. In principle, this could suggest a lesion along the spinothalamic tracts above the spinal cord (at the brainstem level, for example). The weakness of the left leg could be associated with a lower motor neuron syndrome. Lesions were found along the ventral nerve roots exit at the L3 and L4 spinal level. Weakness of both arms were not explained by similar lesions at the lower cervical level. The animal presented discoordination of his hands with a lack of motor grip. We found subpial lesions at the C7-C8 spinal level, which corresponded to the location of the posterior spinocerebellar tract, an important tract for proprioception.

The disability scores did not present major increases between the 49<sup>th</sup> and 63<sup>rd</sup> days PI and corresponded to a stable number of focal and subpial lesions. Clinical symptoms (i.e. weakness and motor grip) were stable, and some improvement was observed for the pain sensation. However, additional symptoms were detected as a positive Babinski and bladder dysfunctions. Babinski sign is part of the upper motor syndrome with lesions that can possibly be found anywhere along the corticospinal tracts.

At 70 days PI, the mEDSS score - despite presenting a minimal increase - was associated with an increased number of focal and subpial lesions. Most of the new lesions were located between T10 and T12 spinal levels. An additional symptom was discoordination of the lower limbs and imbalance, which could be associated with the subpial lesions at the L5 spinal level that were detected within the posterior spinocerebellar tracts.

The mEDSS score presented a significant increase at 77 days PI, which corresponded to an increased number of focal lesions and important subpial involvement. The thoracic level was the primary location of the new focal lesions. The expansion of the subpial lesions was observed at the thoracic and lumbar levels, the latter involving only minimal damage around the ventral vein. Some of the new symptoms (spasticity, tremor, worsening of the tail atonia, hyperalgesia of lower limbs) were not possible to associate with MRI findings. Some other symptoms (reduced motor grip of the feet and paraparesis of lower limbs) could involve the corticospinal tracts of the lower lumbar levels or a lower motor neuron syndrome. However, none of the new lesions were found within the corticospinal tracts. A possible reason could be that the L2-L5 spinal levels presented motion artifacts on the MRI, which made it difficult to visualize new lesions. We observed an increase in the number of lesions within the dorsal column at the thoracic level between T5 and T12. Dorsal columns include

tracts for conscious proprioception.

On the last time point (81 days PI), the mEDSS score was stable, although the EAE score reached a value of 3 due to paraplegia. A worsening of the symptoms (bladder dysfunction, complete loss sensation of the tail) was observed and could be explained by an increased severity of the subpial damage that expanded to the entire lumbar level. Interestingly, the motor grip showed improvement, with only the right-hand exhibiting deficit. The number of focal lesions within the dorsal column kept increasing and reached the L2 level. Some microhemorrhages were visualized within these lesions. The subpial lesion kept expanding as well, with the entire lumbar level becoming severely affected.

### 5.3.4 Postmortem lesion analysis

#### 5.3.4.1 Histopathology description by animal and lesion age group

The lesions selected on the in vivo MRIs were arbitrarily classified into three main age groups: early acute lesions ( $\leq 5$  days old), acute lesions (5 days to 2.5 weeks old), subacute lesions (5.5 weeks old to 11.5 weeks old). Only the lesions from M#1 and M#2 contributed to these three age groups. Due to the relatively small-time gap (two days) between the two in vivo MRIs performed after the immunization of animal M#3, the age of the lesions detected in this animal could only be estimated as ranging from two days to 20 days old (Table 5.4). Therefore, the lesion from this animal could not be classified according to the previously described age groups.

The histopathological characterization in terms of inflammatory response and demyelinating activity observed in these three groups is reported below:

##### (i) Early acute lesions

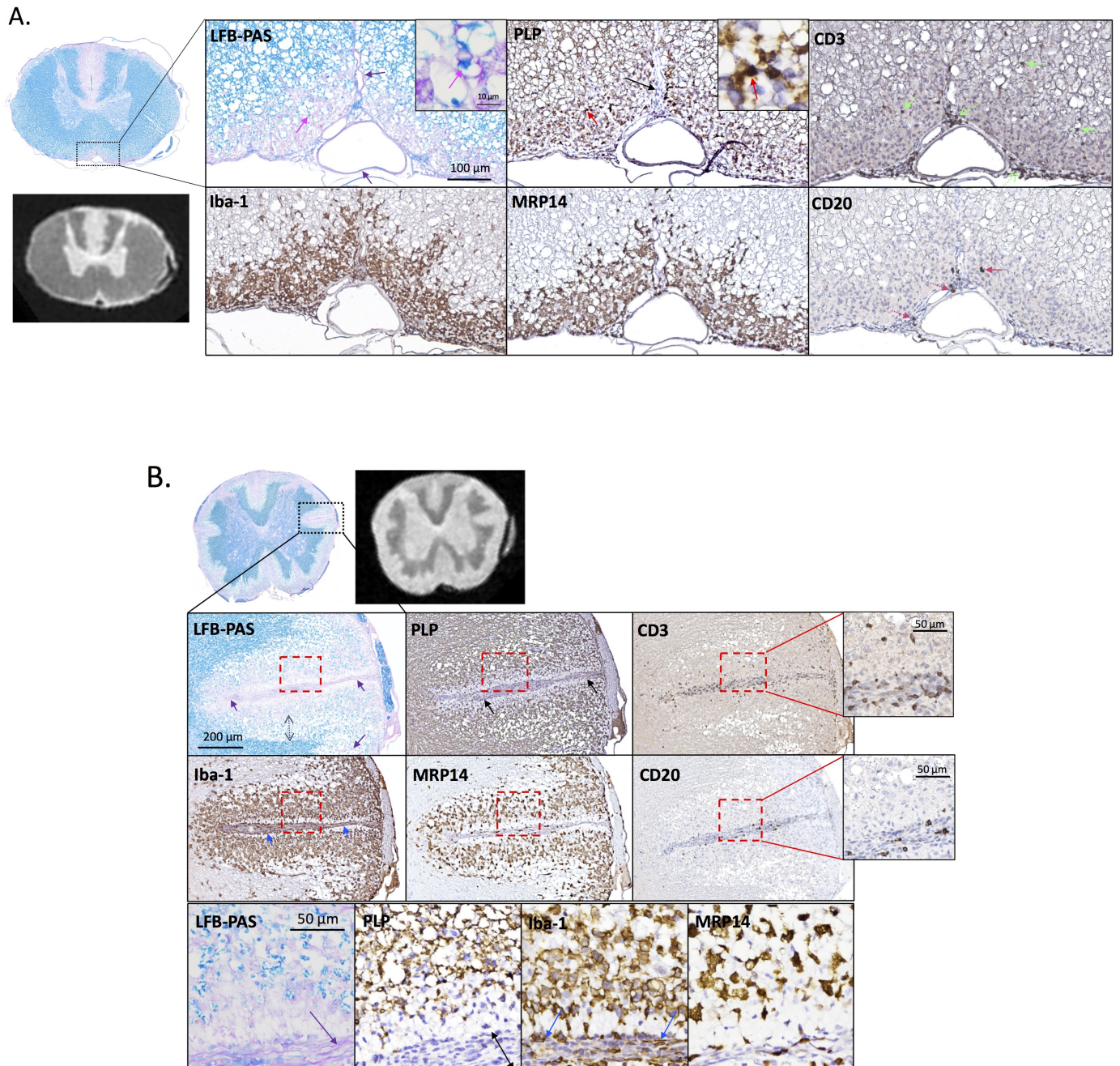
Two representative examples of early acute lesions are shown in Figure 5.18. The demyelinated areas on LFB-PAS were small and constrained to the area around vasculature in the lesion center in the case of focal lesions, or adjacent to the pia in the case of subpial lesions. Ongoing demyelination was confirmed by the presence of macrophages containing myelin debris (pink arrow, Figure 5.18A). Note the lesion borders presented clear spaces with disrupted myelin sheaths and signs of intramyelinic edema. The extent of the edema was more severe in animal M#1 than M#2. On PLP staining, the lesion border was not easily discerned. It showed hypercellularity within the perivascular space and the disrupted myelin within the parenchyma. The presence of dark brown PLP signal (red arrows, Figure 5.18) indicated an early stage of demyelination. Iba-1+ reactive microglia/macrophages were present in both perivascular space and the parenchyma. MRP14+ early macrophages occupied the entire lesion but were less dense within and in proximity to perivascular spaces.



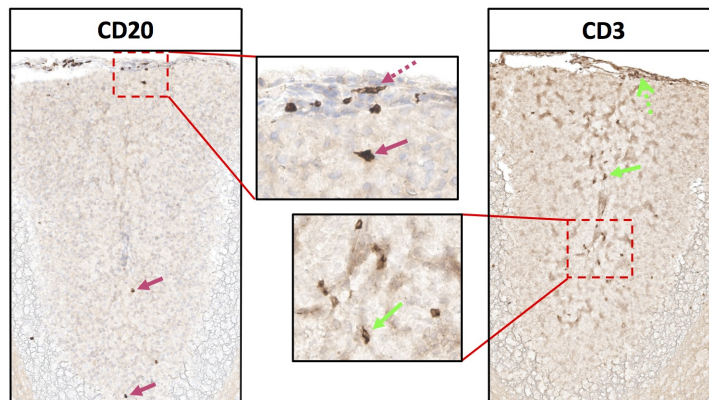
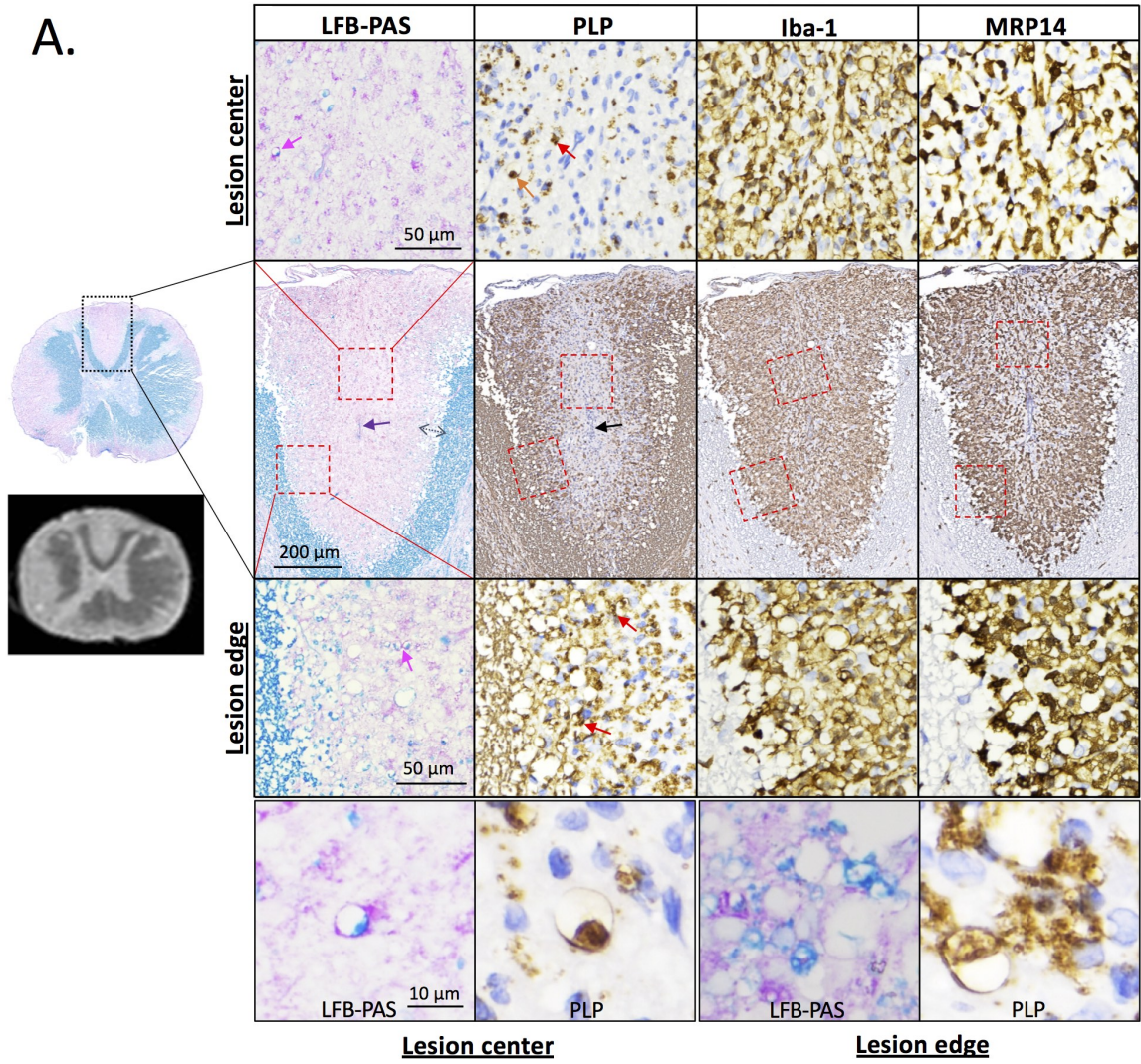
MRP14+ cells seemed more spread between each other compared to Iba-1+ cells, which was observed only for animal M#1. For both animals, we found CD3+ T cells scattered within the parenchyma and perivascular spaces. In the opposite, only a few CD20+ B cells were seen within the parenchyma, and in some cases, were found solely within the perivascular spaces. Regarding the leptomeningeal space, CD3+ T cells were more prominent for animal M#2 and located all around the cord edge, whereas CD20+ B cells were more scarce and only restricted toward the lesional area.

### **(ii) Acute lesions**

Two representative examples of acute lesions are shown in Figure 5.19. Acute lesions typically displayed heterogeneous demyelination pattern and inflammatory cell infiltration. One lesion presented a pattern in accordance with early acute lesions (disrupted myelin sheaths on LFB and PLP). For all other six lesions, marked demyelination through the entire lesional areas with a clear borderline was found on LFB-PAS. Active ongoing demyelination was supported by the presence of myelin debris within macrophages in five lesions on LFB-PAS. PAS-positive signal, corresponding to late myelin degradation products (Bruck et al. 1995), was found through the entire lesional area in these five lesions with some spatial variability. Edema at the lesion edge was potentially present in only one of those lesions (Fig 5.19A, grey arrows on LFB-PAS). On PLP, the extent of demyelination was more diverse. Three large focal lesions, which developed along the cord length based on the in vivo MRI, presented an area of complete demyelination surrounded by a more or less dense myelin debris (“dark brown signal”) (representative example shown on Figure 5.19A). Consequently, the lesion borders were not well-demarcated. PLP myelin debris within macrophages was found across the entire lesion area. Hypercellular aggregates on PLP corresponded with vasculature (veins or venules) and the most severe area of PLP myelin loss. These three lesions displayed severe Iba-1+ and MRP14+ cells infiltration through their entire area. A thin subpial lesion located at the cervical level showed a similar pattern, with PLP myelin debris across the entire subpial thickness. Two small focal lesions displayed a complete demyelination with a clear borderline on both LFB-PAS and PLP (representative example shown on Figure 5.19B). The lesions exhibited decreased cellularity on PLP. Iba-1+ cells were found through the entirety of the lesions, although for one lesion they were absent in the immediate perivascular area. The density of MRP14+ cells was visibly decreased either throughout the entire lesion or only at the lesion center. Similarly to the early acute lesions, CD3+ T cells were scattered within the parenchyma and the perivascular spaces, whereas rare or a few CD20+ B cells were seen. However, a decreased CD3+ T cells were seen within the leptomeningeal space with only rare CD20+ B cells.



**Figure 5.18: Representative histopathological images of two early acute lesions.** The top panel of images (A) depicts a subpial lesion located at the thoracic level around the ventral vasculature of animal M#2. The bottom panel of images (B) depicts a focal lesion located at the lumbar level within the right lateral column of animal M#1. The entire cross-section of the cord is visualized by LFB-PAS and ex vivo MRI (left side of panels). Black and red boxed indicate magnified views. Clear spaces at the lesion border indicate edema on LFB-PAS (gray double-arrows). Blood vessels can be visualized on LFB-PAS by PAS-positive signal (purple arrows). Hypercellularity within the perivascular spaces can be seen on PLP staining. Note the large aggregates depicted by the black arrows. Dark-brown myelin debris can be seen on PLP for images B (red arrows). Iba-1+ activated microglia/macrophages were densely found within the entire lesion area for both animals and were also found along the perivascular space (blue arrows). MRP14+ early macrophages occupied the entire lesion area as well although appeared less dense for animal M#1 with empty spaces around the perivascular spaces. CD3+ T cells were found through the parenchyma (full green arrows) and within the subpial spaces (dotted green arrows). CD20+ B cells were rare within the parenchyma (full pink arrow) but more cells were found within the subpial spaces (dotted pink arrows).



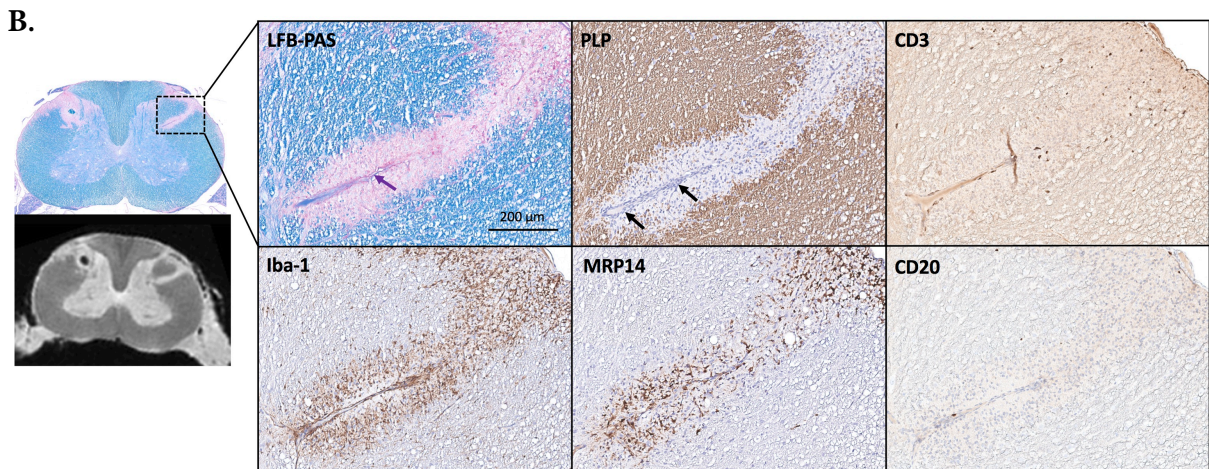


**Figure 5.19:** Representative histopathological images of two acute lesions. Both lesions are 1.5 - 2.5 weeks old and come from the same animal (M#2). The top panel of images (A) depicts a large focal lesion located at the thoracic level within the posterior column (lesion 7 from the quantitative volume analysis, section 5.3.2.1). The bottom panel of images (B) depicts a small focal lesion located at the cervical level within the right lateral column (lesion 1 from the quantitative volume analysis, section 5.3.2.1). The entire cross-section of the cord is visualized by LFB-PAS and ex vivo MRI (left side of panel). Black and red boxes indicate magnified views. Purple, black, red, and gray arrows correspond to the same description as in Figure 5.18. Myelin debris within macrophages can be visualized on the LFB-PAS (pink arrows) at the lesion center and lesion edge, as well on the PLP (orange arrow) at the center of the large focal lesion (A).

### (iii) Subacute lesions

Two representative examples of subacute lesions are shown in Figure 5.20. One lesion displayed some features similar to those of lesions classified as acute. The lesion was relatively small and located at the lumbar level within the left lateral column. Ongoing demyelination was supported by positive myelin debris within macrophages at the lesion edge on LFB. The lesion border was not distinct on PLP, and there was disrupted myelin and hypercellularity in the center. There was a high density of Iba-1+ cells through the entire lesion, although MRP14+ cells seemed reduced. The three other lesions, including the lesion shown in Figure 5.20B, showed complete LFB myelin loss with presence of myelin debris at the edge. PLP staining showed clear complete demyelination with decreased cellularity. In one subpial lesion located along the AMF, Iba-1+ cells were highly reduced within and surrounding the perivascular space. Otherwise, for the two other lesions, Iba-1+ cells were found to be less dense through the entire lesional area. There were very few MRP14+ cells in these older lesions. A minimal to slight infiltration of MRP14+ cells was observed, mostly away from the ventral vasculature, in the subpial lesion. No MRP14+ cells were seen in the other two focal lesions. For one of them, the absence of MRP14+ cells was only restricted in a small portion of the lesion, since the surrounding subpial area was still MRP14+ positive.

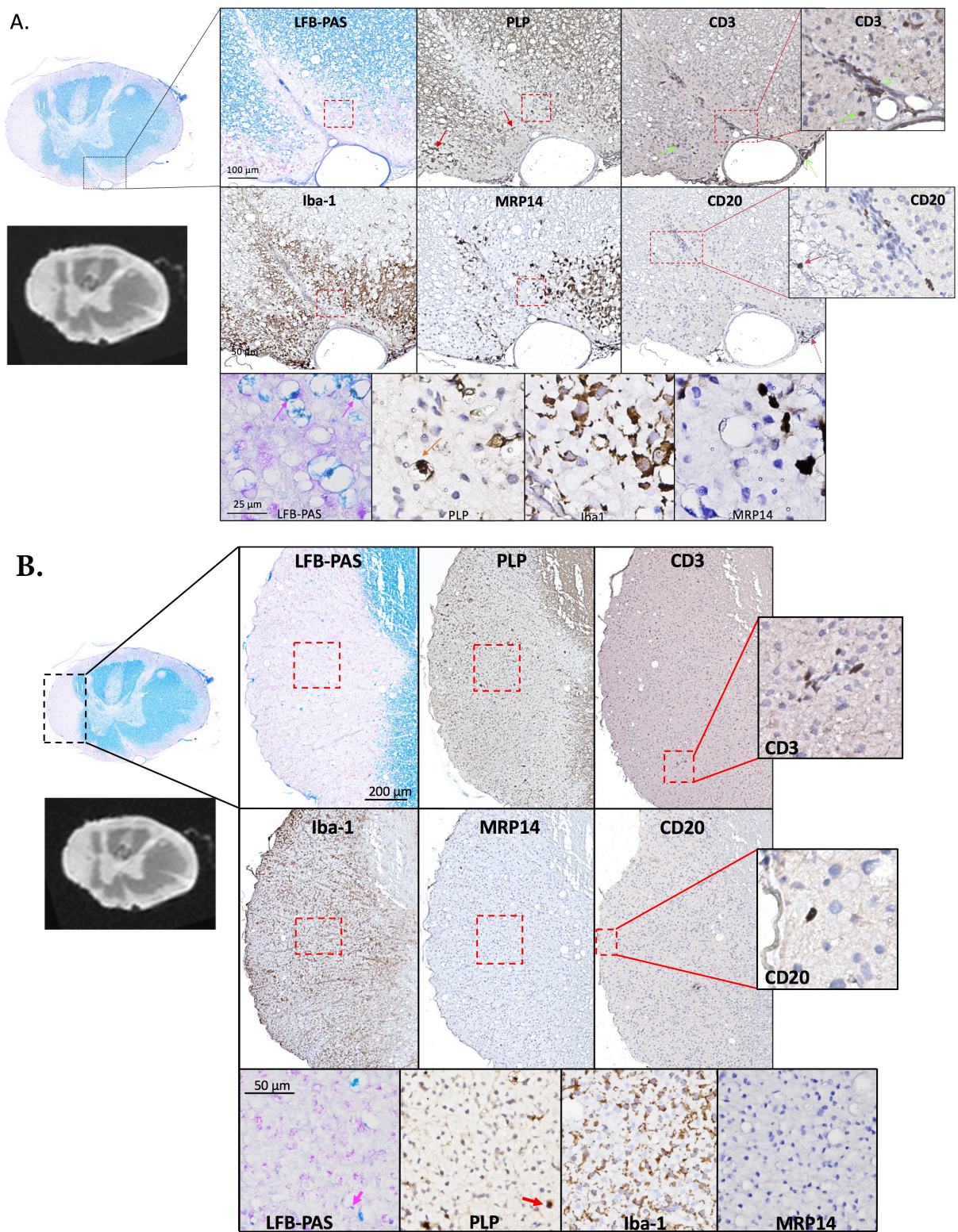


**Figure 5.20:** Representative histopathological images of two subacute lesions. Both lesions are from the same animal, M#2. The top panel of images (A) corresponds to a thin subpial lesion, 6.5-7.5 weeks old, located at the thoracic level around the anterior median fissure. The bottom panel of images (B) correspond to a large focal lesion, 7.5-11.5 weeks old, located at the same thoracic level within the left lateral column (lesion 8 from the quantitative volume analysis, section 5.3.2.1).

All lesions for animal M#3 ranged from 2 days to 20 days old. Because this age range is large relative to the pace of lesion development, this lesion is discussed separately. Two of the lesions were at a very early acute stage (Figure 5.21). Edema was severe through the entire lesional area and was associated with myelin disruption visualized on both LFB-PAS and PLP. There was no sign of myelin debris within macrophages on LFB-PAS. Iba-1 and MRP14 were found through the entire lesions although with a visible decreased density compared to animals M#1 and M#2. The three other lesions were consistent with the early acute stage previously described.

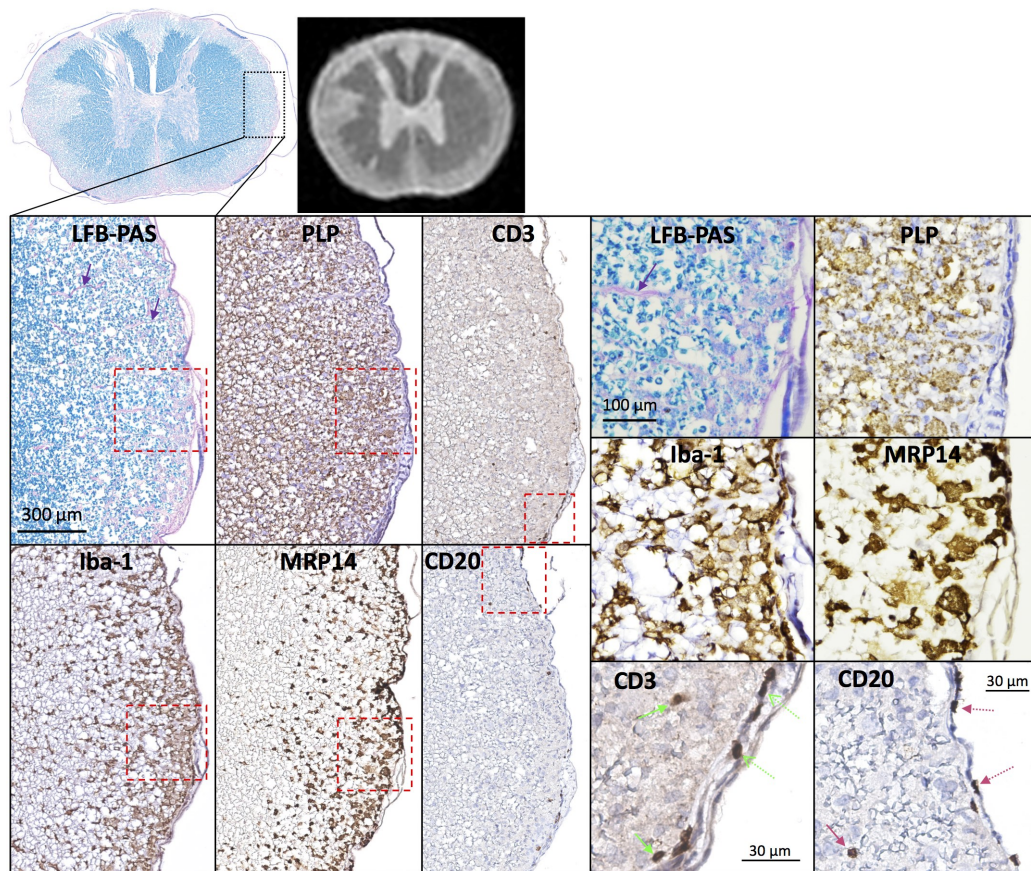


**Figure 5.21:** Representative histopathological images of a lesion from animal M#3. This subpial lesion was dated between 2-20 days old on the MRI. It would correspond to an even earlier stage than the early acute lesions described earlier. There is no evidence yet of myelin debris within macrophages, but the myelin is disorganized on both LFB-PAS and PLP, which could be the very first stage of the demyelination process.

The evolution of the myelin structure using ultra-high magnification is visualized in Figure 5.22. While in control tissue the myelinated white matter appeared densely packed with regional differences (the posterior column contains highly dense thin fibers), we can appreciate the changes in myelin density within the spinal cord EAE lesions. The very early stage of demyelination presented a disorganization of the myelin structures without any signs of myelin debris within macrophages. For the early acute stage, the myelin density was already strongly reduced compared to the control tissue. The ongoing demyelination can be confirmed by presence of myelin debris within macrophages on LFB-PAS, and the presence of dark-brown PLP myelin aggregates associated with an increased cellularity. The center of an acute lesion shows complete demyelination on both LFB-PAS and PLP, whereas the lesion edge looks like more the very early stage of demyelination.

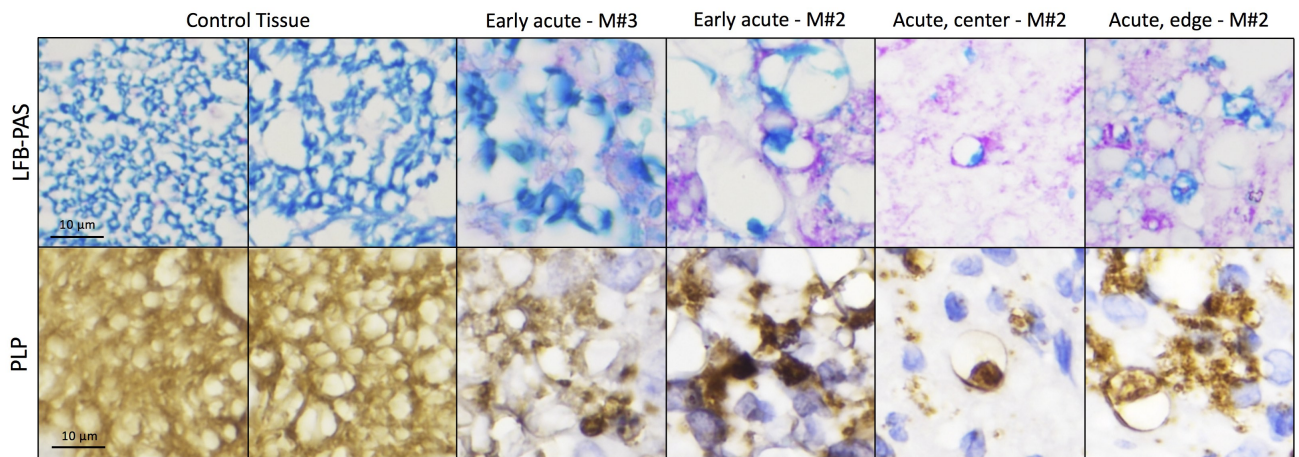


**Figure 5.22:** Evolution of the myelin content based on the lesion age. Higher magnification of the evolution of the myelin structure between a control animal and different EAE lesion age. We can appreciate the highly dense myelin lipid on LFB-PAS and the myelin protein on PLP of the white matter on the control tissue (left control: thoracic cord, posterior column; right control: lumbar cord, lateral column). The early acute M#3 corresponds to the subpial lesion in Figure 5.21; the early acute M#2 from the subpial lesion in Figure 5.18A; the acute lesion M#2 from the focal lesion in Figure 5.19A.

### 5.3.4.2 Quantitative analysis for myelin and inflammatory cells contents

The following graphics represent the distribution of cell density (LFB, PLP, Iba-1, MRP14) for the NAWM and by lesion age groups. Lesion age for animal M#1 consisted of only a single group: 0-5 days. Due to the low number of lesions older than 5.5 weeks and in order to perform statistical tests, for this purpose the lesions were reorganize into five groups: NAWM,  $\leq 5$  days old, 5 days-2.5 weeks old, and 5.5 weeks-11.5 weeks old.

The data did not follow a normal distribution for each group, as assessed by D'Agostino Pearson test. A one-way ANOVA test, robust against the normality assumption, was conducted, together with Tukey's multiple comparison tests, to compare the myelin loss and proportion of inflammatory cells across groups.

There were significant differences for the LFB myelin component between the NAWM and the lesions ( $p < 0.0001$ ). No differences were found between lesion age groups (Figure 5.23A<sub>1</sub>). The PLP myelin component also showed differences between NAWM and all lesions ( $p = 0.0005$  for lesions  $\leq 5$  days, and  $p < 0.0001$  for older lesions). A significant loss of PLP myelin was found between lesion ages  $\leq 5$  days and 5 days-2.5 weeks (Figure 5.23B<sub>1</sub>) ( $p = 0.0003$ ) with a mean difference of 18%, and between  $\leq 5$  days and 5.5 weeks-11.5 weeks ( $p < 0.0001$ ) with a mean difference of 31%. The proportion of Iba-1 inflammatory cells was different between NAWM and all lesions ( $p < 0.0001$ ). However, a weak significant difference was only found between the groups of 5 days-2.5 weeks and 5.5 weeks-11.5 weeks ( $p = 0.03$ ) with a mean difference of 10% (Figure 5.24A<sub>1</sub>). The proportion of MRP14 inflammatory cells (Figure 5.24B<sub>1</sub>) revealed differences between NAWM and lesions younger than 2.5 weeks ( $p < 0.0001$ ) although no differences were found with lesions older than 5.5 weeks. Only lesions older than 5.5 weeks differed significantly from younger lesions ( $p < 0.0001$ ) with a mean difference of 25%.

Regarding the demyelination mechanism process, these results suggest that the LFB-PAS, the lipid component of myelin, was affected first during the early stages of lesion development. Lesions  $\leq 5$  days displayed 19% of LFB myelin components compared to an average of 71% in the NAWM. Despite a lower proportion of PLP within the NAWM (average of 53%), the loss of myelin protein seems to progress slower, with 39.5% of PLP myelin present within lesions younger than 5 days, but only 8.7% for lesions older than 5.5 weeks.

Regarding the inflammatory cell infiltration process, Iba-1 "reactive" cells appeared early in the first days of lesion development, comprising 42% of cell density within lesions  $\leq 5$  days (compared to 2.34% within the NAWM), and seemed to stay consistent over at least the first few weeks of lesion development. For the MRP14 cells, infiltration manifested early as well with 31.4% of cell density within lesions  $\leq 5$  days (compared to 0.34% within NAWM), then to remain stable up to 2.5 weeks old. By 5.5 weeks after lesion development,



MRP14+ cell density has fallen to 6.1%.

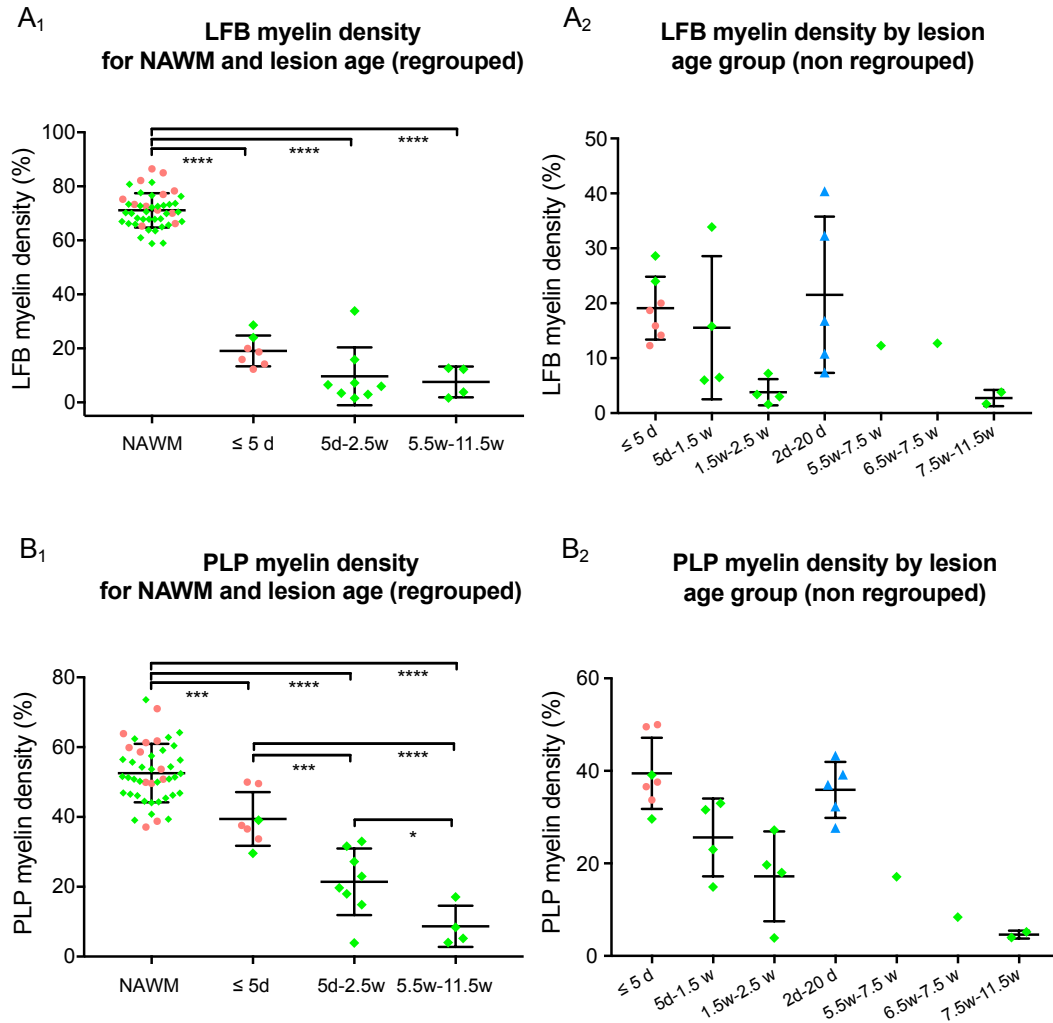


**Figure 5.23:** Quantification of LFB (A) and PLP (B) myelin density for the 18 selected lesions by age categories. Mean and standard deviation are shown. Each dot corresponds to an individual lesion, colored by animal (red: M#1, green: M#2; blue: M#3). A<sub>1</sub> and B<sub>1</sub> correspond to the lesion age regrouped in four categories with the normal appearing white matter (NAWM) provided for comparison. A<sub>2</sub> and B<sub>2</sub> correspond to the raw lesion age groups, better highlighting the trend in animal M#2. \*  $p < 0.05$ , \*\*\*  $p < 0.001$ , \*\*\*\*  $p < 0.0001$

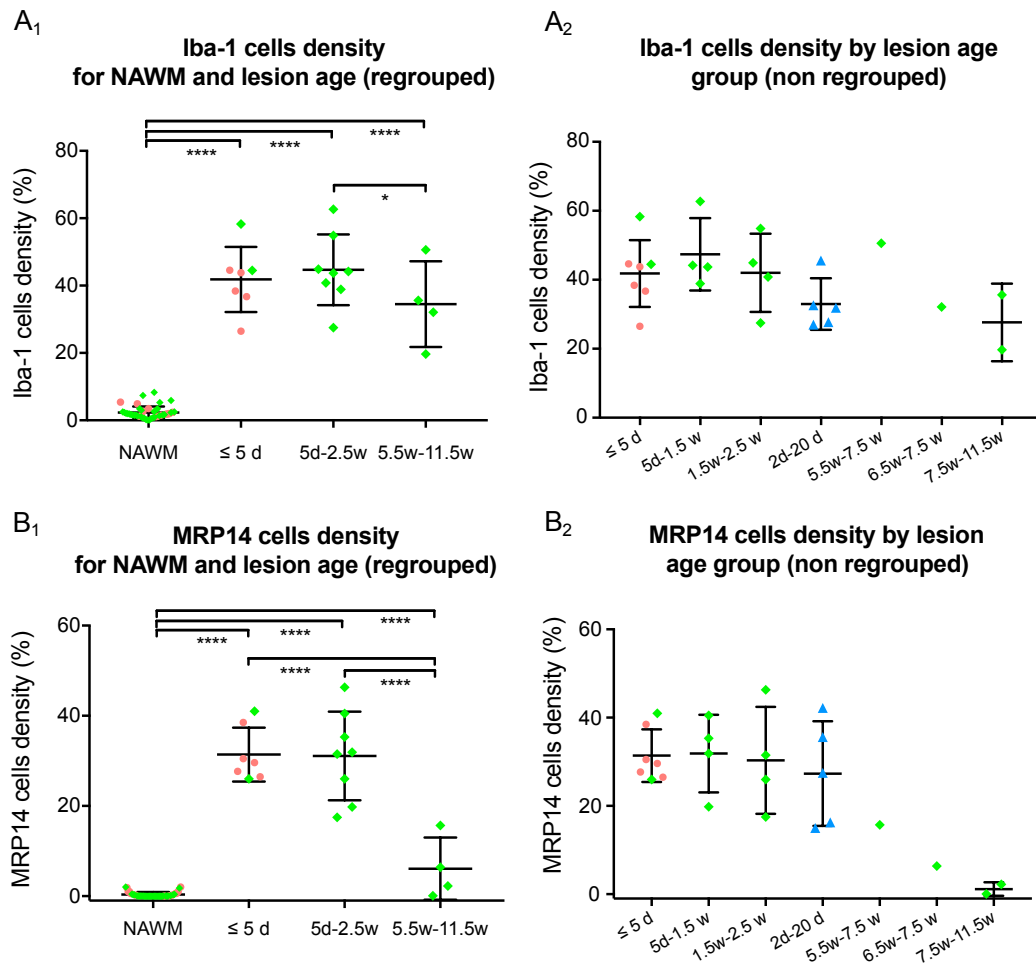


**Figure 5.24:** Quantification of *Iba-1* (A) and *MRP14* (B) inflammatory cells density for the 18 selected lesions by lesion age categories. Mean and standard deviation are shown. Each dot corresponds to an individual lesion, colored by animal (red: M#1, green: M#2, blue: M#3). *A<sub>1</sub>* and *B<sub>1</sub>* correspond to the lesion age regrouped in four categories with the normal appearing white matter (NAWM) provided for comparison. *A<sub>2</sub>* and *B<sub>2</sub>* correspond to the raw lesion age groups that better highlights the trend for animal M#2. \*  $p < 0.05$ , \*\*\*\*  $p < 0.0001$

## 5.4 Discussions

This study characterizes, for the first time, the spatiotemporal evolution of spinal cord lesions in the marmoset EAE model. By acquiring serial in vivo MRI of the entire spinal cord, the following observations can be made: (1) focal lesions tend to appear early in the thoracic and lumbar levels, with the rate of new focal lesions increasing toward the end of the disease; (2) subpial lesions tend to appear early in any of the three levels of the spinal cord; (3) spinal cord lesions experience early demyelination, with severe inflammation leading to complete demyelination within a few weeks; and (4) worsening of the disability scores correlates with the overall increase in spinal cord lesions. These observations highlight the prominent role played by spinal cord lesions during the disease development of this nonhuman primate model of MS, as further discussed below.

The focal lesions detected in this longitudinal study appeared first in the thoracic and lumbar levels, with an increased rate of new focal lesions toward the end of the disease. By the end of the experiment, two-thirds of the focal lesions were located at the thoracic level. In this study, the cervical level was the least affected by focal lesions, whereas in MS the cervical cord is a site of predilection for focal lesions. There is a good agreement between studies demonstrating that focal lesions are twice as likely to be found at the cervical level compared to the thoraco-lumbar levels (Oppenheimer, 1978; Bot et al., 2002, 2004; Galler et al., 2016; Alcaide-Leon et al., 2016). The small number of animals in our cohort could possibly be the reason for this discrepancy. Another reason for this difference could be the disease duration. Actually, our previous postmortem study described in Chapter 3 (Lefeuvre et al., 2019) reported a higher proportion of cervical cord lesions (40% cervical compared to 60% thoraco-lumbar) in animals with longer disease duration (average of 113 days compared to 44 days in this in vivo study). It is also possible that biological differences between this induced model and sporadic MS may impact localization of SC lesions, although a biological explanation for this is currently lacking.

For the first time, we provided the pathological characteristics of spinal cord lesions regarding their age based on in vivo serial MRIs. Like Maggi et al. (2014), we described three main categories of lesions (early acute, acute and subacute) defined by their age on the MRI and the presence of inflammatory cells (Iba-1+ activated microglia and macrophages, and the blood-derived MRP14+ early activated macrophages) and the extend of demyelination (the myelin lipid LFB-PAS and myelin protein PLP).

Spinal cord lesions presented similar stages of demyelination and inflammation compared to the marmoset EAE brain lesions (Maggi et al., 2014; Lee et al., 2018): at first, an intense inflammation defined by Iba-1+ and MRP14+ cells was found through the entire lesion associated with an ongoing demyelination, followed quickly by a complete demyelination of the lesion center with signs of ongoing demyelination at the lesion edge still

associated with a dense inflammation (both Iba-1+ and MRP14+ cells). Finally, complete demyelination of the entire lesional area with a decreased of inflammatory cells was observed.

However, we found variability within each age groups compared to the pathological pattern described in the brain of this marmoset EAE model. A very early stage of demyelination was characterized with a prominent edema associated with disrupted myelin sheets or a limited area of demyelination adjacent to the perivascular space or the leptomeningeal space. The inflammation component seems to sustain longer within the spinal cord lesions. Indeed, brain lesions classified 1 to 5 weeks old displayed MRP14+ cells only at the lesion edge whereas, in our cohort for a similar age group, MRP14+ cells were still found through the entire lesion. Only lesions older than 5.5 weeks presented a change in density of MRP14+ cells. It could also suggest a different timing in the development of spinal cord lesions, with more persistent inflammation. We could speculate the repair mechanisms in the spinal cord may be also different from the brain. It is also possible that we selected more diverse lesion types and shapes for the histopathology analysis compared to the brain study from (Maggi et al., 2014). In our study we did not observe the perivascular inflammatory nodules without demyelination described by Maggi et al. (2014) which was suggested to be the earliest stage of lesion formation in the brain.

In fact, we also observed that the lesion size was an important factor to take into account for this heterogeneity within the same age groups. The volume analysis performed on a subset of in vivo lesions was able to distinguish two main groups of focal lesions. The small lesions visualized on a single MRI slice remained relatively stable from their appearance until the terminal MRI. The large lesions visualized on multiple MRI slices kept enlarging over time. Compared to the brain EAE lesions described in this model, none of the spinal cord lesions detected in vivo decreased in size. This finding is in favor with a slower progression and a more sustained inflammation process.

From a histopathology perspective, the small focal lesions usually presented a sleeve-like or ovoid shape, and quickly reached the chronic active stage of demyelination with lower inflammatory MRP14+ density, whereas larger lesions showed ongoing demyelination with presence of early activated inflammatory MRP14+. The smaller lesions were all located within the lateral column and tended to follow the curvature of a vein (Figure 5.19B) or to display a radial vein running centrally from the tip of the ventral horn to the cord surface (Figure 5.8, lesions 3-5). The large focal lesions located within the posterior column appeared symmetrical, centered around a larger blood vessel. The largest lesions located within the lateral column displayed several veins or venules. For each of them, the area surrounding the vasculature corresponded to the area of greatest demyelination assessed by loss of PLP myelin protein.

The subpial lesions detected in this longitudinal study appeared early in the disease

course by affecting all the three levels of the spinal cord. This finding highlights a main difference with a mice EAE model. [Shrestha et al. \(2017\)](#) investigated for the first time the progression of subpial pathology in mice EAE, actively immunized with MOG(35-55), using confocal microscopy techniques on postmortem SC tissues collected at various time point. They showed an ascending progression of the subpial pathology from lumbar cord to cervical cord, demonstrating that inflammation does not occur simultaneously in all three levels. However, as already mentioned in the discussion of chapter 3, the subpial lesions in MS have been underinvestigated both by imaging and histopathology techniques.

Regarding the disease course evolution, animals with an aggressive disease course (M#1 and M#3) had faster progression (larger proportion of the affected level) and more severe extent (higher reduction of CSA percentage relative to baseline) of their subpial lesions. In general, the thickness of the subpial lesions was larger at the thoracic and lumbar levels (Figure 5.16). These results suggest a worsening of the subpial pathology at the caudal levels of the cord, where the degree of worsening may vary between animals (i.e., in shorter aggressive disease, the mid-thoracic level is severely affected, whereas in longer progressive disease, only the lumbar severely affected). Interestingly, the progressive forms of MS have been associated with higher disability and different types of pathology compared to the RRMS. The patients with progressive forms usually present an increased meningeal inflammation in the brain with a higher number of cortical lesions ([Kutzelnigg et al., 2005](#)). The spinal cord also shows similar pathological findings with a higher degree of meningeal inflammation, which has been associated with diffuse axonal loss in the parenchyma. Interestingly, a histopathology postmortem study from [Magliozzi et al. \(2010\)](#) found that a subset of SPMS patients presented ectopic meningeal B-cell follicle-like structures and was associated with more aggressive disease course, more extensive subpial cortical demyelination and cortical atrophy compared to the SPMS patient without the ectopic lymphoid follicle-like structure. Regarding an MRI in vivo study, [Kearney et al. \(2014\)](#) found higher MTR outer cord abnormalities in the PPMS and SPMS compared to the RRMS. [Lucchinetti et al. \(2011\)](#) observed that meningeal inflammation already occurred in a cohort of early-stage MS and seemed to precede appearance of inflammatory white matter lesions. Investigating the difference of lesion types upon the disease course in the marmoset EAE may be an important tool to understand the disease mechanisms between MS subtypes. It also could be used as a prognosis tool for future MS studies.

Subpial lesions appeared first along the anterior median fissure (AMF), and only by the end of the disease were visible along the entire cord edge (corresponding to a decrease in CSA). Subpial lesions presented similar histopathological patterns as age-matched focal lesions. However, instead of a perivenular configuration seen in focal lesions, it has been suggested that the meningeal inflammation may drive the development of the subpial lesions.

Another major finding of this study was the strong correlation between the total number of focal lesions and the disability scores, contrasting with the weak correlations observed in human studies (Nijeholt et al., 1998; Weier et al., 2012). When performing the analysis at the cord level, a significant correlation was obtained at the thoracic level for the number of focal lesions. This is in line with a previous study where a similar analysis was performed in a relapsing-remitting MS cohort (Stankiewicz et al., 2009). Therefore, we can hypothesize that thoracic and lumbar spinal cord lesions may also have a strong association with the progression of the disability in MS patients. These findings highlight the value of imaging the entire spinal cord length of MS patients with high-resolution.

EAE and mEDSS scores were useful to assess the overall severity of the disease, whereas the functional system scoring was better to explain the specific disabilities caused by the lesions affecting the different spinal cord tracts. In our study, the posterior column was strongly correlated with weakness ( $r = 0.92$ ,  $p \leq .001$ ) and bladder dysfunction ( $r = 0.83$ ,  $p \leq .01$ ), whereas a weaker correlation was found for ataxia ( $r = 0.62$ ,  $p \leq .05$ ). Although we expected the lateral column, which contains the corticospinal tracts responsible for voluntary muscle control, to have the highest correlation, we found instead a weak relation ( $r = 0.34$ ,  $p \leq 0.05$ ) between the lateral columns and weakness. However, the analysis was not performed by tract but by entire column instead.

While these correlations are surprisingly high, they reflect data from only a few animals. In this setting, qualitative descriptions are often more relevant. Indeed, at the individual level, a major increase in EAE score mEDSS coincided with an overall increase of spinal cord lesions, whereas the period of symptom stabilization corresponded to a relatively stable progression of the SC lesions (Figure 5.5).

There were several limitations in this study. It was not possible to provide an exact volume of the focal lesions due to the existence of a significant gap (1.5 mm) between MRI slices. This slice gap might have also led to an underestimation of the total number of lesions but was necessary because of the limitations of the acquisition time. CSA measurement was used as a surrogate marker for the subpial lesions, however CSA could also be affected by other pathology (e.g., atrophy, swelling). This might explain the disconnect between the severe subpial pathology observed at the lower lumbar level on terminal MRI (and confirmed by postmortem MRI) and the relatively small (between -8% and -16%) changes in the CSA measurements (see figure 5.16). This discrepancy could also be caused by the lack of consistency in the slice position, or by the difficulty to measure accurately the cross section of the smallest portion of the spinal cord. Some of the symptoms could not be associated to MRI changes due to the difficulty to image certain areas of the spinal cord. For example, the tail atonia and bladder dysfunctions observed in the animals involved the sacrococcygeal spinal levels which are extremely difficult to image in vivo due to their very small dimensions (<1.5 mm). Finally, the most obvious limitation of this study is the

small number of animals (n=3) that completed this pilot study. Therefore, our results are primarily observational and may not be generalized at this stage.

## **5.5 Conclusion**

In this study, we characterized for the first time the spatiotemporal evolution of spinal cord lesions in the marmoset model with EAE. Using high-quality in vivo serial MRI, we found that both focal and subpial lesions appeared early in the disease course and progressed simultaneously throughout the entire spinal cord, with thoracic and lumbar levels being more damaged. These results further highlight the resemblance of this marmoset EAE model to MS, and its relevance to investigate the development of spinal cord pathology.

# CHAPTER 6

## DISCUSSION AND FUTURE PERSPECTIVES

### **This Chapter contains:**

6.1	Summary . . . . .	141
6.2	Current challenges and proposed solutions . . . . .	142
6.2.1	Difficult detection of early subpial lesion . . . . .	142
6.2.2	Poor reliability for lesion volume/CSA measurements . . . . .	142
6.2.3	Lack of specific MRI information . . . . .	144
6.2.4	Long acquisition times of in vivo MRI sequences . . . . .	146
6.2.5	Incomplete coverage of the CNS . . . . .	147
6.2.6	Tedious manual segmentation . . . . .	147
6.2.7	Variable, and sometime very short, disease course . . . . .	148
6.3	Perspectives . . . . .	150

---

In this last chapter, I summarize the main findings of my thesis, highlight the residual challenges of our studies and propose solutions to overcome them. Finally, I provide some thoughts for future research on this topic.



## 6.1 Summary

For the first time, the spinal cord of the nonhuman primate model of MS, the marmoset EAE, has been thoroughly investigated using MRI. The main objective of this project was to characterize *in vivo* the spatial distribution and temporal evolution of the spinal cord lesions in this model.

To achieve this objective, I first developed a new postmortem MRI setup to acquire high quality images efficiently. Using 3D-printing technology, a spinal cord holder was designed in order to insert and align the spinal cord tissues for overnight scanning. Using this novel approach, two main types of tissue damage in the spinal cord of marmoset EAE were identified on the T2\*-w GRE images: focal lesions within the WM, and subpial WM lesions adjacent to the subarachnoid space. A quantitative analysis of the lesion distribution showed that focal and subpial lesions were found throughout the entire spinal cord length, with high variability across animals. Focal lesions displayed high similarity with MS spinal cord lesions in terms of lesion location and lesion shape. Subpial lesions showed variable thickness across animals. Using MRI-guided histopathology, I characterized these MRI findings pathologically and found variable degrees of demyelination and inflammatory cell density inside these lesions.

After this postmortem study, I focus creating a 12-channel receive-only phased array coil that covers the entire spine of the animal. Working closely with Dr. Afonso Silva's laboratory, I successfully implemented for the first time a customized experimental MRI setup for robustly imaging *in vivo* the entire spinal cord of the marmoset. By using an anatomical coil former that stabilizes the animal's body in a supine position, I established an imaging protocol of the entire spinal cord that provides high-quality images in a single MRI session under 4 hours using an axial proton density-weighted TSE sequence combined with respiratory gating.

Finally, I applied the *in vivo* MRI protocol on several animals immunized with EAE. I assessed for the first time the spatiotemporal evolution of EAE spinal cord lesions in this model. I found that both types of lesions appeared early in the disease course and worsened over the disease course. While focal lesions appeared first in the thoracic and lumbar cord, subpial lesions affected the cervical level as well. With a total of only three EAE animals, group analysis is inherently limited, so my analysis focused primarily on individual animals and provided quantitative measures for selected lesions. The volume analysis for focal lesions showed that lesions either continued to enlarge over time or displayed stable volume from their first appearance. Using the cross-sectional area of the normal-appearing cord to assess indirectly the subpial damage, I found a decreased area (corresponding to increased subpial damage) toward the caudal spinal cord. From a clinical perspective, I was able to find that a relapse, measured by a sharp increase in the EAE and mEDSS scores, was

associated with an overall increase of SC lesion load. Regarding the histopathology, I found similar stages of demyelination and inflammation compared to brain lesions in the same model. However, my preliminary observation shows there is more heterogeneity within each lesion age group in the spinal cord, suggesting that the timing of progression of spinal cord lesions may be different from in the brain.

## 6.2 Current challenges and proposed solutions

Throughout this thesis, I encountered several challenges which I will discuss below:

### 6.2.1 Difficult detection of early subpial lesion

The use of PD-w contrast did not allow a clear visualization of the edge of the spinal cord on all slices due to bright signal coming from the surrounding voxels, primarily composed of CSF and ligaments. This bright signal rendered the detection of subpial lesions difficult at their earliest stages of development. To better visualize the cord edge, MRI sequences that provide cancellation of the CSF signal could be used in the future, such as MP2RAGE, which I applied in a small cohort of MS patients during my thesis (Lefevre et al., 2017). As already introduced in Chapter 1 (Figure 1.21), MP2RAGE at 3T provides high contrast between the normal cord and the CSF. As shown in Figure 6.1, 3T MP2RAGE shows an excellent delineation of the cord edge and clear visualization of lesions located at the cord edge compared with T2\*-w MEDIC.

### 6.2.2 Poor reliability for lesion volume/CSA measurements

The slice gap used in the 2D PD-w axial acquisition was essential to collect in vivo images of the entire length of the spinal cord. However, this slice gap (1.5 mm) prevented exact measurement of lesion volumes. In addition to the slice gap issue, some image artifacts were also observed on the in vivo PD-w axial images (Figure 6.2), which probably affected the reliability of our CSA measurements; these include:

- bright signal at the posterior cord edge colocalizing with the junction of ligaments;
- image distortions due to important differences in magnetic susceptibility at the junctions with the nerve roots and intervertebral cartilages, or due to failed  $B_0$  shimming;
- incorrect alignment of the spinal cord, which emphasized partial volume averaging and produced cord shape distortions.

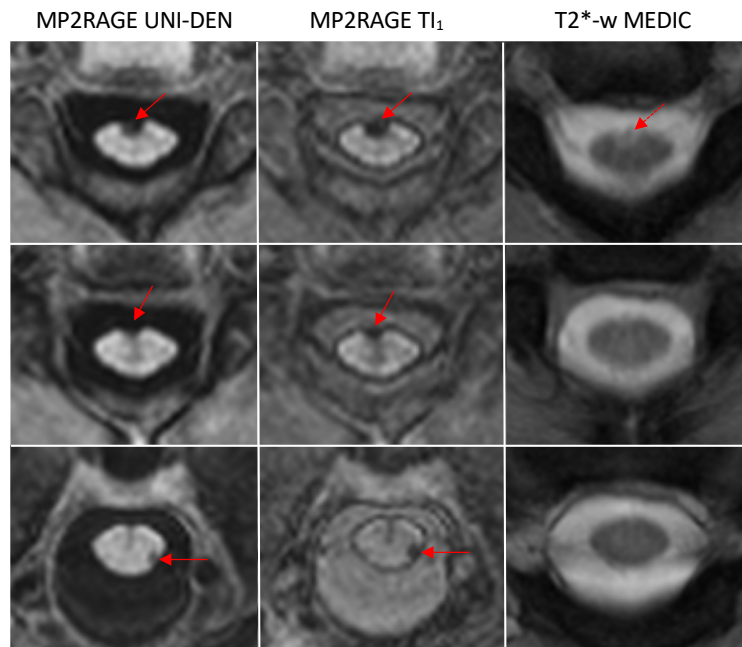


**Figure 6.1:** Improved visualization of spinal cord lesions located at the cord edge using MP2RAGE UNI-DEN as compared to T2\*-w MEDIC sequence. The first inversion time of MP2RAGE ( $TI_1 = 900\text{ms}$ ) nulls the signal from lesions making them appear hypointense compared to the CSF and normal cord tissues. The second inversion time ( $TI_2 = 1440\text{ms}$ ) was chosen to cancel CSF signal (images not shown here). The smaller lesions (second and third rows) present a clear delineation on MP2RAGE, whereas they are not visualized on T2\*-w MEDIC sequence

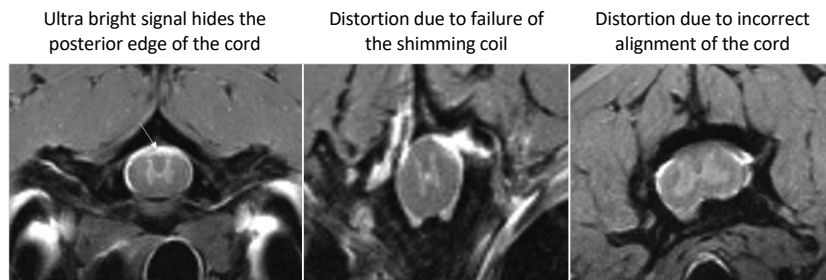


**Figure 6.2:** Types of artifacts seen on in vivo PD-w TSE sequence affecting cross-sectional area measurements. Images acquired in marmosets with EAE

To obtain a more reliable CSA measurement, the MP2RAGE sequence may be useful again. Indeed, MP2RAGE UNI-DEN images display reduced motion artifacts related to breathing and cardiac pulsations, but also an increased fat suppression (Figure 6.3). As a consequence, a more homogeneous signal intensity can be observed across the human spinal cord, and a more consistent image quality can be obtained across serial in vivo MRI images, which could be particularly useful for serial imaging of the marmoset spinal cord.

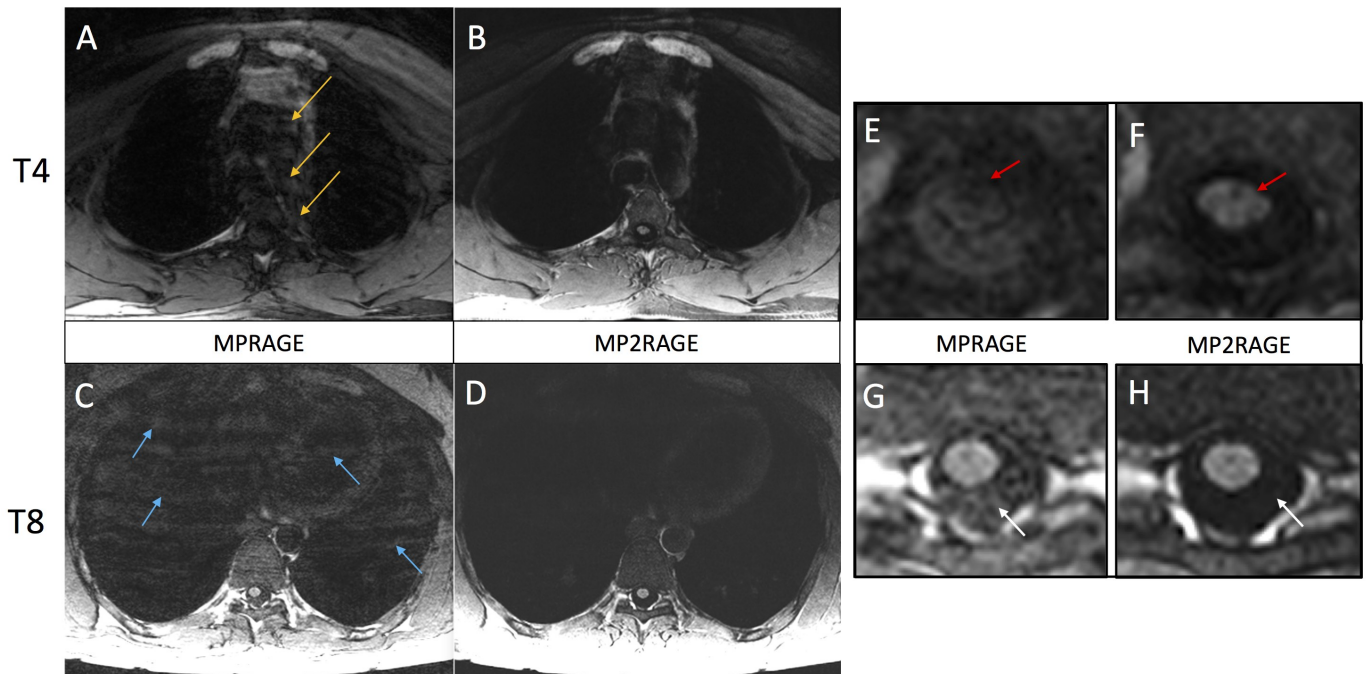


**Figure 6.3:** Comparison of the image quality at 3T between MPRAGE (A, C with their respective magnified view E, G) and MP2RAGE UNI-DEN (B, D with their respective magnified view F,H) at the T4 level (A-B) and T8 level (C-D) from a 32-y.o. man with CIS. The cardiac pulsation (yellow arrows) and respiratory motion (blue arrows) are present on MPRAGE, but are not on MP2RAGE. The improvements in the image quality of MP2RAGE allow a better homogeneity of the signal with an increased visualization of the cord edge (red arrows) and more contrast of the surrounding tissues especially between the cord and CSF (white arrows).

### 6.2.3 Lack of specific MRI information

In this thesis, PD-w contrast was the only contrast acquired during the in vivo scanning in order to obtain the best image quality and best sensitivity to pathology (based on the previous experience of the laboratory in imaging brain lesions in the marmoset). However, this choice came at the cost of limited MRI information. Although extremely sensitive, PD-w contrast is not specific to the pathological processes underlying the formation of lesions. For example, an EAE lesion with prominent edema and early stage demyelination can display a signal intensity similar to an EAE lesion with complete demyelination.

In future SC studies, a multi-contrast protocol could be implemented (similar to that used in marmoset brain imaging). For example, T1-w contrast acquired post-gadolinium would help differentiate acute lesions with edema from chronic demyelinated lesions. T2\*-w contrast may also be extremely useful for detecting the perivenular configuration of the focal lesions, as has been shown in the brain of the marmoset EAE model (Gaitán et al., 2014). The increased susceptibility effect of T2\* weighting can also reflect the accumulation or redistribution of iron, which has been associated with oxidative stress in

marmoset EAE brain lesions (Dunham et al., 2017). Moreover, axial T2\*-w multi-echo GRE images have been shown to provide higher sensitivity compared to T2-w TSE images for lesion detection, with better conspicuity (Martin et al., 2012; Ozturk et al., 2013). However, applying T2\*-w MEDIC in the thoracic cord can be extremely challenging due in part to the increased respiratory-induced magnetic field variations from breathing. We encountered similar challenges in our marmosets when trying to image the spinal cord with T2\*-w GRE sequences. As shown in Figure 6.4, T2\*-w GRE images obtained in vivo in a healthy marmoset showed promising contrast between GM and WM tissues, but suffered from prominent signal losses despite using advanced  $B_0$  shimming routines.

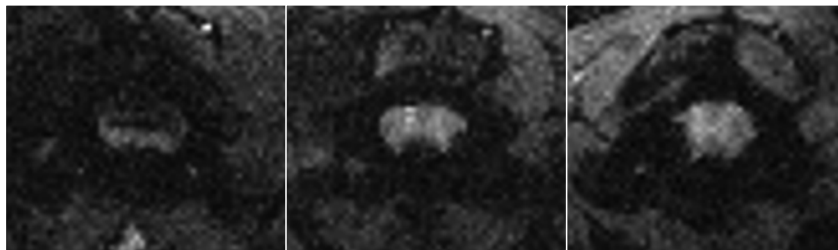


**Figure 6.4:** T2\*-weighted GRE sequence acquired at the cervical cord in a healthy marmoset. Note that this sequence was acquired using the initial 4-element coil, i.e with the previous 4-element coil. MRI parameters: TR/TE/FA= 1000ms/ 22ms/ 70 °; NA=4; resolution of 0.25 x 0.25 x 1.2 mm<sup>3</sup>

Quantitative MRI techniques, such diffusion tensor imaging (DTI), which measures the microscopic motion of water molecules, could be also useful. Indeed, the microscopic architecture of the well-organized longitudinal axons in the spinal cord is an advantage for diffusion-based techniques. Notably, DTI can provide a map of the WM nerve tracts using tractography. DTI has been successfully applied in vivo in a model of spinal cord injury (hemisection) in the common marmoset ((Fujiyoshi et al., 2007). In this work, the authors showed that T2-w MRI displayed a high signal intensity changes only at the level of injury, whereas DTI revealed disruption of the longitudinal axons not only at the injury level but also caudal to the injury, consistent with the histopathology. Furthermore, the authors were able to depict specific SC tract pathways using in vivo diffusion tensor tractography (DTT), such as the corticospinal tracts (lateral CST, anterior CST), spinothalamic tracts, and dorsal column-medial lemniscus.

However, many studies have suggested that DTI also lacks specificity regarding demyelination and axonal loss, which both contribute to the signal changes (Klawiter et al., 2011). It also suffers from a loss of accuracy when inflammation is present (Schmierer et al., 2008) and when crossing fibers exist (Wheeler-Kingshott and Cercignani, 2009). To overcome these issues, diffusion basis spectrum imaging (DBSI) was proposed (Wang et al., 2011, 2015) and shown to improve the quantification of the axial and radial diffusivity

(compared to DTI) by distinguishing axonal loss from myelin content. Additionally, inflammation can be assessed indirectly by the restricted isotropic diffusion fraction which reflects the cellularity and can be differentiated from the extracellular vasogenic edema component measured by the non-restricted isotropic diffusion fraction (Chiang et al., 2014). This technique has been applied on three postmortem MS cervical cords (Wang et al., 2015), which resulted in a good correlation between DBSI metrics and histopathology. Another important finding from Wang et al. (2015) was the robustness of the DBSI technique against CSF contamination, which would be very useful for the subpial area of the spinal cord surrounded by CSF.

#### 6.2.4 Long acquisition times of in vivo MRI sequences

A major challenge of the in vivo “whole cord” protocol was the very long acquisition of the 2D multi-slice PD-w TSE anatomical sequence (25 minutes per sequence, for a total acquisition time of approximately 3 hours). A faster imaging protocol would be extremely useful, especially for allowing full coverage of the spine length without gap between successive slices. One way to achieve this could be to use 3D TSE sequences with variable flip angle. Initially implemented to address the issue of high RF deposition and signal degradation due to relaxation (Busse et al., 2006), the variable flip angle RARE (vfaRARE) imaging technique has shown promising results when applied for the first time in an in vivo pre-clinical setting. In this pilot study, acquired images of the brain and spinal cord of rats 3–4 times faster than using a the corresponding uniform flip angle. The 3D acquisition implemented in this pilot study would be a good solution to image the marmoset spinal cord with isotropic resolution.

Parallel imaging (Deshmane et al., 2012) could also be extremely useful and practical to implement using the phased-array receive coils described in this thesis. With this approach, the acquisition time is reduced by acquiring only a portion of k-space in the phase-encoding direction, which should also coincide with the direction of the coil sensitivity variations. This acceleration technique can be applied to almost any pulse sequences and is now supported by Bruker (Paravision 6.1). In addition to parallel imaging, the simultaneous multi-slice imaging technique (SMS, also called multiband excitation) can drastically reduce the imaging time by acquiring several slices simultaneously using complex RF-pulses (Barth et al., 2016). This technique has been mostly applied for functional MRI and diffusion, although recently, SMS techniques demonstrated successful results for brain imaging using TSE sequences with reduction of the RF power deposition and no SNR penalty (Norris et al., 2014; Gagoski et al., 2015).

### 6.2.5 Incomplete coverage of the CNS

In this thesis, serial imaging of both the spinal cord and brain of the marmosets with EAE could not be performed due to the long acquisition time of our spinal cord protocol. If *in vivo* brain imaging was routinely performed in addition to spinal cord imaging, it might have been possible to differentiate the spatiotemporal contribution of each component of the CNS (i.e. WM brain, cortex, deep gray mater, brainstem, GM and WM spinal cord) to the clinical symptoms observed during the disease of our animals. The development of a brain-spinal cord combined imaging setup should be the next technical step for our marmoset EAE studies. A setup using the current coils (8-element phased-array for brain and our 12-element for spine) could be explored. However, this would require the animal setup from sphinx position (for the brain) to supine position (for the spinal cord). This complicated setup may generate some distress in the animal due to increased manipulation. Another solution could be the creation of a new coil design, which would allow to image both brain and spinal cord without changing the animal position. The new coil design could take inspiration from human imaging setups, which integrate a cervical coil former with the head coil.

### 6.2.6 Tedious manual segmentation

A manual segmentation method was applied in this thesis on focal lesions and CSA measurements. Unfortunately, this method is extremely time-consuming and may be highly variable (intra- as well inter-user variability). Automated segmentation based on deep machine learning has recently shown promising results for the human MS spinal cord, as demonstrated by [Gros et al. \(2019\)](#). In this work, the authors (including a minor contribution from our lab) used an approach based on Convolutional Neural Networks (CNN) to obtain a fully automated framework that segments both the spinal cord and MS lesions. However, successfully training the CNN algorithm was challenging due to the high variability of MS spinal cord lesions in terms of shape, location, and size, as well as the requirement for large amounts of training data (manual segmentations). This variability was also observed in the spinal cord of the marmoset EAE model. Nonetheless, the imaging dataset acquired on our marmoset EAE is homogeneous (same scanner, same MRI acquisition protocol) relative to that obtained from multi-site human studies. Therefore, through a collaboration with Julien Cohen-Adad's laboratory (NeuroPoly, Ecole Polytechnique, Universite de Montreal), an open-source pipeline was developed and implemented for our marmoset spinal cord dataset using a supervised neural network. The architecture used for the network is a simplified version of the original U-net method ([Ronneberger et al., 2015](#)) which has demonstrated to achieve good performances in the field of biomedical images segmentation. The advantages of the CNN with U-net architecture are the robustness with diverse image

appearance and the reduction of the amount of labeled data necessary for training. Figure 6.5 illustrates preliminary segmentation results obtained with this approach.

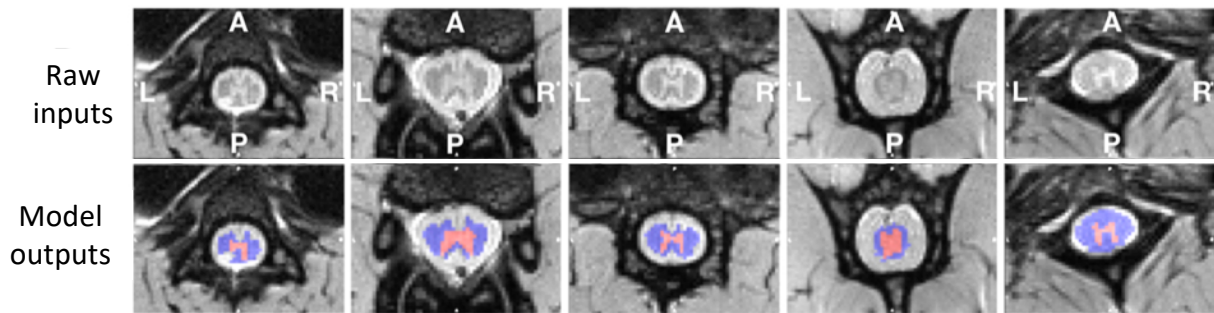


**Figure 6.5:** First results of the automated segmentation using machine-learning (CNN U-net model) performed on the spinal cord of marmosets EAE. Blue: NAWM; red: GM. The model provides a segmentation of the normal appearing white matter (blue) and gray matter (red) to indirectly assess the lesion load but is not yet capable of differentiating subpial lesions from CSF (a task that would be very difficult with currently available image contrasts) (Figure adapted from Paugam et al. (2019)).

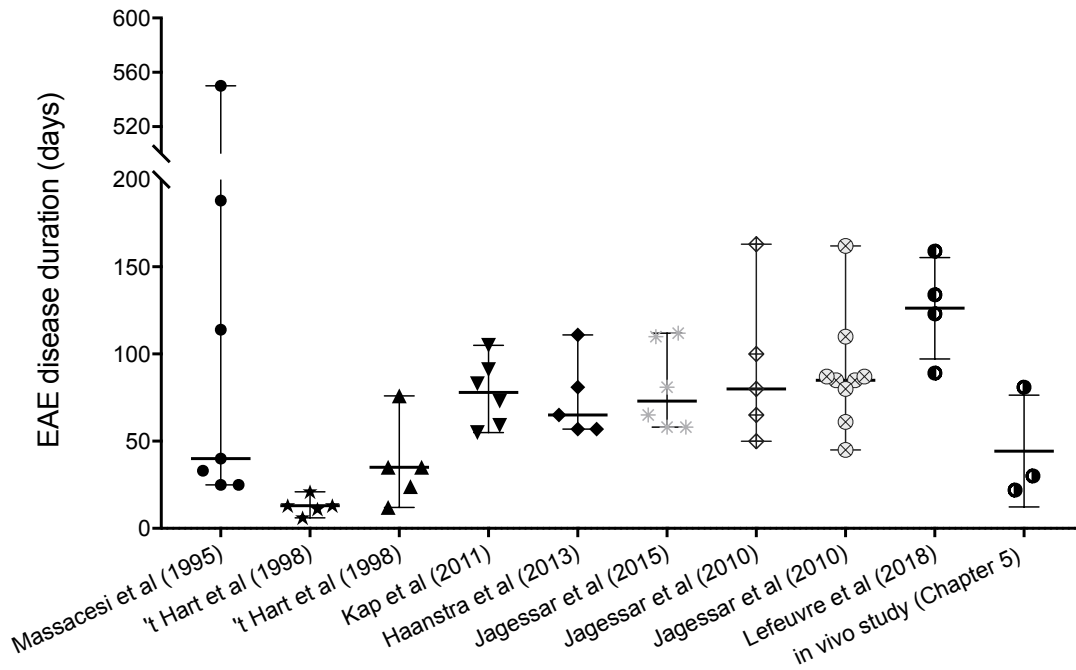
### 6.2.7 Variable, and sometime very short, disease course

The disease course was highly variable across the animals studied in this thesis (see Figure 6.6). Notably, two animals included in our in vivo longitudinal study (Chapter 5) had a very short disease course. Over the span of a single week, these two animals developed their first clinical symptoms and progressed to severe paraplegia, preventing serial imaging. It would be extremely useful to be able to tune the marmoset EAE model to consistently obtain a disease duration long enough to collect sufficient MRI time points for studying the evolution of spinal cord lesions. The figure 6.6 recapitulates the different disease duration collected from the literature on marmoset EAE studies with their respective immunization protocols.

One potential source of variability in clinical course is the use of human white matter homogenate (WMH) mixed with the complete Freund’s adjuvant (CFA) that includes heat-killed Mycobacterium tuberculosis (MT). This type of induction is highly heterogeneous in terms of disease duration, regardless of lab. This variability may be explained by various factors. A first technical challenge may be related to the preparation of the WMH-CFA solution, which requires numerous steps and manipulations, potentially resulting in volume loss due to the high viscosity of the substance. Therefore this preparation can introduce variability regarding the final ratio WM:CFA injected. Some of the variability may also come from the genetic and environmental heterogeneity across marmosets. This diversity is a well-known strength of this model but also can be a major limitation for such small animal cohorts.



Furthermore, the type of immunogen used to induce EAE seems to be an important factor for the disease duration. WMH-CFA tend to produce a greater number of animals with relatively short disease course (less than a month) compared to the rhMOG peptides, which seems to consistently display a life expectancy above 45 days. Moreover, the use of the CFA with rhMOG (initially intended to boost the immunogenicity) was not associated with a more aggressive disease when compared to the use of IFA (absence of MT).



Studies	Massaccesi et al (1995)	't Hart et al (1998)		Kap et al (2011)	Haanstra et al (2013)	Jagessar et al (2015)	Jagessar et al (2010)		Lefeuvre et al (2018)	in vivo study (chap. 5)
Immunogen type	WMH	WMH		rhMOG (1-125)	rhMOG (1-125)	rhMOG (1-125)	rhMOG (34-56)	rhMOG (34-56 + 74-96)	WMH	WMH
CFA (with concentration) or IFA	CFA	CFA	CFA	CFA	IFA	IFA	IFA	IFA	CFA	CFA
	3 mg/ml	6 mg/ml	0.5 mg/ml	N/A	-	-	-	-	1.8 mg/ml	1.8 mg/ml
Bordetella Pertusis or absent (-)	BP	BP	no BP	no BP	no BP	no BP	no BP	no BP	no BP	no BP

**Figure 6.6:** Summary of the different marmoset EAE models reported in the literature with the disease duration of their respective animal cohort. Disease duration in days with median and range (min-max); one data point per animal. Details of the immunization protocol can be find in the table.

### 6.3 Perspectives

Based on my thesis work, I have identified several areas of research which would deserve future investigation:

- **Perform additional in vivo imaging studies of the marmoset EAE spinal cord.** Due to the very small size of the in vivo study presented here (n=3), we still need more insight into the relationship between spinal cord pathology and clinical findings related to physical disability.

- **Conduct additional investigations of the subpial lesions in MS both by imaging and histopathology.** MRI protocols for better visualization of the edges of the human spinal cord should be explored. There is also a need for better characterizing the existence of subpial demyelination using thorough ex vivo (postmortem) imaging and histopathological approaches;

- **Investigate biological biomarkers in the blood or CSF** (such as the presence of meningeal ectopic follicle-like structures discussed in chapter 5.4) in marmosets with EAE. It remains still unclear why some animals studied here have developed thin subpial lesions, whereas others had severe subpial lesions. Analyzing biological biomarkers in addition to MR imaging findings may help to characterize the differences across animals, such as the aggressiveness of the disease or the severity of the pathological features.

- **Investigate the pattern of enhancement of the focal spinal cord lesions** by injecting gadolinium contrast agent intravenously during spinal cord imaging. This would help to increase our understanding of the lesion development in this model.

- **Initiate research exploring connections between a potential failure of the spinal cord drainage system** (called the glymphatics) **and the development of EAE lesions.** The perivascular space have been suggested to play a role in the transportation of CNS fluid, and clearance of product waste from the parenchyma. A recent study speculated an alteration of the parenchymal CSF circulation in the spinal cord of mice with EAE during the symptomatic stage ([Fournier et al., 2018](#)).

- Finally, **testing therapeutic strategies using the marmoset EAE spinal cord** as a readout could be useful given our preliminary link between spinal cord lesion development and abrupt development of clinical symptoms in these animals. However, this would need to be balanced against variability in the model, which lowers statistical power. Nevertheless, if successful, results from such studies could eventually be translated to MS. Indeed, an advantage of the heterogeneity of our marmoset EAE model is that the efficacy of new therapeutic molecules could be assessed in animals with different degrees of disease severity and types of lesions, potentially mimicking the spectrum of MS patients and introducing the ability to observe the radiological and pathological changes induced by various treatments.

## LIST OF PUBLICATIONS AND CONTRIBUTIONS

### Published articles

- **Jennifer A. Lefevre**, Joseph R. Guy, Nicholas J. Luciano, Seung-Kwon Ha, Emily Leibovitch, Mathieu D. Santin, Afonso C. Silva, Steve Jacobson, Stéphane Lehericy, Daniel S. Reich, Pascal Sati. The spectrum of spinal cord lesions in a primate model of multiple sclerosis (2019) *Multiple Sclerosis Journal* <https://doi.org/10.1177/1352458518822408>
- Francois Paugam, **Jennifer Lefevre**, Christian S. Perone, Charley Gros, Daniel S. Reich, Pascal Sati, Julien Cohen-Adad (2019). Open-source pipeline for multi-class segmentation of the spinal cord with deep learning. *Magnetic Resonance Imaging*. <https://doi.org/10.1016/j.mri.2019.04.009>

### Additional contributions

- Charley Gros, Benjamin De Leener, Atef Badji, [and 48 others, including **Jennifer Lefevre**]. Automatic segmentation of the spinal cord and intramedullary multiple sclerosis lesions with convolutional neural networks (2019). *Neuroimage* <https://doi.org/10.1016/j.neuroimage.2018.09.081>
- Dominique Eden, Charley Gros, Atef Badji, [and 42 others, including **Jennifer Lefevre**]. Spatial distribution of multiple sclerosis lesions in the cervical spinal cord (2019) *Brain* <https://doi.org/10.1093/brain/awy352>
- Nathanael J Lee, Seung-Kwon Ha, Pascal Sati, Martina Absinta, Nicholas J Luciano, **Jennifer A Lefevre**, Matthew K Schindler, Emily C Leibovitch, Jae Kyu Ryu, Mark A Petersen, Afonso C Silva, Steven Jacobson, Katerina Akassoglou, Daniel S Reich. Spatiotemporal distribution of fibrinogen in marmoset and human inflammatory demyelination (2018) *Brain* <https://doi.org/10.1093/brain/awy082>

## Oral presentations - International meetings

- *26<sup>th</sup> Annual Meeting of International Society for Magnetic Resonance in Medicine (ISMRM) 2018 - Paris*

“Spatiotemporal development of spinal cord lesions in a primate model of MS.” **Jennifer Lefeuvre**, Pascal Sati, Cecil Yen, Seung Kwon Ha, Wen-Yang Chiang, Mathieu Santin, Steven Jacobson, Afonso Silva, Stéphane Lehericy, Daniel Reich.

- *25<sup>th</sup> Annual Meeting of ISMRM 2017 - Hawaii*

“Improved visualization of the spinal cord lesions in MS using MP2RAGE at 3T.” **Jennifer Lefeuvre**, Sunil Patil, Gunnar Krueger, Tobias Kober, Stéphane Lehericy, Daniel S. Reich, and Govind Nair.

## Poster presentations - International and local meetings

- *Graduate Partnership Program Symposium 2018 - NIH, Bethesda*

“Spatiotemporal development of spinal cord lesions in a primate model of multiple sclerosis.” **Jennifer Lefeuvre**, Pascal Sati, Cecil Yen, Seung Kwon Ha, Wen-Yang Chiang, Mathieu Santin, Steven Jacobson, Afonso Silva, Stéphane Lehericy, Daniel Reich.

- *Americas Committee for Treatment and Research in Multiple Sclerosis (ACTRIMS) 2017 - Orlando*

“MRI of the Thoracic Spinal Cord in Multiple Sclerosis at 7T.” **Jennifer Lefeuvre**, Qi Duan, Jacco A. de Zwart, Peter van Gelderen, Stéphane Lehericy, Steven Jacobson, Daniel S. Reich, Govind Nair.

“Characterization of Spinal Cord Lesions by MRI in Marmoset EAE.” **Jennifer A. Lefeuvre**, Joseph R. Guy, Nicholas J. Luciano, Seung-Kwon Ha, Emily Leibovitch, Mathieu D. Santin, Afonso C. Silva, Steve Jacobson, Stéphane Lehericy, Daniel S. Reich, Pascal Sati.

- *25<sup>th</sup> Annual Meeting of ISMRM 2017 - Hawaii*

“In vivo Magnetic Resonance Imaging of the Marmoset Spinal Cord at 7T” **Jennifer Lefeuvre**, Wen-Yang Chiang, Cecil Yen, Seung-Kwon Ha, Mathieu Santin, Steven Jacobson, Afonso Silva, Stéphane Lehericy, Daniel Reich, Pascal Sati.

- *24<sup>th</sup> Annual Meeting of ISMRM 2016 - Singapore*

“Ultra-high-resolution postmortem imaging of marmoset EAE spinal cords.” **Jennifer A. Lefeuvre**, Joseph R. Guy, Nicholas J. Luciano, Seung-Kwon Ha, Emily Leibovitch, Mathieu D. Santin, Afonso C. Silva, Steve Jacobson, Stéphane Lehericy, Daniel S. Reich, Pascal Sati.

# APPENDIX A

## ADDITIONAL FIGURES

### A.1 Chapter 3: additional figures

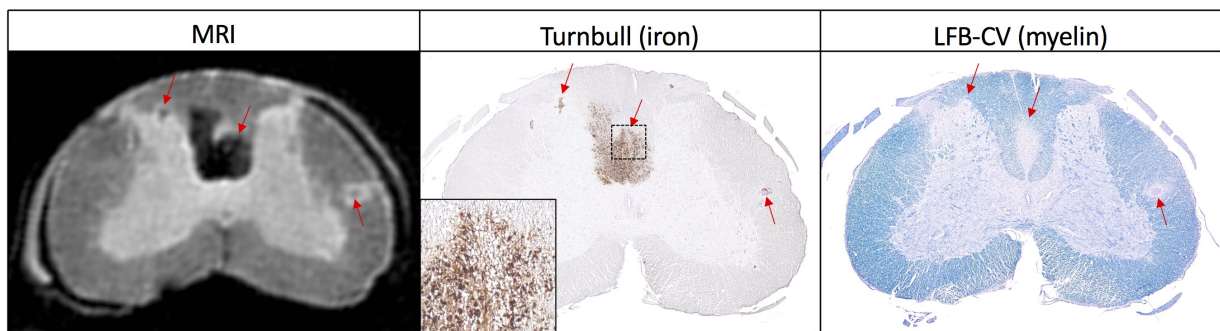


**Figure A.1:** Areas of hemosiderin deposition within lesions of EAE animal M#2. The areas of hypointense signal on the MRI section match perfectly with the positive signal detected on Turnbull staining, which detects iron (red arrows). Note that these hemosiderin deposits may extend beyond areas of abnormal myelin, as shown on the Luxol fast blue-cresyl violet (LFB-CV) stain.

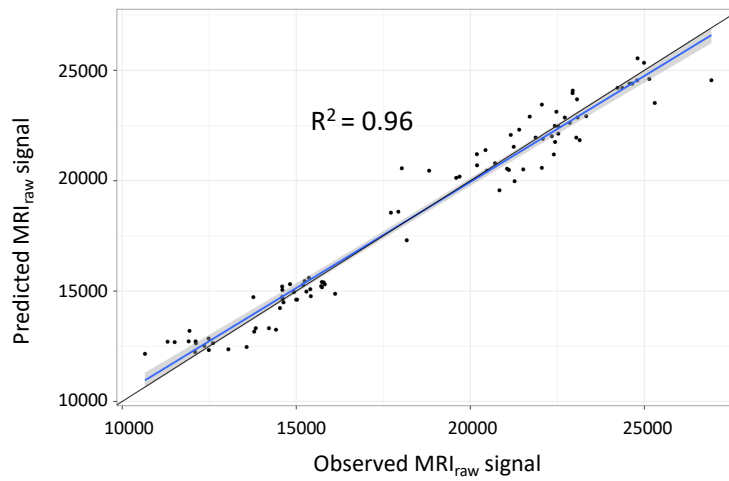


**Figure A.2:** The predicted MRI values from the mixed effects model  $M_2$  versus the observed MRI values, as well as the corresponding regression line (blue). The coefficient of determination,  $R^2$ , is reported within the graphic. The black line corresponds to a perfect model fit with a  $R^2 = 1$ .

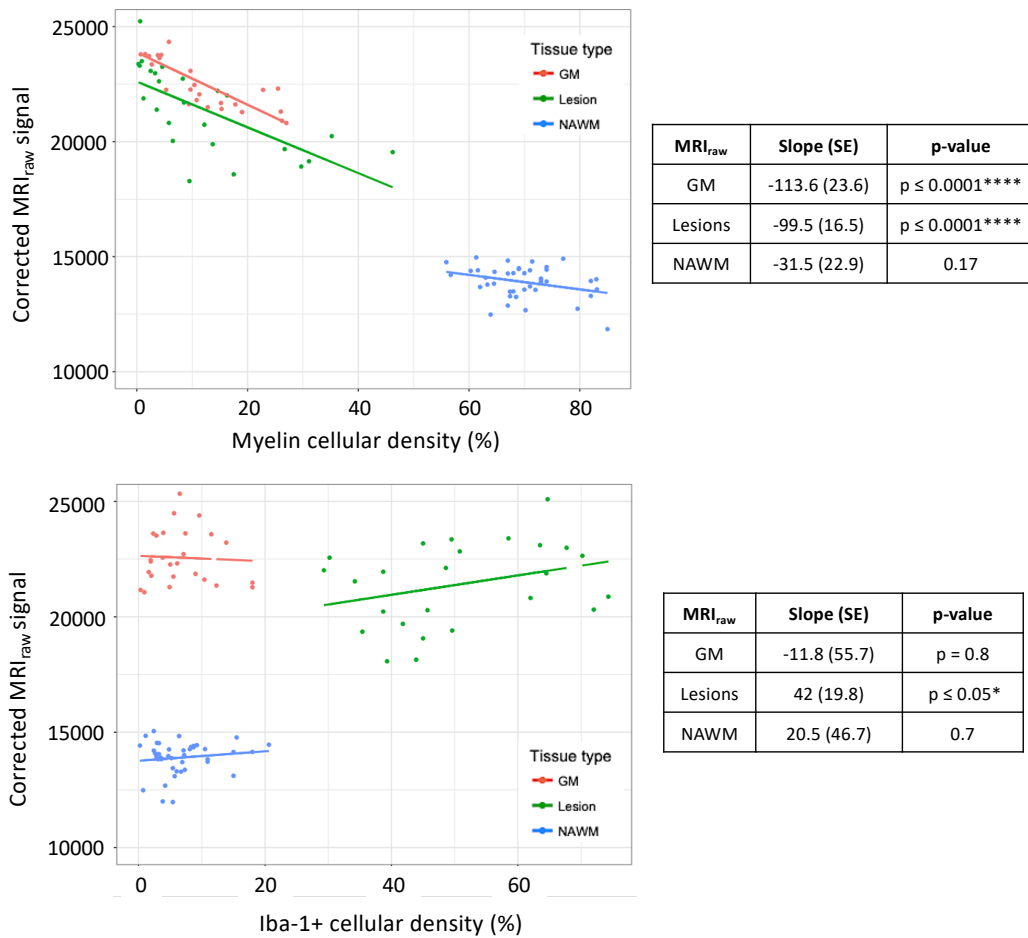


**Figure A.3:** Association between the corrected MRI<sub>raw</sub> signal and the cellular density when applying the linear mixed-effects model  $M_2$ . top: myelin cellular density; bottom: Iba-1+ inflammatory cellular density. The corresponding table includes the statistical results with the mean slope coefficient, the standard error (SE) and p-value for each tissue type.

# APPENDIX B

## ADDITIONAL TABLES

### B.1 Tables for Chapter 3

**Table B.1:** Contrast lesion-to-GM values with the corresponding myelin and inflammatory score for individual lesions. The type of lesions as well their volume (obtained by MRI) are also reported.

Animal	Lesion number	Type of lesions	Volume (mm <sup>3</sup> )	Contrast (lesion-to-GM)	Myelin density score	Inflammatory cells score
M#1	1	focal	3.76	0.94	1	2
M#2	2	focal	0.34	0.92	1	1
M#3	3	focal	0.08	0.97	1	2
M#3	4	focal	0.03	0.94	1	2
M#3	5	focal	0.42	1.07	2	2
M#3	6	focal	1.38	1.02	2	2
M#3	7	focal	0.08	0.98	2	2
M#4	8	focal	0.03	0.96	2	1
M#4	9	focal	0.07	0.98	2	1
M#4	10	subpial	-	1.04	2	2
M#4	11	subpial	-	0.99	2	2

## APPENDIX C

### ADDITIONAL METHODS

#### C.1 Chapter 3: methods for histopathology

**Luxol fast blue staining** Sections were routinely deparaffinized and rehydrated, then incubated at 56C in LFB solution overnight. After washing excess stain with alcohol and distilled water, sections were differentiated in a 0.05% lithium carbonate solution followed by 70% ethyl alcohol. Sections were counterstained with periodic acid shift (PAS) solution.

**Iba-1 immunohistochemistry** Sections were routinely deparaffinized and rehydrated. Antigen retrieval was performed using steamer for 20 minutes in 0.01 M citrate buffer (pH 6). After washing with Tris-buffered saline, endogenous peroxidase activity was blocked with hydrogen peroxide (H<sub>2</sub>O<sub>2</sub>) for 10 min. Prior to primary antibody staining, nonspecific antibody binding was blocked by incubating with skim milk. Sections were incubated with a rabbit polyclonal Iba-1 (1:400; WAKO Pure Chemicals Ind., Osaka, Japan) for one hour at room temperature. After washing three times with Tris-buffered-tween 20, horseradish peroxidase (HRP)-conjugated secondary antibodies (Power vision, Leica, Wetzlar, Germany) were applied for 30 min at room temperature. The final reaction was performed by immersing the sections in a solution of 3,3'-Diaminobenzidine (DAB) (Abcam, Cambridge, UK). The sections were then counterstained with Mayer hematoxylin.

**Turnbull's blue staining** Sections were routinely deparaffinized and rehydrated, then immersed for 90 minutes in an aqueous 2% ammonium sulfide solution (Sigma Aldrich) for detection of total non-heme iron and washed with PBS. Sections were incubated within a solution of 10% potassium ferricyanide + 0.5% HCl during 15 minutes at 37 Celsius. After washing five times with distilled water, the sections were immersed in 0.3% hydrogen peroxide with methanol for 60 more minutes. Tissues were then washed with PBS and iron



---


staining was amplified by DAB (Abcam, Cambridge, UK) until the adequate reaction was visualized and stopped by immersing within distilled water. Sections were counterstained with Mayer hematoxylin.

APPENDIX D

PUBLISHED MANUSCRIPT

## D.1 Article

# The spectrum of spinal cord lesions in a primate model of multiple sclerosis

Jennifer A Lefevre, Joseph R Guy, Nicholas J Luciano, Seung-Kwon Ha, Emily Leibovitch, Mathieu D Santin, Afonso C Silva, Steven Jacobson, Stéphane Lehericy, Daniel S Reich  and Pascal Sati

## Abstract

**Background:** Experimental autoimmune encephalomyelitis (EAE) in the common marmoset is a non-human primate model of multiple sclerosis (MS) that shares numerous clinical, radiological, and pathological features with MS. Among the clinical features are motor and sensory deficits that are highly suggestive of spinal cord (SC) damage.

**Objective:** To characterize the extent and nature of SC damage in symptomatic marmosets with EAE using a combined magnetic resonance imaging (MRI) and histopathology approach.

**Materials and Methods:** SC tissues from five animals were scanned using 7T MRI to collect high-resolution ex vivo images. Lesions were segmented and classified based on shape, size, and distribution along the SC. Tissues were processed for histopathological characterization (myelin and microglia/macrophages). Statistical analysis, using linear mixed-effects models, evaluated the association between MRI and histopathology.

**Results:** Marmosets with EAE displayed two types of SC lesions: focal and subpial lesions. Both lesion types were heterogeneous in size and configuration and corresponded to areas of marked demyelination with high density of inflammatory cells. Inside the lesions, the MRI signal was significantly correlated with myelin content ( $p < 0.001$ ).

**Conclusions:** Our findings underscore the relevance of this nonhuman primate EAE model for better understanding mechanisms of MS lesion formation in the SC.

**Keywords:** Multiple sclerosis, spinal cord, EAE, MRI, marmoset

Date received: 21 September 2018; revised: 27 November 2018; accepted: 2 December 2018

## Introduction

Experimental autoimmune encephalomyelitis (EAE) is the most commonly used animal model for studying multiple sclerosis (MS).<sup>1,2</sup> While mouse EAE models are a vital component of preclinical research in MS, the marmoset EAE model has recently gained some attention due to marmosets' genetic and immunological proximity to humans.<sup>3,4</sup> This nonhuman primate model of MS also bears strong pathological and radiological similarities to MS,<sup>5</sup> while still maintaining practicality as a model, making it an excellent system for studying the mechanisms of lesion formation in the brain.<sup>6</sup>

Among the varied clinical symptoms experienced by marmosets with EAE, motor and sensory deficits are

often present, which strongly suggest the presence of demyelinated lesions in the spinal cord (SC). A few histopathological studies have reported the presence of pathology in SC tissues from marmosets with EAE.<sup>3,7–10</sup> However, these studies did not characterize in a comprehensive manner the extent of the SC pathology.

Magnetic resonance imaging (MRI) is a noninvasive and sensitive tool for detecting pathology in the central nervous system (CNS). However, MRI of the SC is challenging, especially in small animals like the common marmoset, due to the extremely small dimensions of the cord. Therefore, we investigated the SC pathology by postmortem MRI, where high signal-to-noise ratio can be obtained to produce high-quality

Multiple Sclerosis Journal

1–10

DOI: 10.1177/  
1352458518822408

© The Author(s), 2019.  
Article reuse guidelines:  
sagepub.com/journals-  
permissions

Correspondence to:

Pascal Sati

Translational Neuroradiology  
Section, National Institute of  
Neurological Disorders and  
Stroke, National Institutes of  
Health, 10 Center Drive MSC  
1400, Building 10 Room  
5C103, Bethesda, MD 20852,  
USA.

satip@ninds.nih.gov

Jennifer A Lefevre

Translational Neuroradiology  
Section, National Institute of  
Neurological Disorders and  
Stroke, National Institutes of  
Health, Bethesda, MD,  
USA/Institut du Cerveau  
et de la Moelle—ICM,  
Centre de NeuroImagerie  
de Recherche—CENIR,  
Sorbonne Universités, Paris,  
France

Joseph R Guy

Nicholas J Luciano

Seung-Kwon Ha

Daniel S Reich

Pascal Sati

Translational Neuroradiology  
Section, National Institute of  
Neurological Disorders and  
Stroke, National Institutes of  
Health, Bethesda, MD, USA

Mathieu D Santin

Stéphane Lehericy

Institut du Cerveau et de

la Moelle—ICM, Centre

de NeuroImagerie de

Recherche—CENIR,

Sorbonne Universités, Paris,

France

Emily Leibovitch

Steven Jacobson

Viral Immunology Section,

National Institute of

Neurological Disorders and

Stroke, National Institutes of

Health, Bethesda, MD, USA

Afonso C Silva

Cerebral Microcirculation

Section, Laboratory of

Functional and Molecular

Imaging, National Institute of

Neurological Disorders and

Stroke, National Institutes of

Health, Bethesda, MD, USA

**Table 1.** Demographic and clinical information of the five marmosets included in this study.

Animal	Immunization	Sex	Age (years)	Disease duration (days)	EAE score at termination	Clinical symptoms
M#1	WMH	M	3.6	134	3	Weight loss, lethargy, ataxia, severe weakness, sensory loss, vision loss
M#2	WMH	F	4.6	159	3	Apathy, tetraparesis, sensory loss, vision loss
M#3	WMH	F	2.9	123	N/A	N/A
M#4	WMH	F	1.5	89	N/A	N/A
M#5	None	F	4.9	–	–	–

WMH: white matter homogenate; M: male; F: female; N/A: not available.  
Note that clinical information for M#3 and M#4 was not tracked over the course of the disease. Disease duration is measured as time from immunization to termination. EAE scores are defined in Kap et al.<sup>13</sup>

and high-resolution images. These ex vivo MRI images can then be used to guide precisely any subsequent tissue sampling for histology and to evaluate pathologically specific areas of the CNS affected by EAE.<sup>11</sup>

In this study, we used an experimental approach combining ex vivo MRI with histopathology, with the goal of characterizing the extent and nature of the pathology affecting the SC in the marmoset model of MS.

## Materials and methods

### EAE induction

All common marmosets (*Callithrix jacchus*) used in this study were housed at the National Institutes of Health (NIH) Intramural Research facilities, in accordance with the standards of the American Association for Accreditation of Laboratory Animal Care and the NINDS Animal Care and Use Committee. Five adult marmosets (mean age=3.5 years (range: 1.5–4.9), four females) were included in this study. Four animals were induced with EAE using white matter (WM) homogenate in complete Freund's adjuvant<sup>12</sup> which in our hands produces a disease that bears strong radiological similarities to MS.<sup>5</sup> The fifth animal was used as a healthy, non-EAE control. Animals were frequently weighed and scored according to an EAE scale based on clinical symptoms.<sup>13</sup> Table 1 provides the demographics and clinical summary of these animals. Once the animals showed paraplegia and/or 20% weight loss, the experiment was terminated by performing transcardial perfusion fixation with cold 4% paraformaldehyde under anesthesia. The spine was removed and stored in 4% neutral buffered formalin.

### MRI acquisition

After extraction and preparation of the SC samples (see Supplemental Figure 1), MRI was performed on a 7T/30cm MRI scanner (Bruker BioSpin Corp., Ettlingen, Germany) equipped with a 15cm gradient set of 450 mT/m strength (Resonance Research Inc., Billerica, MA, USA). A proton-only transmit–receive volume coil (25mm inner diameter; Bruker) was used for imaging the tissue samples, which were loaded in plastic tubes. During each scanning session, a three-dimensional (3D)  $T_2^*$ -weighted gradient-echo sequence with an in-plane resolution of 70  $\mu\text{m}$  and a slice thickness of 200  $\mu\text{m}$  was acquired four times consecutively for a total acquisition time of 12 hours (see Supplemental Table 1 for acquisition parameters).

### Image analysis

All four acquisitions were first averaged using the MIPAV image analysis software (NIH, Bethesda, MD, USA; <http://mipav.cit.nih.gov>). After an N4-bias-field correction<sup>14</sup> was applied to correct for intensity inhomogeneity, images were upsampled to an in-plane axial resolution of 35  $\mu\text{m} \times 35 \mu\text{m}$  and a 70  $\mu\text{m}$  slice thickness and concatenated to generate a single-image volume of the entire SC using ImageJ software (NIH, Bethesda, MD, USA; <https://imagej.nih.gov/ij/>) and MIPAV. Finally, the different spinal level segments were annotated based on the location of the nerve roots.<sup>15</sup>

Focal lesions (areas of abnormal signal intensity within the WM) were manually segmented (ITK-SNAP version 3.2.0) using triplanar viewing mode. Lesions were classified according to their volume using the following arbitrary categories: small (0.009–0.06  $\text{mm}^3$ ), medium (0.06–0.4  $\text{mm}^3$ ), and large (>0.4  $\text{mm}^3$ ). The specific position of the focal lesions

was also recorded as anterior, posterior, and lateral (left/right). Subpial lesions were also manually segmented on selected images at three different levels of the cord (C7, T7, and L3). Regions-of-interest (ROIs) of the entire cross-sectional cord, normal appearing white matter (NAWM), and gray matter (GM) were drawn manually (Supplemental Figure 2) using a semi-automated tool in JIM V.7.0 (Xinapse Systems, Leicester, UK). The relative thickness of subpial lesions (areas of abnormal signal intensity along the edge of the WM) was characterized as a percentage of total WM using the following formula:

$$\text{ROI}_{\text{subpial area}} / (\text{ROI}_{\text{CSA cord}} - \text{ROI}_{\text{GM area}}) * 100.$$

where CSA cord is the cross-sectional area of the cord. The degree of severity for the subpial lesions was arbitrarily defined as low if <20%, intermediate if between 20% and 50%, and high if >50%.

#### Histopathology

Focal and subpial lesions with a variety of sizes, shapes, and locations identified by ex vivo MRI were targeted during the cutting process (transaxial cuts of 3-mm-thick slabs). Slabs from the control animal were selected at similar cord levels for comparison purposes. A total of 32 slabs were cut and then embedded in paraffin wax. These paraffin-embedded slabs were sectioned in 5- $\mu\text{m}$ -thick slices to find the lesions detected by MRI. Luxol fast blue with periodic acid-Schiff (LFB-PAS) staining, anti-ionized calcium-binding adapter molecule 1 (Iba-1) immunohistochemistry, and 3,3'-diaminobenzidine (DAB)-enhanced Turnbull staining were performed on a subset of slices containing lesions. Details of the staining protocols are provided in the supplemental material. Digital pictures of the stained slides were generated using a Zeiss Observer 1 microscope (ZEN blue software; Zeiss, Thornwood, NY, USA) at 10 $\times$  optical zoom with a pixel resolution 0.7  $\mu\text{m}$  and exported as TIFF files.

#### MRI-histopathological comparison

A semi-quantitative comparison was performed by selecting 11 different lesions (9 focal and 2 subpial) on MRI and rating their corresponding histological images. A contour line for each lesion was first drawn on each histological image using the following procedure. MRI images were first coregistered to the corresponding LFB-PAS histology images using thin-plate splines with control points initialized manually (MIPAV). Lesions were then segmented on MRI images by using an intensity-level threshold. The corresponding contour line was defined using the

region(s) of interest (ROI) tool and propagated to the histological images. The contrast between lesion and GM was computed using the following formula and reported for these selected lesions.

$$\text{Contrast}_{\text{lesion-to-GM}} = \frac{\text{Signal intensity}_{\text{lesion}}}{\text{Signal intensity}_{\text{GM}}}$$

The level of demyelination inside the contoured lesions was rated on LFB-PAS using the following grading system: 0 = normal myelin density, 1 = reduced myelin density, and 2 = completely demyelinated. The level of inflammation was rated on Iba-1 using the following grading system: 0 = absent/few inflammatory cells, 1 = moderate density of inflammatory cells, and 2 = high density of inflammatory cells.

A more quantitative comparison between MRI and histopathology was performed using regression models (see “Statistical analysis”) on the coregistered ex vivo MRI, LFB-PAS, and Iba-1 images. To generate data for fitting the statistical models, a total of 92 ROIs were drawn manually on LFB-PAS images using ImageJ at different cross-sectional cord locations (WM, GM, and lesion) of several sections (8–14 ROIs per section; Supplemental Figure 3). ROIs were then propagated to the corresponding MRI images and Iba-1 staining. From each staining, the function “color deconvolution” (ImageJ) was applied to extract the channel corresponding to the stain of interest (LFB channel for the myelin component of LFB-PAS and DAB channel for the inflammatory cells of Iba-1). Mean signal intensity for each ROI was computed on both MRI and grayscale-deconvoluted staining images.

#### Statistical analysis

The nonparametric two-tailed Mann Whitney test (Prism v7.0b) was performed to test any association between the  $\text{Contrast}_{\text{lesion-to-GM}}$  values and histopathology scores. To assess the association between MRI and histopathology signals and identify which variables influenced the MRI signal, we performed regression models and evaluated different statistical models, summarized in Table 2. In all models, the independent variable was the histopathology and the dependent variable was the MRI signal intensity. Two linear mixed-effects models ( $M_1$  and  $M_2$ ) were used with random effect of section, to account for the correlated observations taken from the same section. A simple linear model  $M_0$  was run for completeness.  $M_2$ , the most complex model, included an interaction term to test the hypothesis that the relationship between MRI and pathology depends on the tissue type (NAWM, GM, and lesions). We evaluated these different

**Table 2.** Summary of the different regression models applied to the data with their respective Akaike information criteria results for the different myelin models (using the LFB-PAS histology) and inflammation models (using the Iba-1).

Models	Dependent variable	Fixed effects	Interaction term	Random effect	Myelin model		Inflammation model	
					AIC	$\Delta$ AIC	AIC	$\Delta$ AIC
$M_0$	MRI	Histopathology, tissue type	No	No	1640.6	91.6	1618.4	20.1
$M_1$	MRI	Histopathology, tissue type	No	Section	1557.8	8.8	1598.3	0
$M_2$	MRI	Histopathology, tissue type	Yes	Section	1549	0	1599.3	1

AIC: Akaike information criteria; MRI: magnetic resonance imaging.

regression models for both LFB (called the myelin model) and Iba-1 (called the inflammation model) by comparing their Akaike information criteria (AIC)<sup>16</sup> values; the best model was considered to have the lowest AIC value. Because AIC values are ordinal and give a rank of the model goodness-of-fit, the  $\Delta$ AIC values are reported as well:

$$\Delta\text{AIC}(n) = \text{AIC}(n) - \text{AIC}_{\min}$$

where  $n$  denotes the model of interest and  $\text{AIC}_{\min}$  the minimum AIC of all the models tested. Regression results were considered significant for  $p \leq 0.05$ . The coefficient of determination,  $R^2$ , was reported to evaluate the goodness-of-fit using the method of Nakagawa and Schielzeth<sup>17</sup> adapted for the linear mixed-effects models. Statistical analysis and graphical visualization were performed using R version 3.3.3 and RStudio (1.0.143). The lme4 package version 1.1-16 was used to fit the mixed-effects model using restricted maximum likelihood estimation.

## Results

All immunized animals developed clinical signs between 65 and 100 days post-immunization and reached EAE scores  $\geq 2.5$  at the time of sacrifice. Disease duration (from immunization to death) ranged from 71 to 159 days (mean: 113 days; Table 1). All four EAE animals displayed SC abnormalities on postmortem MRI images (Figure 1). Focal WM lesions with various sizes and shapes were observed at different cord levels (Figure 1, red arrows). A total of 85 focal WM lesions were segmented on the MRI images across the four EAE animals: 34 lesions (40%) were found at the cervical level, 40 (47%) at the thoracic level, and 11 (13%) at the lumbar level (Table 3); 57 lesions (67%) were classified as small (average volume:  $0.028 \text{ mm}^3$ ), 24 lesions (28%) as medium-sized ( $0.11 \text{ mm}^3$ ), and 4 lesions (5%) as large ( $2.54 \text{ mm}^3$ ; Table 3); 69 focal WM lesions

(81%) were located in the lateral WM, 15 lesions (18%) were located in the posterior WM, and only 1 lesion was found in the anterior WM (Table 3). Subpial WM lesions were also observed along the entire cord, with variable thickness (Figure 1, green arrows). Three animals (M1, M2, and M3) displayed thin subpial WM lesions (relative thickness  $\leq 20\%$ ) throughout their entire cords, whereas one animal (M4) showed thicker subpial WM lesions (relative thickness = 39%) in the lumbar portion of the cord (Table 4).

Anatomical features observed on MRI were visually matched on histological sections in control and EAE animals (Figure 2). In the control animal, both MRI and histology depicted normal WM with dark gray (denoted here as “isointense”) MRI signal (Figure 2a<sub>1</sub>), normal LFB staining (Figure 2b<sub>1</sub>), and absence of “reactive” inflammatory cells on Iba-1 (Figure 2c<sub>1</sub>). In the EAE animals, focal and subpial WM cord lesions detected as areas of hyperintense MRI signal (Figure 2a<sub>2</sub>–a<sub>4</sub>) corresponded to areas of clear demyelination characterized by low LFB (Figure 2b<sub>2</sub>–b<sub>4</sub>) staining, as well as intense inflammation demonstrated by strong Iba-1 staining (Figure 2c<sub>2</sub>–c<sub>4</sub>).

The semi-quantitative analysis performed on a subset of 11 lesions revealed heterogeneity in myelin content and density of inflammation (Supplemental Table 2). This heterogeneity is illustrated by representative examples of a completely demyelinated lesion (Figure 3a<sub>2</sub> and a<sub>3</sub>) with intense inflammation (Figure 3a<sub>4</sub>) and a partially demyelinated lesion (Figure 3b<sub>2</sub> and b<sub>3</sub>) with moderate inflammation (Figure 3b<sub>4</sub>). The semi-quantitative analysis also indicated an association between MRI signal and myelin content/density of inflammatory cells (Supplemental Table 2). Completely demyelinated lesions (score=2) showed a significantly higher  $\text{Contrast}_{\text{lesion-to-GM}}$  value than lesions with partial demyelination (score=1; Figure

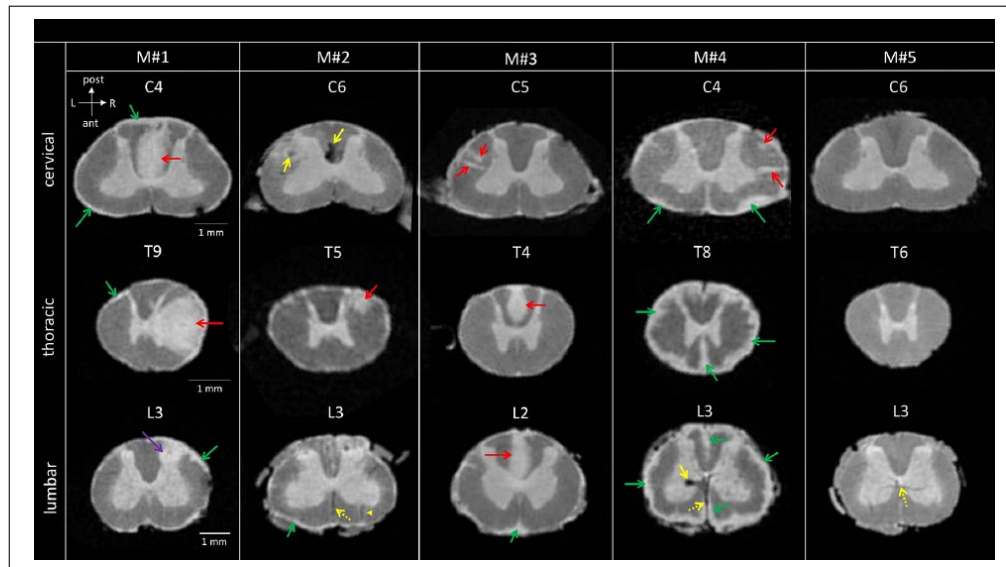


**Figure 1.** High-resolution postmortem MRI scans of four marmoset spinal cords with EAE (M#1, M#2, M#3 and M#4) and one healthy control (M#5) showing cervical, thoracic, and lumbar spinal cord levels. Anatomical orientation axes are included (white arrows): anterior (ant), posterior (post), left (L), and right (R). Heterogeneity of the focal lesions (red arrows) and subpial lesions (green arrows) in terms of size, shape, and location can be observed across the marmosets with EAE. Areas of hypointense signal (yellow arrows) were sometimes observed in these animals (M#2, C6 and M#4, L3), most likely originating from blood deposits (see Supplemental Figure 4). Parenchymal vessels with deoxygenated blood could also be visualized as dark thin lines (yellow dotted arrows, L3 for M#2, M#4 and M#5), sometimes running centrally through a focal lesion (yellow arrowhead, M#2, L3). Note the mass effect produced by a large tumefactive lesion (M#1, T9, red arrow) that involves most of the right lateral column and some of the GM. Another lesion involving the GM (purple arrow) could also be found within the dorsal horn at the lumbar level (M#1, L3). Various degrees of confluence for the subpial lesions can be appreciated. For three animals (M#1, M#2, and M#3), subpial lesions were subtle and not confluent whereas animal M#4 displayed partially confluent (C4) and completely confluent subpial lesions at the caudal levels of the SC (T8 and L3).

**Table 3.** Characterization of the focal lesions by spinal cord level, size, and white matter location in the four marmosets with EAE.

	Animal	M#1	M#2	M#3	M#4	Average across marmosets
Number of focal WM lesions by cord level	Cervical	11	5	10	8	8.5
	Thoracic	9	10	10	11	10
	Lumbar	1	2	5	3	2.8
Number of focal lesions classified by size and corresponding average volume (STD) in mm <sup>3</sup>	Small	10; 0.025 (0.013)	9; 0.033 (0.014)	21; 0.028 (0.009)	17; 0.026 (0.013)	14; 0.028 (0.01)
	Medium	9; 0.14 (0.1)	8; 0.13 (0.089)	2; 0.078 (0.003)	5; 0.086 (0.022)	6; 0.12 (0.08)
	Large	2; 4.18 (0.59)	0	2; 0.9 (0.68)	0	1; 2.54 (1.96)
Number of focal WM lesions by location	Posterior	9	1	3	2	3.8
	Left lateral	8	10	20	10	6.9
	Right lateral	3	6	2	10	5.3
	Anterior	1	0	0	0	0.25

WM: white matter; STD: standard deviation; EAE: experimental autoimmune encephalomyelitis.

**Table 4.** Characterization of the subpial lesions as a percentage of the total white matter for selected spinal levels in the four marmosets with EAE.

	Animal	M#1	M#2	M#3	M#4	Average across marmosets
Relative thickness (% of white matter) of subpial lesions by cord level	Cervical C7	18	15	5	30	17
	Thoracic T7	16	20	11	54	25
	Lumbar L3	19	14	10	39	21

EAE: experimental autoimmune encephalomyelitis.

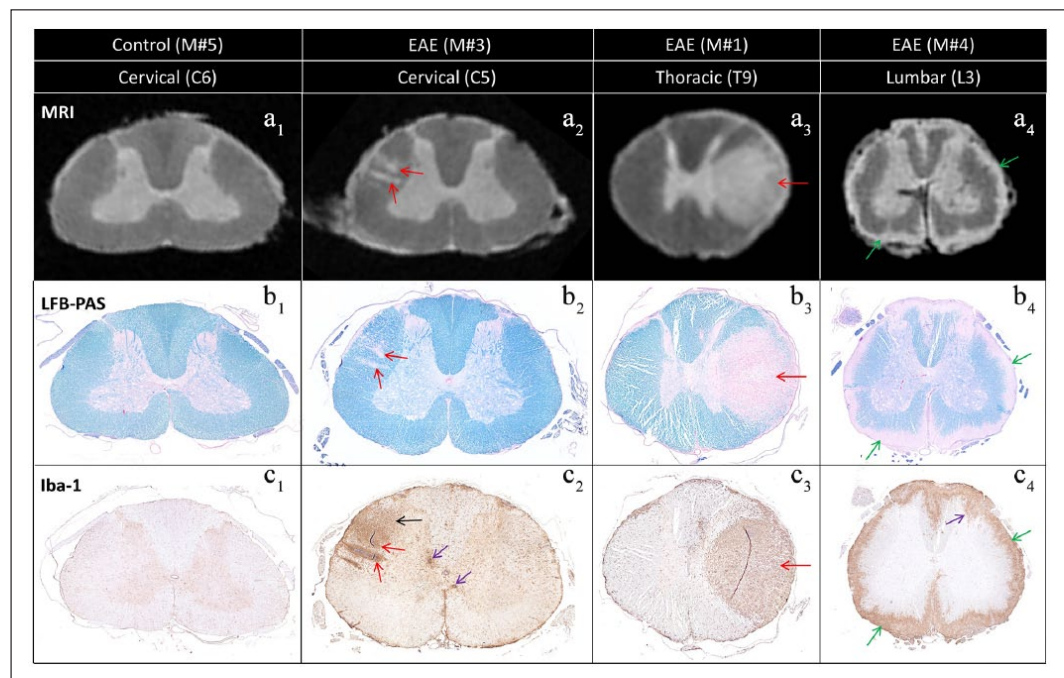


**Figure 2.** Comparison between (a<sub>1</sub>) MRI scans and histopathology (b<sub>1</sub> and c<sub>1</sub>) sections from a control animal (M#5) and three EAE animals (M#3, M#1, and M#4). Two small focal lesions detected by MRI in the cervical section (a<sub>2</sub>, red arrows) correspond to two small demyelinated areas (b<sub>2</sub>, red arrows) with intense inflammatory cell infiltration (c<sub>2</sub>, red arrows). Also note the more diffuse inflammatory cell infiltration located posterior to the two lesions, not captured by MRI (c<sub>2</sub>, black arrow). The large tumefactive focal lesion detected by MRI in the thoracic section (a<sub>3</sub>, red arrow) matches an area of demyelination (b<sub>3</sub>, red arrow) and inflammatory cell infiltration (c<sub>3</sub>, red arrow). A similar correspondence between MRI and histopathology is observed at the lumbar level (a<sub>4</sub>, b<sub>4</sub>, and c<sub>4</sub>) for the subpial lesion (green arrows). Although not visible on the MRI, inflammation can be found within the GM (purple arrows), either infiltrating the dorsal horn (c<sub>4</sub>) or as small foci (c<sub>2</sub>).

4). A similar trend was observed when comparing lesions with high density of Iba-1 cells (score=2) against lesions with a moderate density of cells (score=1), although the difference in Contrast<sub>lesion-to-GM</sub> values was not significant in this case (Figure 4).

The quantitative analysis performed on the individual 92 ROIs revealed a lower AIC value when an interaction term for tissue type and random effect for sections were added in the myelin model ( $M_2$ ; see Table 2). Figure 5 illustrates the

importance of the random effect when predicting MRI intensities. In the  $M_2$  regression model,  $R^2$  of 0.96 indicated that 96% of the variability in the MRI data was explained by the predictors (fixed and random effects) in this model (Supplemental Figure 5);  $p$  values and mean slope coefficients from the linear mixed-effects model  $M_2$  are summarized in Supplemental Table 3. Significant and strong positive associations were found between LFB and MRI values for both lesional and GM tissues. No significant association was seen between



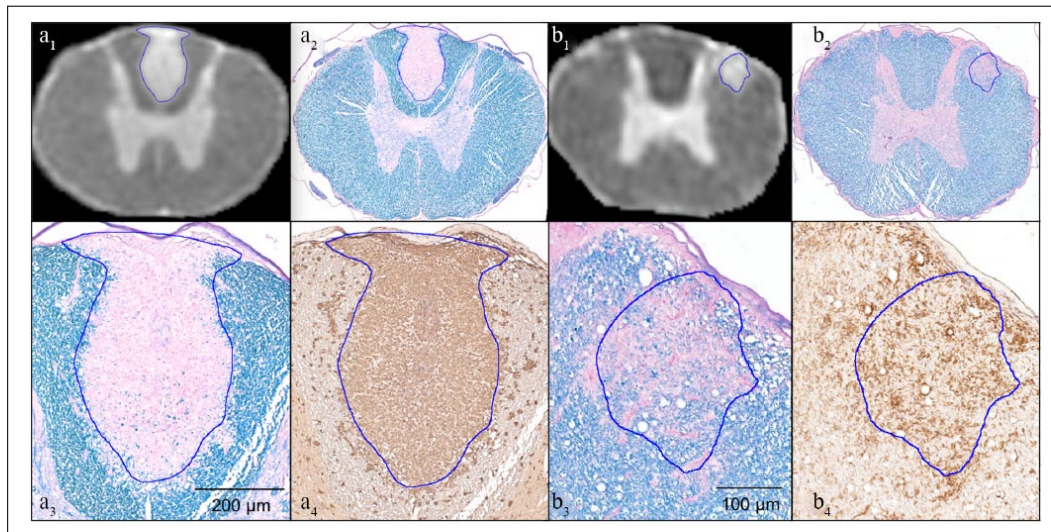


**Figure 3.** MRI scans ( $a_1$  and  $b_1$ ) coregistered to the corresponding LFB-PAS images ( $a_2$  and  $b_2$ ) for defining the lesion contour ROI (blue lines). Magnified views of the lesions for LFB-PAS ( $a_3$  and  $b_3$ ) and Iba-1 ( $a_4$  and  $b_4$ ).  $a_3$  and  $a_4$  show complete myelin loss and uniform intensity of inflammatory cells throughout the entire lesion.  $b_3$  and  $b_4$  show a partially demyelinated lesion with moderate inflammation.

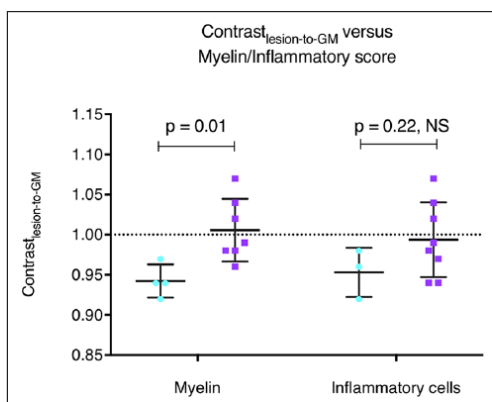


**Figure 4.** Contrast<sub>lesion-to-GM</sub> values for each white matter lesion ( $n = 11$ ) grouped according to histopathological scores for myelin and inflammatory cells (light blue: score = 1; purple: score = 2).

the LFB and MRI values in the NAWM, but the variation in MRI signal intensity within NAWM was comparatively small. A negligible difference in AIC values was observed when adding an interaction term in the inflammation models (Table 2). The lowest AIC value was obtained for  $M_1$ , which includes random effects but no interaction term. No significant association was found between the Iba-1 and the MRI signal (slope (standard error) =  $-10$  (10.9);  $p = 0.35$ ).

## Discussion

In this study, we investigated the SC pathology in marmosets with EAE using a combined MRI–histopathological approach. By acquiring high-resolution ex vivo MRI, we first identified two types of lesions: (1) focal lesions located within the WM of the SC, and (2) subpial lesions along the WM abutting the subarachnoid space. By comparing our ex vivo MRI images with histology, we then demonstrated that these lesions corresponded to areas of demyelination and inflammation.

Similar to focal MS lesions,<sup>18,19</sup> focal EAE lesions were found throughout the SC of the marmoset, with a prevalent localization in the lateral and posterior columns. We observed a heterogeneous distribution in terms of number and size of the focal lesions, which is also consistent with the lesion heterogeneity described in MS patients.<sup>20</sup> To our knowledge, only one histopathological study has reported the presence of diffuse subpial demyelination in the MS SC.<sup>21</sup> In our model, subpial EAE lesions were distributed throughout the animal's SC and showed variable thicknesses across animals. Note that these subpial lesions were difficult to visualize by post-mortem MRI without first performing a laminectomy. Indeed, the tissues (bones, fat, and muscles) surrounding the SC generated magnetic susceptibility-related artifacts that hid these subtle lesions located at the edge of the cord (Supplemental Figure 6). Thus, we hypothesize the technical issues combined with comparatively

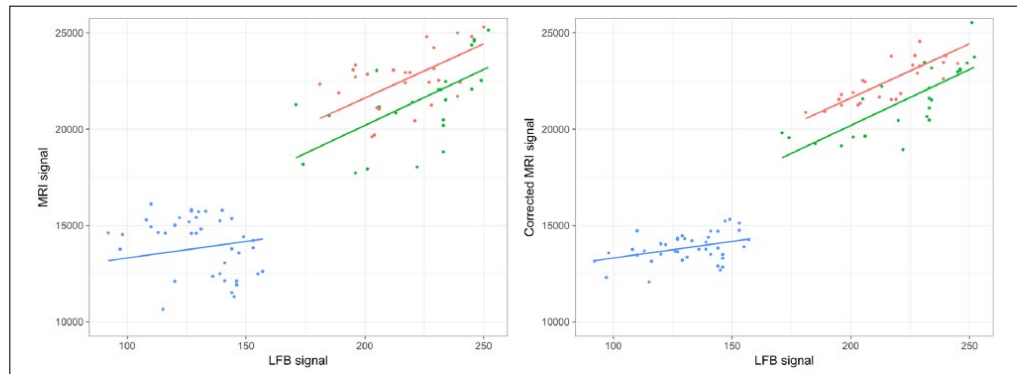


**Figure 5.** Left: relationship between the observed MRI signal intensity values and LFB signal intensity using myelin model  $M_2$ . Each dot represents the individual ROI values according to their tissue type. The fitted line represents the estimated MRI values for fixed effect only. Right: representation of the random effect correction on the MRI value estimations. The corrected MRI signal was obtained by removing the estimated random effect value from the mixed-effect model for each section. The residual variation, which is neither explained by fixed effect nor random effect, is shown by the distance between the individual dot and its corresponding value within the fitted line. (Green: lesion; red: gray matter; blue: NAWM.)

low-resolution MRI might explain why subpial cord lesions have not been yet reported by MRI in MS patients. A recent *in vivo* imaging study of the cervical cord in MS found a decrease in magnetization transfer ratio values for the outermost voxels,<sup>22</sup> which could correspond to the subpial pathology observed in our study, but this would need to be verified histopathologically.

For lesion types, our histopathological evaluation revealed variable degrees of demyelination and inflammatory cell densities, which most likely reflects different stages of lesion development, as recently demonstrated for marmoset brain lesions.<sup>6</sup> Note that the small focal inflammatory demyelinated lesions appeared to follow parenchymal blood vessels, whereas the larger subpial inflamed demyelinated lesions detected in our model are consistent with a leptomeningeal inflammatory origin, as is postulated to be the case for subpial cortical lesions.<sup>23,24</sup>

By performing a quantitative comparison between MRI and histopathology using regression models, we established a strong association between the  $T_2^*$ -weighted MRI signal intensity and the amount of myelin derived from the LFB-PAS staining intensity within the GM and lesional areas. By contrast, the association between the MRI signal and the density of inflammatory cells was weaker (Figure 4). The use of a linear mixed-effects model allowed us to improve the prediction of MRI values by correcting for the correlation within section (Figure 5). These results highlight the fact that  $T_2^*$ -weighted MRI signal can be highly

sensitive to demyelination (although not specific) and corroborate previous postmortem studies investigating MRI and its pathological correlates in the MS SC.<sup>25</sup>

Important limitations of this study were the use of a single, postmortem timepoint with a single MRI contrast ( $T_2^*$ -weighting). The postmortem timepoint illuminates the SC lesion load when symptoms are severe (20% weight loss or paraplegia), but cannot provide the spatiotemporal context of the pathology. In addition, because we were not able to scan these SCs *in vivo*, we have no information regarding the age and the blood–brain–barrier integrity of the lesions analyzed here. Both of these processes can play a role in the development of vasogenic edema and expansion of the interstitial space, which can also impact signal intensity on postmortem MRI. Finally, our MRI sequence was optimized to provide the best delineation between lesions and NAWM. Therefore, lesions affecting the GM of the SC could not be easily identified by MRI in this study, although we detected GM pathology by histology in some of our sections (Figures 2 and 3, purple arrows).

## Conclusion

In this study, we investigated SC tissues from marmosets with EAE showing symptoms suggestive of SC damage. Using a combined MRI–histopathological approach, we established the existence of two types of WM SC lesions: focal WM lesions with characteristics (location, distribution, and size) overlapping those found in human MS SC, and subpial WM

lesions, which so far have been underinvestigated in MS. We found that both focal and subpial EAE lesions detected by MRI corresponded to areas of demyelination and marked inflammation. Our findings underscore the relevance of this nonhuman primate model of MS for understanding mechanisms of lesion formation in the SC. Future work is needed to investigate the characteristics (especially on MRI) of SC subpial lesions in MS, as well as to study *in vivo* the spatiotemporal development of SC pathology in the marmoset with EAE.

### Acknowledgements

The authors wish to thank Cecil Chern-Chyi Yen who helped with troubleshooting the scanner used in this study; Sam Antonio and James O'Malley in the NIH animal facility for marmoset care and project support; and Gina Norato, NINDS statistician, for her help to apply the linear mixed-effect models.

This research was presented in part at the 24th annual meeting of the International Society for Magnetic Resonance in Medicine (Singapore, 2016).

### Declaration of Conflicting Interests

The author(s) declared the following potential conflicts of interest with respect to the research, authorship, and/or publication of this article: J.A.L., J.R.G., N.J.L., S.-K.H., E.L., M.D.S., A.C.S., S.J., S.L., D.S.R., and P.S. declared no potential conflicts of interest with respect to the research, authorship, and/or publication of this article.

### Funding

The author(s) disclosed receipt of the following financial support for the research, authorship, and/or publication of this article: This research was supported by the Intramural Research Program of the National Institute of Neurological Disorders and Stroke.

### Supplemental material

Supplemental material for this article is available online.

### ORCID iD

Daniel S Reich  <https://orcid.org/0000-0002-2628-4334>

### References

1. Baxter AG. The origin and application of experimental autoimmune encephalomyelitis. *Nat Rev Immunol* 2007; 7(11): 904–912.
2. Linker RA and Lee DH. Models of autoimmune demyelination in the central nervous system: on the way to translational medicine. *Exp Transl Stroke Med* 2009; 1: 5.
3. Massacesi L, Genain CP, Lee-Parritz D, et al. Active and passively induced experimental autoimmune encephalomyelitis in common marmosets: a new model for multiple sclerosis. *Ann Neurol* 1995; 37(4): 519–530.
4. Kap YS, Laman JD and 't Hart BA. Experimental autoimmune encephalomyelitis in the common marmoset, a bridge between rodent EAE and multiple sclerosis for immunotherapy development. *J Neuroimmune Pharmacol* 2010; 5(2): 220–230.
5. Absinta M, Sati P and Reich DS. Advanced MRI and staging of multiple sclerosis lesions. *Nat Rev Neurol* 2016; 12(6): 358–368.
6. Maggi P, Macri SM, Gaitan MI, et al. The formation of inflammatory demyelinated lesions in cerebral white matter. *Ann Neurol* 2014; 76(4): 594–608.
7. Hart BA, Bauer J, Muller HJ, et al. Histopathological characterization of magnetic resonance imaging-detectable brain white matter lesions in a primate model of multiple sclerosis: a correlative study in the experimental autoimmune encephalomyelitis model in common marmosets (*Callithrix jacchus*). *Am J Pathol* 1998; 153(2): 649–663.
8. 't Hart BA and Massacesi L. Clinical, pathological, and immunologic aspects of the multiple sclerosis model in common marmosets (*Callithrix jacchus*). *J Neuropathol Exp Neurol* 2009; 68(4): 341–355.
9. Laman JD, vanMeurs M, Schellekens MM, et al. Expression of accessory molecules and cytokines in acute EAE in marmoset monkeys (*Callithrix jacchus*). *J Neuroimmunol* 1998; 86(1): 30–45.
10. Villoslada P, Hauser SL, Bartke I, et al. Human nerve growth factor protects common marmosets against autoimmune encephalomyelitis by switching the balance of T helper cell type 1 and 2 cytokines within the central nervous system. *J Exp Med* 2000; 191(10): 1799–1806.
11. Guy JR, Sati P, Leibovitch E, et al. Custom fit 3D-printed brain holders for comparison of histology with MRI in marmosets. *J Neurosci Methods* 2016; 257: 55–63.
12. Lee NJ, Ha SK, Sati P, et al. Spatiotemporal distribution of fibrinogen in marmoset and human inflammatory demyelination. *Brain* 2018; 141(6): 1637–1649.
13. Kap YS, Smith P, Jagessar SA, et al. Fast progression of recombinant human myelin/oligodendrocyte glycoprotein (MOG)-induced experimental autoimmune encephalomyelitis in marmosets is associated with the activation of MOG34–56-

- specific cytotoxic T cells. *J Immunol* 2008; 180(3): 1326–1337.
14. Tustison NJ, Avants BB, Cook PA, et al. N4ITK: improved N3 bias correction. *IEEE Trans Med Imaging* 2010; 29(6): 1310–1320.
  15. Watson C, Sengul G, Tanaka I, et al. The spinal cord of the common marmoset (*Callithrix jacchus*). *Neurosci Res* 2015; 93: 164–175.
  16. Akaike H. Information theory and an extension of the maximum likelihood principle. In: Petrov BN and Csaki F (eds) 2nd international symposium on information theory, Tsahkadsor, Armenia, USSR, September 2–8, 1971, Budapest: Akademia Kiado, 1973, pp. 267–281.
  17. Nakagawa S and Schielzeth H. A general and simple method for obtaining R<sup>2</sup> from generalized linear mixed-effects models. *Methods Ecol Evol* 2013; 4(2): 133–142.
  18. Oppenheimer DR. The cervical cord in multiple sclerosis. *Neuropathol Appl Neurobiol* 1978; 4(2): 151–162.
  19. Weier K, Mazraeh J, Naegelin Y, et al. Biplanar MRI for the assessment of the spinal cord in multiple sclerosis. *Mult Scler* 2012; 18(11): 1560–1569.
  20. Nijeholt GJ, Bergers E, Kamphorst W, et al. Post-mortem high-resolution MRI of the spinal cord in multiple sclerosis: a correlative study with conventional MRI, histopathology and clinical phenotype. *Brain* 2001; 124(Pt. 1): 154–166.
  21. Androdias G, Reynolds R, Chanal M, et al. Meningeal T cells associate with diffuse axonal loss in multiple sclerosis spinal cords. *Ann Neurol* 2010; 68(4): 465–476.
  22. Kearney H, Yiannakas MC, Samson RS, et al. Investigation of magnetization transfer ratio-derived pial and subpial abnormalities in the multiple sclerosis spinal cord. *Brain* 2014; 137(Pt. 9): 2456–2468.
  23. Reich DS, Lucchinetti CF and Calabresi PA. Multiple Sclerosis. *N Engl J Med* 2018; 378(2): 169–180.
  24. Choi SR, Howell OW, Carassiti D, et al. Meningeal inflammation plays a role in the pathology of primary progressive multiple sclerosis. *Brain* 2012; 135(Pt. 10): 2925–2937.
  25. Schmierer K, McDowell A, Petrova N, et al. Quantifying multiple sclerosis pathology in post mortem spinal cord using MRI. *Neuroimage* 2018; 182: 251–258.

Visit SAGE journals online  
journals.sagepub.com/  
home/msj

 SAGE journals

- Absinta, M., Sati, P., and Reich, D. S. (2016). Advanced mri and staging of multiple sclerosis lesions. *Nature Reviews Neurology*, 12(6):358.
- Alcaide-Leon, P., Pauranik, A., Alshafai, L., Rawal, S., Oh, J., Montanera, W., Leung, G., and Bharatha, A. (2016). Comparison of sagittal fse t2, stir, and t1-weighted phase-sensitive inversion recovery in the detection of spinal cord lesions in ms at 3t. *American Journal of Neuroradiology*, 37(5):970–975.
- Androdias, G., Reynolds, R., Chanal, M., Rittleng, C., Confavreux, C., and Nataf, S. (2010). Meningeal t cells associate with diffuse axonal loss in multiple sclerosis spinal cords. *Annals of neurology*, 68(4):465–476.
- A't Hart, B., Bauer, J., Muller, H.-J., Melchers, B., Nicolay, K., Brok, H., Bontrop, R. E., Lassmann, H., and Massacesi, L. (1998). Histopathological characterization of magnetic resonance imaging-detectable brain white matter lesions in a primate model of multiple sclerosis: a correlative study in the experimental autoimmune encephalomyelitis model in common marmosets (*callithrix jacchus*). *The American journal of pathology*, 153(2):649–663.
- A't Hart, B., Laman, J. D., Bauer, J., Blezer, E., van Kooyk, Y., and Hintzen, R. Q. (2004a). Modelling of multiple sclerosis: lessons learned in a non-human primate. *The Lancet Neurology*, 3(10):588–597.
- A't Hart, B., Vogels, J., Bauer, J., Brok, H. P., and Blezer, E. (2004b). Non-invasive measurement of brain damage in a primate model of multiple sclerosis. *Trends in molecular medicine*, 10(2):85–91.
- Bagnato, F., Hametner, S., Boyd, E., Endmayr, V., Shi, Y., Ikonomidou, V., Chen, G., Pawate, S., Lassmann, H., Smith, S., et al. (2018). Untangling the r2\* contrast in multiple sclerosis: A combined mri-histology study at 7.0 tesla. *PloS one*, 13(3):e0193839.
- Barry, R. L., Vannesjo, S. J., By, S., Gore, J. C., and Smith, S. A. (2018). Spinal cord mri at 7t. *Neuroimage*, 168:437–451.
- Barth, M., Breuer, F., Koopmans, P. J., Norris, D. G., and Poser, B. A. (2016). Simultaneous multislice (sms) imaging techniques. *Magnetic resonance in medicine*, 75(1):63–81.
- Baxter, A. G. (2007). The origin and application of experimental autoimmune encephalomyelitis. *Nature Reviews Immunology*, 7(11):904.

- Beck, E., Sati, P., Sethi, V., Kober, T., Dewey, B., Bhargava, P., Nair, G., Cortese, I., and Reich, D. (2018). Improved visualization of cortical lesions in multiple sclerosis using 7t mp2rage. *American Journal of Neuroradiology*, 39(3):459–466.
- Boneschi, F. M., Vacchi, L., Rovaris, M., Capra, R., and Comi, G. (2013). Mitoxantrone for multiple sclerosis. *Cochrane Database of Systematic Reviews*, (5).
- Bot, J., Barkhof, F., à Nijeholt, G. L., Bergers, E., Polman, C., Ader, H., and Castelijns, J. (2000). Comparison of a conventional cardiac-triggered dual spin-echo and a fast stir sequence in detection of spinal cord lesions in multiple sclerosis. *European radiology*, 10(5):753–758.
- Bot, J. C., Barkhof, F., à Nijeholt, G. L., van Schaardenburg, D., Voskuyl, A. E., Ader, H. J., Pijnenburg, J. A., Polman, C. H., Uitdehaag, B. M., Vermeulen, E. G., et al. (2002). Differentiation of multiple sclerosis from other inflammatory disorders and cerebrovascular disease: value of spinal mr imaging. *Radiology*, 223(1):46–56.
- Bot, J. C., Blezer, E. L., Kamphorst, W., Lycklama à Nijeholt, G. J., Ader, H. J., Castelijns, J. A., Bergers, E., Ravid, R., Polman, C., and Barkhof, F. (2004). The spinal cord in multiple sclerosis: relationship of high-spatial-resolution quantitative mr imaging findings to histopathologic results. *Radiology*, 233(2):531–540.
- Breckwoldt, M. O., Gradl, J., Hähnel, S., Hielscher, T., Wildemann, B., Diem, R., Platten, M., Wick, W., Heiland, S., and Bendszus, M. (2017). Increasing the sensitivity of mri for the detection of multiple sclerosis lesions by long axial coverage of the spinal cord: a prospective study in 119 patients. *Journal of neurology*, 264(2):341–349.
- Brok, H. P., Uccelli, A., de Rosbo, N. K., Bontrop, R. E., Roccatagliata, L., de Groot, N. G., Capello, E., Laman, J. D., Nicolay, K., Mancardi, G.-L., et al. (2000). Myelin/oligodendrocyte glycoprotein-induced autoimmune encephalomyelitis in common marmosets: the encephalitogenic t cell epitope pmog24–36 is presented by a monomorphic mhc class ii molecule. *The Journal of Immunology*, 165(2):1093–1101.
- Browne, P., Chandraratna, D., Angood, C., Tremlett, H., Baker, C., Taylor, B. V., and Thompson, A. J. (2014). Atlas of multiple sclerosis 2013: a growing global problem with widespread inequity. *Neurology*, 83(11):1022–1024.
- Brownlee, W. J., Swanton, J. K., Altmann, D. R., Ciccarelli, O., and Miller, D. H. (2015). Earlier and more frequent diagnosis of multiple sclerosis using the mcdonald criteria. *J Neurol Neurosurg Psychiatry*, 86(5):584–585.
- Busse, R. F., Hariharan, H., Vu, A., and Brittain, J. H. (2006). Fast spin echo sequences with very long echo trains: design of variable refocusing flip angle schedules and generation of clinical t2 contrast. *Magnetic Resonance in Medicine: An Official Journal of the International Society for Magnetic Resonance in Medicine*, 55(5):1030–1037.
- Calabrese, M., Romualdi, C., Poretto, V., Favaretto, A., Morra, A., Rinaldi, F., Perini, P., and Gallo, P. (2013). The changing clinical course of multiple sclerosis: a matter of gray matter. *Annals of neurology*, 74(1):76–83.
- Casteleyn, C., Bakker, J., Breugelmans, S., Kondova, I., Saunders, J., Langermans, J., Cornillie, P., Van Den Broeck, W., Van Loo, D., Van Hoorebeke, L., et al. (2012). Anatomical description and morphometry of the skeleton of the common marmoset (*calithrix jacchus*). *Laboratory animals*, 46(2):152–163.

- Chang, Y., Bae, S. J., Lee, Y. J., Hwang, M. J., Lee, S. H., Lee, J., Lee, S. K., and Woo, S. (2007). Incidental magnetization transfer effects in multislice brain mri at 3.0 t. *Journal of Magnetic Resonance Imaging: An Official Journal of the International Society for Magnetic Resonance in Medicine*, 25(4):862–865.
- Chiang, C.-W., Wang, Y., Sun, P., Lin, T.-H., Trinkaus, K., Cross, A. H., and Song, S.-K. (2014). Quantifying white matter tract diffusion parameters in the presence of increased extra-fiber cellularity and vasogenic edema. *Neuroimage*, 101:310–319.
- Choi, S. R., Howell, O. W., Carassiti, D., Magliozzi, R., Gveric, D., Muraro, P. A., Nicholas, R., Roncaroli, F., and Reynolds, R. (2012). Meningeal inflammation plays a role in the pathology of primary progressive multiple sclerosis. *Brain*, 135(10):2925–2937.
- Chong, A., Chandra, R., Chuah, K., Roberts, E., and Stuckey, S. (2016). Proton density mri increases detection of cervical spinal cord multiple sclerosis lesions compared with t2-weighted fast spin-echo. *American Journal of Neuroradiology*, 37(1):180–184.
- Cook, L. L., Foster, P. J., Mitchell, J. R., and Karlik, S. J. (2004). In vivo 4.0-t magnetic resonance investigation of spinal cord inflammation, demyelination, and axonal damage in chronic-progressive experimental allergic encephalomyelitis. *Journal of Magnetic Resonance Imaging: An Official Journal of the International Society for Magnetic Resonance in Medicine*, 20(4):563–571.
- Cordonnier, C., de Seze, J., Breteau, G., Ferriby, D., Michelin, E., Stojkovic, T., Pruvo, J. P., and Vermersch, P. (2003). Prospective study of patients presenting with acute partial transverse myelopathy. *Journal of Neurology*, 250(12):1447–1452.
- Costello, K., Halper, J., Kalb, R., Skutnik, L., and Rapp, R. (2018). The use of disease-modifying therapies in multiple sclerosis, principles and current evidence—a consensus paper by the multiple sclerosis coalition. march 2017. *Accessed January*, 5:06–16.
- Courtine, G., Bunge, M. B., Fawcett, J. W., Grossman, R. G., Kaas, J. H., Lemon, R., Maier, I., Martin, J., Nudo, R. J., Ramon-Cueto, A., et al. (2007). Can experiments in nonhuman primates expedite the translation of treatments for spinal cord injury in humans? *Nature medicine*, 13(5):561.
- De Groot, C., Bergers, E., Kamphorst, W., Ravid, R., Polman, C., Barkhof, F., and Van der Valk, P. (2001). Post-mortem mri-guided sampling of multiple sclerosis brain lesions: increased yield of active demyelinating and (p) reactive lesions. *Brain*, 124(8):1635–1645.
- DeLuca, G. C., Alterman, R., Martin, J. L., Mittal, A., Blundell, S., Bird, S., Beale, H., Hong, L. S., and Esiri, M. M. (2013). Casting light on multiple sclerosis heterogeneity: the role of hla-drbl on spinal cord pathology. *Brain*, 136(4):1025–1034.
- Denic, A., Johnson, A. J., Bieber, A. J., Warrington, A. E., Rodriguez, M., and Pirko, I. (2011). The relevance of animal models in multiple sclerosis research. *Pathophysiology*, 18(1):21–29.
- Deshmane, A., Gulani, V., Griswold, M. A., and Seiberlich, N. (2012). Parallel mr imaging. *Journal of Magnetic Resonance Imaging*, 36(1):55–72.
- Dietemann, J., Thibaut-Menard, A., Warter, J., Neugroschl, C., Tranchant, C., Gillis, C., Eid, M. A., and Bogorin, A. (2000). Mri in multiple sclerosis of the spinal cord: evaluation of fast short-tan inversion-recovery and spin-echo sequences. *Neuroradiology*, 42(11):810–813.

- Duan, Q., Nair, G., Gudino, N., De Zwart, J. A., Van Gelderen, P., Murphy-Boesch, J., Reich, D. S., Duyn, J. H., and Merkle, H. (2015). A 7t spine array based on electric dipole transmitters. *Magnetic resonance in medicine*, 74(4):1189–1197.
- Dula, A. N., Pawate, S., Dortch, R. D., Barry, R. L., George-Durrett, K. M., Lyttle, B. D., Dethrage, L. M., Gore, J. C., and Smith, S. A. (2016). Magnetic resonance imaging of the cervical spinal cord in multiple sclerosis at 7t. *Multiple Sclerosis Journal*, 22(3):320–328.
- Dunham, J., Bauer, J., Campbell, G. R., Mahad, D. J., van Driel, N., van der Pol, S., t Hart, B. A., Lassmann, H., Laman, J. D., van Horssen, J., et al. (2017). Oxidative injury and iron redistribution are pathological hallmarks of marmoset experimental autoimmune encephalomyelitis. *Journal of Neuropathology & Experimental Neurology*, 76(6):467–478.
- Duyn, J. H. (2012). The future of ultra-high field mri and fmri for study of the human brain. *Neuroimage*, 62(2):1241–1248.
- Einstein, E. R., Robertson, D. M., DiCaprio, J. M., and Moore, W. (1962). The isolation from bovine spinal cord of a homogeneous protein with encephalitogenic activity. *Journal of neurochemistry*, 9(4):353–361.
- Falkiewicz, T. (1926). Zur pathologie der multiplen sklerose. *Arb. a. d. neurol. Inst. a. d. Wien. Univ*, (8):28–172.
- Fischer, M. T., Wimmer, I., Höftberger, R., Gerlach, S., Haider, L., Zrzavy, T., Hametner, S., Mahad, D., Binder, C. J., Krumbholz, M., et al. (2013). Disease-specific molecular events in cortical multiple sclerosis lesions. *Brain*, 136(6):1799–1815.
- Fog, T. (1950). TOPOGRAPHIC DISTRIBUTION OF PLAQUES IN THE SPINAL CORD IN MULTIPLE SCLEROSIS. *Archives of Neurology Psychiatry*, 63(3):382–414.
- Fournier, A. P., Gauberti, M., Quenault, A., Vivien, D., Macrez, R., and Docagne, F. (2018). Reduced spinal cord parenchymal cerebrospinal fluid circulation in experimental autoimmune encephalomyelitis. *Journal of Cerebral Blood Flow & Metabolism*, page 0271678X18754732.
- Freund, J., Stern, E., and Pisani, T. (1947). Isoallergic encephalomyelitis and radiculitis in guinea pigs after one injection of brain and mycobacteria in water-in-oil emulsion. *Journal of immunology (Baltimore, Md.: 1950)*, 57(2):179–194.
- Frostell, A., Hakim, R., Thelin, E. P., Mattsson, P., and Svensson, M. (2016). A review of the segmental diameter of the healthy human spinal cord. *Frontiers in neurology*, 7:238.
- Fujiyoshi, K., Yamada, M., Nakamura, M., Yamane, J., Katoh, H., Kitamura, K., Kawai, K., Okada, S., Momoshima, S., Toyama, Y., et al. (2007). In vivo tracing of neural tracts in the intact and injured spinal cord of marmosets by diffusion tensor tractography. *Journal of Neuroscience*, 27(44):11991–11998.
- Gagoski, B. A., Bilgic, B., Eichner, C., Bhat, H., Grant, P. E., Wald, L. L., and Setsompop, K. (2015). Rare/turbo spin echo imaging with simultaneous multislice wave-caipi. *Magnetic resonance in medicine*, 73(3):929–938.
- Gaitán, M. I., Maggi, P., Wohler, J., Leibovitch, E., Sati, P., Calandri, I. L., Merkle, H., Massacesi, L., Silva, A. C., Jacobson, S., et al. (2014). Perivenular brain lesions in a primate multiple sclerosis model at 7-tesla magnetic resonance imaging. *Multiple Sclerosis Journal*, 20(1):64–71.



- Gaitán, M. I., Sati, P., Inati, S. J., and Reich, D. S. (2013). Initial investigation of the blood-brain barrier in ms lesions at 7 tesla. *Multiple Sclerosis Journal*, 19(8):1068–1073.
- Gaitán, M. I., Shea, C. D., Evangelou, I. E., Stone, R. D., Fenton, K. M., Bielekova, B., Massacesi, L., and Reich, D. S. (2011). Evolution of the blood–brain barrier in newly forming multiple sclerosis lesions. *Annals of neurology*, 70(1):22–29.
- Galler, S., Stellmann, J.-P., Young, K., Kutzner, D., Heesen, C., Fiehler, J., and Siemonsen, S. (2016). Improved lesion detection by using axial t2-weighted mri with full spinal cord coverage in multiple sclerosis. *American Journal of Neuroradiology*, 37(5):963–969.
- Gareis, D., Wichmann, T., Lanz, T., Melkus, G., Horn, M., and Jakob, P. M. (2007). Mouse mri using phased-array coils. *NMR in Biomedicine: An International Journal Devoted to the Development and Application of Magnetic Resonance In vivo*, 20(3):326–334.
- Gilmore, C., Geurts, J., Evangelou, N., Bot, J., Van Schijndel, R., Pouwels, P., Barkhof, F., and Bö, L. (2009). Spinal cord grey matter lesions in multiple sclerosis detected by post-mortem high field mr imaging. *Multiple Sclerosis Journal*, 15(2):180–188.
- Gilmore, C. P., Bö, L., Owens, T., Lowe, J., Esiri, M. M., and Evangelou, N. (2006). Spinal cord gray matter demyelination in multiple sclerosis—a novel pattern of residual plaque morphology. *Brain pathology*, 16(3):202–208.
- Gros, C., De Leener, B., Badji, A., Maranzano, J., Eden, D., Dupont, S. M., Talbott, J., Zhuoquiong, R., Liu, Y., Granberg, T., et al. (2019). Automatic segmentation of the spinal cord and intramedullary multiple sclerosis lesions with convolutional neural networks. *Neuroimage*, 184:901–915.
- Guclu, C. C., Boskamp, E., Zheng, T., Becerra, R., and Blawat, L. (2004). A method for preamplifier-decoupling improvement in quadrature phased-array coils. *Journal of Magnetic Resonance Imaging: An Official Journal of the International Society for Magnetic Resonance in Medicine*, 19(2):255–258.
- Guy, J. R., Sati, P., Leibovitch, E., Jacobson, S., Silva, A. C., and Reich, D. S. (2016). Custom fit 3d-printed brain holders for comparison of histology with mri in marmosets. *Journal of neuroscience methods*, 257:55–63.
- Haast, R. A., Ivanov, D., Formisano, E., and Uludağ, K. (2016). Reproducibility and reliability of quantitative and weighted t1 and t2 mapping for myelin-based cortical parcellation at 7 tesla. *Frontiers in neuroanatomy*, 10:112.
- Held, P., Dorenbeck, U., Seitz, J., Fründ, R., and Albrich, H. (2003). Mri of the abnormal cervical spinal cord using 2d spoiled gradient echo multiecho sequence (medic) with magnetization transfer saturation pulse. a t2\* weighted feasibility study. *Journal of neuroradiology. Journal de neuroradiologie*, 30(2):83–90.
- Herren, R. Y. and Alexander, L. (1939). Sulcal and intrinsic blood vessels of human spinal cord. *Archives of Neurology & Psychiatry*, 41(4):678–687.
- Hofstetter, H. H., Shive, C. L., and Forsthuber, T. G. (2002). Pertussis toxin modulates the immune response to neuroantigens injected in incomplete freund’s adjuvant: induction of th1 cells and experimental autoimmune encephalomyelitis in the presence of high frequencies of th2 cells. *The Journal of Immunology*, 169(1):117–125.

- Jagessar, S. A., Kap, Y. S., Heijmans, N., van Driel, N., van Straalen, L., Bajramovic, J. J., Brok, H. P., Blezer, E. L., Bauer, J., Laman, J. D., et al. (2010). Induction of progressive demyelinating autoimmune encephalomyelitis in common marmoset monkeys using mog34-56 peptide in incomplete freund adjuvant. *Journal of Neuropathology & Experimental Neurology*, 69(4):372–385.
- Kabat, E. A., Wolf, A., and Bezer, A. E. (1947). The rapid production of acute disseminated encephalomyelitis in rhesus monkeys by injection of heterologous and homologous brain tissue with adjuvants. *Journal of experimental medicine*, 85(1):117–130.
- Kap, Y. S., Bauer, J., Driel, N. v., Bleeker, W. K., Parren, P. W., Kooi, E.-J., Geurts, J. J., Laman, J. D., Craigen, J. L., Blezer, E., et al. (2011). B-cell depletion attenuates white and gray matter pathology in marmoset experimental autoimmune encephalomyelitis. *Journal of Neuropathology & Experimental Neurology*, 70(11):992–1005.
- Kap, Y. S., Smith, P., Jagessar, S. A., Remarque, E., Blezer, E., Strijkers, G. J., Laman, J. D., Hintzen, R. Q., Bauer, J., Brok, H. P., et al. (2008). Fast progression of recombinant human myelin/oligodendrocyte glycoprotein (mog)-induced experimental autoimmune encephalomyelitis in marmosets is associated with the activation of mog34–56-specific cytotoxic t cells. *The Journal of Immunology*, 180(3):1326–1337.
- Kearney, H., Miszkiel, K., Yiannakas, M., Ciccarelli, O., and Miller, D. (2013). A pilot mri study of white and grey matter involvement by multiple sclerosis spinal cord lesions. *Multiple Sclerosis and Related Disorders*, 2(2):103 – 108.
- Kearney, H., Miszkiel, K. A., Yiannakas, M. C., Altmann, D. R., Ciccarelli, O., and Miller, D. H. (2016). Grey matter involvement by focal cervical spinal cord lesions is associated with progressive multiple sclerosis. *Multiple Sclerosis Journal*, 22(7):910–920. PMID: 26432854.
- Kearney, H., Yiannakas, M. C., Samson, R. S., Wheeler-Kingshott, C. A., Ciccarelli, O., and Miller, D. H. (2014). Investigation of magnetization transfer ratio-derived pial and subpial abnormalities in the multiple sclerosis spinal cord. *Brain*, 137(9):2456–2468.
- Kilsdonk, I. D., Jonkman, L. E., Klaver, R., van Veluw, S. J., Zwanenburg, J. J., Kuijer, J. P., Pouwels, P. J., Twisk, J. W., Wattjes, M. P., Luijten, P. R., et al. (2016). Increased cortical grey matter lesion detection in multiple sclerosis with 7 t mri: a post-mortem verification study. *Brain*, 139(5):1472–1481.
- Kim, J. H. and Song, S.-K. (2013). Diffusion tensor imaging of the mouse brainstem and cervical spinal cord. *Nature protocols*, 8(2):409.
- Klarica, M., Radoš, M., Erceg, G., Petošić, A., Jurjević, I., and Orešković, D. (2014). The influence of body position on cerebrospinal fluid pressure gradient and movement in cats with normal and impaired craniospinal communication. *PLoS One*, 9(4):e95229.
- Klawiter, E. C., Schmidt, R. E., Trinkaus, K., Liang, H.-F., Budde, M. D., Naismith, R. T., Song, S.-K., Cross, A. H., and Benzinger, T. L. (2011). Radial diffusivity predicts demyelination in ex vivo multiple sclerosis spinal cords. *Neuroimage*, 55(4):1454–1460.
- Kramann, N., Neid, K., Menken, L., Schlumbohm, C., Stadelmann, C., Fuchs, E., Brück, W., and Wegner, C. (2015). Increased meningeal t and plasma cell infiltration is associated with early subpial cortical demyelination in common marmosets with experimental autoimmune encephalomyelitis. *Brain pathology*, 25(3):276–286.

- Kranz, P. G. and Amrhein, T. J. (2019). Imaging approach to myelopathy: Acute, subacute, and chronic. *Radiologic Clinics*, 57(2):257–279.
- Kuhlmann, T., Ludwin, S., Prat, A., Antel, J., Brück, W., and Lassmann, H. (2017). An updated histological classification system for multiple sclerosis lesions. *Acta neuropathologica*, 133(1):13–24.
- Kurtzke, J. F. (1983). Rating neurologic impairment in multiple sclerosis: an expanded disability status scale (edss). *Neurology*, 33(11):1444–1444.
- Kutzelnigg, A., Lucchinetti, C. F., Stadelmann, C., Brück, W., Rauschka, H., Bergmann, M., Schmidbauer, M., Parisi, J. E., and Lassmann, H. (2005). Cortical demyelination and diffuse white matter injury in multiple sclerosis. *Brain*, 128(11):2705–2712.
- Laman, J. D., van Meurs, M., Schellekens, M. M., de Boer, M., Melchers, B., Massacesi, L., Lassmann, H., Claassen, E., and A't Hart, B. (1998). Expression of accessory molecules and cytokines in acute eae in marmoset monkeys (*callithrix jacchus*). *Journal of neuroimmunology*, 86(1):30–45.
- Lassmann, H. and Bradl, M. (2017). Multiple sclerosis: experimental models and reality. *Acta neuropathologica*, 133(2):223–244.
- Lavi, E. and Constantinescu, C. S. (2008). *Experimental models of multiple sclerosis*. Springer Science & Business Media.
- Lee, N. J., Ha, S.-K., Sati, P., Absinta, M., Luciano, N. J., Lefevre, J. A., Schindler, M. K., Leibovitch, E. C., Ryu, J. K., Petersen, M. A., et al. (2018). Spatiotemporal distribution of fibrinogen in marmoset and human inflammatory demyelination. *Brain*, 141(6):1637–1649.
- Lefevre, J. A., Guy, J. R., Luciano, N. J., Ha, S.-K., Leibovitch, E., Santin, M. D., Silva, A. C., Jacobson, S., Lehericy, S., Reich, D. S., et al. (2019). The spectrum of spinal cord lesions in a primate model of multiple sclerosis. *Multiple Sclerosis Journal*.
- Lefevre, J. A., Patil, S., Krueger, G., Kober, T., Lehericy, S., Reich, D. S., and Nair, G. (2017). Improved visualization of the spinal cord lesions in multiple sclerosis using mp2rage at 3t. *Proceedings of the 25th International Society of Magnetic Resonance in Medicine*.
- Leibovitch, E. C., Caruso, B., Ha, S. K., Schindler, M. K., Lee, N. J., Luciano, N. J., Billioux, B. J., Guy, J. R., Yen, C., Sati, P., et al. (2018). Herpesvirus trigger accelerates neuroinflammation in a nonhuman primate model of multiple sclerosis. *Proceedings of the National Academy of Sciences*, 115(44):11292–11297.
- Lublin, F. D., Reingold, S. C., Cohen, J. A., Cutter, G. R., Sørensen, P. S., Thompson, A. J., Wolinsky, J. S., Balcer, L. J., Banwell, B., Barkhof, F., et al. (2014). Defining the clinical course of multiple sclerosis: the 2013 revisions. *Neurology*, 83(3):278–286.
- Lublin, F. D., Reingold, S. C., et al. (1996). Defining the clinical course of multiple sclerosis: results of an international survey. *Neurology*, 46(4):907–911.
- Lucchinetti, C., Brück, W., Parisi, J., Scheithauer, B., Rodriguez, M., and Lassmann, H. (2000). Heterogeneity of multiple sclerosis lesions: implications for the pathogenesis of demyelination. *Annals of Neurology: Official Journal of the American Neurological Association and the Child Neurology Society*, 47(6):707–717.

- Lucchinetti, C. F., Popescu, B. F., Bunyan, R. F., Moll, N. M., Roemer, S. F., Lassmann, H., Brück, W., Parisi, J. E., Scheithauer, B. W., Giannini, C., et al. (2011). Inflammatory cortical demyelination in early multiple sclerosis. *New England Journal of Medicine*, 365(23):2188–2197.
- Maggi, P., Macri, S. M. C., Gaitán, M. I., Leibovitch, E., Wholer, J. E., Knight, H. L., Ellis, M., Wu, T., Silva, A. C., Massacesi, L., et al. (2014). The formation of inflammatory demyelinated lesions in cerebral white matter. *Annals of neurology*, 76(4):594–608.
- Maggi, P., Sati, P., and Massacesi, L. (2017). Magnetic resonance imaging of experimental autoimmune encephalomyelitis in the common marmoset. *Journal of neuroimmunology*, 304:86–92.
- Magliozzi, R., Howell, O. W., Reeves, C., Roncaroli, F., Nicholas, R., Serafini, B., Aloisi, F., and Reynolds, R. (2010). A gradient of neuronal loss and meningeal inflammation in multiple sclerosis. *Annals of neurology*, 68(4):477–493.
- Martin, N., Malfair, D., Zhao, Y., Li, D., Traboulsee, A., Lang, D., and Vertinsky, A. T. (2012). Comparison of merge and axial t2-weighted fast spin-echo sequences for detection of multiple sclerosis lesions in the cervical spinal cord. *American Journal of Roentgenology*, 199(1):157–162.
- Massacesi, L., Genain, C. P., Lee-Parritz, D., Letvin, N. L., Canfield, D., and Hauser, S. L. (1995). Active and passively induced experimental autoimmune encephalomyelitis in common marmosets: a new model for multiple sclerosis. *Annals of Neurology: Official Journal of the American Neurological Association and the Child Neurology Society*, 37(4):519–530.
- McDonald, W. I., Compston, A., Edan, G., Goodkin, D., Hartung, H.-P., Lublin, F. D., McFarland, H. F., Paty, D. W., Polman, C. H., Reingold, S. C., et al. (2001). Recommended diagnostic criteria for multiple sclerosis: guidelines from the international panel on the diagnosis of multiple sclerosis. *Annals of Neurology: Official Journal of the American Neurological Association and the Child Neurology Society*, 50(1):121–127.
- McRobbie, D., Moore, E., Graves, M., and Graves, M. (2003, 2006). *MRI: From Picture to Proton*. Cambridge University Press.
- Mogatadakala, K. V., Bankson, J. A., and Narayana, P. A. (2008). Three-element phased-array coil for imaging of rat spinal cord at 7t. *Magnetic resonance in medicine*, 60(6):1498–1505.
- Montalban, X., Hauser, S., Kappos, L., Arnold, D., Bar-Or, A., Comi, G., De Seze, J., Giovannoni, G., Hartung, H., Hemmer, B., et al. (2017). Ocrelizumab versus placebo in primary progressive multiple sclerosis. *New England Journal of Medicine*, 376(3):209–220.
- Nair, G., Absinta, M., and Reich, D. S. (2013). Optimized t1-mprage sequence for better visualization of spinal cord multiple sclerosis lesions at 3t. *American Journal of Neuro-radiology*, 34(11):2215–2222.
- Nakagawa, S. and Schielzeth, H. (2013). A general and simple method for obtaining r2 from generalized linear mixed-effects models. *Methods in Ecology and Evolution*, 4(2):133–142.

- Nijeholt, G., Van Walderveen, M., Castelijns, J., Van Waesberghe, J., Polman, C., Scheltens, P., Rosier, P., Jongen, P., and Barkhof, F. (1998). Brain and spinal cord abnormalities in multiple sclerosis. correlation between mri parameters, clinical subtypes and symptoms. *Brain: a journal of neurology*, 121(4):687–697.
- Nijeholt, G. L. à., Bergers, E., Kamphorst, W., Bot, J., Nicolay, K., Castelijns, J., van Waesberghe, J., Ravid, R., Polman, C., and Barkhof, F. (2001). Post-mortem high-resolution mri of the spinal cord in multiple sclerosis: a correlative study with conventional mri, histopathology and clinical phenotype. *Brain*, 124(1):154–166.
- Norris, D. G., Boyacioglu, R., Schulz, J., Barth, M., and Koopmans, P. J. (2014). Application of pins radiofrequency pulses to reduce power deposition in rare/turbo spin echo imaging of the human head. *Magnetic resonance in medicine*, 71(1):44–49.
- Norton, W. T. and Cammer, W. (1984). Isolation and characterization of myelin. In *Myelin*, pages 147–195. Springer.
- O’Brien, K. R., Kober, T., Hagmann, P., Maeder, P., Marques, J., Lazeyras, F., Krueger, G., and Roche, A. (2014). Robust t1-weighted structural brain imaging and morphometry at 7t using mp2rage. *PloS one*, 9(6):e99676.
- Olitsky, P. K. and Yager, R. H. (1949). Experimental disseminated encephalomyelitis in white mice. *Journal of experimental medicine*, 90(3):213–224.
- Oppenheimer, D. (1978). The cervical cord in multiple sclerosis. *Neuropathology and applied neurobiology*, 4(2):151–162.
- Ozturk, A., Aygun, N., Smith, S. A., Caffo, B., Calabresi, P. A., and Reich, D. S. (2013). Axial 3d gradient-echo imaging for improved multiple sclerosis lesion detection in the cervical spinal cord at 3t. *Neuroradiology*, 55(4):431–439.
- Paugam, F., Lefeuvre, J., Perone, C., Gros, C., Reich, D. S., Sati, P., and Cohen-Adad, J. (2019). Open-source pipeline for multi-class segmentation of the spinal cord with deep learning. *Magnetic Resonance Imaging*.
- Pender, M., Nguyen, K., and Willenborg, D. (1989). Demyelination and early remyelination in experimental allergic encephalomyelitis passively transferred with myelin basic protein-sensitized lymphocytes in the lewis rat. *Journal of neuroimmunology*, 25(2-3):125–142.
- Philpott, C. and Brotchie, P. (2011). Comparison of mri sequences for evaluation of multiple sclerosis of the cervical spinal cord at 3 t. *European journal of radiology*, 80(3):780–785.
- Polman, C., Matthaei, I., De Groot, C., Koetsier, J., Sminia, T., and Dijkstra, C. (1988). Low-dose cyclosporin a induces relapsing remitting experimental allergic encephalomyelitis in the lewis rat. *Journal of neuroimmunology*, 17(3):209–216.
- Polman, C. H., Reingold, S. C., Banwell, B., Clanet, M., Cohen, J. A., Filippi, M., Fujihara, K., Havrdova, E., Hutchinson, M., Kappos, L., et al. (2011). Diagnostic criteria for multiple sclerosis: 2010 revisions to the mcdonald criteria. *Annals of neurology*, 69(2):292–302.
- Pomeroy, I. M., Matthews, P. M., Frank, J. A., Jordan, E. K., and Esiri, M. M. (2005). Demyelinated neocortical lesions in marmoset autoimmune encephalomyelitis mimic those in multiple sclerosis. *Brain*, 128(11):2713–2721.

- Poonawalla, A. H., Hou, P., Nelson, F. A., Wolinsky, J. S., and Narayana, P. A. (2008). Cervical spinal cord lesions in multiple sclerosis: T1-weighted inversion-recovery mr imaging with phase-sensitive reconstruction. *Radiology*, 246(1):258–264.
- Reen, G. K., Silber, E., and Langdon, D. W. (2017). Multiple sclerosis patients’ understanding and preferences for risks and benefits of disease-modifying drugs: A systematic review. *Journal of the neurological sciences*, 375:107–122.
- Reich, D. S., Lucchinetti, C. F., and Calabresi, P. A. (2018). Multiple sclerosis. *New England Journal of Medicine*, 378(2):169–180. PMID: 29320652.
- Reynolds, R., Roncaroli, F., Nicholas, R., Radotra, B., Gveric, D., and Howell, O. (2011). The neuropathological basis of clinical progression in multiple sclerosis. *Acta neuropathologica*, 122(2):155–170.
- Rivers, T. M., Sprunt, D., and Berry, G. (1933). Observations on attempts to produce acute disseminated encephalomyelitis in monkeys. *Journal of Experimental Medicine*, 58(1):39–53.
- Roemer, P. and Edelstein, W. (1987). Ultimate sensitivity limits of surface coils. In *SMRM 6th Annual Meeting*, volume 410.
- Roemer, P. B., Edelstein, W. A., Hayes, C. E., Souza, S. P., and Mueller, O. M. (1990). The nmr phased array. *Magnetic resonance in medicine*, 16(2):192–225.
- Ronneberger, O., Fischer, P., and Brox, T. (2015). U-net: Convolutional networks for biomedical image segmentation. In *International Conference on Medical image computing and computer-assisted intervention*, pages 234–241. Springer.
- Rovira, A., Auger, C., and Alonso, J. (2013). Magnetic resonance monitoring of lesion evolution in multiple sclerosis. *Therapeutic advances in neurological disorders*, 6(5):298–310.
- Rovira, À., Wattjes, M. P., Tintoré, M., Tur, C., Yousry, T. A., Sormani, M. P., De Stefano, N., Filippi, M., Auger, C., Rocca, M. A., et al. (2015). Evidence-based guidelines: Magnims consensus guidelines on the use of mri in multiple sclerosis—clinical implementation in the diagnostic process. *Nature Reviews Neurology*, 11(8):471.
- Sati, P., Oh, J., Constable, R. T., Evangelou, N., Guttmann, C. R., Henry, R. G., Klawiter, E. C., Mainero, C., Massacesi, L., McFarland, H., et al. (2016). The central vein sign and its clinical evaluation for the diagnosis of multiple sclerosis: a consensus statement from the north american imaging in multiple sclerosis cooperative. *Nature Reviews Neurology*, 12(12):714.
- Schellenberg, A. E., Buist, R., Yong, V. W., Del Bigio, M. R., and Peeling, J. (2007). Magnetic resonance imaging of blood–spinal cord barrier disruption in mice with experimental autoimmune encephalomyelitis. *Magnetic Resonance in Medicine: An Official Journal of the International Society for Magnetic Resonance in Medicine*, 58(2):298–305.
- Schindler, M. K., Sati, P., and Reich, D. S. (2017). Insights from ultrahigh field imaging in multiple sclerosis. *Neuroimaging Clinics*, 27(2):357–366.
- Schluesener, H. J., Sobel, R. A., and Weiner, H. L. (1988). Demyelinating experimental allergic encephalomyelitis (eae) in the rat: treatment with a monoclonal antibody against activated t cells. *Journal of neuroimmunology*, 18(4):341–351.

- Schmierer, K., McDowell, A., Petrova, N., Carassiti, D., Thomas, D., and Miquel, M. (2018). Quantifying multiple sclerosis pathology in post mortem spinal cord using mri. *Neuroimage*, 182:251–258.
- Schmierer, K., Wheeler-Kingshott, C. A., Tozer, D. J., Boulby, P. A., Parkes, H. G., Yousry, T. A., Scaravilli, F., Barker, G. J., Tofts, P. S., and Miller, D. H. (2008). Quantitative magnetic resonance of postmortem multiple sclerosis brain before and after fixation. *Magnetic Resonance in Medicine: An Official Journal of the International Society for Magnetic Resonance in Medicine*, 59(2):268–277.
- Sengul, G., Watson, C., Tanaka, I., and Paxinos, G. (2013). Atlas of the spinal cord: Mouse, rat, rhesus, marmoset and human.
- Shrestha, B., Jiang, X., Ge, S., Paul, D., Chianchiano, P., and Pachter, J. S. (2017). Spatiotemporal resolution of spinal meningeal and parenchymal inflammation during experimental autoimmune encephalomyelitis. *Neurobiology of disease*, 108:159–172.
- Solomon, A. J., Naismith, R. T., and Cross, A. H. (2019). Misdiagnosis of multiple sclerosis: Impact of the 2017 mcdonald criteria on clinical practice. *Neurology*, 92(1):26–33.
- Solomon, A. J. and Weinshenker, B. G. (2013). Misdiagnosis of multiple sclerosis: frequency, causes, effects, and prevention. *Current neurology and neuroscience reports*, 13(12):403.
- Sombekke, M. H., Wattjes, M. P., Balk, L. J., Nielsen, J. M., Vrenken, H., Uitdehaag, B. M., Polman, C. H., and Barkhof, F. (2013). Spinal cord lesions in patients with clinically isolated syndrome. *Neurology*, 80(1):69–75.
- Sospedra, M. and Martin, R. (2005). Immunology of multiple sclerosis. *Annu. Rev. Immunol.*, 23:683–747.
- Stankiewicz, J., Neema, M., Alsop, D., Healy, B., Arora, A., Buckle, G., Chitnis, T., Guttmann, C., Hackney, D., and Bakshi, R. (2009). Spinal cord lesions and clinical status in multiple sclerosis: A 1.5 t and 3 t mri study. *Journal of the neurological sciences*, 279(1-2):99–105.
- 't Hart, B. A. and Massacesi, L. (2009). Clinical, pathological, and immunologic aspects of the multiple sclerosis model in common marmosets (*callithrix jacchus*). *Journal of Neuropathology & Experimental Neurology*, 68(4):341–355.
- Tanuma, N., Shin, T., and Matsumoto, Y. (2000). Characterization of acute versus chronic relapsing autoimmune encephalomyelitis in da rats. *Journal of neuroimmunology*, 108(1-2):171–180.
- Thompson, A. J., Banwell, B. L., Barkhof, F., Carroll, W. M., Coetzee, T., Comi, G., Correale, J., Fazekas, F., Filippi, M., Freedman, M. S., et al. (2018). Diagnosis of multiple sclerosis: 2017 revisions of the mcdonald criteria. *The Lancet Neurology*, 17(2):162–173.
- Traboulsee, A., Simon, J., Stone, L., Fisher, E., Jones, D., Malhotra, A., Newsome, S., Oh, J., Reich, D., Richert, N., et al. (2016). Revised recommendations of the consortium of ms centers task force for a standardized mri protocol and clinical guidelines for the diagnosis and follow-up of multiple sclerosis. *American Journal of Neuroradiology*, 37(3):394–401.
- Tustison, N. J., Avants, B. B., Cook, P. A., Zheng, Y., Egan, A., Yushkevich, P. A., and Gee, J. C. (2010). N4itk: improved n3 bias correction. *IEEE transactions on medical imaging*, 29(6):1310.

- Vannesjo, S., Eippert, F., Kong, Y., Clare, S., Miller, K., and Tracey, I. (2016). Breathing-induced b0 field fluctuations in the cervical spinal cord at 7t. In *Proceeding at: 24th Annual Meeting of the International Society for Magnetic Resonance in Medicine (ISMRM)*.
- Vavasour, I. M., Laule, C., Li, D. K., Traboulsee, A. L., and MacKay, A. L. (2011). Is the magnetization transfer ratio a marker for myelin in multiple sclerosis? *Journal of Magnetic Resonance Imaging*, 33(3):710–718.
- Villoslada, P., Hauser, S. L., Bartke, I., Unger, J., Heald, N., Rosenberg, D., Cheung, S. W., Mobley, W. C., Fisher, S., and Genain, C. P. (2000). Human nerve growth factor protects common marmosets against autoimmune encephalomyelitis by switching the balance of t helper cell type 1 and 2 cytokines within the central nervous system. *Journal of Experimental Medicine*, 191(10):1799–1806.
- Waksman, B. H., Porter, H., Lees, M. D., Adams, R. D., and Folch, J. (1954). A study of the chemical nature of components of bovine white matter effective in producing allergic encephalomyelitis in the rabbit. *Journal of Experimental Medicine*, 100(5):451–471.
- Wang, Y., Sun, P., Wang, Q., Trinkaus, K., Schmidt, R. E., Naismith, R. T., Cross, A. H., and Song, S.-K. (2015). Differentiation and quantification of inflammation, demyelination and axon injury or loss in multiple sclerosis. *Brain*, 138(5):1223–1238.
- Wang, Y., Wang, Q., Haldar, J. P., Yeh, F.-C., Xie, M., Sun, P., Tu, T.-W., Trinkaus, K., Klein, R. S., Cross, A. H., et al. (2011). Quantification of increased cellularity during inflammatory demyelination. *Brain*, 134(12):3590–3601.
- Watson, C., Sengul, G., Tanaka, I., Rusznak, Z., and Tokuno, H. (2015). The spinal cord of the common marmoset (*callithrix jacchus*). *Neuroscience research*, 93:164–175.
- Wattjes, M. P., Rovira, À., Miller, D., Yousry, T. A., Sormani, M. P., De Stefano, N., Tintoré, M., Auger, C., Tur, C., Filippi, M., et al. (2015). Evidence-based guidelines: Magnims consensus guidelines on the use of mri in multiple sclerosis—establishing disease prognosis and monitoring patients. *Nature Reviews Neurology*, 11(10):597.
- Weier, K., Mazraeh, J., Naegelin, Y., Thoeni, A., Hirsch, J. G., Fabbro, T., Bruni, N., Duyar, H., Bendfeldt, K., Radue, E.-W., Kappos, L., and Gass, A. (2012). Biplanar mri for the assessment of the spinal cord in multiple sclerosis. *Multiple Sclerosis Journal*, 18(11):1560–1569. PMID: 22539086.
- Wheeler-Kingshott, C. A. and Cercignani, M. (2009). About “axial” and “radial” diffusivities. *Magnetic Resonance in Medicine: An Official Journal of the International Society for Magnetic Resonance in Medicine*, 61(5):1255–1260.
- Winkelman, N. W. and Eckel, J. L. (1932). FOCAL LESIONS OF THE SPINAL CORD DUE TO VASCULAR DISEASE. *Journal of the American Medical Association*, 99(23):1919–1926.
- Zhao, W., Cohen-Adad, J., Polimeni, J. R., Keil, B., Guerin, B., Setsompop, K., Serano, P., Mareyam, A., Hoecht, P., and Wald, L. L. (2014). Nineteen-channel receive array and four-channel transmit array coil for cervical spinal cord imaging at 7t. *Magnetic resonance in medicine*, 72(1):291–300.
- ‘t Hart, B. A., van Kooyk, Y., Geurts, J. J., and Gran, B. (2015). The primate autoimmune encephalomyelitis model; a bridge between mouse and man. *Annals of clinical and translational neurology*, 2(5):581–593.



